AROMATIZATION OF ALKANES OVER Pt INCORPORATED MOLECULAR SIEVES: CATALYTIC AND MOLECULAR MODELING STUDIES

A THESIS

submitted to the

UNIVERSITY OF PUNE

for the degree of

DOCTOR OF PHILOSOPHY

in

CHEMISTRY

By

SURESH B. WAGHMODE

CATALYSIS DIVISION

NATIONAL CHEMICAL LABORATORY

PUNE - 411 008, INDIA

MAY 2002

Dedicated to
My
Family & Teachers…

CERTIFICATE

This is to certify that the work incorporated in the thesis, **“Aromatization of alkanes over Pt incorporated molecular sieves: catalytic and molecular modeling studies”** submitted by **Mr. Suresh B. Waghmode,** for the Degree of ***Doctor of Philosophy,*** was carried out by the candidate under our supervision in the Catalysis Division, National Chemical Laboratory, Pune, INDIA. Such material as has been obtained from other sources has been duly acknowledged in the thesis.

Dr. S. Sivasanker	**Dr. R. Vetrivel**
Research Guide	Research Co-Guide

ACKNOWLEDGEMENT

It is a pleasure to acknowledge with respect the invaluable guidance, numerous discussions, constructive suggestions and support given by Dr. S. Sivasanker, Deputy Director, NCL, Pune through out the course of this investigation. His constant encouragement, insight and close attention to details have lead to the successful completion of this work.

I wish to express my sincere gratitude and indebtness to Dr. R. Vetrivel, GE Bangalore for his co-guidance, through provoking discussions and help rendered through out the course of this investigation without which I would not have completed this work successfully.

I wish to offer my sincere thanks to Dr. A.V. Ramaswamy, Head, Catalysis Division for encouragement and providing all the facilities to carry out the investigation.

I am also deeply indebted to Dr. B.S. Rao, Dr. V.P. Shiralkar, Dr. S. Ganapathy, Dr. S.G. Hegde, Dr. D. Srinivas, Dr. M.K. Dongre, and Dr. C. Gopinath for the stimulating discussions and constant personal help they rendered throughout the course of this investigation.

I wish to express my thanks to Dr. K.J. Waghmare, Dr. V. Ramaswamy, Dr. A.J. Chandwadkar, Dr. H.S. Soni, Dr. S.A. Pardhy, Dr. S.P. Mirajkar, Dr. S.S. Tamankar, Dr. C.V.V. Satyanarayana, Dr. S.B. Halligudi, Dr. Rajmohanan, Dr. V. Bokade, Dr. P. Manikandan, Dr. S.V. Awate, Dr. A. A. Belhekar, Dr. K.R. Kamble, Ms. M.S. Agashe, Mrs. N.E. Jacob, Ms V. Samuel, Mr. P.K. Purushothaman, Kumbhar, Katti, Madhu, Milind and Jagtap and all the other scientific and nonscientific staff in the Catalysis Division, NCL, for their help and cooperation given to me in completing my research work successfully.

I would like to thank my friends, Suhas K., Karuna, Sindhu, Ramesh, Siddhesh, Tapan, Anil, Venkat, Raja, Bennur, Smita, Balu, Suhas C., Raja T., Vasu, Abhimanyu, Rajendra, Vijayraj, Sachin, Prashant, Prafull, Roshan, Naresh and Rohit for their cheerful co-operation and help through out this investigation. I also thank my friends Milind, Vinay, Kailas, Uddhav, Shivnand, Anil, Vallabh, Sunil, Ilias, Shiju, Thomas, Anand, Chandrkumar, Sailaja, Laha, Patra, Mulla, Sabde, Dr. Gore, Anuji, Mahesh, Pretti, Pallavi, Sharda and my many other friends for their wholehearted help and discussion.

Finally, no words can express my feelings towards may parents, brothers, Parshuram, Santosh and my wife Rohini, for their love and unfailing support. This work would never have received the present shape had it not been backed by their constant encouragement and patience.

Finally, my thanks are due to Dr. P. Ratnasamy, Director, National Chemical Laboratory, for permitting me to carry out my research work at NCL and to the Council of Scientific & Industrial Research, New Delhi, for my fellowship award.

SURESH B. WAGHMODE

CONTENTS

LIST OF ABBRIVATIONS

atm.	Atmosphere
1 a.u.	27.21161 eV
BEA	Zeolite Beta
DFT	Density Functional Theory
EM	Energy Minimization
FAU	Faujasite
ECP	Effective Core Potential
ETS-10	Engelhard Titanosilicate -10
FTIR	Fourier Transform Infra Red
1 eV	23.06 kcal
GAMESS	General Atomic and Molecular Electronic Structure System
HC	Hydrocarbon
HDS	Hydrodesulfurization
HF	Hartree-Fock
HOMO	Highest Occupied Molecular Orbital
HREM	High Resolution Electron Microscope
IR	Infra Red
1 kcal	4.184 Kilo joule
kcal	Kilo calorie
LCAO	Linear Combination of Atomic Orbital
LTL	Linde Type L
LUMO	Lowest Unoccupied Molecular Orbital
MD	Molecular Dynamics
MG	Molecular Graphics
ml	Milliliter
MNDO	Modified Neglect of Diatomic Overlap
mol	Mole
12-MR	Twelve Membered Ring
NMR	Nuclear Magnetic Resonance
Oh	Octahedra
QC	Quantum Chemical
Td	Tetrahedra
Temp.	Temperature
TPD	Temperature Programmed Desorption
TS-1	Titanosilicalite-1
UV-Vis	Ultra Violet Visible
wt	Weight
WHSV	Weight Hourly Space Velocity
XPS	X-ray Photoelectron Spectroscopy
XRD	X-ray Diffraction

CHAPTER 1

INTRODUCTION

1.1. AROMATIZATION OF ALKANES

The aromatization of *n*-alkanes is an industrially important reaction; it is one of the major reactions occurring during the reforming of naphtha fractions for the production of aromatics or high-octane gasoline. *n*-Alkanes possess low-octane numbers (octane number of *n*-hexane = 19; *n*-heptane = 0 and *n*-octane = 19) while aromatic compounds with the same carbon numbers possess much larger octane numbers (octane number of benzene = 99; toluene = 124 and *m*-xylene = 145). Hence, the aromatization of alkanes (especially *n*-alkanes) is important in improving the octane number of the naphtha. A typical aromatization reaction is shown below:

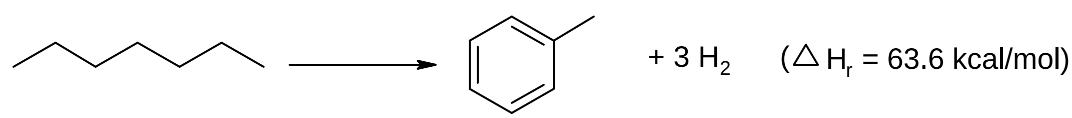

Scheme 1.1: Typical example of an aromatization reaction.

Aromatization reactions are endothermic (Scheme 1.1) and favored at high temperatures. The reforming of naphtha is therefore, generally carried out at temperatures in the range of 753 - 793 K.

1.2. CATALYTIC NAPHTHA REFORMING

Catalytic reforming was originally developed to produce high-octane gasoline from straight run naphtha for automotive applications. Subsequently, applications have extended to the production of aromatics, LPG, H_2 and to the upgrading of olefinic stocks and raffinates. Both dual functional and mono functional catalytic reforming catalysts/ processes are available, the former process being the most widely used and suited for a wide range of feedstocks. In monofunctional reforming, only the metallic function takes part in the reaction and is suited mainly for the dehydrocyclization of C_6-C_8 *n*-alkanes.

1.2.1. Dual Functional Catalytic Reforming: In the early 1940s, chromia-alumina and subsequently, molybdena catalysts were used in catalytic reforming. A breakthrough in catalytic reforming was the commercialization by UOP (Universal Oil Products, USA) of the platforming process based on a Pt-alumina catalyst, which was an order of magnitude more active than the earlier oxide catalysts. The early Pt-Al_2O_3 catalysts had about 0.3 to 0.6 wt % Pt supported on a fluorided η-Al_2O_3 (later, chlorided γ-Al_2O_3). The next improvement in catalytic reforming came with the introduction of the bimetallic Pt-Re catalyst by Chevron, USA in 1969. Subsequently, other bimetallic and multi-metallic catalysts containing promoters such as Ir, Sn and Ge have come into practice.

The conventional reforming catalysts operate primarily by a dual functional mechanism, the acid sites of the support (chlorided-alumina) taking part in isomerization and cyclization reactions and the metallic function acting as the dehydrogenation-hydrogenation agent.

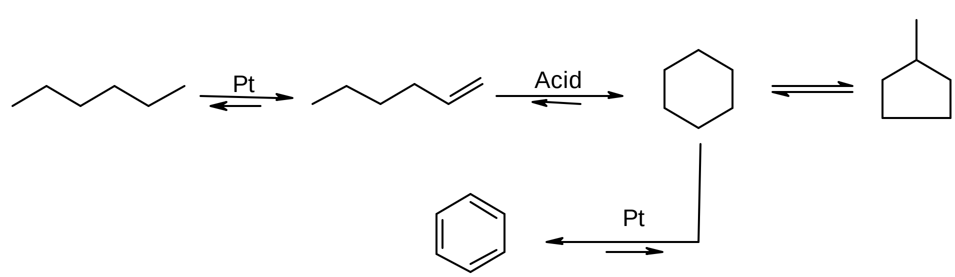

Scheme 1.2. Steps in the dehydrocyclization of *n*-hexane to benzene over a bifunctional reforming catalyst.

For example, the transformation of *n*-hexane to benzene is believed to take place according to the following steps (Scheme 1.2).[1]

1. Dehydrogenation to hexenes (metal catalyzed)
2. Isomerization to cyclohexane (acid catalyzed)
3. Dehydrogenation of cyclohexane to benzene (metal catalyzed).

The major reactions that take place during the reforming of a naphtha fraction are: i) dehydrogenation of naphthenes to aromatics (e.g. methylcyclohexane to toluene), ii) dehydrocyclization of alkanes to aromatics (e.g. *n*-heptane to iso-heptanes to toluene), iii) hydoisomerization of alkanes (e.g. *n*-heptane to iso-heptanes and alkylcyclohexanes) iv) isomerization of alkyl aromatics and v) hydrogenolysis and hydrocracking.

Table 1.1 Thermodynamic data for typical reforming reactions[1]

Reaction	K_p at 773 K, atm.	ΔH_r, kcal/mol of hydrocarbon
Cyclohexane $\rightleftharpoons$ benzene + $2H_2$	6 X 10^5	52.8
Methylcyclopentane $\rightleftharpoons$ cyclohexane	0.086	-3.8
n-Hexane $\rightleftharpoons$ benzene + 4 H_2	0.78 X 10^5	63.6
n-Hexane $\rightleftharpoons$ 2-methylpentane	1.1	-1.4
n-Hexane $\rightleftharpoons$ 1-hexene + H_2	0.037	31.0

The thermodynamic data for typical reactions taking place during the reforming of naphtha are presented in Table 1.1. Except dealkylation, hydrogenolysis and hydrocracking reactions, which lower liquid yield, the other reactions are the desired ones. The reactions, i) and ii) are highly endothermic while iii) to v) are mildly exothermic making the overall reforming process endothermic. The dehydrogenation and dehydrocyclization reactions decrease with pressure while the hydrogenolysis and hydrocracking reactions increase with pressure. All the reactions are favored at high temperatures. Thus, reforming is best carried out at low pressures and high temperatures. Under these conditions, though, the catalysts tend to deactivate faster, especially the monometallic (Pt only) catalysts due to rapid coke deposition. The major advantage of the bi- and multi-metallic catalysts over the monometallic catalyst is their greater ability to operate at lower pressures and higher temperatures, conditions conducive for aromatics production. The typical conditions of the reforming operation are: monometallic catalysts, pressure of 20 - 40 bars and temperature of 753 – 793 K; multi-metallic catalysts, pressure of 2 - 10 bars and temperature of 773 – 810 K.

The feedstock for naphtha reforming is generally straight run naphtha, which contains 10 to 50 ppm of S. The boiling range of the naphtha fraction will depend on the requirement; for gasoline production, a full range naphtha (353-453K) may be used. Naphtha reforming catalysts are S-intolerant and the S content has to be brought down to < 5 ppm for monometallic catalysts and < 0.5 ppm for bi- and multi-metallic catalysts. The S tolerance of a given catalyst depends on the severity of operation, the more severe (low pressure and high temperature) the operation, the less the S to be present in the feed. The feed S is brought to the desired specifications by hydrodesulfurization (HDS) over Co-Mo-alumina catalysts.

1.2.2. Monofunctional Catalytic Reforming: The major drawbacks of bifunctional catalysts are their inability to transform significant amounts of the C_6 hydrocarbons such as *n*-hexane and methyl cyclopentane into aromatics and the occurrence of simultaneous parallel reactions such as isomerization and hydrogenolysis leading to low selectivity to aromatics. Dehydrocyclization of C_6-C_8 alkanes has been reported to occur with high selectivities for aromatics over Pt-supported on basic zeolites such as

Pt-K-LTL.[2] Based on the above catalysts, a new process (AROMAX) has been commercialized by Chevron.[3] Other basic zeolites such as Pt-M-BEA and Pt-M-ETS-10 (where M = Li, Na, K, Rb, Cs, Mg, Ca, Sr or Ba) have also been reported to possess larger dehydrocyclization activities than Pt-Al_2O_3.[4-6]

Many possible reasons have been suggested for the spectacular activity of Pt-M-LTL. These are: i) there is an electronic interaction between the zeolite and the Pt metal,[7,8] ii) structural parameters of the zeolite are responsible,[9] iii) collimation and head-on interaction of *n*-hexane molecules with Pt,[10] iv) inhibition of carbon deposition over the Pt atoms,[11] and v) high dispersion and stability of Pt.[12,13] Based on studies on benzene hydrogenation and *n*-hexane reforming studies over a series of Pt-M-LTL catalysts exchanged with different alkali metal ions (Li, Na, K, Rb or Cs), Besoukhanova *et al.*[7] have shown that the activity of the catalyst increases with the basicity of the exchanged ion (Cs > Rb > K > Na > Li). Based on the IR vibrational frequency shifts of CO adsorbed on Pt, the authors have concluded that the Pt particles in these catalysts are electron rich from interaction with the basic O^{2-} ions in the lattice.[7] Larsen and Haller[8] have made similar conclusions based on their study of competitive hydrogenation of toluene and benzene over Pt-M-LTL, where M = Mg, Ca or Ba.

On the other hand, Tauster and Steger[10] agree with Derouane and Vanderveken[9] that the pore openings in LTL-zeolite collimate diffusing *n*-hexane molecules leading to their end-on adsorption over the Pt clusters situated inside the cancrinite cages. Such end-on adsorption should facilitate 1- 6 ring closure leading to aromatization. Other workers[13] have also reported that the structural effect of the LTL zeolite is responsible for the exceptional dehydrocyclization activity of these catalysts. Davis and Derouane[12] reported that Pt supported on basic Mg(Al)O mixed oxide prepared from hydrotalcites also makes a good catalyst for the aromatization of *n*-hexane. Even though some structural features of zeolites may assist 1-6 ring cyclization, it is strongly evident that the enhanced dehydrocyclization activity of Pt supported on alkaline supports is a result of electronic interactions between the support and the Pt. Thus, Larsen and Haller[8] have suggested that the electron rich nature of Pt in Pt-K-LTL is responsible for its greater S sensitivity, in contrast to the greater S-tolerance of Pt-H-FAU, which is electron deficient.[13]

1.3. ZEOLITES AS CATALYSTS AND SUPPORTS

Zeolites are microporous inorganic compounds, the pores and voids arising from their framework structure. Zeolites are made up of an extensive linkage of SiO_4^{4-} and AlO_4^{5-} tetrahedra joined together through the oxygen atoms.[14-16] Strictly speaking, the term zeolite is restricted to aluminosilicates; but in practice, the field now encompasses microporous aluminophosphates, germanates, borates and titanosilicates. The term "zeolite" meaning "boiling stone" in Greek (*zeo* = boil and *lithos* = stone) was coined by Cronstedt[17] in 1756, to describe the behavior of the newly discovered mineral stilbite, which lost water on heating. According to Smith,[18] "a zeolite is an aluminosilicate with a framework structure enclosing cavities occupied by large ions and water molecules, both of which have considerable freedom of movement, permitting ion exchange and reversible dehydration". In aluminosilicates, additional cations are incorporated interstitially within the lattice so as to compensate the negative charges created by the incorporation of Al^{3+} ions in the SiO_4 framework. The framework contains pores and voids, the nature and dimensions of which depend on the arrangement of the [SiO_4] and [AlO_4] tetrahedra to create the framework. The charge balancing cations are present in the channels and voids close to the Al^{3+} ions.

The effective pore sizes in zeolites range from ~3 Å to over 10 Å, just sufficient to permit the diffusion and catalytic transformation of most organic molecules of commercial interest. This fact combined with the possibility of generating active sites inside the channels and cavities, and the large surface area created by these channels and voids makes zeolites unique catalysts that can be considered as catalytic microreactors.[19]

1.4. STRUCTURE AND CLASSIFICATION OF ZEOLITES

The primary building units of the zeolite structure are the individual tetrahedral TO_4 units, where T is Si^{4+} or Al^{3+}. A secondary building unit (SBU) consists of selected geometric groupings of these tetrahedra. These building units, which generally consist of 4, 6 and 8 membered rings, 4-1, 5-1 and 4-4-1 branched rings[15] can be used to describe most of the known zeolite structures. For a broader classification of microporous materials, which includes titanosilicates, additional types of building units are required. Classification of zeolites can be made on the basis of their morphological characteristics,[17,20-22] crystal structure,[14,23] chemical composition,[14,24] effective pore diameter[14,25] and natural occurrence.[20] The classification of zeolites according to their chemical composition (Si/Al ratio) is:[24] (a) low silica, Si/Al = 1 to 1.5 [A, FAU (X), sodalite etc.]; (b) medium silica, Si/Al = 1.5 to 10 [FAU (Y), LTL, mordenite etc.]; (c) high silica, Si/Al = 10 to several thousands (ZSM-5, -11, SSZ-31, -24, -42, EU-1 etc.) and (d) Al free (silicalite-1, 2, MCM-41 etc.). Some of the common zeolites and micro- and mesoporous materials are listed in Table 1.2.

Zeolites can also classified according to their pore opening as: (a) small pore (dia. = 3 - 4 Å; A, chabazite etc.), (b) medium pore (dia. = 4 to 10 Å; ZSM-5, -11 SAPO-11, ferrierite etc.), (c) large pore (dia. = 10 to 20 Å; X, Y, BEA, ETS-10 etc.)

and mesopore (dia. ≥ 20 Å; MCM-41, VPI-18, EMS etc.). Zeolites can also be classified according to the dimensionality of the pores, i.e., one-dimensional (1D), two-dimensional (2D) and three-dimensional (3D). The crystallographic unit cell of a zeolite may be represented by the general formula (1.1). [20]

$$M^{n+}_{x/n}\,[AlO_2)_x(SiO_2)_y].\ mH_2O, \text{ where } y \geq x \qquad (1.1)$$

Table 1.2 Classification of some typical microprous and mesoporous materials based on their pore diameter, pore dimension and Si/Al ratio

Molecular sieve type	IZA code	Si/Al ratio	Ring size[a]	Pore dia. (Å)[b]	Pore dimensionality	Relative pore size
Linde type A	LTA	1 - 1.5	8-8-8	4.1	3	Small
Chabazite	CHA	1 - 1.5	8-8-8	3.8 x 3.8	3	Small
ZSM-5	MFI	7 – 100	10-10-10	5.4 x 5.6	3	Medium
ZSM-11	MEL	20 – 90	10-10-10	5.3 x 5.4	3	Medium
ZSM-48	-	50 ≥	10	5.3 x 5.6	1	Medium
SAPO-11	AEL	-	10	3.9 x 6.3	1	Medium
Faujasite (Y)	FAU	1.5 - 3.0	12-12-12	7.4	3	Large
Faujasite (X)	FAU	1.0 - 1.5	12-12-12	7.4	3	Large
Linde type L	LTL	4.5-12.0	12	7.1	1	Large
Beta	BEA	10 – 100	12-12	6.4 x 7.6	3	Large
ETS-10	E	-	12-12-7	4.9 x 7.6	3	Large
VPI-5	VPI	-	18	12.1	1	Very large
MCM-41	-	-	-	20-100	1	Meso

[a] number of T or O atoms comprising smallest rings in channel, [b] pore diameter of largest channel.

The ratio x/ y is smaller than or equal to one because aluminate tetrahedra cannot be neighbours in the framework of zeolites, i.e. Al-O-Al linkages are forbidden according to the Löwenstein rule [16] and 'm' is the number of water molecules. The sum (x + y) is the total number of tetrahedral sites. The properties of zeolites of great practical importance are their ability to sorb organic substances, to act as cation exchangers and to catalyze a wide variety of reactions.

1.5. BASIC ZEOLITE CATALYSTS

Interest in acidic and basic zeolites has been fuelled by their wide use; first as heterogeneous catalysts, where 'shape-selectivity' conferred upon the materials by their microporous structure is often important. The use of zeolites as heterogeneous acid catalysts has attracted much attention primarily because they are the major catalysts used in petroleum refining; for example the cracking process, which is the largest among the industrial chemical process uses acidic zeolites as catalysts. In contrast to the extensive studies on heterogeneous acidic catalysts, much less research has been carried out on the study of heterogeneous basic catalysts. The presence of basic centers in some oxides has been recognized for a long time as being important in catalysis.[26,29] Pines *et al.*[30] reported in 1955 that sodium metal dispersed on alumina was an effective catalyst for double bond migration of alkenes. Kokes *et al.*[31,32] reported in 1972 that hydrogen molecule is adsorbed on zinc oxide by acid-base interactions to form proton (H^+) and hydride (H^-) species on the surface. The catalytic activities of basic zeolites were reported by Yashima *et al.*[33] in early 70s.

Different types of heterogeneous basic catalysts[33] are listed in Table 1.3. In addition to the above mentioned catalysts, a number of basic materials have been reported to act as heterogeneous basic catalysts. The substitution of Al in a SiO_4 framework generates a charge imbalance, which must be countered. This is done by a supplementary counter ion, the most important of which (in zeolite chemistry) being the proton in the acidic zeolites. These protons are easily exchangeable. When this charge is balanced by cations like K, Cs and Rb, they generate a basic nature. The significance of these ions can be shown quite easily by comparisons of experiments over H exchanged zeolites and their equivalent cationic (such as Li, Na, K, Rb, Cs, Mg, Ca, Sr and Ba etc.) forms of the zeolites. The zeolitic proton has been used as efficient solid acid catalysts in several industrial reactions and different cation exchanged zeolites have been found useful as solid base catalysts in several reactions.

Table 1.3 Types of heterogeneous basic catalysts[33]

Heterogeneous basic catalyst type	Examples
Single Metal oxides	Alkali and alkaline earth metal oxides, ThO_2, ZrO_2, ZnO, TiO_2 and rare-earth oxides
Zeolites	Alkali ion exchanged zeolites, Alkali oxides loaded zeolites
Supported alkali metal ions	Alkali metal oxides on alumina or silica or alkaline earth oxides, Alkali metals and alkali metal hydroxides on alumina
Clay minerals	Hydrotalcite, chrysolite, sepiolite etc.
Non-oxide	KF supported on alumina, Lanthanide imide and nitride on zeolite

The basicity of a zeolite depends on the cations that are present, the T-O-T angles and the distance between the T atom and oxygen. This has, in turn, led to an increased interest in understanding the structure, active sites and properties of zeolites. Basicity originates from the framework O^{2-} ions. It may also originate from other sites through hydrolysis of metal ions, from exchanged oxide clusters, supported metals, or reducing centers. It may also be associated with acidity in acid-base pairs.

1.5.1. Brønsted Sites: The negatively charged lattice of Si - Al zeolites does not lead to the existence of basic framework OH^- groups. The basic OH groups reported are linked to extra-framework species. Small clusters of alkaline earth metal oxides (MgO or CaO) in FAU cages have been shown to generate basic hydroxyls,[34,35] identified by FTIR, with vibration bands at 3685 (Mg-FAU) and 3675 cm^{-1} (Ca-FAU).[36]

$$M^{2+}(H_2O) \rightarrow M^{2+}\,OH^- + H^- \qquad (1.2)$$

1.5.2. Structural Basicity: The framework oxygens bearing the negative charge of the lattice are the structural basic sites. In many structures all the oxygen atoms are accessible to adsobate or reactant molecules as in faujasite zeolite (FAU). In less open structures like LTL and mordenite zeolites, some oxygen atoms belong to cages that are too small to be accessible. It follows that only a part of all the existing basic oxygens will interact with adsorbate or reactant molecules in these zeolites. Another characteristic of the oxygen atom sites is that they are fixed between two T atoms. They are not mobile like protons in acidic zeolites and cations in basic zeolites. The H^+ ion may move to reactants or adsorbates while the molecules have to approach the lattice oxygen in a configuration that is favorable for the formation of the reaction intermediate.

The zeolite chemical composition and the structure type affect oxygen basicity. In zeolites, the most negative oxygens belong to the AlO_4 tetrahedra.[37] The charge on oxygen, which is a measure of basicity, can be computed.[38,39] Another factor influencing the oxygen charge is the T-O-T bond angle. The electronic charge on oxygen (basic strength) increases when the T-O-T angles are narrower and the T-O distances are longer.[37,40] In non-protonic zeolites the T-O-T angle varies to a large extent and gives rise to O^{2-} with a variety of possible basic strengths. The basicity varies depending on the Al location in the lattice, on the nature of the cation (i.e. identity, content, valency or location) and on the accessibility of framework oxygens. Hence, the basicity of specific oxygen atoms actually involved in adsorption or catalytic processes cannot be predicted based on bond angle measurements alone.

1.5.3. Clusters of Oxides and Hydroxides: Very small clusters of basic oxides (MgO, CaO, ZnO) can be encapsulated in zeolite cages to prepare basic catalysts.[27,38,39,41-45] It is reported that MgO and CaO clusters were generated in Mg-FAU (Y) and Ca-FAU (Y) upon heating above 773-873 K;[41] the clusters were present inside the supercages (confirmed by ESR, IR and XRD). Clusters of MgO and M_2O (M = Na, K, Rb and Cs) were prepared in FAU (Y and X) zeolites by soaking them in solutions of magnesium dimethoxide (alcoholic solutions) or alkali acetates (aqueous solutions).[41] Strong basic sites were obtained in the Mg case only if the ensemble (Mg and O) forms an MgO lattice, while isolated M_2O species produced strong basicity in the case of the alkali metal oxides.[41]

Another method to introduce basic clusters into zeolites is to impregnate the zeolites within a compatible pH range, with solutions of salts or hydroxides and drying or calcining. For instance, the addition of a hydroxide (KOH or CsOH etc.) to the zeolite increased the basicity of the zeolite. This was confirmed by the increased chain selectivity in the alkylation of toluene with methanol.[45-47] Two general trends are observed in the properties of these materials. Firstly, exchanged zeolites are less basic than those containing additional clusters of oxides. Secondly, carbonates are formed very easily from these oxides with atmospheric CO_2.

1.5.4. Alkali Metal Clusters: Interaction of alkali metal vapours with zeolites generates colored products, which often possess basic properties. It was first reported that Na_6^{5+} and Na_4^{3+} paramagnetic centers were formed in alkali FAU (X and Y) zeolites.[48,49] Simultaneously, small neutral metal clusters were formed in alkaline FAU (X and Y) outside the zeolite framework.[50,51] These materials can be used as quantum dots.[52,53] The formation of Na_6^{5+}, Na_5^{4+}, Na_4^{3+}, K_3^{2+} has been reported in zeolites A and FAU in addition to other alkali metal species.[50,51,54-58] The dependence of selectivity in the alkylation of toluene with methanol upon the acidic and non-acidic character of zeolites was first mentioned by Sidirenko *et al.*[59] This was further studied in detail and the formation of ethylbenzene and styrene was linked to basic sites in FAU (X and Y) exchanged with K, Rb and Cs cations.

Alkaline molecular sieves may be formed by hydroxides or oxides, not only in basic or neutral Si-Al zeolites,[20,35,36,37-45,46-48] but also in mesoporous molecular sieves. While Na-MCM-41 and Cs-MCM-41 (prepared by ion exchange) are active in base catalyzed Knovenagel condensation, cesium acetate impregnated MCM-41 is active in Michael addition and appears to be a promising super base catalyst.[60]

1.5.5. Species and Clusters Related to Basic Centers:

1.5.5.1. Acid-base pairs: The existence of acid-base sites in zeolites has been reported.[59,61] The cation acts as the Lewis acid[62,63] and the framework oxygen as the base. For a given Al content the acid character prevails for cations with a high electronegativity. The basic properties increase in parallel with the Al content of the zeolite.

1.5.5.2. Metal carbonyls: A large amount of work has been devoted to the study of the formation and properties of transition metal complexes encapsulated inside the voids of zeolites.[64-67] The zeolite acts as a solvent, an anion and a ligand.[64,65] Among all the complexes, metal carbonyls are of particular importance as potential catalysts for hydrogenation, isomerization, hydroformylation and carbonylation.[65] The influence of zeolite basicity has been considered recently with reference to the properties of encapsulated carbonyls of Pt,[68] Mo,[69] Os,[70] Rh,[71] or Ir.[72] The thermal stability of $Fe(CO)_5$ is higher in Na-FAU (X) than in Na-FAY (Y), reflecting a stronger interaction of the carbonyl with the Al rich zeolite.[73]

1.6. CHARACTERIZATION OF BASIC SITES

The surface properties of basic catalysts can be calculated by various methods including the following. No single method provides the complete information. An understanding of the structure, reactivity, strength and the number of basic sites on the surfaces can be obtained by a combination of many methods. These methods are briefly described in the following sections.

1.6.1. Experimental Approaches:

1.6.1.1. X-ray diffraction (XRD): The acidity of the OH groups and corresponding basicity of the oxygen can be correlated to the T-O-T bond angles determined from XRD[40] studies. However, this method does not distinguish Al-O-Si or Si-O- Si species of the framework. The measured angles represent only an average for any oxygen type considered.

1.6.1.2. X-ray photoelectron spectroscopy (XPS): The binding energy (BE) of oxygen is a measure of its basicity. As the BE (O_{1S}) decreases, electron pair donation becomes easier. Okamoto *et al.*[74] studied the effects of zeolite composition and the type of cation on the binding energy (BE) of the constituent elements for FAU (X and Y) zeolites ion exchanged with a series of alkali cations as well as H-forms of A, FAU (X, Y) and mordenite.[75,76] The BE (O_{1s}) of a zeolite directly delineates the electron density of the framework oxygen. On the basis of XPS features of zeolites, Okamoto *et al.*[74] also proposed a bonding model of a zeolite as shown in Fig. 1.1. Configurations I and II are in resonance. In configuration I, extra-framework cations form covalent bonds with framework oxygens, while in configuration II, the cations form fully ionic bondings with the negatively charged zeolite lattice. As the electronegativity of the cations increases and approaches that of oxygen, the contribution of configuration I increase to reduce the net charge of the lattice. This explains the dependence of BE (O_{1s}) on the electronegativity of the cation. However, the XPS method applies only to few surface layers of the catalysts.

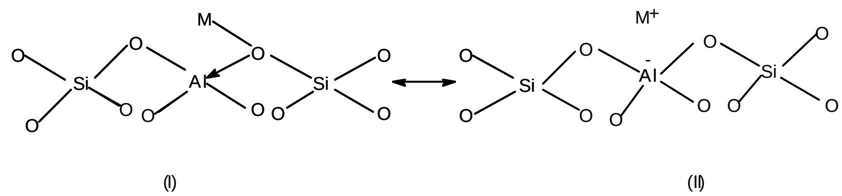

Fig. 1.1. Schematic bonding model of a zeolite.

1.6.1.3. Nuclear magnetic resonance spectroscopy (NMR): The chemical shift (δ) of an atom observed in NMR spectroscopy may be related to the charge and the bond angle associated with that atom in the crystalline structure.[77] ^{17}O NMR distinguishes the various species, Si-O-Si (δ = 44 to 52 ppm), Si-O-Al (δ_0 = 31 to 40 ppm) and Si-O-Ga (δ_0 = 28 - 29 ppm), in zeolites A, FAU (Y, X) and sodalite.[78,79] The decrease in the chemical shift of oxygen (δ) as the T atom changes from Si to Al and Ga is attributed to an increase in negative charge on oxygen (basicity), as Si is replaced by Al and in Ga the zeolite structure.[54]

1.6.1.4. Indicator method: The basic strength of solid surfaces may be expressed in terms the acidity function ($H\_$) as proposed by Paul and Long.[80] The H_- function is defined by the following equation.[80,81]

$$H\_ = pK_{BH} + \log [B^-] / [BH] \qquad (1.3)$$

where $[B^-]$ is the conjugate base and pK_{BH} is the logarithm of the dissociation constant of BH. The reaction of the indicator BH with the basic site (B) is:

$$BH + \underline{B} = B^- + \underline{B}H^+ . \quad (1.4)$$

1.6.1.5. Temperature programmed desorption (TPD) of carbon dioxide: Thermoprogrammed desorption can give valuable information on the interaction of acid molecules with basic sites. This method may give access to the strength and the number of basic sites present. The strength and amount of basic sites are reflected in the desorption temperature and the peak area, respectively, in TPD plots. However, it is difficult to express the strength on a definite scale and count the number of sites quantitatively. Relative strengths and relative numbers of basic sites on the different catalysts can be estimated by carrying out the TPD experiments under the same conditions.[82]

1.6.1.6. UV-absorption and luminescence spectroscopy: UV absorption and luminescence spectroscopies give information about the coordination states of the surface sites.[83,84] They have been used to study the co-ordination and nature of Si, Al and Ti species.

1.6.1.7. Temperature programmed desorption (TPD) of hydrogen: This method gives information about the co-ordination state of the surface ion pairs when combined with other methods such as UV-absorption and luminescence spectroscopies. The number of each ion pair could be counted if the TPD is accurately measured with proper calibration. This method has been applied to the MgO surface. Hydrogen is heterolytically dissociated on the surface of MgO to form H^+ and H^-, which are adsorbed on MgO.[85,86]

1.6.1.8. IR of adsorbed carbon dioxide*:* The choice of a good probe for the measurement of basicity is a major problem. It should react specifically with the basic sites under consideration (framework oxygen, basic hydroxyls, oxide cluster). A variety of probe molecules are known for the characterization of basic sites (O^{2-} and OH^{-}) on oxides.[27, 87-89] For a probe molecule to behave ideally, they must possess certain properties and fulfill certain criteria. Such criteria for the selection of probe molecules were first formulated by Paukshtis *et al.*,[90] Knözinger,[91] Lercher *et al.*,[92] Kustov[93] and Wakabayashi and Domen.[94] The guidelines for the selection of an ideal probe molecule are: a) a detectable spectral response is induced by acid-base interaction between the acidic probe and a surface base, b) the probe molecule should interact with basic sites, c) frequency shift must be measurable with sufficient accuracy and d) the probe molecule should be as small as possible so as to permit access of sites in narrow pores.

The adsorption of carbon dioxide appears to involve both physical adsorption and chemisorption. The kinetic diameter of a CO_2 molecule is 3.3 Å; it can enter both 10-MR and 12-MR easily. Deuterated chloroform[95] and pyrrole[96,97] interact with basic sites through H bonding. CO can interact with basic O^{2-} sites forming carbonates and CO_2^{2-} ions.[88] CO_2 forms a variety of carbonates including mono- and bicarbonates, polycarbonates or hydrogen carbonates. Many different modes of CO_2 adsorption have been proposed; interactions with the cation or the oxygen of the oxides[98] are shown in Fig. 1.2. CO_2 adsorption gives information about the adsorbed state of CO_2 on the surface of the catalyst. CO_2 interacts strongly with a basic site and, therefore, the surface structure including basic sites is estimated from the adsorbed state of CO_2.

Recently Davis *et al.*[99] studied the interactions of CO_2 on Rb supported on MgO, TiO_2, Al_2O_3 and SiO_2 by IR spectroscopy.

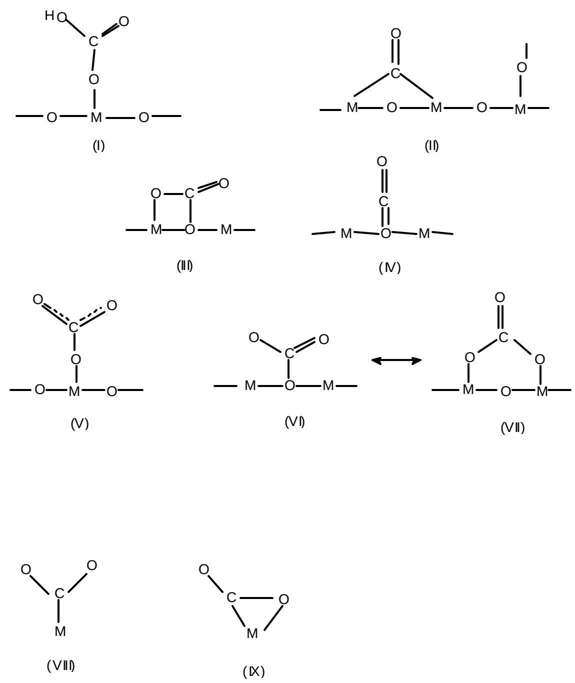

Fig. 1.2. Adsorbed CO_2 species on metal oxides and metals.

They reported that the strongest basic sites formed by the incorporation of Rb were found on Rb/ MgO, which contained significant carbonate species even after heating to 773 K. Carbonates were not present on the other heat-treated Rb catalysts. The least basic support, silica, is thought to react with Rb to form a highly disordered, weakly basic surface silicate. Auroux *et al.*[98] have studied the acidobasic properties of various oxides. According to them CO_2 molecules can be adsorbed on positive and negative surfaces. The adsorbed CO_2 (carbonates) may then block the surface sites. The different ways CO_2 adsorption occurs on the surface of oxides can be summarized: a) adsorption on the hydroxyl group with formation of a superficial hydroxycarbonyl ion [Fig. 1.2(I)]; b) adsorption on the metal cation and dissociation of the resulting species [Fig. 1.2(II)]; c) adsorption on the metal ion and the neighboring oxygen ion and formation of a bidentate carbonate group [Fig. 1.2(III)]; d) adsorption on the oxygen vacancy and formation of a superficial carbonyl group [Fig. 1.2(IV)] and e) adsorption on the metal ions with participation of oxygen in excess and formation of a carbonate [Fig. 1.2 (V)/ (VI)/ (VII)].

1.6.1.9. IR of pyrrole: Pyrrole is an amphoteric molecule and interacts with framework oxygens.[96,97] Pyrrole has been used as a probe molecule for the measurement of the strength of basic sites.[100] The N-H infrared vibration decreases from 3430 cm^{-1} in the pure liquid down to around 3200 cm^{-1} upon the NH···O interaction with the framework oxygens of basic sites.[96,97] Basic strength may be estimated from the value of the shift of the N-H vibration upon interaction with zeolite basic sites.[96] Barthomeuf measured the shifts of N-H vibration of pyrrole adsorbed on alkali ion- exchanged zeolites[101,102] and related them to the charge on the oxygen calculated from Sanderson's intermediate electronegativities (Fig. 1.3). The shift increases with the negative charge on the oxide ion.

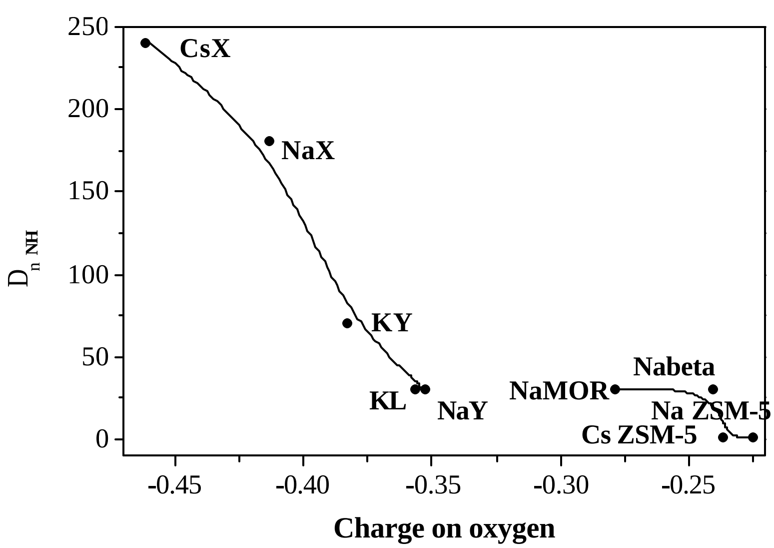

Fig. 1.3. Change in the NH vibration of pyrrole (Dn_{NH} with respect to n_{NH} of pure liquid) as a function of the charge on oxygen over ion exchanged zeolites.[101]

The negative charge is associated closely with the strength of the basic site. The basic strengths of alkali ion exchanged zeolites are in the order: CsX > NaX > KY > NaY, KL, Na-mordenite, Na-beta.

1.6.2. Computational Approaches: X-ray diffraction provides valuable information regarding the structure and geometry of crystals. However, XRD gives lattice constants and fractional co-ordinates averaged all over the crystal and hence, it is difficult to obtain information about the local geometry around a particular site of interest. NMR gives information only regarding typical kinds of local geometries. FTIR gives the average interaction of the framework structure. It is not possible to find out T-O-T angles, active sites of zeolite and charge transfer from the zeolite. Hence, there is a need for complimentary computational information. As the chemistry and reactivity of zeolites ultimately depend on many atomic properties such as proton affinity, ion exchange capability, T-O-T angle, shape selectivity, location of the active site as well as the nature of the framework atoms etc., quantifying the individual effect that each property has on the zeolite is a difficult experimental task. On the other hand, computational studies can provide us more useful information. There have been a large number of computational studies over zeolites to derive the properties that are difficult to access experimentally. The principal techniques used in computational studies of zeolites are force field and quantum chemical calculation methods.

Computer simulation at electronic level and atomic level are possible with quantum mechanics and classical mechanics, respectively. These methods are fairly standardized for chemical applications and their principles are described in the following sections.

1.6.2.1. Molecular modeling: The partial charges on oxygen atoms of zeolite framework can be calculated, which is characteristic of the basicity of zeolite.[38,39] It is important to have information on both the strength and the number of basic sites in a basic material.[102-105] A large amount of research has been devoted to computational calculations on the acidity of zeolites[37,40,106-113] using *ab initio* or semi-empirical approaches. A similar approach can be adopted to estimate properties of basic sites. *Ab initio* calculations performed on small model clusters of cationic zeolites show that the absolute value of the charge on oxygen (i.e. the basic strength) increases for the cationic forms in the order: H < Li < Na.[113]

1.6.2.2. Sanderson electronegativity (S_{int}): Sanderson proposed the intermediate electronegativity (S_{int}) of a given material as the mean electronegativity reached by all the atoms as a result of electron transfer during the formation of the compound. Mortier[114] was the first to apply the Sanderson principle of equalization of electronegativities to zeolites.[38] For a given compound $P_pQ_qR_r$, the intermediate electronegativity (S_{int}) is given by equation (1.5),

$$S_{int} = (S^p_P\ S^q_Q\ S^r_R)^{1/(p+q+r)} \quad (1.5)$$

where S_j denotes the electronegativity of atom j. One can estimate the basicity from S_{int} values.

1.6.2.3. Molecular graphics (MG): The use of MG in elucidating and analyzing simulation results has been demonstrated by Freeman and Catlow.[115] In energy EM calculations, the structure of the relaxed zeolite and the geometry of the adsorption site can be visualized and analyzed using molecular graphics. In molecular dynamics (MD) simulations, the migration of molecules in real time can be animated. The shape selective properties of zeolites can be qualitatively predicted with the aid of molecular graphics fittings. The interactive matching of molecules with zeolite pores can predict which molecules can enter the pores to react with the active sites of the catalyst on the basis of either their size or steric requirements before performing detailed calculations.

1.6.2.4. Zeolite structure building: Models of zeolite lattices are built from the X-ray crystal structure reports. The asymmetric unit co-ordinates and the crystallographic space group information are used to build the unit cell. The symmetry operators are further used to build an infinite lattice. The crystal structure database provided as part of the InsightII[116] software package is useful for this purpose.

1.6.2.5. Zeolite cluster building: Once the infinite solid lattice of zeolite is built as a molecular model, a suitable part of the lattice is chosen for representing the active site. The size of the cluster is chosen in order to simulate the properties realistically without having to spend too much of computational resources. The procedure for termination of the cluster is discussed in detail elsewhere (section 2.6).

1.6.2.6. Quantum chemical calculations: The above-discussed techniques are mainly used for adsorption and diffusion studies on zeolites. For the application of the zeolites as a useful catalyst, the mechanism of the reaction following the adsorption of molecules on the active sites has to be understood. The catalytic activity of a zeolite depends upon the acidic strength of the bridging hydroxyl group. The acidic strength of the bridging hydroxyl group in turn, is a function of the local geometry around the acidic group. The force field based methods are not suitable to obtain information about the geometries of the acidic groups, mechanism of the reaction, ability for proton transfer, transition state of the reaction, electronic properties of the material and other related properties. Quantum chemical calculation methods provide a better understanding of the above properties for the desired material.[117,118] These methods provide a fundamental understanding of the structural properties, acidic strength (Brønsted sites), proton affinity, vibrational frequencies, NMR chemical shifts and other related properties of the molecules and zeolites. However, the size of the cluster model is restricted due to the heavy demand on the computer CPU and so realistic models need to be used taking care of boundary effects.

Quantum chemical calculations are divided into two types, semi-empirical methods (such as CNDO, MNDO etc.) and non-empirical methods (*ab initio*, density functional theory (DFT) etc.). Semi-empirical methods neglect many of the differential overlap approximations while the non-empirical methods evaluate all overlap integrals. The goal of either method is to obtain the wave function of orbital $\phi\ (r)$ occupied by each electron, the eigenvalue (or orbital energy) ε_i corresponding to that orbital, the total energy E_{tot} and the atomic force F on each atom by solving the Schrödinger wave equation. Quantum chemical calculation is a fairly standard technique used for studying chemisorption and diffusion of organic molecules in zeolites. The use of quantum chemical methods in zeolite systems is two fold: i) it can be used to identify reaction pathways and sorbed intermediate species in the cages of zeolites and ii) reactivity can be studied using finite molecular clusters to represent a particular site in the zeolite structure.[119-129] Potential parameters derived from *ab initio* methods are also used for obtaining structural informations of zeolites. Generally, calculations on zeolites involve the use of zeolite fragments treated as clusters so as to mimic the infinite crystal. The cluster size depends on the level of approximation or sophistication of the calculations. A plausible way to terminate the cluster is to embed it in a surrounding lattice of zeolite structure represented as point charges or alternatively terminates it with hydrogen atoms. More details on quantum chemical calculations on zeolite systems can be found in a review by Sauer.[118] However, the computational efforts involved are large for these types of calculations. An alternative way to overcome the limitation of small cluster models was used by Redondo and Hay who used semi-empirical quantum chemical calculations (MNDO) to study acid sites in zeolite ZSM-5.[130] In their study, each of the 12 distinct T-sites was modeled by a large cluster of the appropriate geometry containing about 100 atoms. Chatterjee and Vetrivel[131,132] studied the role of templating organic molecules in the synthesis of ZSM-5 using MNDO method. An extensive study to bring out the influence of clusters with varying size used in *ab initio* calculations were presented by van Santen and coworkers.[133]

1.6.2.7. Classical mechanical calculations

1.6.2.7.1. Force field: The forces acting between the atoms in a molecule or a chemical system could be mathematically defined through force field expressions. The results of all classical simulation methods (energy minimization, Monte Carlo, molecular dynamics) depend directly on the reliability of the force field parameters used. The interatomic potential V for a system of 'n' particles describes the variation of the total potential energy of the system as a function of the nuclear coordinates, r_1,-------,r_n. i.e.

$$V = V(r_1, \text{-----------}, r_n) \quad (1.6)$$

In practice, V is generally broken down into 'pair,' 'three-body,' 'four-body' and higher order terms:

$$V = \sum_{i,j=1} V(r_i, r_j) + \sum_{i,j,k=1} V(r_i, r_j, r_k) + \sum_{i,j,k,l=1} V(r_i, r_j, r_k, r_l) + ------ \quad (1.7)$$

The majority of simulations approximate V simply by the pair potential term, which is usually decomposed into Coulombic and non-Coulombic terms (ϕ); the first term represents the long-range electrostatic interactions between a pair of atoms with effective charges q_i and q_j while the second term is a two-body short-range interaction.

$$V(r) = \sum_{ij} \frac{q_i q_j}{r_{ij}} \tag{1.8}$$

The short-range pair potential term further comprises of the bonded and non-bonded terms. The bonded term is used for modeling the covalent and semi covalent systems. The non-bonded terms are given by Lennard-Jones or Buckingham potential. Either formal charges[134-136] or ionic charges[137-140] of atoms are used to describe the Coulomb term. The use of formal charges with appropriate defined potentials for zeolites was justified by Jackson and Catlow,[134] while van Beest *et al.*[137] gave a set of recommended partial charges derived using quantum chemical methods.

Inter-atomic potentials can be calculated directly using quantum mechanical methods ranging from electron gas techniques[138] to *ab initio* quantum chemical calculations using Hartree-Fock method.[139] DFT has also been used to calculate the potential parameters.[136] This method has been used to calculate inter-atomic potentials.

1.6.2.7.2. Energy minimization (EM): Energy minimization technique is used to obtain the minimum energy configuration of a molecule or crystal, where the interatomic interactions are known through force field expressions. A wide variety of algorithms are available, which are classified according to the order of the derivative of the total energy function that is employed in the calculation. The more well known algorithms for the energy minimization procedure are steepest descent, conjugate gradient and Newton Raphson methods. The first two methods involve first derivation while the last method involves second derivatives of the energy. These methods are used for understanding the diffusion and sorption of organic molecules in zeolites.[140] These methods require the specification of an initial configuration or 'starting point'; the energy is calculated using knowledge of force field expressions and parameters.

The system is then driven down in energy to the nearest minimum. The simplest methods employ the energy function alone and search over configuration space until the minimum is located. There is another major difficulty in the minimization techniques; they can only be guaranteed to locate the nearest local minimum to the starting point of the calculation. The only real solution to the problem is to sample large numbers of starting points in order to ensure that all low energy minima have been identified. Despite these limitations, energy minimization techniques are straight forward, robust and readily applicable. These methods are ideally suited to large and complex systems such as zeolites. Fruitful applications of this method have been reported in zeolite science to model crystal structures[141,142] and sorption sites.[143,144] This method has been used to optimize the distance between Pt_5:Benzene and Pt_5:H_2S molecules in this work.

<u>1.6.2.7.3. Monte Carlo (MC) technique:</u> The MC simulation method is well suited to the study of molecules sorbed in zeolites. The simulation proceeds via the generation of successive configurations of the ensemble by a series of random moves, which can be a molecular translation, molecular rotation, insertion, or deletion of a molecule etc. Once a sufficient number of configurations are generated, ensemble averages are calculated. Depending upon the type of ensemble used for the study of the system in Monte Carlo, the method is called metropolis MC, grand canonical MC, canonical MC, configurational biased MC, etc. In generating such ensembles, it is essential to formulate an ‘acceptance’ criterion, that is a procedure that determines whether a new configuration created by a move will be acceptable within the ensemble. MC simulations are most commonly run in the canonical (NVT) ensemble in which both volume and temperature are fixed. MC simulations are performed on ensembles containing several thousand particles, to which periodic boundary conditions are applied in the case of the simulation of zeolites. The simulation again starts with an equilibration phase during which the system is equilibrated followed by a 'simulated run' in which, typically, several million configurations are generated.[145] Monte Carlo is particularly suitable for studying the distribution of the sorbed molecules in zeolites with variation of temperature.[146,147] This method can be used to locate the sorption site, determine sorption equilibria and various thermodynamic functions at higher temperatures.[148-150] Stroud *et al.*[148] have studied the adsorption of methane in zeolite A and calculated the heat capacity, isosteric heat of adsorption and adsorption isotherms using MC methods. Yashonath *et al*.[149] attempted to understand the binding and mobility of sorbed methane as a function of temperature inside zeolite FAU. Recently, Smith and coworkers[151-154] have studied the location and conformation of *n*-alkanes in different zeolites using a novel Monte Carlo technique called configurational-bias Monte Carlo. Freeman *et al.*[155] have developed a technique, which blends molecular dynamics, Monte Carlo and energy minimization methods to locate the global energy minimum site for sorbed molecules.

1.6.2.7.4. Molecular Dynamics (MD): In MD methods, the system is simulated and studied by an ensemble of particles, which are contained in a simulation box. Periodic boundary conditions are applied and the basic simulation box is repeated infinitely in all three directions. MD simulation is the most powerful computational technique available for obtaining information on the time dependent properties of molecular or atomic motions in zeolite crystals. It is used to obtain thermodynamic quantities and detailed dynamical information on sorption and diffusion processes in zeolite systems. For instance, the extent to which intermolecular vibration and framework motion assist sorption and diffusion of molecules can be simulated. The major limitation is its inability to model diffusion of larger sorbed molecules and electronic polarizability due to the huge amount of computer time and memory requirements. MD technique proceeds by deriving explicit numerical solution of Newton's equation of motion. It requires the initial coordinates and velocities of particles, which are assigned based on X-ray crystal structure and temperature of simulation. With the knowledge of the interatomic potential among the particles, the forces acting on the particle can be calculated. The following statistical mechanical ensembles are more commonly used during the molecular dynamics simulations: a) micro canonical ensemble (NVE), which is an ensemble with constant number of particles, volume and energy, b) canonical ensemble (NVT), which is an ensemble with constant number of particles, volume and temperature and c) isobaric-isothermal ensemble (NPT), which is the ensemble with constant number of particles, pressure and temperature. One important factor in MD simulation is the choice of Δt. It must be smaller than the time scale of any important dynamical process at the atomic or molecular level. Thus, it must be at least an order of magnitude smaller than the typical period of atomic vibrations (10^{-12} - 10^{-13} s). Of the three types of algorithms used in contemporary MD studies, namely the Verlet,[156] Beeman[157] and Gear,[158] the Verlet method with leap-frog formulation has been found to be readily applicable for studying zeolitic materials.[159] One of the most useful properties of a zeolite is its ability to control the diffusion of the different sorbed molecules, which can be calculated from MD simulations. The property of usual interest in MD simulations is the diffusion coefficient, which is calculated from the well-known Einstein formula as given below:

$$D = \lim_{t \to \infty} \frac{\left\langle | r(t) - r(0) |^2 \right\rangle}{6t} \tag{1.9}$$

where r(t) and r(0) are respectively the final and initial positions of a particle, for a time interval t and D is the diffusion coefficient. The numerator, $\langle |r(t) - r(0)|^2 \rangle$ is generally called mean square displacement of the particle. All methods are based on solving the classical mechanics equation. These methods have been used to obtain a detailed understanding about diffusion, adsorption and reaction mechanisms in zeolites. Previous work on the application of MD to zeolite systems concentrated on the diffusion of small molecules in zeolite pores. The dynamics of large molecules such as porphyrins inside FAU zeolite has recently been studied.[160] Other typical examples of MD simulations of hydrocarbons in zeolites are those of Hernandez and Catlow[161] and Demontis and Suffritti.[162] Although this method has not been used in the investigation reported in this thesis, the above description is provided for the sake of completion of the computational approaches discussion.

1.7. SCOPE AND OBJECTIVE OF THE THESIS

Naphtha reforming has been reported to proceed with high aromatic selectivity on Pt loaded basic (LTL or ETS-10) zeolites. The exact reason for the high selectivity of these zeolites is still a matter of discussion. Several reasons such as pore geometry, shape selectivity, Pt dispersion, charge on Pt and absences of coke deposition have been proposed. The experimental activity and aromatic selectivity of these catalysts needs to be further examined by carrying out catalytic experiments and computational calculations. Some questions that need to be answered are: i) how do the catalytic behavior of different Pt loaded alkaline zeolites compare? ii) how do the their activities and selectivities relate with the electronic properties of the Pt ? iii) what is the reason for higher activities ? is it ease of benzene desorption and finally why does H_2S poison these catalysts easily ? This work has been taken up to find answers to the above questions.

The objective of this work is to investigate the reasons for the superior aromatization selectivity of Pt supported on basic zeolites. The electronic interaction between the support and the Pt cluster is investigated through quantum chemical calculations (*ab initio* Hartree-Fock) for different Pt-zeolites possessing different composition and structure. The zeolites investigated include LTL, FAU, BEA and ETS-10. The experimental activities of the Pt-zeolites in *n*-hexane aromatization are correlated to the electronic structure of Pt supported over different zeolite/ molecular sieve. To achieve this accomplishment, we carried out:

1) Synthesis of the molecular sieves FAU, LTL, BEA and ETS-10.
2) Exchanging the extra-framework cation in the molecular sieves with different alkali and alkaline earth ions and incorporation of Pt.
3) Characterization of the modified molecular sieves by physico-chemical and spectroscopic methods such as XRD, N_2 sorption, H_2 chemisorption, FTIR, TPD of CO_2, IR and MAS-NMR.
4) Evaluation of the catalytic activity of these catalysts for the *n*-hexane aromatization.
5) Design and create molecular models for clusters of LTL, FAU, BEA and ETS-10 with and without the Pt-clusters supported on these clusters.
6) Calculate the binding energy and charge on the Pt (Mulliken Population) by *ab initio* Hartree-Fock methods; simulate the adsorption of benzene and deactivation due to adsorption of H_2S.
7) Establish relationship between experimental activity of the catalysts and the electronic charge on Pt.
8) Understand the reasons for the activity and poisoning of Pt supported on zeolites as well as derives guidelines for designing more efficient catalysts.

1.8. OUTLINE OF THE THESIS

The thesis has been divided into six chapters including this introductory chapter

Chapter 2 is divided into two parts. Part A describes the synthesis procedures adopted in the preparation and modification of the molecular sieves, viz. LTL, FAU, BEA and ETS-10. The original calcined molecular sieve materials were exchanged with alkali and alkaline earth metal halides and later loaded with $Pt[NH_3]_4Cl_2$. Characterization studies of these materials were done by XRD, SEM, N_2 sorption studies, UV-Vis and MAS-NMR. The basicity of the different zeolites was characterized by FTIR spectra of adsorbed CO_2, TPD of CO_2 and intermediate electronegativity (S_{int}) calculations.

Part B describes the computational methodology used in molecular modeling. It describes the framework structure of different zeolites, such as LTL, FAU, BEA and ETS-10, T-O-T angles and their active sites. Electronic properties of the various Pt clusters with different geometries and shapes are presented. The various cluster models of the molecular sieves used in the calculations are presented and discussed. Molecular fitting procedure for incorporating Pt_5 cluster with adsorbed benzene and adsorbed H_2S in the molecular sieves is presented.

Chapter 3 deals with the catalytic results of the aromatization of *n*-hexane in the vapor phase over Pt-M-zeolites (where, M = H, Li, to Cs and Mg to Ba and zeolite = LTL, FAU and BEA). The three zeolites can be arranged in the following order with respect to conversion: zeolite BEA > LTL > FAU and selectivity: LTL > BEA > FAU. The H-forms of these zeolites possess higher *n*-hexane isomerization and cracking activities. The influence of the various reaction parameters such as time on stream, contact time, temperature, mole ratio of *n*-hexane to hydrogen and platinum content have been investigated for the different Pt-catalysts.

Chapter 4 describes computation to fix the location of Al and the orientation of Pt_5 cluster in LTL, FAU and BEA. The results of the Hartree-Fock calculations, namely the electronic properties of the zeolite clusters, such as binding energy and charge on alkali metals (Mulliken population) with and without Pt_n (n = 1 and 5) are also presented. The binding energy of the Pt-cluster and the average charge per Pt in the cluster are reported. The electronic properties of benzene and H_2S adsorbed over Pt-M-zeolites are also presented. The relationship between the average electronic charge per platinum in the Pt-zeolite clusters and experimental aromatization activity as well as selectivity of the zeolite catalysts is examined.

Chapter 5 is presented into two parts. Part A describes the vapor phase aromatization of *n*-hexane over Pt-M-ETS-10 molecular sieves. Pt-Ba-ETS-10 is found to be the most active catalyst. The influence of various reaction process parameters is presented. Part B describes the results of *ab initio* calculations over ETS-10 cluster model. The influence of the location of M^{n+} cations is examined. The electronic properties of Pt_5 located nearer to [TiO_6] and [SiO_4] sites are investigated. The relationship between the actual activity of the Pt-M-ETS-10 catalysts and the average electronic charge per platinum is brought out.

Chapter 6 presents an overall summary of the results obtained.

1.9. REFERENCES

1. B.C. Gates, J.R. Katzer and G.C.A. Schuit, in "*Chemistry of Catalytic Processes*", McGraw-Hill, New York, (1979) 184.
2. J.R Bernard, in "*Proceedings of the 5th International Zeolite Congress*", Naples, Rees L.V.C, ed., Heyden, London, (1980) 686.
3. P.W. Tamm, D.H. Mohr and C.R. Wilson, *Stud. Surf. Sci. Catal*, 38 (1987) 335.
4. J. Zheng, J.L. Dong, Q.H. Xu, Y. Lui, and A.Z. Yan, *Appl. Catal.* A, 126 (1995)

141.

5. T.K. Das, A.J. Chandwadkar and S. Sivasanker, *Stud. Surf. Sci. Catal.*, 113 (1998) 455.
6. A. Philippou, M. Naderi, N. Pervaiz, J. Rocha and M.W. Anderson, *J. Catal*, 178 (1998) 174.
7. C. Besoukhanova, J. Guidot, D. Barthomeuf, M. Breysse and J.R. Bernard, *J. Chem. Soc. Faraday Trans.*, I, 77 (1989) 1595.
8. G. Larson and G.L. Haller, *Catal. Lett.*, 3 (1989) 103.
9. E.G. Derouane and D. Vanderveken, *Appl. Catal.*, 45 (1988) L15.
10. S.J. Tauster and J.J. Steger, *J. Catal.*, 125 (1990) 387.
11. J.M. Newsam, B.G. Silbernagel, A.R. Garcia, M.T. Melchow and S.G. Fung, *Stud. Surf. Sci. Catal.*, 67 (1991) 211.
12. R.J. Davis and E.G. Derouane, *Nature*, 349 (1991) 313.
13. R.A. Dalla Betta and M. Boudart, in "*Proceedings of the 5th International Congress on Catalysis*", J.M. Hightower eds., North Holland, Amsterdam, 2 (1973) 1329.
14. R.M, Barrer, "*Hydrothermal Chemistry of Zeolites*", Academic Press, New York, (1982).
15. R. Szostak, "*Molecular Sieves, Principles of Synthesis and Identification*", Van Nostrand Reinhold Catalysis Series, New York, (1989).
16. W. Löwenstein, *Am. Miner.*, 39 (1957) 92.
17. A.F. Cronstedt, *Svenska Vetenskaps Akademiens Handlingar*, Stockholm, 17 (1756) 120.
18. J.V. Smith, *Chem. Rev.*, 88 (1988) 149.
19. A. Corma, *Chem. Rev.*, 95 (1995) 559.
20. D.W. Breck, "*Zeolite Molecular Sieves: Structure Chemistry and Use*", Wiley, London, (1974).
21. W.H. Meier and D.H. Olson, "*Atlas of Zeolite Structures Types*", Butterworths-Heinemann, Boston, MA, 3rd ed., (1992).
22. W.L. Bragg, "*The Atomic Structures of Minerals*", Cornell University Press, Ithaca, New York, (1937).
23. W.H. Meier, "*Molecular Sieves*", *Soc. of Chem. Ind.*, London, 10 (1968).

24. E.M. Flanigen, in *"Proceedings of the 5th International Conference on Zeolites"*, ed., L.V.C. Rees, Naples, Italy, June 2-6 (1980) 760.

25. L.B. Sand, *Econ. Geol.*, (1967) 191.

26. H. Pines and J. Manassen, *Adv. Catal*, 16 (1966) 49.

27. K. Tanabe, *"Solid Acids and Bases"*, Kodansha, Tokyo, 1970.

28. M. Ai, *Bull. Jpn. Petrol Inst.*, 18 (1976) 50.

29. H. Pines and M.W. Stalick, "*Base Catalyzed Reactions of Hydrocarbons and Related Compounds*", Academic Press, New York, 1977.

30. H. Pines, J.A. Vaseley and V.N. Ipatieff, *J. Am. Chem. Soc.*, 77 (1955) 6314.

31. R.J. Kokes and A.L. Dent, *Advan. Catal.*, 22 (1972) 1.

32. R.J. Kokes, in "*Proceedings of the 5th International Congress on Catalysis*", Miami Beach, FL, (1972) 1.

33. T. Yashima, K. Sato, T. Hayasaka and N. Hara, *J. Catal.*, 26 (1972) 303.

34. D. Barthomeuf, *Cat. Rev. Sci. Eng.*, 38 (1996) 521.

35. C. Mirodatos, P. Pichat and D. Barthomeuf, *J. Phys. Chem.*, 80 (1976) 1335.

36. C. Mirodatos, A. Abou Kais, J. C. Vedrine, P. Pichat and D. Barthomeuf, *J. Phys. Chem.*, 80 (1976) 2366.

37 R.A. van Santen, B.W.H. van Beest and A.J.M. de Man, in "*Guidelines for Mastering the Properties of Molecular Sieves*", D. Barthomeuf, E.G. Derouane and W. Hölderich, eds., NATO ASI series, Plenum Press, New York, *Ser. B: Physics*, 221 (1990) 201.

38. R.T. Sanderson, "*Chemical Bonds and Bond Energy*", Academic Press, New York, 1976.

39. R.T. Sanderson, *J. Am. Chem. Soc.*, 105(1983) 2259.

40. G.V. Gibbs, E.P. Meagher, J.V. Smith and J.J. Pluth, *ACS Symp. Ser.*, 40 (1977) 19.

41. A. Abou-kais, C. Mirodatos, J. Massardier, D. Barthomeuf and J.C. Vedrine, *J. Phys. Chem.*, 81 (1977) 397.

42. P.E. Hathway and M. E. Davis, *J. Catal*, 116 (1989) 263, 279.

43. T. Turk, F. Sabin and A. Vogler, *Mater. Res. Bull.*, 27 (1992) 1003.

44. M. Lasperas, H. Cambon, D. Brunel, I. Rodriguez and P. Geneste, *Microp. Mater.*, 1 (1993) 343.

45. H. Tsuji, F. Yagi, H. Hattori and K. Kita, in "*Proc. 10th International Congress on Catalysis*", L. Guczi,, F. Solymosi and P. Tetenyi, eds., Akademiai Kiado, Budapest, B, (1993) 1171.
46. J. Engelhardt, J. Szanyi and B. Jover, *Acta Symp. Ibero-Amer. Catal.* 9th, 2 (1984) 1435.
47. C. Lacroix, A. Deluzarche, A. Kiennemann and A. Boyer, *J. Chem. Phys.*, 81 (1984) 473, 481, 486.
48. D. Barthomeuf and V. Barbarin, *French Pat.*, (1989) 2 623 423.
49. J. A. Rabo, C. L. Angell, P. H. Kasai and V. Schomaker, *J. Faraday. Soc.*, 4 (1966) 328.
50. P.P. Edwards, M.R. Harrison, J. Klinowski, S. Ramdas, J.M. Thomas, D.C. Johnson and C.J. Page, *J. Chem. Soc. Chem. Commun.*, (1984) 982.
51. L.R.M. Martens, W.J.M. Vermeiren, P.J. Grobet and P.A. Jacobs, *Stud. Surf. Sci. Catal.*, 31 (1987) 531.
52 G.A. Ozin, *Adv. Mater.*, 4 (1992) 612.
53. E. Trescos, F. Rachdi, L.C. de Menorval, F. Fajula, T. Nunes and G. Feio, *J. Phys. Chem.*, 97 (1993) 11855.
54. J.A. Rabo, C.L. Angell, P.H. Kasai and V. Schomaker, *Disc. Faraday, Soc.*,. 4 (1966) 328.
55. P.H. Kasai and R.J. Bishop, Jr., *J. Phys. Chem.*, 77 (1973) 2308
56. L.R.M. Martens, P.J. Grobet and P.A. Jacobs, *Nature*, 315 (1985) 568.
57. Bo Xu and L. Kevan, *J. Phys. Chem.*, 96 (1992) 2642.
58. H. Nakayama, D.D. Klug, C.I. Ratcliffe and J.A. Ripmeester, *J. Am. Chem. Soc.*, 116 (1994) 9777.
59. Y. N. Sidorenko, P. N. Galich, V. S. Gutyrya, V. G. II and I. E. Neimak, *Dokl. Akad. Nauk, SSSR*, 173 (1967) 132.
60. K.R. Kloestra and H. van Bekkum, *J. Chem. Soc., Chem. Commun.*, (1995) 1005.
61. T. Yashima, H. Suzuki and N. Hara, *J. Catal.*, 33 (1974) 486.
62. J. W. Ward, in "*Zeolites Chemistry and Catalysis*" J. Rado, ed., *ACS Monograph*, 171 (1976) 226, 233.
63. J.W. Ward, *J. Catal.*, 10 (1968) 34.

64. J.H. Lunsford, *Catal. Rev*., 12 (1975) 137.

65. C. Naccache and Y.B. Taarit, in "*Proceedings of the 5th International Conference on Zeolites*", Naples, L.V.C. Rees, ed., Heyden, London, (1980) 592.

66. G.A. Ozin and C. Gil, *Chem. Rev.*, 89 (1989) 1749.

67. M. Ichikawa, *Adv. Catal*., 38 (1992) 283.

68. A. de Mallmann and D. Barthomeuf, *Catal. Lett*., 5 (1990) 293.

69. Y. Okamoto, T. Imanaka, K. Asakura and Y. Iwasawa, *J. Phys. Chem*., 95 (1991) 3700.

70. P.L. Zhou, S.D. Maloney and B.C. Gates, *J. Catal*., 129 (1991) 315.

71. T.J. Lee and B.C. Gates, *J. Mol. Catal*., 71 (1992) 335.

72. S. Kawi, J.R. Chang and B.C. Gates, *J. Catal*., 142 (1993) 585.

73. H.M. Ziethen and A.X. Trautwein, *Stud. Surf. Sci. Catal*., 46 (1989) 789.

74. Y. Okamoto, M. Ogawa, A. Maezawa and T. Imanaka, *J. Catal*., 112 (1988) 427.

75. M. Huang, A. Adnot, S. Kaliaguine and K. Kaliaguine, *J. Am. Chem. Soc.*, 114 (1992) 10005.

76. M. Huang, A. Adnot and S. Kaliaguine, *J. Catal*., 137 (1992) 322.

77. G. Engelhardt and D. Michel, "*High Resolution Solid-State NMR of Silicates and Zeolites*", Wiley, New York, 1987; G. Engelhardt, *Stud. Surf. Sci. Catal*, 52 (1991) 151.

78. H.K.C. Timken, G.L. Turner, J.P. Gilson, L.B. Welsch and E. Oldfield, *J. Am. Chem. Soc*., 108 (1986) 7231.

79. H.K.C. Timken, N. Janes, G.L. Turner, S.L. Lambert, L.B. Welsch and E. Oldfield, *J. Am. Chem. Soc.*, 108 (1986) 7236.

80. M. A. Paul and F.A. Long, *Chem. Rev.*, 57 (1957) 1.

81. L. P. Hammett, "*Physical Organic Chemistry*", McGraw-Hill: New York, 1940, Chapter IX.

82. J. Take, N. Kikuchi and Y. Yoneda, *J. Catal*., 21 (1971) 164.

83. R.L. Nelson and J.W. Hale, *Disc. Faraday Soc*., 52 (1958) 77.

84. A.J. Tench and G.T. Pott, Chem. *Phys. Lett*., 26 (1974) 590.

85. T. Ito, M. Kuramoto, M. Yoshida and T. Tokuda, *J. Phys. Chem*., 87 (1983)

4411.

86. T. Ito, T. Murakami and T. Tokuda, *J. Chem. Soc. Trans. Faraday I*, 79 (1983) 913.

87. K. Tanabe, M. Misono, Y. Ono and H. Hattori, *Stud. Surf. Sci. Catal.*, 51 (1989) 14, 215, 225.

88. J.C. Lavalley, *Trends Phys. Chem.*, 2 (1991) 305.

89. C. Lahousse, J. Bachelier, J.C. Lavalley, H.L. Pernot and A.M. Le Govic, *J. Mol. Catal*, 87 (1994) 329.

90. E.A. Paukshtis and E.N. Yurchenko, *Russ. Chem. Rev.*, 52 (1983) 42.

91. H. Knözinger, in "*Handbook of Heterogeneous Catalysis*" ed. G. Ertl, H. Knözinger and J. Weitkamp, Wiley-VCH, Weinheim 2 (1997) 707.

92. J.A. Lercher, C. Grundling and G. Eder-Mirth, *Catal. Today*, 27 (1996) 353.

93. L.M. Kustov, *Top. Catal.*, 4 (1997) 131.

94. F. Wakabayashi and K. Domen, *Catal. Surveys Jpn.*, 1 (1997) 181.

95. E.A. Paukshtis, N.S. Kotsarenko and L.G. Karakchiev, *React. Kin. Kat. Lett.*, 12 (1979) 315.

96. P.O. Scokart and P.G. Rouxhet, *Bull. Soc. Chim., Belge*, 90 (1981) 983.

97. P.O. Scokart and P.G. Rouxhet, *J. Chem. Soc. Faraday Trans.*, I, 76 (1980) 1476.

98. A. Auroux and A. Gervasini, *J. Phys. Chem.*, 94 (1990) 6371.

99. E.J. Doscocil, S.V. Bordawekar and R.J. Davis, *J. Catal*, 169 (1997) 327.

100. H. Tsuji, F. Yagi and H. Hattori, *Chem. Lett.*, 1881 (1991).

101. D. Barthomeuf, *J. Phys. Chem.*, 55 (1978) 138.

102. D. Barthomeuf, *Stud. Surf. Sci. Catal.*, 65 (1991) 157.

103. D. Barthomeuf, *J. Phys. Chem.*, 88 (1984) 42.

104. D. Barthomeuf, in "*Acidity and Basicity of solids*", J. Fraissard and L. Petrakis, eds., NATO, ASI Series C, 444 (1994) 181.

105. D. Barthomeuf and A de Mallmann, *Stud. Surf. Sci. Catal*, 37 (1988) 365.

106. I.N. Senchenya, V.B. Kazansky and S. Beran, *J. Phys. Chem.*, 90 (1986) 4857.

107. P.J. O'Malley and J. Dwyer, *J. Phys. Chem.*, 92 (1988) 3005.

108. S. Beran and J. Dubsky, *J. Phys. Chem.*, 83 (1979) 2358.

109. G.M. Zhidomirov and V.B. Kazansky, *Adv. Catal.*, 34 (1986) 131.

110. E.G. Derouane and J.G. Fripiat, *J. Phys. Chem.*, 91 (1987) 145.

111. E. Kassab, K. Seiti and M. Allavena, *J. Phys. Chem.*, 92 (1988) 67.

112. P.J. O'Malley and J. Dwyer, *Chem. Phys. Lett*., 143 (1988) 97.

113. A. Goursot, F. Fajula, C. Daul and J. Weber, *J. Phys. Chem.*, 92 (1988) 4456.

114. W.J. Mortier, *J. Catal*, 55 (1978) 138.

115. C. Freeman and R. Catlow, *Chem. Ind*., London, (1990) 796.

116. InsightII, Discover, supplied by Molecular Simulations Inc., USA.

117. R.A. van Santen and G.J. Kramer, *Chem. Rev.*, 95 (1995) 637.

118. J. Sauer, *Chem. Rev.*, 89 (1989) 199.

119. G.M. Zhidomirov and V.B. Kazansky, *Adv. Catal*., 34 (1986) 131.

120. R. Vetrivel, C.R.A. Catlow and E.A. Colbourn, *Proc. R. Soc.*, London, A, 417 (1988) 81.

121. R. Vetrivel, C.R.A. Catlow and E.A. Colbourn, *J. Phys. Chem.*, 93 (1989) 4594.

122. G.J. Kramer and R.A. van Santen, *J. Am. Chem. Soc.*, 115 (1993) 2887.

123. E.H. Teunissen, R.A. van Santen, A.P.J. Jansen and F.B. van Duijneveldt, *J. Phys. Chem*., 97 (1993) 203.

124. E. Broclawik, H. Himei, M. Yamadaya, M. Kubo, A. Miyamoto and R. Vetrivel, *J. Chem., Phys*., 103 (1995) 2102.

125. H. Himei, M. Yamadaya, M. Kubo, R. Vetrivel, E. Broclawik and A. Miyamoto, *J. Phys. Chem.*, 99 (1995) 12461.

126. M. Yamadaya, H. Himei, T. Kanougi, Y. Oumi, M. Kubo, A. Stirling, R. Vetrivel, E. Broclawik and A. Miyamoto, *Stud. Surf. Sci. Catal*., 105 (1997) 1485.

127. R. Shah, J.D. Gale and M.C. Payne, *J. Phys. Chem.*, 100 (1996) 11688.

128. P.E. Sinclair and C.R.A. Catlow, *J. Chem. Soc., Faraday Trans*., 92 (1996) 2099.

129. P.E. Sinclair and C.R.A. Catlow, *J. Chem. Soc., Faraday Trans*., 93 (1997) 333.

130. A. Redondo and P.J. Hay, *J. Phys. Chem.*, 97 (1993) 11754.

131. A. Chatterjee and R. Vetrivel, *J. Chem. Soc., Faraday Trans*., 91 (1995) 4313.

132. A. Chatterjee and R. Vetrivel, *J. Mol. Catal*., 106 (1996) 75.

133. G.J. Kramer, A.J.M. de Man and R.A. van Santen, *J. Am. Chem. Soc.*, 113 (1991) 6435.

134. R.A. Jackson and C.R.A. Catlow, *Mol. Simul.*, 1 (1988) 207.

135. J. Purton, R.H. Jones, C.R.A. Catlow and M. Leslie, *Phys. Chem. Miner.*, 19 (1993) 392.

136. M. Sierka and J. Sauer, *Faraday Discuss.*, 106 (1997) 41.

137. B.W.H. van Beest, G.J. Kramer and R.A. van Santen, Phys. *Rev. Lett.*, 64 (1990) 1955.

138. W.C. Mackrodt and R.F. Stewart, *J. Phys. Chem.*, 12 (1979) 5015.

139. J.D. Gale, C.R.A. Catlow and W.C. Mackrodt, *Mod. Simul. Mater. Sci. Eng*, 1 (1992) 73.

140. R.C. Deka and R. Vetrivel, *Chem. Commun.*, (1996) 2397; *J. Catal.*, 174 (1998) 88.

141. R.G. Bell, R.A. Jackson and C.R.A. Catlow, *J. Chem. Soc., Chem. Commun.*, (1990) 782.

142. C.R.A. Catlow, J.M. Thomas, C.M. Freeman, P.A. Wright and R.G. Bell, *Proc. R. Soc.*, London. A, 442 (1993) 85.

143. A.R. George, C.M. Freeman and C.R.A. Catlow, *Zeolites*, 17 (1996) 466.

144. A.R. George, C.R.A. Catlow and J.M. Thomas, *Micro. Mater.*, 11 (1997) 97.

145. C.R.A. Catlow, S.C. Parker and M.P. Allen, in "*Computer Modelling of Fluids, Polymers and Solids*", NATO Series, Kluwer Academic Publishers, Dordrecht, 293 (1990).

146. D. Douguet, R.J.M. Pellenq, A. Boutin, A.H. Fuchs and D. Nicholson, *Mol. Simul.*, 17 (1996) 225.

147. B. Smit and C.J.J. den Ouden, *J. Phys. Chem.*, 92 (1989) 7169.

148. H.J.F. Stroud, E. Richard, P. Limcharoen and N.G. Parsonage, *J. Chem. Soc., Faraday Trans., 1*, 72 (1976) 72.

149. S. Yashonath, J.M. Thomas, A.K. Nowak and A.K. Cheetham, *Nature*, 331 (1988) 20 601.

150. J. Karger, M. Petzold, H. Pfeifer, S. Ernst and J. Weitkamp, *J. Catal.*, 136 (1992) 283.

151. B. Smith and J.I. Siepmann, *Science*, 264 (1994) 1118.

152. B. Smith and J.I. Siepmann, *J. Phys. Chem.*, 98 (1994) 8442.

153. S.P. Bates, W.J.M. van Well, R.A. van Santen and B. Smit, *J. Am. Chem. Soc.*,

118 (1996) 6753.

154. S.P. Bates, W.J.M. van Well, R.A. van Santen and B. Smit, *J. Phys. Chem.*, 100 (1996) 17573.

155. C.M. Freeman, C.R.A. Catlow, J.M. Thomas and S. Brode, *Chem. Phys. Lett.*, 186 (1991) 137.

156. L. Verlet, *Phys. Rev*., 159 (1967) 98.

157. D. Beeman, *J. Comput. Phys.*, 20 (1976) 130.

158. C.W. Gear, "*Numerical Initial Value Problems in Ordinary Differential Equations,*" Prentice Hall Publishers, New York (1971).

159. P. Demontis and G.B. Suffritti, *J. Phys. Chem.* B, 101 (1997) 5789.

160. T. Sato, K. Sugao, Y. Oumi, R. Vetrivel, M. Chatterjee, A. Chatterjee, M. Kubo, A. Stirling, A. Fahmi and A. Miyamoto, *Appl. Surf. Sci*., 119 (1997) 346.

161. E. Hernandez and C.R.A. Catlow, *Proc. R. Soc.*, London, A, 448 (1995) 143.

162. P. Demontis and G.B. Suffritti, *Chem. Rev*., 97 (1997) 2845.

CHAPTER 2

METHODS AND CHARACTERIZATION

PART A: SYNTHESIS AND CHARACTERIZATION OF MOLECULAR SIEVES

In this section, the procedures adopted for the preparation of the various basic catalysts are described. The various methods used in the characterization of the catalysts and the physico-chemical characteristics of the catalysts are presented. Detailed characterization of the basicity of the catalysts has been carried out by TPD and FTIR spectroscopy of adsorbed CO_2.

2.1. SYNTHESIS OF MOLECULAR SIEVES

2.1.1. Synthesis of Zeolite LTL: Zeolite-LTL was synthesized following published procedures[1] using the gel composition in terms of oxides:

$$2.62\ K_2O: 10\ SiO_2: Al_2O_3: 158H_2O.$$

Fumed silica was used as the silica source and pseudobochmite (Catapal-B) was used as the alumina source. In a typical synthesis,[1] KOH (9.0 g) and pseudobochmite (1.55 g Catapal-B) were dissolved in 45 g demineralized water and fumed silica (2.0 g) was added to it. The mixture was stirred for 2 h and transferred to a teflon lined stainless steel autoclave. The gel was heated at 415 K for 108 h. The product was filtered, washed with distilled water and dried at 383 K for 6 h.

2.2.2. Synthesis of Zeolite BEA: Zeolite-BEA was synthesized based on published procedures[2,3] using the gel composition in terms of oxides:

$$0.53\ Na_2O: 0.47\ K_2O: 30\ SiO_2: Al_2O_3: 25\ Et_4NOH: 750\ H_2O.$$

Tetra ethyl ammonium hydroxide (TEAOH; 89.6 g; Aldrich 40 wt % in H_2O) was added to 59.4 g of demineralized water. To the above solution, NaCl (0.5 g; Loba Fine

Chemie, India, 99 %) and KCl (1.4 g; Loba Fine Chemie, India, 99 %) were added and stirred till dissolution. To the above solution, 29.5 g of fumed silica (Cab-O-Sil 99 %, Fluka) was added and stirred until the gel became homogeneous. In a separate beaker, 20 g of demineralized water and NaOH (0.3 g; Loba Fine Chemie, India 99 %) were mixed. To this solution 1.8 g of sodium aluminate (48.68 % Al_2O_3 39.0 % Na_2O and 12.32 % H_2O) was added and the mixture was stirred for 30 min. This gel was added to the earlier gel and stirred until a homogeneous mixture was obtained. The final gel was then transferred to a teflon lined stainless steel autoclave. The gel was kept at room temperature for 20 h at 408 K. The product was filtered, washed with distilled water and dried at 383 K for 6 h.

2.1.3. Synthesis of Zeolite FAU: Zeolite-FAU was synthesized according to a reported procedure[4] using the gel composition in terms of oxides:

$$4.62\ Na_2O: 10.0\ SiO_2: Al_2O_3: 180\ H_2O.$$

2.1.3.1. Seed gel preparation: The gel composition was: 10.67 Na_2O: Al_2O_3: 10 SiO_2: 180 H_2O. NaOH (4.1 g; Loba Fine Chemie, India, 99 %) was dissolved in 20 g of demineralized water. To the above solution, sodium aluminate (2.1 g; 48.68 % Al_2O_3, 39.0 % Na_2O and 12.32 % H_2O) was added and the solution was stirred for 30 min. To the above gel, 22.7 g of sodium silicate (28.6 % SiO_2, 8.82 % Na_2O and 62.58 % H_2O) solution was added and stirred for 30 min. Then this gel was transferred to a polyproplene bottle and capped. The gel was kept at room temperature for 24 h.

2.1.3.2. Gel synthesis and crystallization: The gel composition for the zeolite synthesis was: 4.3 Na_2O: Al_2O_3: 10 SiO_2: 180 H_2O. NaOH (0.14 g) was dissolved in 13.1 of demineralized water. To this solution, 13.1 g of sodium aluminate (48.68 % Al_2O_3 39.0 % Na_2O and 12.32 % H_2O) was added and stirred until it dissolved. To this gel 142.4 g sodium silicate (28.6 % SiO_2, 8.82 % Na_2O and 62.58 % H_2O) solution was added and stirred vigorously for 1 h. Next, 16.5 g of the seed gel was added slowly under rapid stirring. The final gel was stirred for 1h, and then transferred to a teflon lined stainless steel autoclave. The gel was heated at 368 K for 24 h. The product was filtered, washed with distilled water and dried at 383 K fro 6 h.

2.1.4. Synthesis of Molecular Sieve ETS-10: The hydrothermal synthesis of ETS-10 molecular sieve was carried out following a published procedure[5] using $TiCl_4$ with the following gel composition:

$$3.70\ Na_2O: 0.95\ K_2O;\ TiO_2: 5.71\ SiO_2: 171\ H_2O.$$

In a typical synthesis, 52.5 g of sodium silicate (28.6 % SiO_2. 8.82 % Na_2O and 62.58 % H_2O) and 40 g distilled water were stirred vigorously for 30 min. To this solution, 9.3 g NaOH in 40 g of demineralized water was added. After this, dropwise addition of 32.8 g of $TiCl_4$ solution (25.42 wt % $TiCl_4$, 25.92 wt % HCl and 48.60 wt % H_2O) was done with vigorously stirring. A colored solution was obtained. Finally 7.8 g of $KF_2 \cdot H_2O$ was added and the mixture was stirred well. The pH of the gel was 11.2 ± 0.2. The mixture was then transferred to a stirred stainless steel autoclave (Parr Instruments, USA) for crystallization under stirred condition. The temperature was kept at 473 K with a stirring speed of 200 r.p.m. for 16 h. After crystallization, the product was filtered and washed with demineralized water till the pH of filtrate was 10.7 ± 0.1. The product was dried at 383 K for 6 h.

2.2. MODIFICATION OF MOLECULAR SIEVES

2.2.1. Ion Exchange: Ion exchange of the different molecular sieves, LTL, BEA, FAU and ETS-10 was carried out at 353 K using 40 ml of the required metal chloride solution per gram of the solid sample for 6h. The ion exchange was carried out thrice. The ion exchanged molecular sieves were washed with demineralized water and dried at 383K for 10h. All the samples were finally calcined at 753 K for 6 h in flowing dry air. The chemical compositions of the ion exchanged samples are presented in Tables 2.1 to 2.4.

***2.2.2. Impregnation of Platinum**:* Loading of Pt over the different alkali and alkaline earth metal exchanged molecular sieves was carried out by a wet impregnation method using $[Pt(NH_3)_4Cl_2]$ (Aldrich, 99.5 % purity). Different platinum loadings in the range of 0.2 to 0.8 wt % were carried out. A known amount of the freshly calcined sample was added to the aqueous Pt salt solution containing the required amount of Pt to obtain the desired weight percent loading. The mixture was evaporated to dryness at 333 K. After impregnation, the samples were dried at 383 K for 6 h and finally calcined at 753 K for 6 h in air.

2.3. CHARACTERIZATION

***2.3.1. X-ray Diffraction**:* Powder X-ray diffraction patterns of all the samples were recorded using a Rigaku (Model D-MAX II VC, Japan) X-ray diffractometer with Ni-filtered Cu-Kα radiation (λ = 1.540 Å). The sample was ground well and dried at 383 K for 4 h. All the samples were scanned in the 2 θ range of 4 to 45 degrees with at a scan rate of one degree min^{-1}. The typical XRD patterns of the molecular sieves (calcined samples) are shown in Fig. 2.1 (a to D) for LTL, BEA, FAU and ETS-10, respectively. The d values were compared with literature values for LTL, BEA, FAU and ETS-10 molecular sieves and were found to be similar.[1-5]

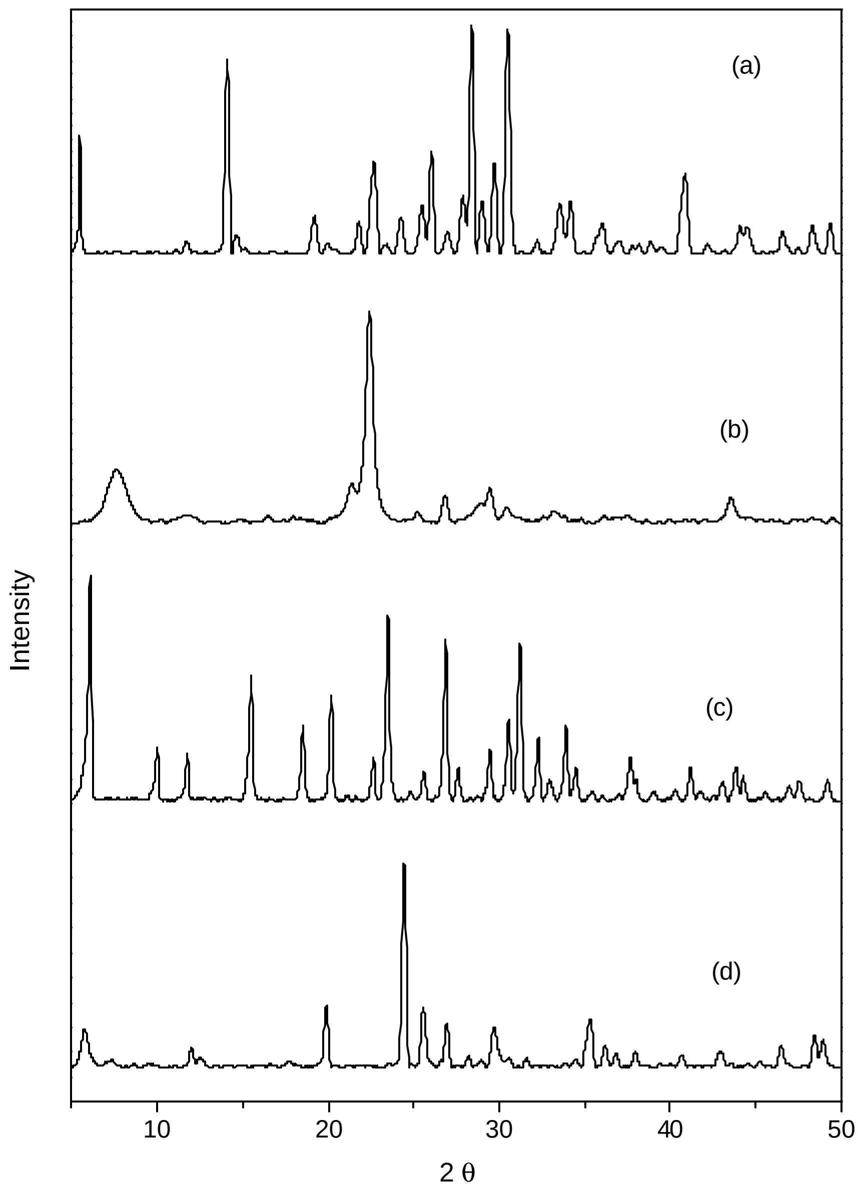

Fig. 2.1. XRD patterns of the molecular sieves: (a) LTL; (b) BEA; (c) FAU and (d) ETS-10.

The intensities of the X-ray diffraction lines of the as synthesized samples were slightly larger than those of the calcined samples. The intensities for the cation exchanged samples decreased slightly and were in the order: Li > Na ≅ Mg > K ≅ Ca ≅ Sr > Rb > Ba > Cs-zeolite. Similar results have been reported by Engelhardt *et al.*[6]

2.3.2. BET Surface Area: The surface areas of the samples were calculated from N_2 sorption isotherms using the BET procedure (NOVA Model 1200). The surface areas of the various cation exchanged zeolite samples are presented in Tables 2.1 to 2.4 for LTL, BEA, FAU and ETS-10, respectively. The surface areas were found to be larger for the H forms of the zeolites. The surface area decrease with increasing size of the cation (H > Li > Na > K > Rb > Cs and Mg > Ca > Sr > Ba) as shown in Tables 2.1 to 2.4. Surface areas of the H forms of the molecular sieves were in the order: H-BEA > H-FAU > H-LTL > H-ETS10.

2.3.3. Chemical Analysis: Wet chemical methods were used to determine the chemical composition of the crystalline materials. A known amount of the sample was taken in a platinum crucible with a lid and heated to a high temperature (1000 K) for 5 h. The sample was then cooled in an inert atmosphere (desiccator) and weighed. The difference between the weights gave the weight loss on ignition. The dry weight of the sample was noted.

Table 2.1 Chemical composition of ion exchanged M-LTL samples (M = H, Li, Na, K, Rb, Cs Mg, Ca, Sr and Ba)

Cation exchanged	Chemical composition	BET Surface area, m^2/g
H	$H_{6.35}K_{2.10}(Al_{8.45}Si_{30.55}O_{72})$	612
Li	$Li_{7.14}K_{1.31}(Al_{8.45}Si_{30.55}O_{72})$	598
Na	$Na_{7.06}K_{1.39}(Al_{8.45}Si_{30.55}O_{72})$	578
K	$K_{8.45}(Al_{8.45}Si_{30.55}O_{72})$	569
Rb	$Rb_{6.95}K_{1.49}(Al_{8.45}Si_{30.55}O_{72})$	532
Cs	$Cs_{6.32}K_{2.13}(Al_{8.45}Si_{30.55}O_{72})$	510
Mg	$Mg_{3.73}K_{1.08}(Al_{8.45}Si_{30.55}O_{72})$	589
Ca	$Ca_{3.72}K_{1.20}(Al_{8.45}Si_{30.55}O_{72})$	578
Sr	$Sr_{3.70}K_{1.45}(Al_{8.45}Si_{30.55}O_{72})$	542
Ba	$Ba_{3.38}K_{1.68}(Al_{8.45}Si_{30.55}O_{72})$	511

The sample was then treated with four drops of concentrated H_2SO_4 and 5 ml of HF (50 wt %) and evaporated on the hot plate to remove silicon in the form of H_2SiF_6.

Table 2.2 Chemical composition of ion exchanged M-BEA samples (M = H, Li, Na, K, Rb, Cs Mg, Ca, Sr and Ba)

Cation exchanged	Chemical composition	BET Surface area, m^2/g
H	$H_{3.10}Na_{0.22}(Al_{3.32}Si_{60.68}O_{128})$	714
Li	$Li_{2.91}Na_{0.41}(Al_{3.32}Si_{60.68}O_{128})$	706
Na	$Na_{3.32}(Al_{3.32}Si_{60.68}O_{128})$	695
K	$K_{2.96}Na_{0.36}(Al_{3.32}Si_{60.68}O_{128})$	671
Rb	$Rb_{2.74}Na_{0.58}(Al_{3.32}Si_{60.68}O_{128})$	592
Cs	$Cs_{2.85}Na_{0.47}(Al_{3.32}Si_{60.68}O_{128})$	548
Mg	$Mg_{1.48}Na_{0.26}(Al_{3.32}Si_{60.68}O_{128})$	701
Ca	$Ca_{1.41}Na_{0.50}(Al_{3.32}Si_{60.68}O_{128})$	689
Sr	$Sr_{1.45}Na_{0.44}(Al_{3.32}Si_{60.68}O_{128})$	613
Ba	$Ba_{1.37}Na_{0.58}(Al_{3.32}Si_{60.68}O_{128})$	589

Table 2.3 Chemical composition of ion exchanged M-FAU samples (M = H, Li, Na, K, Rb, Cs Mg, Ca, Sr and Ba)

Cation exchanged	Chemical composition	BET Surface area, m^2/g
H	$H_{54.55}Na_{4.49}Si_{136.96}Al_{59.04}O_{384}$	674
Li	$Li_{49.03}Na_{10.01}Si_{136.96}Al_{59.04}O_{384}$	653
Na	$Na_{59.04}Si_{136.96}Al_{59.04}O_{384}$	646
K	$K_{47.99}Na_{11.05}Si_{136.96}Al_{59.04}O_{384}$	638
Rb	$Rb_{39.88}Na_{19.62}Si_{136.96}Al_{59.04}O_{384}$	614
Cs	$Cs_{36.77}Na_{22.27}Si_{136.96}Al_{59.04}O_{384}$	582
Mg	$Mg_{23.48}Na_{12.08}Si_{136.96}Al_{59.04}O_{384}$	642
Ca	$Ca_{22.49}Na_{10.70}Si_{136.96}Al_{59.04}O_{384}$	632
Sr	$Sr_{21.06}Na_{13.47}Si_{136.96}Al_{59.04}O_{384}$	615
Ba	$Ba_{20.54}Na_{14.50}Si_{136.96}Al_{59.04}O_{384}$	590

This procedure was repeated thrice to ensure that all the silicon species were evaporated. Then it was heated on a Bunsen flame to red heat for 5 h, cooled in a desiccator (in an inert atmosphere) and weighed. The loss was recorded and was due to the silica present in the sample. The residue was dissolved in 2 ml of concentrated hydrochloric acid and two drops of hydrofluoric acid (50 wt %) and diluted to a known volume. The solution was then analyzed for the desired elements such as Pt, Ti, Al, Ba, Cs, Sr, Rb, Ca, K, Mg, Na or Li by atomic absorption spectroscopy (AAS).

Ti estimation was also carried out by a spectroscopic method as reported by Vogel.[7] In this method, a known volume (diluted) of the solution was taken in a volumetric flask and 2 ml of dilute H_2O_2 (2 ml of 50 % H_2O_2 diluted to 50 ml) added to it. In this procedure titanium forms an yellow Ti(IV) peroxo complex with H_2O_2.

Table 2.4 Chemical composition of ion exchanged M-ETS-10 samples (M = H, Li, Na, K, Rb, Cs Mg, Ca, Sr and Ba)

Cation exchanged	Chemical composition	BET Surface area, m^2/g
H	$H_{29.1}Na_{1.02}K_{2.3}(Ti_{16.21}Si_{79.74}O_{208})$	502
Li	$Li_{21.2}Na_{5.4}K_{3.7}(Ti_{16.21}Si_{79.74}O_{208})$	452
Na	$Na_{27.2}K_{4.0}(Ti_{16.21}Si_{79.74}O_{208})$	449
K	$Na_{8.6}K_{22.4}(Ti_{16.21}Si_{79.74}O_{208})$	440
Rb	$Rb_{12.1}Na_{15.2}K_{3.9}(Ti_{16.21}Si_{79.74}O_{208})$	419
Cs	$Cs_{10.2}Na_{16.3}K_{5.4}(Ti_{16.21}Si_{79.74}O_{208})$	388
Mg	$Mg_{11.2}Na_{6.3}K_{3.4}(Ti_{16.21}Si_{79.74}O_{208})$	428
Ca	$Ca_{11.9}Na_{7.4}K_{2.3}(Ti_{16.21}Si_{79.74}O_{208})$	412
Sr	$Sr_{12.2}Na_{5.3}K_{2.4}(Ti_{16.21}Si_{79.74}O_{208})$	402
Ba	$Ba_{11.2}Na_{7.2}K_{2.3}(Ti_{16.21}Si_{79.74}O_{208})$	390

The intensity of the color is proportional to the titanium species present in the solution. Sufficient amount of H_2SO_4 was present in the final solution to prevent the condensation of metatitanic acid. The temperature of the solution was kept constant at 298 K. The results of the chemical analysis are presented in Tables 2.1 to 2.4 for LTL, BEA, FAU and ETS-10, respectively.

2.3.4. Scanning Electron Microscopy (SEM): The crystallite size and morphology of the calcined and as synthesized samples were determined by SEM (Model JSM 5200, JEOL, Japan) (Fig. 2.2). The samples were sputtered with gold to prevent surface charging and thermal damage from the electron beam.

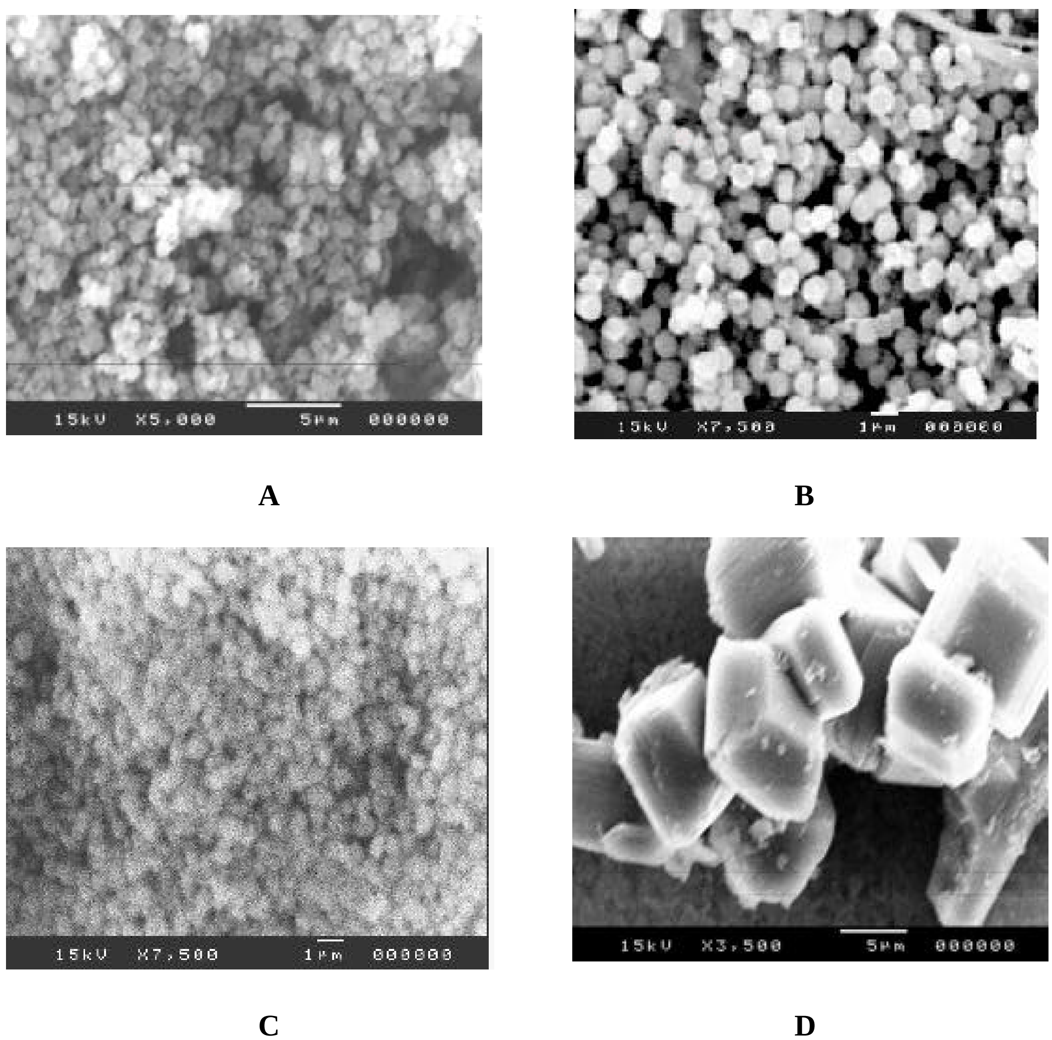

Fig. 2.2. Crystal morphology of A) LTL, B) BEA, C) FAU and D) ETS-10.

The LTL sample consists of small crystals with uniform size (~ 0.5 µm) as seen in Fig. 2.2 (A). The SEM micrograph of BEA shows uniform hexagonal crystals with ~ 1 µm crystal size (Fig. 2.2 B). The SEM micrograph of FAU reveals hexagonal and cubic shaped uniform crystals of less than 1 µm (Fig. 2.2 C). The ETS-10 sample is found to consist of large crystals of nearly uniform size (10-15 µm and thickness of about 5-8 µm; Fig. 2.2 D). A similar morphology was reported by Das *et al.*[8] and Rocha *et al.*[9] for ETS-10 samples crystallized by them.

2.3.5. Ultraviolet Spectroscopy: Neat samples (2.5 g) were used to record the ultraviolet (UV) spectra. UV spectra were recorded on a Shimadzu instrument (Model No. Shimadzu UV-2550) in the range of 200 to 800 cm^{-1}. The spectra were obtained in the diffuse reflectance mode using $BaSO_4$ as a reference.

Comparing the UV-Vis spectra of the zeolites (M-LTL, M-BEA and M-FAU), it is observed that the prominent band at 275 nm and 225 nm correspond to Si and Al coordination. Li-LTL samples show absorbance at 243 nm, the band shifting to 246 nm for K-LTL and 252 nm for Cs-LTL (Fig. 2.3 A). M-BEA and M-FAU also exhibit similar bands [Li-BEA (260 nm), K-BEA (266 nm), Cs-BEA (272 nm) (Fig. 2.3 B) and Li-FAU (258 nm); K-FAU (262 nm) and Cs-FAU (265 nm) Fig. 2.3 C]. The diffuse reflectance spectra in the UV-visible region of M-ETS-10 (M = Li, K, Cs and Ba) are presented in Fig. 2.3 D. The broad absorption in the region 250 to 325 nm suggests the presence of Ti^{4+} in octahedral coordination.[10] M-ETS-10 samples exhibit shift of the absorption band on exchanging with more basic cations, the bands for Li, K, Cs and Ba being at 260, 262, 275 and 279 nm, respectively. These absorbance bands are associated with the $O^{2-} \rightarrow Ti^{4+}$ charge transfer transition.[10]

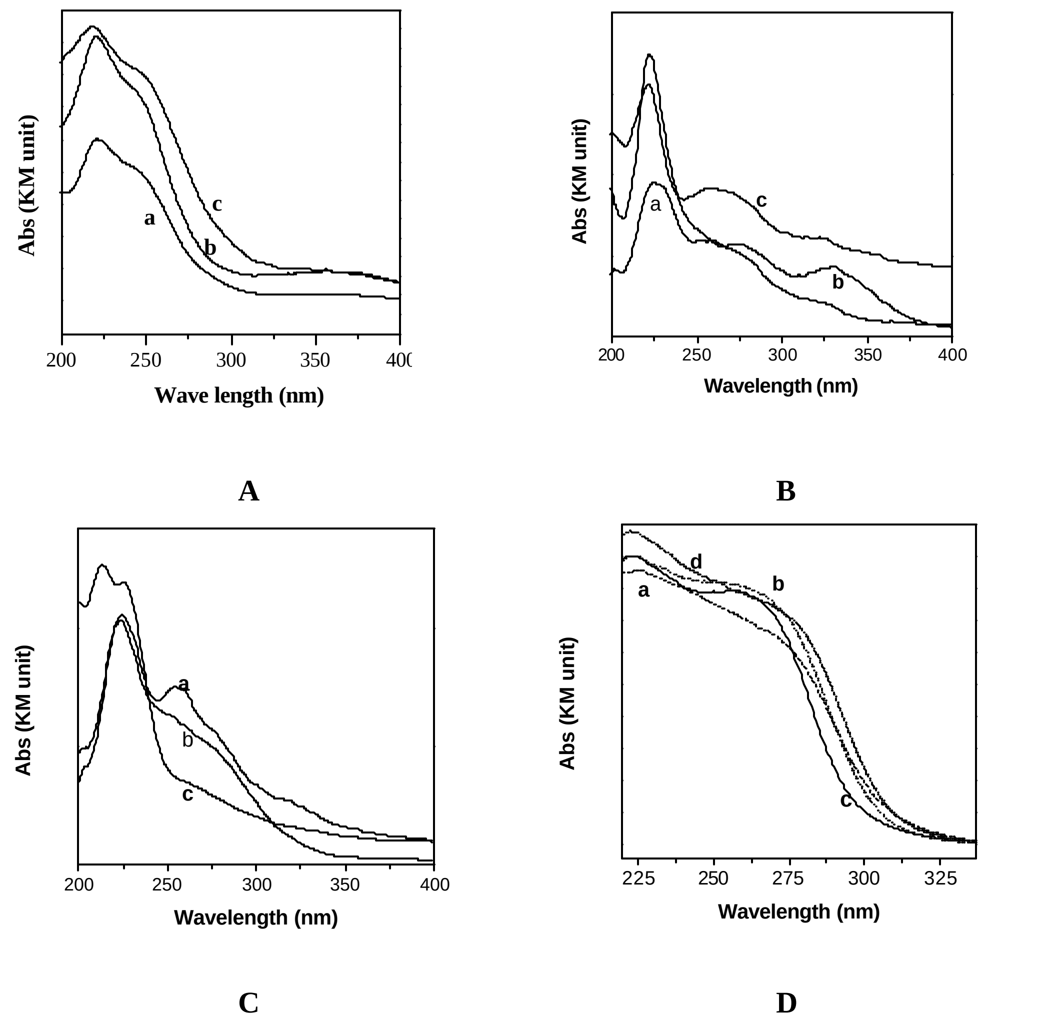

Fig. 2.3. UV-Vis diffuse reflectance spectra of M-molecular sieve samples. A = M-LTL, B = M-BEA, C = M-FAU and D = M-ETS-10 (M = Li, K, Cs and Ba for a, b, c and d, respectively).

In contrast, this charge transfer transition is found centered at ~ 200 nm in TS-1,[11] where Ti is in tetrahedral coordination and at ~ 255 nm in ETS-4[12] a small pore analog of ETS-10.

2.3.6. Infrared Spectroscopy of Framework Region: FTIR spectra were recorded in the framework region (400 to 1300 cm^{-1}) in transmittance mode. KBr pellets containing 1 mg zeolite and 300 mg KBr (dried) were prepared (under 5 ton pressure) and used for analysis. Spectra were recorded with a Nicolet FTIR spectrometer (Model 60 SX B) with 2 cm^{-1} resolution and averaged over 500 scans.

2.3.6.1. Vibrations of Si-O-Si bonds: The vibrational modes of Si-O-Si bonds in tetrahedral silica polymorphs have bands in three regions, i.e. 1300 - 950 cm^{-1} (very strong band, ν_1), 850 - 600 cm^{-1} (medium strong, ν_2) and near 450 cm^{-1} (strong, ν_3). The strongest complex band ν_1 observed in the 1300 - 950 cm^{-1} region is associated with the asymmetric stretching of Si-O-Si bridges (Table 2.5). This mode is frequently split, due to either the in-phase (ν_1') or the out-of phase coupling (ν_1'') of the asymmetric stretching modes of the nearest Si-O-Si groups.[13] In other words, this mode somewhat couples with the symmetric and asymmetric stretching of the four Si-O bonds of the SiO_4 tetrahedra. The ν_2 mode is essentially a bending mode of the Si-O-Si bridges, although mixed with a asymmetric stretching mode, as suggested by Flanigen *et al.*[14] The lowest frequency IR mode ν_3 is associated with the out-of-plane deformation of the Si-O-Si bridges; so it is a “rocking” mode. The additional peak at around 420 cm^{-1} is due to the pore opening of the zeolites.

2.3.6.2. Vibrational modes involving Ti ions: According to the structure of ETS-10, Ti-O-Ti bent bridging oxygens exist, providing three optical modes, i.e. an asymmetric Ti-O-Ti stretching, a symmetric stretching/ in plane deformation mode, and an out of plane rocking mode. Similarly, the structural oxygen atoms bridging between one Ti and one Si atom provide Si-O-Ti asymmetric modes, symmetric stretching/ in plane deformation modes and Si-O-Ti asymmetric stretching of Ti silicate (where Ti is isolated and octahedrally coordinated) near 960 cm^{-1} with medium strong intensity. Ti-O-Si bond also shows a rocking mode near 510 cm^{-1}. The band around 750 cm^{-1} region is likely to be due to the symmetric stretching of the Ti-O-Ti bridge.

FTIR spectra of different cation exchanged samples are shown in Figs. 2.4 to 2.7 for M-LTL, M-BEA, M-FAU and M-ETS-10 (M = Li to Cs and Mg to Ba) samples. In the case of LTL samples (Fig. 2.4 A), the prominent band at 1020 cm^{-1} is found to shift towards higher frequencies with increasing size of the cation from Li to Cs. A shoulder between 1200 and 1250 cm^{-1} is also found to shift towards higher frequencies. The presence of a M^{n+} cation in the vicinity of the anionic oxygen of the framework in the n-membered ring interacts electrostatically and leads to a concomitant reduction in the Si-O and / Al-O bond strength in the ring. The greater the charge transfer from oxygen to the M^{n+} cations, the weaker will be these bonds. Therefore, the vibrational bands will shift according to the ratio of electronic charge to cationic radius. Similar results are also observed in the case of alkaline earth cation

Table 2.5 Frequencies of framework vibrations

Observed band position (cm^{-1})	Type of vibration
1,070	Si-O stretching
780	Ti-O stretching
690	Ti-O stretching
570	Si-O rocking, O-Ti-O bending
450	O-Si-O bending, O-Ti-O bending
	Ti-O rocking
Internal tetrahedra	Si-O-Si and Si-O-Al
1250 and 950	asymmetric stretching (ν_1)
760	Si-O-Si and Si-O-Al, symmetric stretching (ν_2)
700	Si-O-Si and Si-O-Al, symmetric stretching (ν_3)
External linkage	
650-500	Double ring
300-420	Pore opening

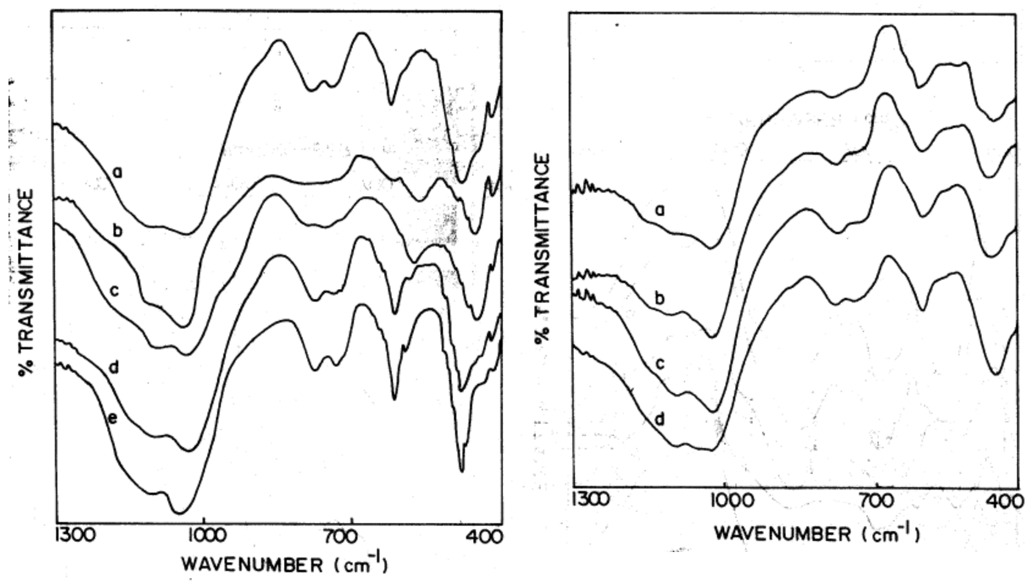

A **B**

Fig. 2.4. **FTIR spectra of M-LTL samples in the framework region. A): a) H, b) Li, c) Na, d) K, e) Rb and f) Cs and B): a) Mg, b) Ca, c) Sr and d) Ba.**

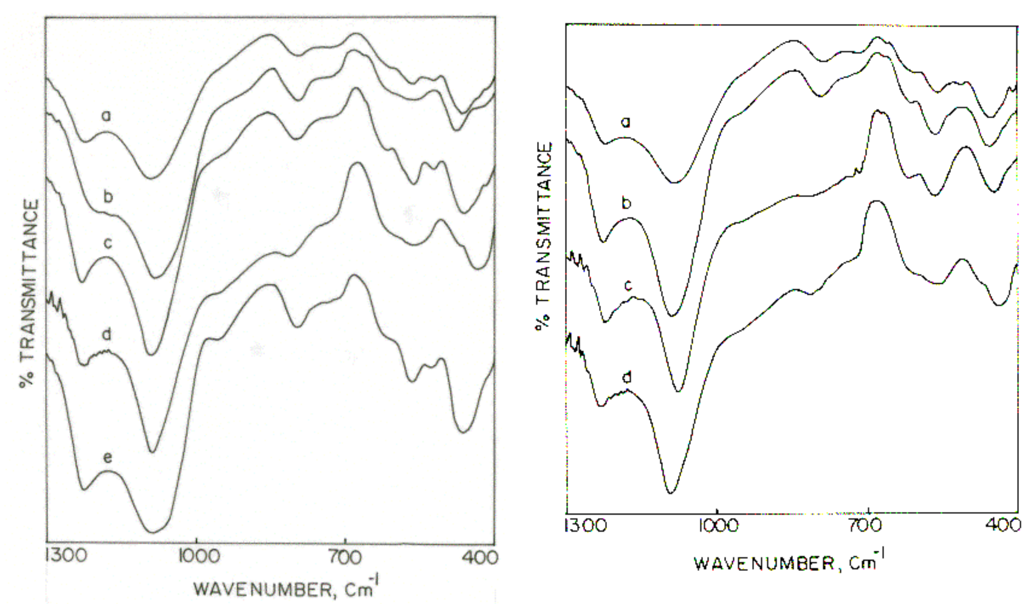

A **B**

Fig.2.5. **FTIR spectra of M-BEA samples in the framework region. A): a) H, b) Li, c) Na, d) K, e) Rb and f) Cs; B): a) Mg, b) Ca, c) Sr and d) Ba.**

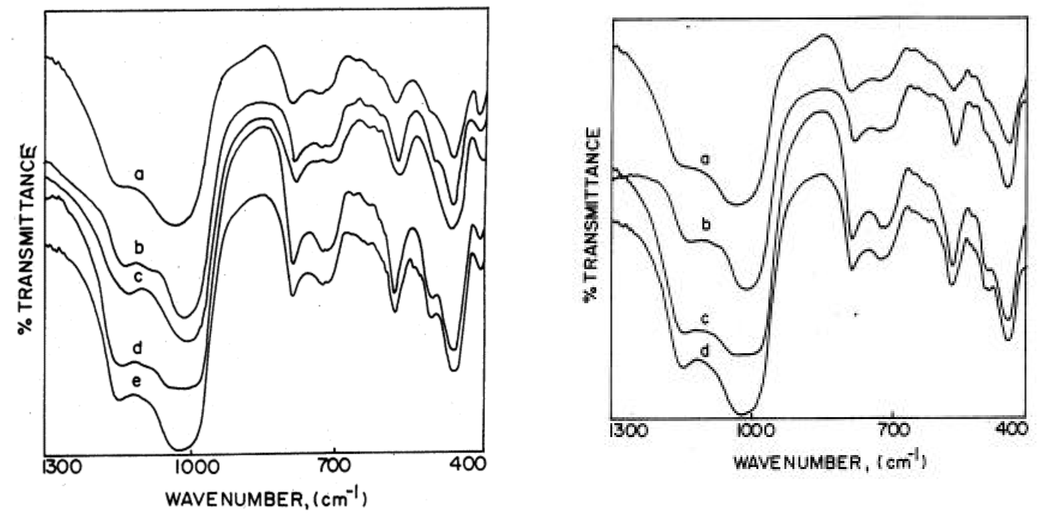

A **B**

Fig. 2.6. FTIR spectra of M-FAU samples in the framework region. A): a) H, b) Li, c) Na, d) K, e) Rb and f) Cs and B): a) Mg, b) Ca, c) Sr and d) Ba.

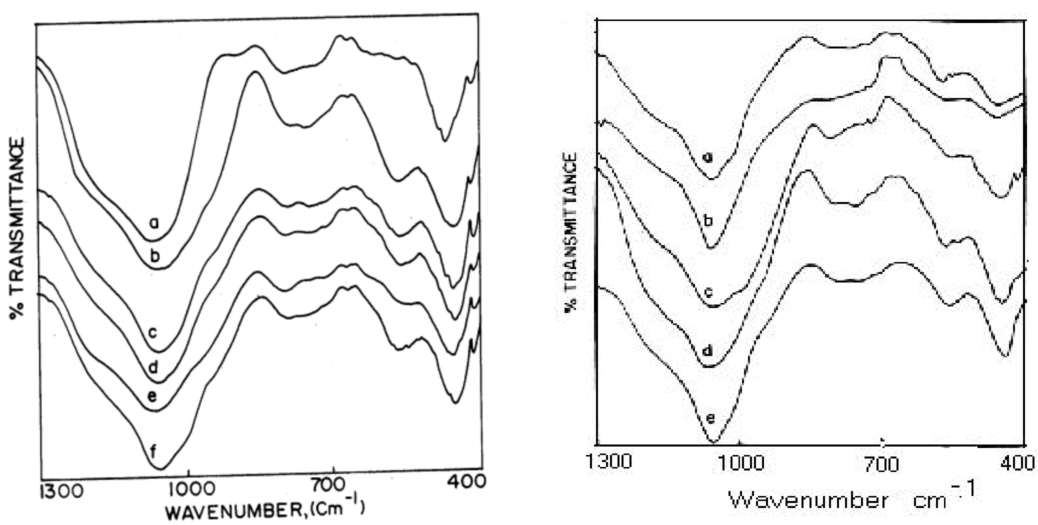

A **B**

Fig.2.7. FTIR spectra of M-ETS-10 samples in the framework region. A): a) H, b) Li, c) Na, d) K, e) Rb and f) Cs and B): a) Mg, b) Ca, c) Sr, d) Ba and e) As synthesized.

exchanged samples (Mg to Ba, Fig. 2.4 B) and in the case of M-BEA and M-FAU zeolite samples. (Figs. 2.5, and 2.6, respectively).

ETS-10 molecular sieves are zorite structures containing zig-zag chains of corner-sharing TiO_6 octahedral and tetrahedral silicate units (giving rise Ti-O-Si and Ti-O-Ti chain structures). The Ti ions exist with an octahedral coordination involving four short bonds with the tetrahedral silicate unit and two long bonds along the Ti chain, the Na and K cations are present in between. These structural units are responsible for the typical vibrational features. The frequencies of prominent bands shift towards higher frequencies on cation exchange from Li to Cs and Mg to Ba (Fig. 2.7; A and B, respectively). Similar results have been reported in the literature.[15-17]

2.3.7. Infrared Spectroscopy of Adsorbed CO_2: FTIR spectra were recorded in the range of 4000 to 800 cm^{-1} using a Nicolet 60 SXB spectrometer with 2 cm^{-1} resolution, averaging over 500 scans. For spectra of adsorbed CO_2, self-supported sample wafers were used. The sample was pressed into thin wafers (5-6 mg/cm^2), evacuated (10^{-5} torr) at 673 K and cooled to 298 K to record the spectrum of the pure sample. Ultra pure CO_2 (99.999 % pure, Linde Air) was then adsorbed on the sample at 5 mm equilibrium pressure for 1 h and another spectrum was recorded. Then part of the CO_2 gas was pumped out to maintain an equilibrium pressure 0.4 mm and the spectrum was recorded again.

CO_2 being amphoteric in nature can be used to monitor both Lewis acid centers and Lewis base centers on metal oxides and zeolite surfaces. It is a linear molecule having $D_{\alpha v}$ symmetry and three fundamental vibrations, one stretching vibration ν_1, which is Raman active appearing as a doublet at 1285 and 1388 cm^{-1} and two IR active vibrations, the doubly degenerate deformation ν_2 at 667 $cm^{-1}$and the anti symmetric stretch ν_3 at 2349 cm^{-1}.[17] The IR spectrum of adsorbed CO_2 varies distinctly from the gas phase spectrum and three types of adsorption have been distinguished: a) on unreactive surfaces, the infrared spectrum of adsorbed CO_2 shows mostly the ν_3 vibration near 2343 cm^{-1}, b) the adsorption of CO_2 on reactive surfaces may give rise to several adsorbed species, such as carbonate, bicarbonate and formate, which exhibit characteristic adsorption bands[18-20] and c) CO_2 can also function as a ligand in different complexes of transition metals as highly perturbed structures. These CO_2 species have a characteristic pair of adsorption bands in the region 1200 - 1700 cm^{-1}. This type of bond is formed when electrons are donated to a CO_2 molecule and a CO_2^- anion is formed. But such an anion is stable only at low temperatures.

CO_2 is a weakly acidic (amphoteric) molecule and is expected to adsorb on the basic sites of the zeolites. The intensity of the IR bands of CO_2 in the CO_3 region (chemisorbed CO_2) can be used to quantify the relative basicity of different samples. The relative band intensity of adsorbed CO_2 in FTIR spectra (1200 - 1750 cm^{-1}) at 0.4 and 5 mm equilibrium pressure observed over different cation exchanged samples is presented in Table 2.6. Going by the relative intensities of the IR bands, basicity increases with increasing electropositive nature of the exchanging cation, Li to Cs, and the zeolites can be arranged in the order of basicity as: Cs-LTL > Cs-ETS-10 > Cs-BEA > Cs-FAU.

Considering the possible cation distribution on different crystallographic sites in LTL,[21] FAU[22,23] and BEA[24] zeolites, under ion exchange conditions used in this study, most of the Cs cations should be located in the channels and supercages and channel intersections, respectively. CO_2 has a kinetic diameter of 3.3 Å and it cannot enter the cancranite cages of LTL, sodalite cages in FAU and 6-MR of BEA type zeolites; so, it can only interact with cations in the intersection of channels. Carbon

Table 2.6 Relative basicity of alkali metal exchanged samples from FTIR studies

Samples	Relative intensity of IR spectra of CO_2[a]		S_{int}
	FTIR (0.4)[b]	FTIR (5)[c]	
Cs-LTL	130	166	3.46
Cs-BEA	105	97	4.16
Na-FAU	12	7	3.79
Cs-FAU	36	24	3.67
Li-ETS-10	78	84	3.49
Na-ETS-10	82	96	3.44
K-ETS-10	108	123	3.34
Rb-ETS-10	120	129	3.22
Cs-ETS-10	125	132	3.14
Ba-ETS-10	112	126	3.66

[a] sum of the intensities of the bands in the range, 1200-1700 cm^{-1} and [b and c] spectra recorded at 0.4 and 5.0 mm equilibrium pressure, respectively.

dioxide will adsorb on metals and basic oxides in many forms, the symmetrical, monodentate, bidentate and bridged forms.[20] The interaction of chemisorbed CO_2 is believed to be through transfer of electronic charge to the CO_2 molecule from the alkali metal, the interaction increasing with the size of the metal ion. Besides, the simultaneous interaction of the alkali cation and O^{2-} anion with adsorbed CO_2 may also be taking place. The increasing shift in the high and low frequency bands and the increasing frequency difference between the bands on going from Li^+ to Cs^+ exchanged samples indicate increasing interaction with CO_2. Solymosi and Knözinger[21] have proposed $\Delta\nu$ values of 0, 100, 300 and > 400 cm^{-1} for symmetrical, monodentate, bidentate and bridged confirmations of adsorbed CO_2 species, on interacting surfaces, respectively. Going by this concept, the $\Delta\nu$ values observed for CO_2 on Li^+, Na^+, K^+ and Cs^+ exchanged M-ETS-10 samples indicate the presence of mainly monodentate and bidentate types of adsorbed species (vide infra). The concentration of bidentate species increases with the basicity of the alkali metal (vide infra).

2.3.7.1. Zeolite LTL: CO_2 can interact with the basic sites present in the 12-MR pore system. It forms complex M··O=C=O species giving rise to adsorption bands due to anti-symmetric stretching vibrations (ν_3 mode). In Fig. 2.8 A, the FTIR spectra of CO_2 adsorbed on zeolites Cs-LTL and Cs-BEA (a and b, respectively are presented). The differences between the two high frequency bands around 1700 cm^{-1} and the corresponding two low frequency bands around 1380 cm^{-1} are about 300 cm^{-1}. Corresponding bands are observed at 1675, 1647, 1389 and 1343 cm^{-1} (Fig. 2.8 B, c and d). In Table 2.7, the corresponding band positions are given of which the most intense and dominating band positions are indicated. From the data presented, it appears that adsorption of CO_2 on the zeolite samples studied involves both physical and chemical interactions because all modes of vibrations are observed in the spectra.

2.3.7.2. Zeolite BEA: The band position for CO_2 adsorption (CO_3 vibration region) is presented in Table 2.8. The wave number differences between the bands are consistent with the reported results and the bands can be ascribed to bidentate type of species. Cs-BEA exhibits a weak CO_2 adsorption band at 2345 cm^{-1} (Fig. 2.8 A). This is in good agreement with that reported in the literature for BEA samples.[25] It also shows weak chemisorption bands at 1625 and 1384 cm^{-1} that persist even after evacuation [Fig. 2.8 B (c and d) and Table 2.8]. This may be due to CO_2 adsorbed on the large cations present in the channel intersections. It should be pointed out that only three cations per unit cell are present in the channel transections of BEA, which is a high silica zeolite (Table 2.2). By comparison with the reported data for alumina, they can be assigned to hydrogen carbonates or monodentate carbonates.[26,27]

2.3.7.3. Zeolite FAU: The distributions of cations in different sites are 16, 32 and 48 per unit cell for I, II and III type of sites, respectively.[28] Cs cations can occupy only the site II locations in FAU because of steric constraints in other sites. The prominent ν_3 mode vibrational band at 2354 is shifted to 2345 cm^{-1} for Na-FAU (Fig. 2.9 A and Table 2.7). It also shows weak adsorptions at the positions, 1670, 1640, 1384 and 1360 $cm^{-1}$and 1698, 1649 and 1342 cm^{-1} for Na and Cs-FAU, respectively (Fig. 2.9 B). In the literature, different values between 2343 and 2355 cm^{-1} have been reported for the ν_3 mode of adsorbed CO_2.[29]

Table 2.7 FTIR spectral bands (ν_3 vibration mode) of physisorbed CO_2 on M-LTL, BEA and FAU zeolites

Sample	Prominent band	Shoulder bands	
Cs-LTL	2359	2343	2332
Cs-BEA	2360	2341	2331
Na-FAU	2354	-	-
Cs-FAU	2345	2331	-

Table 2.8 Frequencies of bands for different forms of carbonate specie formed on M-LTL, M-BEA and M-FAU zeolites

Samples	Type I (Anti symmetric)			Type II (Symmetric)		
	cm^{-1}	cm^{-1}	$\Delta\nu$	cm^{-1}	cm^{-1}	$\Delta\nu$
Cs-LTL	1675	1379	296	1647	1343	304
Cs-BEA	1674	1384	290	1625	1348	277
Na-FAU	1670	1384	286	1640	1360	280
Cs-FAU	1698	-	-	1649	1342	307

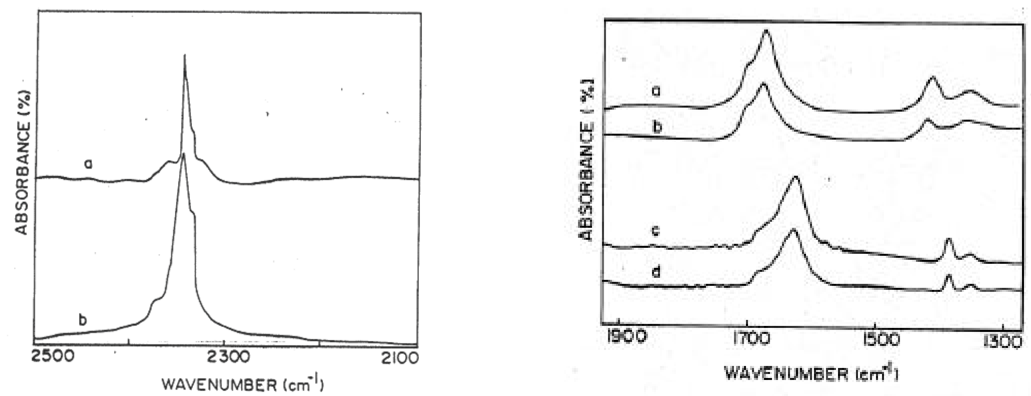

A **B**

Fig. 2.8. **A) FTIR spectra (298 K) in the CO_3 vibration region of adsorbed CO_2 on: a) Cs-LTL and b) Cs-BEA at 5 mm equilibrium pressure.**

B) FTIR spectra (298 K) of adsorbed CO_2 on Cs-LTL and Cs-BEA: a, b) Cs-LTL and c, d) Cs-BEA (a, c at 5 mm and b, d at 0.4 mm equilibrium pressure, respectively).

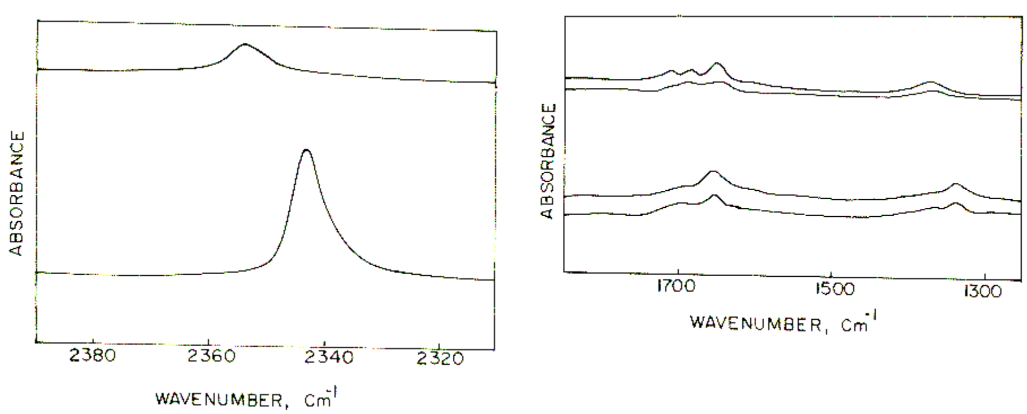

A **B**

Fig. 2.9. **A) FTIR spectra (298 K) in the CO_3 vibration region of adsorbed CO_2 on: a) Na-FAU and b) Cs-FAU at 5 mm equilibrium pressure.**

B) FTIR spectra (298 K) of adsorbed CO_2 on Na-FAU and Cs-FAU: a, b) Na-FAU and c, d) Cs-FAU (a, c at 5 mm and b, d at 0.4 mm equilibrium pressure, respectively).

2.3.7.4. Molecular sieve ETS-10: FTIR spectra of adsorbed CO_2 on alkali metal exchanged ETS-10 molecular sieves are shown in Fig. 2.10 wherein the bands due to the anti symmetric stretching ν_3 vibration of physisorbed CO_2 on Li, Na, K, Rb, Cs and Ba-ETS-10 are seen. They appear at 2356, 2352, 2347, 2345, 2344 and 2346 cm^{-1}, respectively (Fig. 2.10; Table 2.9). As the ionic radii of the alkali metal cations and the metal oxygen bond length increase, the electron donating ability (to adsorb CO_2) increases and hence the ν_3 anti symmetric stretching frequency shifts to lower wave numbers.

The FTIR spectra in the region of carbonate vibrations (chemisorbed CO_2, 1975 to 1275 cm^{-1}) are presented in Fig. 2.11 A and B. Adsorption of CO_2 shows two sets of bands, each set consisting of a band due to anti symmetric and another to symmetric stretching. The frequencies of these bands for different cationic forms of ETS-10 are presented in Table 2.10. The relative intensities of these bands marginally decrease with decrease in equilibrium pressure, but persist even after evacuation up to 10^{-5} torr. From these results it is clear that the exchanged alkali metal modifies the adsorptive property of ETS-10. It is possible that M-ETS-10 possesses active CO_2 adsorption sites on the surface of the framework as well as in the bulk of the intra pore volume. The topology of the surface and the intra pore volume determine the energetics of CO_2 adsorption and hence, the ν_3 mode band positions. Of all the arguments developed for explaining the FTIR spectra of adsorbed CO_2 on alkali modified zeolite surfaces, those of Bonelli *et al.*[30] are very important. From FTIR, adsorption microcalorimetry and quantum chemical calculations they concluded that cation-CO_2 interaction alone cannot account for the nature of the spectra of CO_2 adsorbed on such samples, and the presence of nearby framework anionic O^{2-} should also be considered. Their

Table 2.9 Vibrational bands (ν_3 vibration mode) of physisorbed CO_2 on M-ETS-10 zeolites

Samples	Prominent band (cm^{-1})	Shoulder bands (cm^{-1})	
Li	2356	2379	2330
Na	2352	2380	2331
K	2347	2381	2331
Rb	2345	2382	2332
Cs	2344	2384	2332
Ba	2346	2381	-

Table 2.10 Frequencies of vibrations of bands for different forms of carbonate specie adsorbed on M-ETS-10 molecular sieves

M	Type I (Anti symmetric)			Type II (Symmetric)		
	cm^{-1}	cm^{-1}	$\Delta\nu$	cm^{-1}	cm^{-1}	$\Delta\nu$
Li	1651	1339	312	1625	-	-
Na	1651	1335	316	1629	-	-
K	1651	1333	318	1632	-	-
Rb	1652	1330	322	1634	1279	355
Cs	1652	1327	325	1642	1280	362
Ba	1649	-	-	1625		

calculations showed that in the series from Li^+ to Cs^+, the cation becomes a progressively weaker Lewis acid for CO_2 adsorption; simultaneously the adjacent anionic framework becomes progressively stronger base causing internal compensation. This type of internal compensation is probably responsible for the small change in the frequency of the type I CO_3 band (Table 2.10). The large $\Delta\nu$ suggesting a bidentate type of adsorption further corroborates this view.

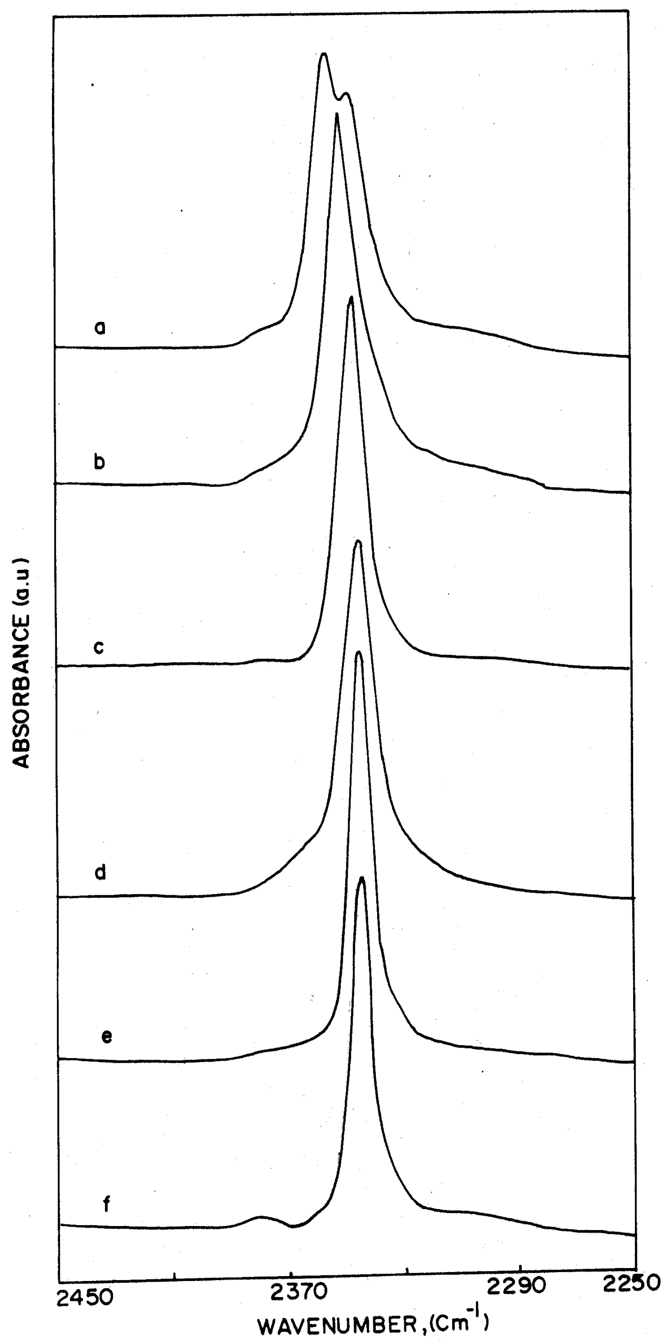

Fig.2.10. FTIR spectra (298 K) of adsorbed CO_2 in the CO_3 vibration region in M-ETS-10 [M = (a) Li, (b) Na, (c) K, (d) Rb, (e), Cs and (f) Ba (f)] at 5 mm equilibrium pressure of CO_2

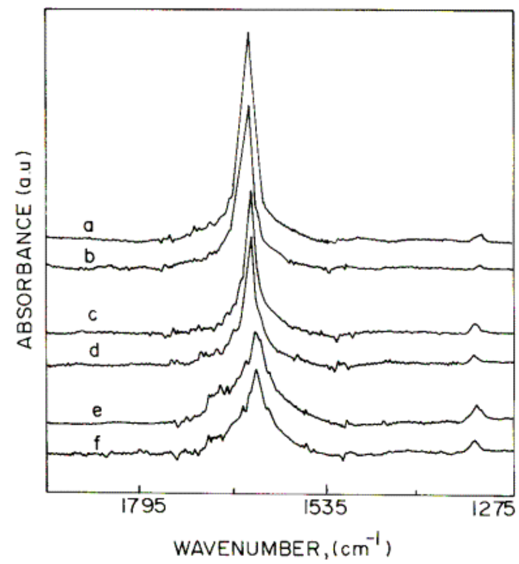

A

Fig. 2.11. FTIR spectra (298 K) of adsorbed CO_2 on alkali metal exchanged ETS-10 samples: a, b) Li, c, d) Na and e, f) K (a, c and e at 5 mm and b, d and f at 0.4 mm equilibrium pressure of CO_2, respectively).

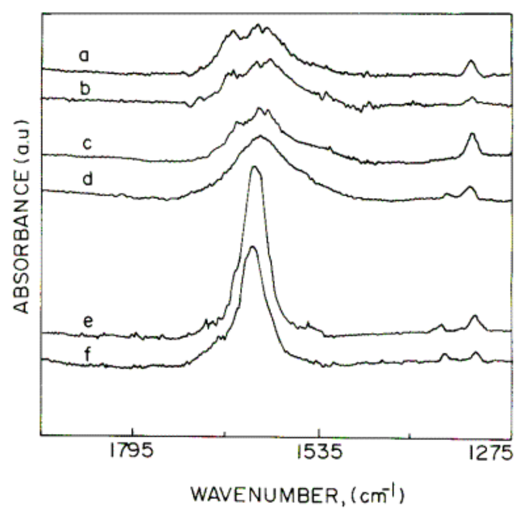

B

Fig.2.11. FTIR spectra (298 K) of adsorbed CO_2 on alkali metal exchanged ETS-10 samples: a, b) Rb, c, d) Cs and e, f) Ba (a, c and e at 5 mm and b, d and f at 0.4 mm equilibrium pressure of CO_2, respectively).

2.3.8. Comparison of Intensity (FTIR) of Adsorbed CO_2 with S_{int}: The intermediate electronegativity of the M-ETS-10 samples calculated according to the Sanderson equation[31] is presented in Table 2.6 and 2.14. It is noticed that S_{int} correlates with the basicity of the samples as determined by CO_2 adsorption. In the case of M-ETS-10, the calculated intermediate electronegativity also correlates well with a decrease on in ν_3 frequencies in the spectra of physisorbed CO_2 (shown in Fig. 2.12 A). Further correlation is deduced between the ionic radii of cations and the ν_3 frequencies of CO_2 (Fig. 2.12 B). This suggests an increasing M-CO strength with increasing cation radius. In other words the overall trend of basicity in ETS-10 is similar to that observed in other zeolites; basicity increases with increasing in the cation size: Li < Na < K < Ba < Rb < Cs-ETS-10.

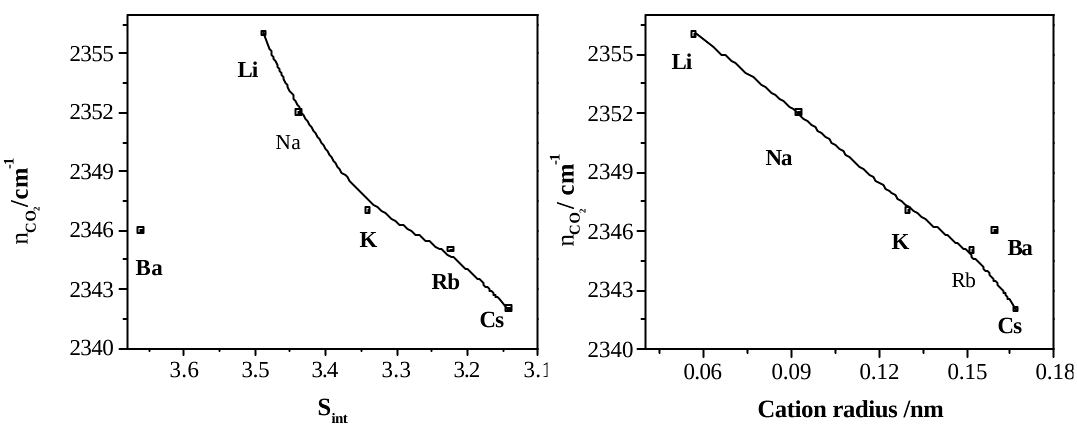

A **B**

Fig. 2.12. A) Relationship between intermediate electronegativity of M-ETS-10 and n_3 stretching band frequency of adsorbed CO_2.

B) Correlation between n_3 stretching band frequency of adsorbed CO_2 (at 0.4 mm equilibrium pressure) and the radius of the ion exchanged cation.

2.3.9. Temperature Programmed Desorption of Adsorbed CO_2: Temperature programmed desorption (TPD) of probe molecules like ammonia, pyridine, CO_2 and pyrrole is a widely used method for the determination of acidity-basicity characteristics of solid catalysts, due to the ease and reproducibility of the method.[32,33] CO_2 is frequently used as a probe molecule to determine basicity because of its small molecular size, stability and acidic character.

Characterization of the basicity of the different ion exchanged samples has been carried out by the TPD of adsorbed CO_2. In a typical temperature programmed desorption (TPD) experiment, about 400 mg of oven-dried sample (383 K for 16 h.) was taken in a 'U' shaped quartz cell. The catalyst sample was packed in one arm of the sample tube on a quartz wool bed. The temperature was monitored with the aid of thermocouples located near the sample from outside and on the top of the sample. The gas flows were monitored by highly sensitive mass flow controllers. Prior to TPD studies, the catalyst sample was pretreated by passage of high purity helium (50 ml min^{-1}) at 773 K for 2 h. After pretreatment, the sample was cooled to room temperature in helium, then saturated by passage of highly pure CO_2 (11.1 % CO_2 in He) at 303 K for 2 h. The catalyst sample was subsequently flushed at 313 K for 2 h to remove the physisorbed CO_2. TPD analysis was carried out from ambient temperature to 823 K at a heating rate of 10 K. The CO_2 concentration in the effluent stream was monitored using a thermal conductivity detector (instrument model: AutoChem 2910; Micromeritics, USA) and the areas under the peaks were integrated by use of GRAMS/ 32 software to determine the amount of CO_2 desorbed during TPD. TCD calibration was performed by passing known volumes of CO_2.

2.3.9.1. Zeolite LTL: The results of the TPD of adsorbed CO_2 of cation exchanged M-LTL samples are presented in Table 2.11. The TPD plots of various alkali and alkaline earth metal exchanged M-LTL (where M = Li, Na, Rb, K, Cs, Ca, Mg, Sr and Ba) samples are shown in Fig. 2.13. It was found that most of the CO_2 desorbed below 750 K with desorption peak maxima in the range of 420 to 620 K (Table 2.11). Based on the deconvoluted plots, it is seen that more than one type of adsorbed CO_2 specie are

Table 2.11 TPD data obtained over different alkali and alkaline earth metal exchanged LTL molecular sieve (M-LTL)

M	Temp. of peak maximum (K)		CO_2 desorbed
	Major peak	Minor peak	mmol/g
Li	418	540	57.4
Na	452	555	62.3
K	511	560	66.5
Rb	548	551	105.5
Cs	620	628	132.1
Mg	421	-	70.2
Ca	442	502	75.8
Sr	460	560	91.4
Ba	580	-	107.3

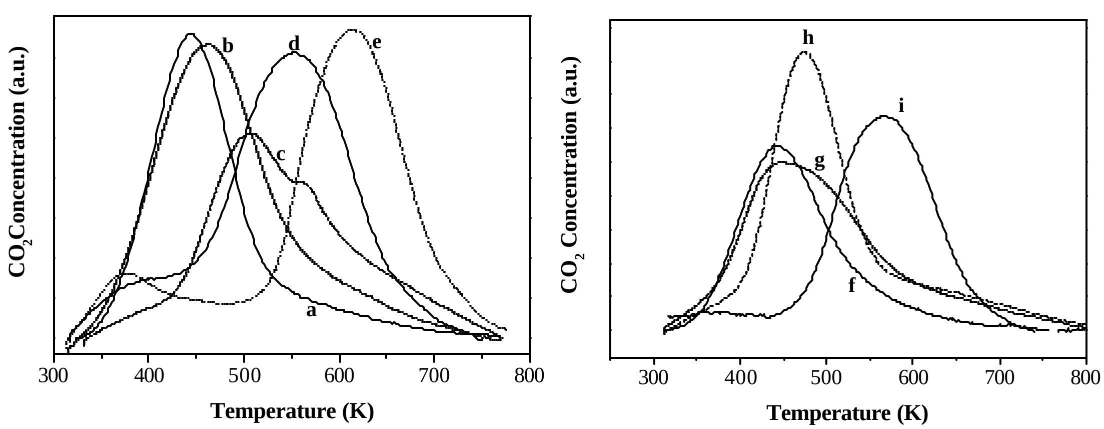

Fig. 2.13. TPD plots of CO_2 adsorbed on different cation exchanged LTL samples. (a) Li, (b) Na, (c) K, (d) Rb, (e) Cs, (f) Mg, (g) Ca, (h) Sr and (i) Ba.

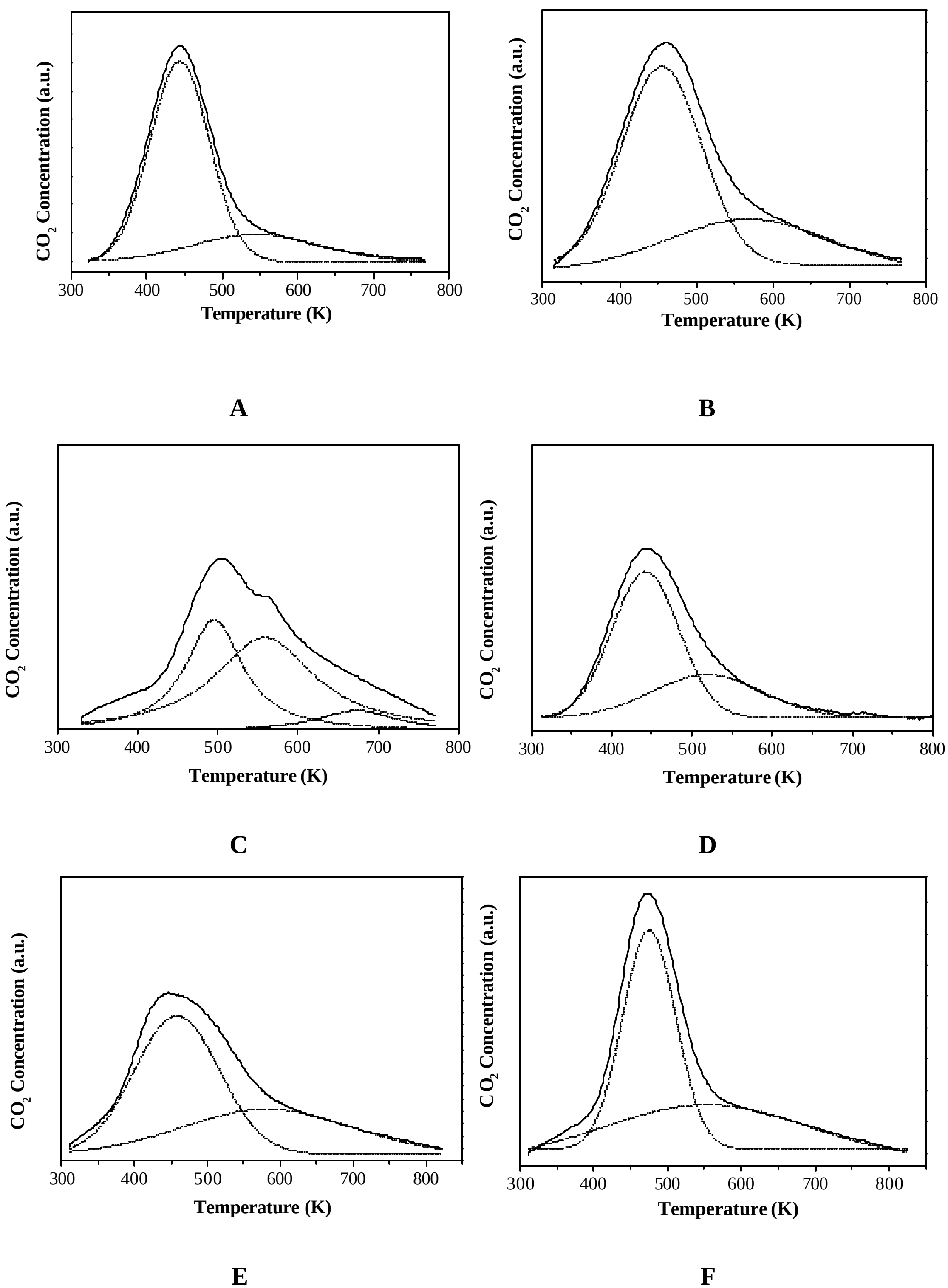

Fig. 2.14. **TPD profiles of M-LTL samples. The deconvoluted curves are shown in dotted lies [(A) Li, (B) Na, (C) K, (D) Mg, (E) Ca and (F) Sr].**

present at the surface (Fig. 2.14). These are probably CO_2 adsorbed at different locations or in different forms. The presence of different types of adsorbed CO_2 was already pointed out by IR studies. The major CO_2 desorption peak for the samples is in the order: Li < Mg < Ca < Na < Sr < K < Rb < Ba < Cs - LTL. The temperature of the desorption maximum is related to the strength of adsorption of CO_2. Hence, the basicity of the different samples also will follow the same order as above.

2.3.9.2. Zeolite BEA and FAU: The CO_2 uptake and the desorption peak temperatures for M-BEA and M-FAU are given in the Table 2.12. The uptake increases as the basicity increases from Li to Cs and Mg to Ba cations. The plots for different alkali and alkaline earth metal loaded M-BEA and M-FAU are shown in Fig. 2.15 A and B, respectively.

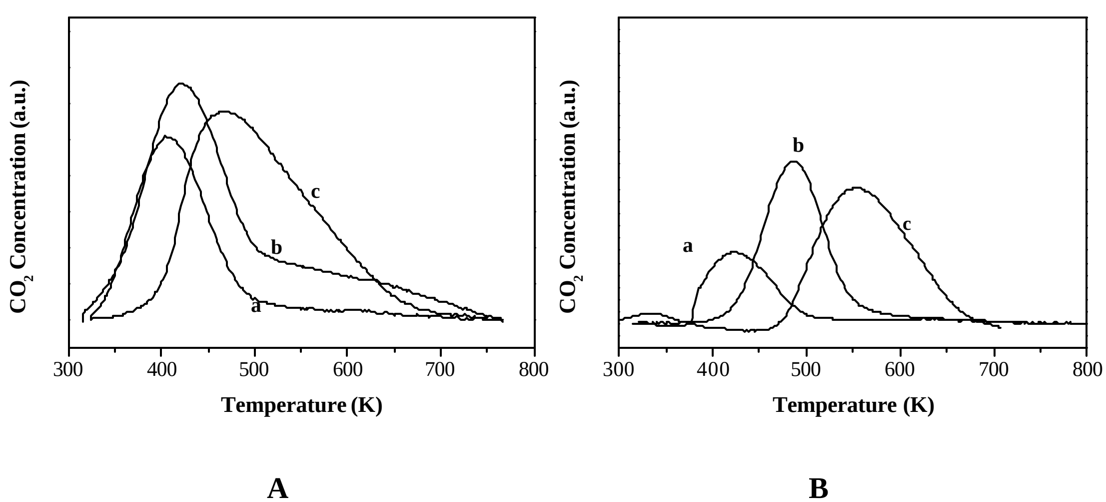

Fig. 2.15. TPD plots of CO_2 adsorbed on different cation exchanged samples. A: BEA and B: FAU; (a) Li, (b) Ba and (c) Cs.

Table 2.12 TPD data of CO_2 over different alkali and alkaline earth metal exchanged zeolites (M-BEA and M-FAU)

Alkali metal	BEA		FAU	
	Temp. at peak maximum (K)	CO_2 desorbed mmol/g	Temp. at peak maximum	CO_2 desorbed mmol/g
Li	405	57.5	436	43.3
K	421	63.4	456	45.6
Cs	569	70.5	521	48.6
Ba	421	71.1	489	59.6

2.3.9.3. Molecular sieve ETS-10: The typical TPD plots of CO_2 desorption from M-ETS-10 samples are presented in Fig. 2.16. The plots were deconvoluted to separate the two types of desorbed CO_2. Some of the deconvoluted plots are shown in Fig. 2.17. The CO_2 desorption is given in Table 2.13, which shows that it increases from Li to Cs and Mg to Ba. As already observed, the temperature of the peak maximum of the major peak increases with the cation size, i.e. basicity of the samples.

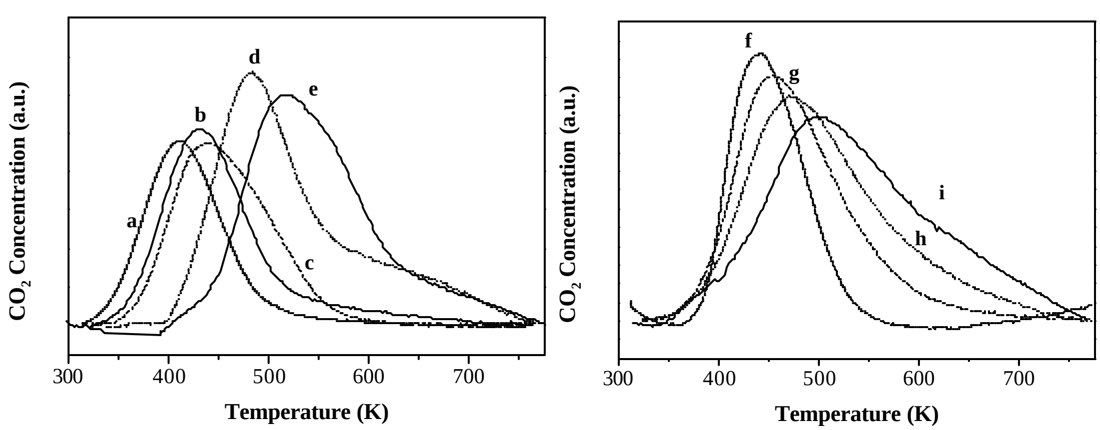

Fig. 2.16. TPD plots of CO_2 adsorbed on different cation exchanged samples (M-ETS-10): (a) Li, (b) Na, (c) K, (d) Rb and (e) Cs, (a) Mg, (b) Ca, (c) Sr and (d) Ba refers to samples.

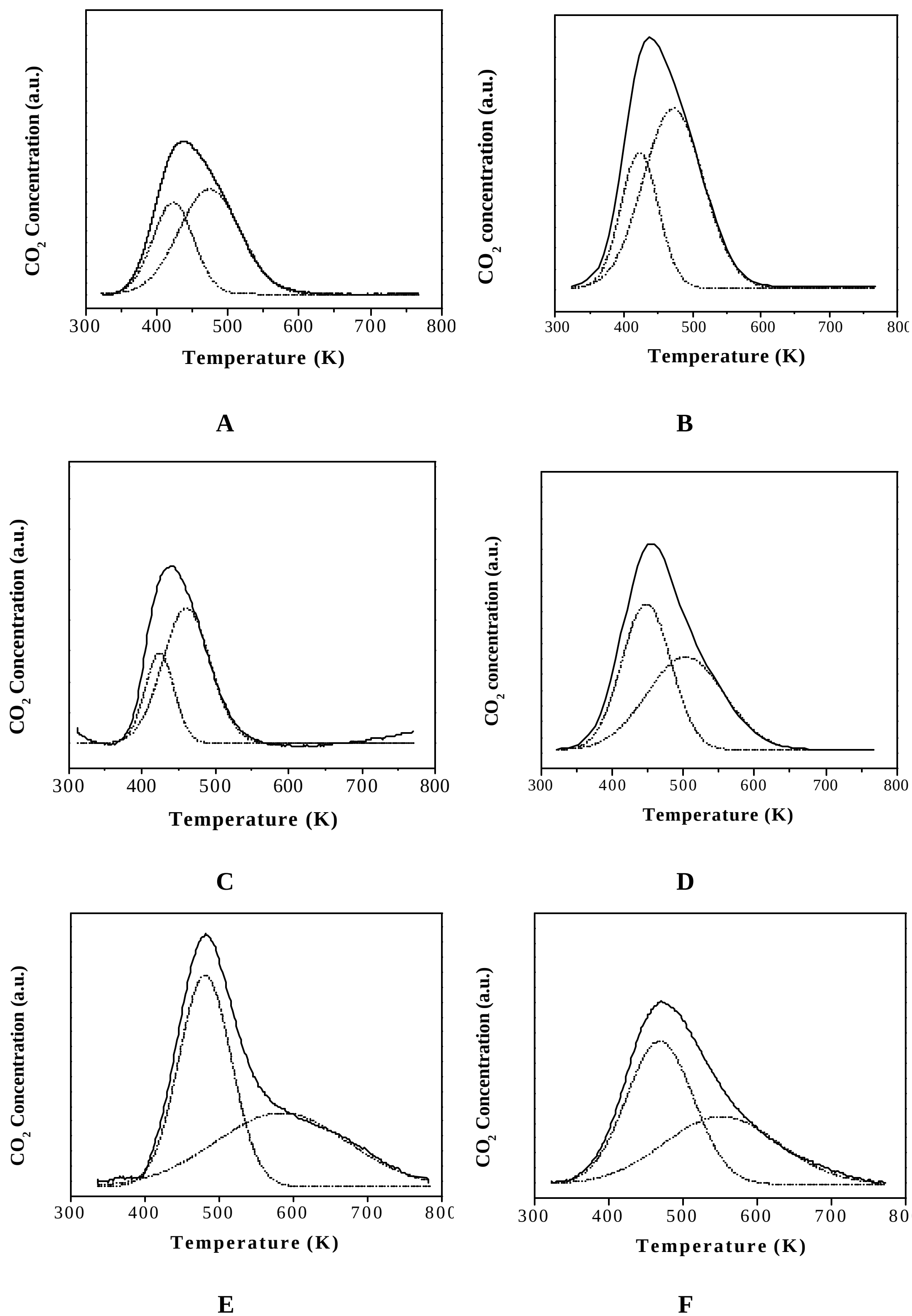

Fig. 2.17. The TPD profiles of M-ETS-10. The deconvoluted curves are shown as dotted lines: (A) Li, (B) K, (C) Rb, (D) Cs, (E) Sr and (F) Ba.

Table 2.13 TPD data obtained over different alkali and alkaline earth metal exchanged ETS-10 samples (M-ETS-10)

M	Temp. of peak maximum (K)		CO_2 desorbed
	Major peak	Minor peak	mmol/g
Li	400	-	68.9
Na	420	-	70.8
K	442	471	71.3
Rb	484	598	76.6
Cs	526	618	88.8
Mg	421	-	63.3
Ca	452	505	70.2
Sr	470	560	83.6
Ba	480	570	88.7

2.3.10. Intermediate Electronegativity (S_{int}): The intermediate electronegativity of M-LTL, M-BEA, M-FAU and M-ETS-10 were calculated on the basis of Sanderson's Electronegativity equalization principle principle.[31] These values are presented in Table 2.14 along with the calculated charge on oxygen. Generally, with an increase in the basicity of the exchanged ions, the S_{int} value decreases and charge on oxygen increases. The order of decreasing S_{int} values and increasing oxygen charge for different samples is: H < Mg < Ca < Sr < Ba < Li < Na < K< Rb < Cs. Based on S_{int} values, the order of decreasing basicity of the molecular sieves is: ETS-10 > LTL > FAU > BEA.

2.3.11. Comparison of TPD Data with S_{int} values: The CO_2 desorbed from the samples is found to correlate with the intermediate electronegativity values and charge on oxygen (Table 2.14) for the different samples (Fig. 2.18 A and B; 2.19 A and B). The amount of CO_2 'adsorbed' (desorbed) increases with a decrease in S_{int} and an increase is oxygen charge. This increase is very sharp for alkaline earth exchanged

LTL samples compared to other samples. Apparently zeolite structural effects and cation location also influence CO_2 adsorption (and basicity).

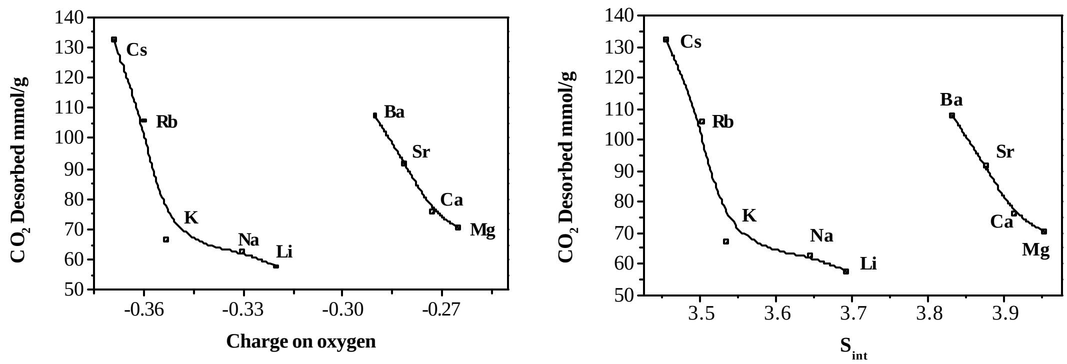

A B

Fig. 2.18. A) Relationship between CO_2 desorbed and charge on oxygen in M-LTL.

B) Relationship between CO_2 desorbed and S_{int} of M-LTL samples.

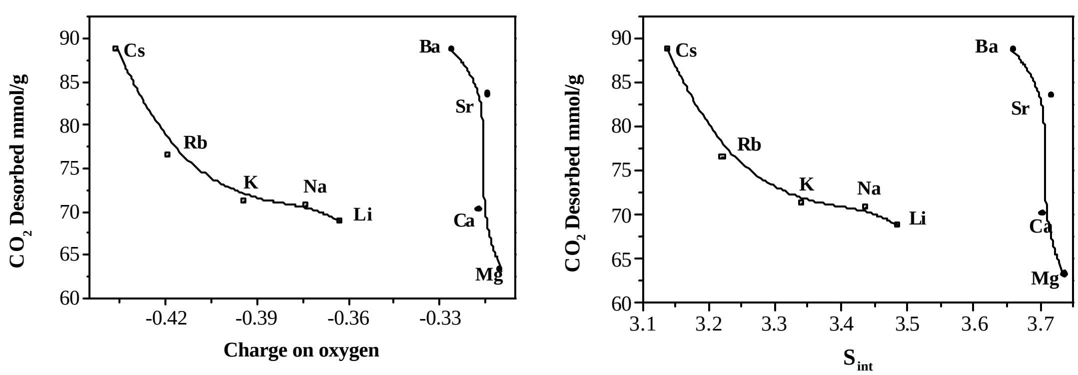

A B

Fig. 2.19. A) Relationship between CO_2 desorbed and charge on oxygen in M-ETS-10.

B) Relationship between CO_2 desorbed and S_{int} of M-ETS-10 samples.

Table 2.14 Intermediate electronegativity and oxygen charge of different ion exchanged samples

M	LTL		BEA		FAU		ETS-10	
	S_{int}	OC*	S_{int}	OC*	S_{int}	OC*	S_{int}	OC*
H	3.967	-0.262	4.323	-0.210	4.126	-0.228	3.961	-0.263
Li	3.693	-0.320	4.225	-0.229	3.794	-0.298	3.486	-0.363
Na	3.645	-0.330	4.212	-0.232	3.794	-0.298	3.437	-0.374
K	3.534	-0.353	4.179	-0.239	3.709	-0.316	3.340	-0.394
Rb	3.502	-0.360	4.172	-0.246	3.700	-0.318	3.222	-0.419
Cs	3.457	-0.369	4.155	-0.249	3.674	-0.324	3.140	-0.436
Mg	3.953	-0.265	4.308	-0.214	4.015	-0.252	3.738	-0.310
Ca	3.912	-0.273	4.286	-0.217	4.006	-0.254	3.704	-0.317
Sr	3.876	-0.281	4.282	-0.218	3.983	-0.258	3.718	-0.314
Ba	3.833	-0.290	4.270	-0.220	3.955	-0.264	3.660	-0.326

* Charge on oxygen

2.3.12. Pt Dispersion Measurement by H_2 Chemisorption: Dispersion of platinum on the catalysts was determined by hydrogen chemisorption at room temperature.[35] 2.5 g. of a freshly calcined sample was loaded in a 'U' shaped quartz glass sample holder. The sample was heated at 723 K for 4 h and evacuated at 723 K at 10^{-5} torr for 3 h. The sample was cooled in vacuum and dead space measurements were made using He at room temperature in the equilibrium pressure range between 5 to 450 torr. Then the sample was reduced at 673 K for 5 h and degassed at 723 K (Pt-M-LTL, Pt-M-FAU and Pt-M-BEA) and 673 K (Pt-M-ETS-10) under vacuum (10^{-5} torr) for 3 h. The samples were then cooled to room temperature in vacuum and high purity hydrogen (99.9 %) was adsorbed in the equilibrium pressure range between 5 to 450 torr. The equilibrium time for adsorption was 60 min. An adsorption isotherm was plotted for the sample. After this, the sample was evacuated at 10^{-5} torr pressure at room temperature for 4 h, to remove the weakly adsorbed hydrogen. A second adsorption isotherm was carried out at room temperature in the same pressure range. The amount of H_2 adsorbed was calculated as the difference between the two-adsorption isotherms. The platinum dispersion was calculated for different cation exchanged samples assuming a H/Pt stoichiometry of 1 and these values are presented in Table 2.15. The dispersion values are high being mostly in the range 0.6 to 0.9. A general trend of increasing dispersion with cation size (basicity) is noticed. The reason for this is not clear.

Table 2.15. Platinum dispersion of M-molecular sieve samples (Pt = 0.6 wt %)

Zeolite	M	Dispersion D (H/Pt)
LTL	Li	0.62
	K	0.74
	Cs	0.87
	Ba	0.92
BEA	Li	0.68
	K	0.76
	Cs	0.81
	Ba	0.85
FAU	Li	0.53
	K	0.64
	Cs	0.69
	Ba	0.74
ETS-10	Li	0.49
	K	0.62
	Cs	0.79
	Ba	0.83

PART B: MOLECULAR MODELING METHODOLOGY

This section describes the detailed methodology used in the different calculations. It also describes the zeolite framework structures, TOT angles and molecular fitting of the Pt_6 clusters inside the LTL, BEA, FAU and ETS-10 clusters. In this study, molecular graphics and quantum chemical calculations are used to analyze the results.

2.4. CALCULATION METHODOLOGY

The Hartree-Fock[36,37] method has been used for the study of the electronic properties of various zeolite cluster models in this study. It is a single determinant method for determining the electronic structure of molecules. The most obvious simplification to the Schrödinger equation involves the separation of variables, that is, the replacement of the many-electron wavefunction by a product of one electron wavefunctions. The simplest acceptable replacement is termed as Hartree-Fock or single determinant wavefunction. It involves a single determinant of products of one-electron functions, termed as spin orbitals. Each spin orbital is written as a product of a space part ψ, which is a function of the coordinates of a single electron and referred to as a molecular orbital. One of two possible spin parts, α or β is assigned to each spin orbital. Only two electrons may occupy a given molecular orbital and they must be of opposite spin. The Hartree-Fock approximation leads to a set of coupled differential equations, each involving a single electron. While they may be solved numerically, it is advantageous to introduce one additional approximation, namely Linear Combination of Atomic Orbitals (LACO).

2.4.1. LCAO Approximation: In practice, the molecular orbitals are expressed as linear combinations of a finite set (a basis set). They have prescribed functions known as basis functions (ϕ). The ϕ are usually centered at the nuclear positions (although they do not need to be); they are referred to as atomic orbitals. The molecular orbital (ψ) is expressed as the LCAO approximation.

$$\psi_i = \sum_{u}^{basis-functions} C_{\mu i} \phi_\mu \qquad (2.1)$$

2.4.2. Roothaan-Hall equation: The Hartree-Fock and LCAO approximations taken together and applied to the electronic Schrödinger equation leads to the Roothaan-Hall equation.[38]

$$\sum_{\nu}^{basis-function} (F_{\mu\nu} - \underline{\varepsilon}_{\mu\nu} S_{\mu\nu}) C_{\nu i} = 0 \qquad (2.2)$$

This equation accounts for the kinetic and potential energies of individual electrons and interactions among them. Methods resulting from solution of the Roothaan-Hall equations are termed as Hartree-Fock or *ab initio* methods. The corresponding energy for an infinite (complete) basis set is termed the Hartree-Fock (HF) energy.

2.4.3. Basis Set: For practical reasons, HF calculations make use of basis sets of Gaussian-type functions. These are closely related to exact solutions of the hydrogen atom and comprise a polynomial in the cartesian coordinates (x,y,z) followed by an exponential in r^2. Several series of the Gaussian basis sets are available such as minimal STO-3G, split-valance (3-21G, 6-31G), etc. Compact effective potential, which replaces the atomic core electrons in molecular calculations, are available for heavy elements in the 1st and 2nd row of periodic table.[39-41] The angular-dependent components of these potentials are presented by compact ones and two term Gaussian type expressions are obtained directly from appropriate equations. They are then used in molecular orbital calculations, where the atomic cores are chemically inactive.

All neutral systems considered in this study are closed shells and hence restricted Hartree-Fock (RHF) calculations have been used. The calculations have been done using an effective core potential (ECP) according to Stevens *et al.*[39-41] The detailed choices for deriving a useful and compact form of such effective core potentials in order to make them applicable for molecular or cluster calculations are explained by Stevens *et al*.[39-41]

Computations were carried out using General Atomic and Molecular Electronic Structure System (GAMESS) package.[42] The calculations were performed in a cluster of 32 Sun Ultra-450 workstations (National Param Supercomputing Facility) at Center for Development of Advanced Computing, Pune and in a Silicon Graphics Octane workstation.

2.5. FRAMEWORK STRUCTURES OF MOLECULAR SIEVES

2.5.1. Zeolite LTL: The aluminosilicate framework of LTL has been reported[21,28] to have polyhedral cages formed by six membered rings (6-MR) and four membered rings (4-MR). The unit cell of the LTL zeolite is [$M_XSi_{(36-X)}Al_XO_{72}$]. There are four types of non-framework cationic sites A, B, C and D shown in Fig. 2.20. Site A is located in the center of the hexagonal prism and is partially occupied by alkali metal cation. Site B is in the center of the cancrinite cavity and is fully occupied by alkali metal cation. Site C is located midway between the centers of two adjacent cancrinite cavities. Site D is the only cation position approachable from the main 12-MR channel close to the wall separating 8-MR as shown in Fig. 2.20. The cations at site D are the only exchangeable ones at room temperature.[21,28] The next most likely to be exchanged

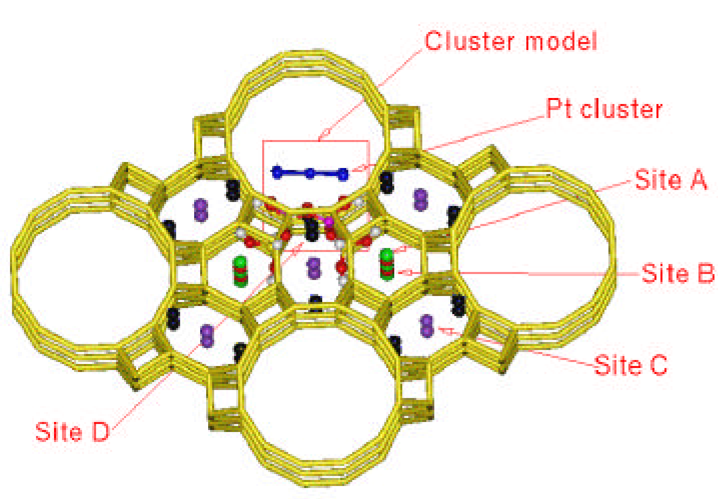

Fig. 2.20. **Molecular graphics picture shows the framework structure of zeolite - LTL. The labeled positions refer to the various extra-framework cation sites. The highlighted segment is used for the *ab initio* calculations.**

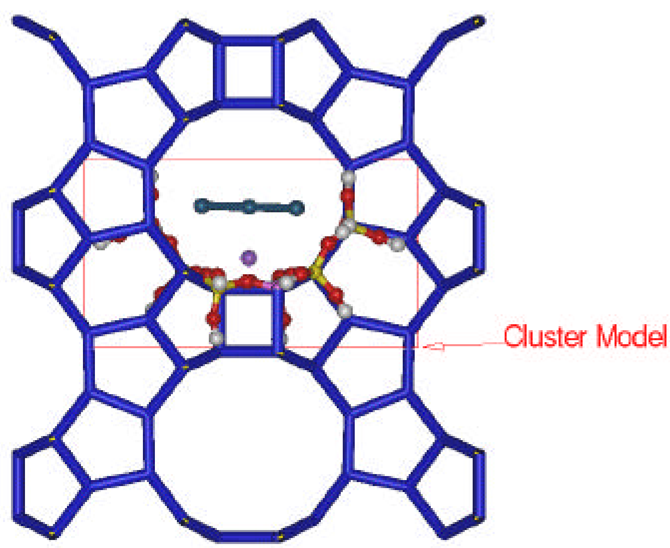

Fig. 2.21. **Molecular graphics picture of BEA lattice, as viewed along 010 plane. The highlighted segment is used for the *ab initio* calculations.**

cation is located at site C. The model of LTL is reported by an eight 8-MR cluster, which is the window between the 12-MR and 8-MR along the 'c' axis (Fig. 2.20).

2.5.2. Zeolite BEA: Zeolite beta was first synthesized at Mobil Research and Development Laboratories[43] in 1967 and its crystal structure was solved in 1988.[24] The first clues to the crystal structure of the zeolite BEA came out of chemical and physical property measurements.[44] The observation that complete exchange of cations in BEA is possible[24,45] indicates the presence of channels instead of cages. Zeolite BEA is easily synthesized with SiO_2/ Al_2O_3 ratios in the range of 20-50. The unit cell of the BEA zeolite is $[M_XSi_{(64-X)}Al_XO_{128}]$. The framework structure of zeolite BEA is made up of interconnected rings of 4, 5 and 6-MR (Fig. 2.21) leading to the main 12-MR. The exact locations of the extra framework cations is not available in the literature. The cation has been located in the 6-MR in the cluster model used in this study.

2.5.3. Zeolite FAU: Zeolite FAU has hexagonal prisms, sodalite cages and super cages. Many distinct types of cationic sites have been reported in FAU, three of which are significant for cation occupancy.[22] These three types of non-framework cationic sites (I, II and III) are shown in Fig.2.22. In a unit cell of FAU, $[M_XSi_{(192-X)}Al_XO_{384}]$, there are 96 possible locations for non-framework cations. The 96 locations are distributed as: 16, 32 and 48 in cation sites I, II and III, respectively. According to crystallographic data, sites I and II are the most likely occupied sites.[22] Site I (M_I) is inside the hexagonal prism, whereas site II (M_{II}) is located inside the supercage at a six-ring window of the sodalite cage.[22]

2.5.4. Molecular sieve ETS-10: The first information on microporous titanosilicates appeared in 1967 when Young[46] reported the synthesis of titanosilicates under similar conditions as aluminosilicates. These materials were called titanium zeolites. The framework of ETS-10 is composed of tetrahedral [SiO_4] and octahedral [TiO_6] units. The TiO_6 units are connected to each other to form a -Ti-O-Ti-O-Ti- chain. The structure can be envisaged to be constructed from rods consisting of two chains of silicate 5-rings connected by octahedral titanate units, as shown in Fig. 2.23. In 1973 a naturally occurring alkaline titanosilicate identified as *zorite* was discovered[46] in trace quantities in the Siberian Tundra. In 1988 and 1990 two independent reports by Kuznicki[47,48] and Chapman and Roe[49] discussed synthetic structures that appeared to mimic zorite. Comparisons with the natural mineral were largely based upon similarities between X-ray diffraction patterns of the synthetic (ETS-4) and natural zorite. It was then realized that a new family of titanosilicate molecular sieves containing tetrahedral and octahedral framework atoms had been discovered.

The crystal structure model of ETS-10 has been proposed by Anderson *et al.*[51-53] based on chemical analysis, structural modeling, XRD, HREM and high-resolution MAS-NMR studies. ETS-10 possesses a three-dimentional (3-D) 12-MR pore system. Neither disorder nor faulting in ETS-10 should result in pore system blockage; indeed, some types of planar faults increase pore access. The structure is made up of interconnected rings of 3, 4, 5, 7 and 12 members. The projection of ETS-10 lattice along the 'a' axis is shown in Fig. 2.23. Each Ti is connected via oxygen to four Si atoms in two 3-MR and also via oxygen to other two Ti atoms. All Si atoms, except those at the apex of each 5-MR are connected to three Si atoms and one Ti atom via oxygen [Si(3Si, 1Ti)]. The apical Si in each 5-MR is a [Si(4Si, 0Ti)] unit. Two rods of Ti perpendicular to each other join together by forming 7-MR. The Ti chain (rods) are regularly arranged along 'x' and 'y' axis with a period of 15 Å and a large channel with 12-MR aperture is formed. Two ordered polymorphs of ETS-10, A and B, analogous to BEA[24,45] have been described by Anderson *et al.*[50-52]

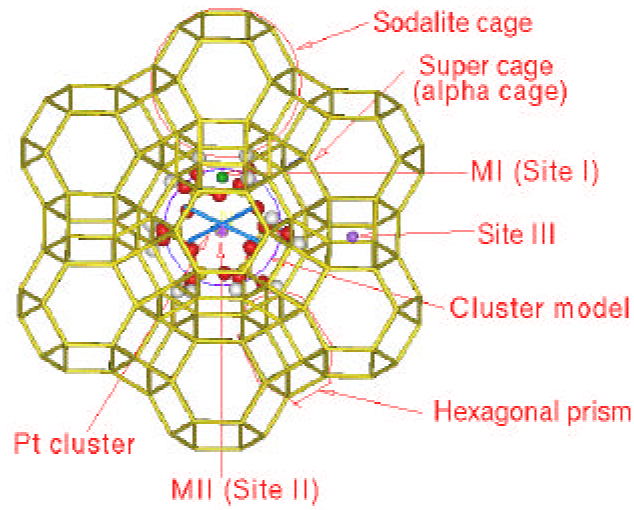

Fig. 2.22. Molecular graphics picture of FAU lattice, as viewed through 12-MR; cationic positions are shown. The cluster used in the *ab initio* calculations is highlighted.

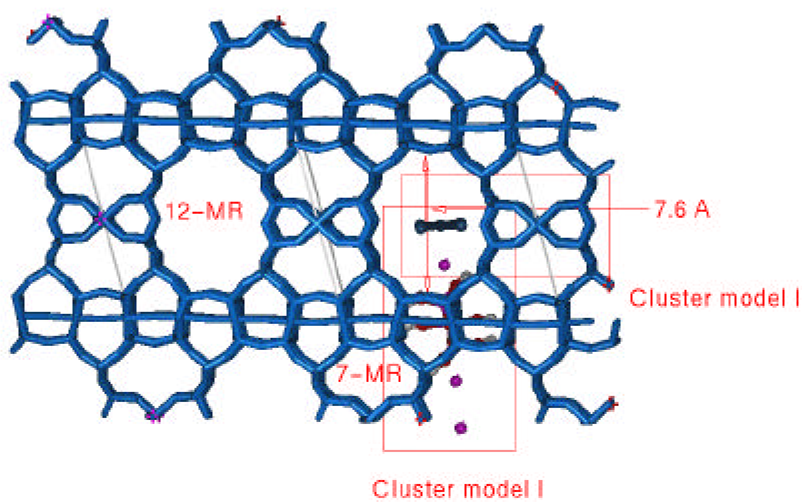

Fig. 2.23. Molecular graphics picture of ETS-10 lattice, as viewed along either 'a' or 'b' directions. ABCDABCD stacking of layers containing 12-MR are shown. Two cluster models used in the *ab initio* calculations representing the presence of Pt_5 nearer to $[TiO_6]$ and $[SiO_4]$ groups are highlighted.

2.6. CLUSTER MODELS OF MOLECULAR SIEVES

All cluster models used in this study were generated using software programs MSI supplied by Molecular Simulations Inc., USA and SPARTAN. The cluster generation procedure is described in detail in chapter 1 (section 1.6.2.5). The O-H distance was kept as 1.03 Å. The vector of the O-H bond was kept the same as the O-Si bond of the lattice. The unsaturated valencies of the terminal oxygen atoms were saturated with hydrogen atoms.

2.6.1. Zeolite LTL: A cluster model having the formula [$M_2Si_6Al_2O_{24}H_{16}$] (where M = Li, Na, K, Rb, Cs, Mg(OH), Ca(OH), Sr(OH) and Ba(OH) from the lattice of zeolite LTL[21,28] shown inside box in Fig. 2.20 was generated and used in these studies. The Si/Al ratio is three in the zeolite cluster model. This cluster geometry is described in detail in chapter 4 (section 4.3.1). The inter-atomic distances used in the calculations are presented in Table 2.16. The two Al atoms are located at the two T_1 sites of 12-MR. According to the reported literature,[21] T_1 sites in the 12-MR are the most favorable ones for aluminum substitution. The substitution of Al atoms in suitable T_1 and T_2 sites was also considered, as allowed by the Löwenstein rule.[56] The excess negative charge of the cluster created by Al atoms was compensated by cations located in site D.

2.6.2. Zeolite BEA: A cluster model having the formula of [$MSi_9AlO_{30}H_{20}$] (where M = Li, Na, K, Rb, Cs, Mg(OH), Ca(OH), Sr(OH) and Ba(OH) from the lattice of polymorph A of zeolite BEA[24] is considered. The cluster is shown inside the box in Fig. 2.21. This cluster geometry is described in detail in the chapter 4 (section 4.3.2). The 6-MR, wherein one of the silicon in site T_1 is replaced by aluminum and the resulting negative charge compensated by an extra-framework cation (M), was chosen for developing the cluster model as it was found that the T_1 position was the most favorable location for Al. The T_1 position is in the 12-MR and also accessible through 5 and 6-MR pore openings.[53,54] The extra-framework cation is located in the middle of the 6-MR. The T-O-T angles and distances used in the generation of the cluster 3models were taken published crystal structures for LTL,[21] BEA,[24] FAR[22] and ETS-10.[50]

2.6.3. Zeolite FAU: A cluster model having the formula of $[M_2Si_4Al_2O_{18}H_{12}]$ (where M = Li, Na, K, Rb, Cs, Mg(OH), Ca(OH), Sr(OH) and Ba(OH) from the lattice of FAU shown inside the box in Fig. 2.22 was generated. The cluster representing a 6-MR of zeolite FAU structure containing one Al in T_1 or T_2 location was investigated. Two possible distributions of two aluminum atoms in 6-MR as allowed by the Löwenstein rule were considered. It was observed that the presence of two Al atoms at the farthest positions was energetically the most favorable. The excess negative charge of the cluster with two Al atoms was compensated by two cations (M_I and M_{II}) located at sites I and II, respectively. The geometry of the cluster was derived from the crystal structure of zeolite FAU reported by Mortier *et al.*[22]

2.6.4. Molecular sieve ETS-10: A cluster model having the formula of $[M_2TiSi_4O_{16}H_{10}]$ from the lattice of ETS-10 has been created from the crystal structure of ETS-10 - polymorph B [(Unit cell: $\{[M^+]_{32}\ [(TiO_3)]_{16}[SiO_2]_{80}\}$, (where M^+ = Li^+, Na^+, K^+, Rb^+ or Cs^+)].[51] The major pores in ETS-10 are 12-MR channels (Fig. 2.23). These channels are intersected by smaller 7, 5 and 3-MR channels in such a way that the walls of the 12-MR channels are linked with pockets with 7, 5, 4 and 3-MR openings. The Ti - atoms are accessible through pore openings, some of which are blocked by the exchanged alkali metal ions.

Table 2.16. Inter-atomic distance values used in the present calculations

Bonding atoms	Atom-to-atom distance (Å)
Pt-Pt	2.77
Si-O	1.55 - 1.59
Al-O	1.64 - 1.74
Li-O	2.16
Na-O	2.42
Mg-O*	2.29
K-O	2.78
Ca-O*	2.65
Rb-O	2.92
Sr-O*	2.79
Cs-O	3.07
Ba-O*	3.00
Pt-C	3.75
Pt-Li	2.35
Pt-Na	2.60
Pt-Mg	2.47
Pt-K	2.92
Pt-Ca	2.83
Pt-Rb	3.10
Pt-Sr	2.97
Pt-Cs	3.25
Pt-Ba	3.18

* Ionic radii of M^+ state only

2.7. ELECTRONIC PROPERTIES OF THE PLATINUM CLUSTER MODELS

A single platinum atom and clusters containing several atoms were considered. Initial trial calculations were performed using the Extended Hückel method of Hoffmann[55] using computer aided composition of atomic orbital (CACAO) package.[56] Different geometries of the Pt_n cluster (where n = 1 to 12) were modeled. The total energy of the platinum cluster was calculated for different cluster sizes and shapes. Binding energy of the cluster per platinum atom was calculated according to equation (2.3).

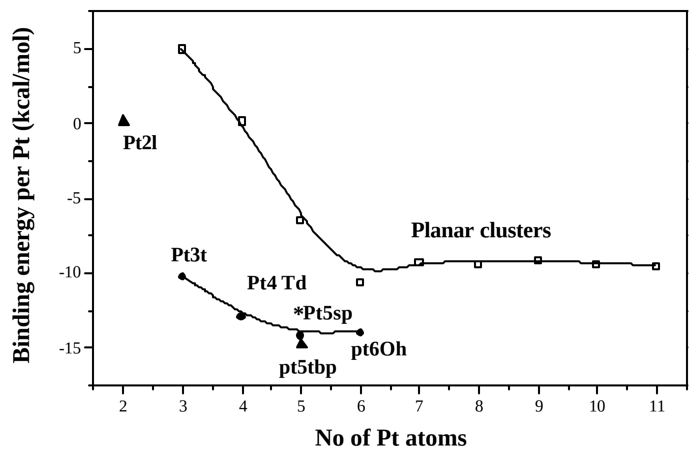

Fig. 2.24. Binding energy per platinum atom is plotted against the number of platinum atoms in the clusters (l = linear, t = trigonal, Td = tetrahedral, tbp = trigonal bipyramid, sp = planar (in 111 plane), Oh = octahedral and * used in studies).

These binding energy values per platinum atom are plotted against the number of platinum atoms in the cluster (Fig. 2.24). The total energy of the cluster increases with its size. When the number of platinum atoms in the cluster increases to more than six, they start to exhibit metallic properties. It is observed that Pt_5 (tbp), Pt_5 (sp) and Pt_6 (Oh) clusters are the more stable ones (among those investigated) based on the binding energy per platinum atom (Fig. 2.24). Going from a single Pt atom to a Pt_5 cluster, there is a drastic variation in the electronic properties.

$$\text{B.E. per Pt} = \{\text{T.E.}\ (Pt_n) - (n \times \text{T.E.}\ [Pt_1]\}/n \qquad (2.3)$$

2.8. ZEOLITE-METAL-MOLECULE INTERACTIONS

2.8.1. Molecular Fitting of Pt_5 Cluster in the Zeolite: A single platinum atom or a Pt_5 cluster has been modeled in different locations of Pt-M-LTL, Pt-M-FAU and Pt-M-BEA catalysts by suitable clusters. The major pores in these zeolites are 12-MR channels (Figures. 2.20 to 2.23). Given the large size of a Pt atom (2.77 Å), only atomically dispersed Pt atoms and small Pt clusters such as Pt_5 can be present inside the pores and cages of the zeolites investigated. Ferrari *et al.*[54] have used a Pt_4 cluster in their DFT calculations on CO adsorption over Pt supported on zeolites. Earlier workers have reported the occurrence of small Pt clusters (4–10 atoms) inside the cavities of different zeolites.[57-59] Gallezot[60] has analyzed the radial distribution function obtained from X-ray data and showed that Pt atoms in the supercages of zeolite FAU are present as small clusters rather than as normal 'fcc' structures. Pan *et al.*[53] have studied the size of the Pt clusters inside FAU zeolite by HREM imaging. They report that particles smaller than 10 Å are present inside the zeolite channels. In view of the above reports, a square planar Pt_5 cluster of size, 5.54 x 4.80 Å (from a 111 plane) has been used in these studies. The dimension of a Pt_5 (sp) cluster can ideally fit inside the channels or cages of the zeolites being investigated. The [111] plane is the most energetically stable low index plane of Pt. It is expected to be the most favored plane of 'fcc' metals for hydrocarbon transformations.[61] The small concentration of Pt (0.4 wt %) and good dispersion values of 0.53 to 0.92 % in the Pt-M-zeolite suggest that significant portion of Pt exists as dispersed atoms or small clusters. Hence, the electronic structures of monomeric Pt and small clusters (Pt_5) deposition on model clusters of zeolites have been investigated in these studies. The Pt atoms (or clusters) present inside the 12-MR channels will be directly accessible to the diffusing *n*-hexane molecules. The electronic properties of Pt_5 were extremely sensitive to the distance of

Pt from the zeolite surface. Calculations were performed by keeping the Pt-M distance as the sum of ionic radius of M^+ and the covalent radius of Pt. Different orientations of Pt_5 were considered such as perpendicular, diagonal and parallel to the zeolite cluster. The Pt_5 atom cluster parallel to the zeolite cluster was the most energetically favorable conformation. Hence such a conformation was considered for all the three Pt-zeolite clusters. In LTL, the Pt clusters can be present in 12-MR channels and these will be accessible to the reactant. The Pt clusters located above the 8-MR and inside the 12-MR of LTL (Fig. 2.20) is considered. In zeolite BEA, the Pt_5 cluster is located in the 12-MR channel above the 6-MR (Fig. 2.21). In the case of FAU, a Pt_5 cluster present above site II (M_{II}) inside the supercage is considered (Fig. 2.22), whereas in ETS-10, the Pt_5 cluster is located in the 12-MR channel (Fig. 2.23).

There are several possible locations for Pt in ETS-10. Single Pt atoms present inside the 7-MR may also be accessible to the reactant molecules through the 12-MR channels in their end-on orientation due to the small size (3 Å) of the 7-MR openings. This structural fitting analysis has lead to the conclusion that Pt in 7-MR cages are available only to terminal carbons, while small clusters such as Pt_5 present inside the 12-MR pores will be more accessible to the entire molecule. Two distinctly different locations for the Pt cluster are possible inside the 12-MR. One location is close to [TiO_6] Oh site and another is close to a [SiO_4] Td site. Pt_5 in both these locations were modeled with suitable clusters and the electronic properties of Pt in the two locations were calculated. The interaction energy between two chemical entities such as M and zeolite, M-zeolite and Pt_5, Pt_5 and benzene was calculated by equation (2.4):

B.E.= T.E. [both entities] - {T.E. [entity1] + T.E.[entity2]} (2.4)

2.8.2. Electronic Properties of the Pt_5: Benzene Cluster Model: The distance between a benzene molecule and a Pt_5 atom cluster was optimized. The favorable distance between Pt_5 and benzene is found to be 3.75 Å (Fig. 2.25). The electronic charge on Pt and C is plotted as a function of the distance between Pt_5 atom cluster and benzene. As the distance between the Pt_5 and benzene increases, the average charge on Pt becomes more positive and simultaneously the average charge on C (C_6H_6) becomes more negative. The above trends clearly indicate that adsorption of benzene on Pt_5 occurs through donation of electrons by benzene to the platinum cluster.

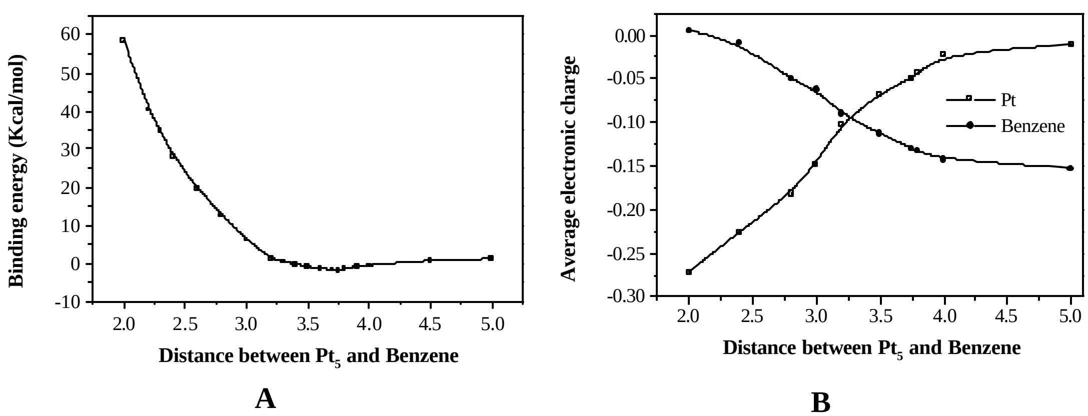

Fig. 2.25. A) Influence of the distance between Pt_5 and benzene on binding energy. B) Average electronic charge on Pt and C as a function of the distance between Pt_5 and benzene.

2.8.3. Electronic Properties of the Pt_5: H_2S Cluster Model: The distance between H_2S and a Pt_5 atom cluster was optimized (shown in Fig. 2.26) following the same procedure explained above for benzene. The favorable distance between Pt_5 and H_2S was found to be 3.40 Å. The adsorption of H_2S over the Pt_5 cluster shows two minima, a shallow one at 2.3 Å and a deeper one at 3.4 Å. The distance at the deeper minimum is used for studying the adsorption of H_2S.

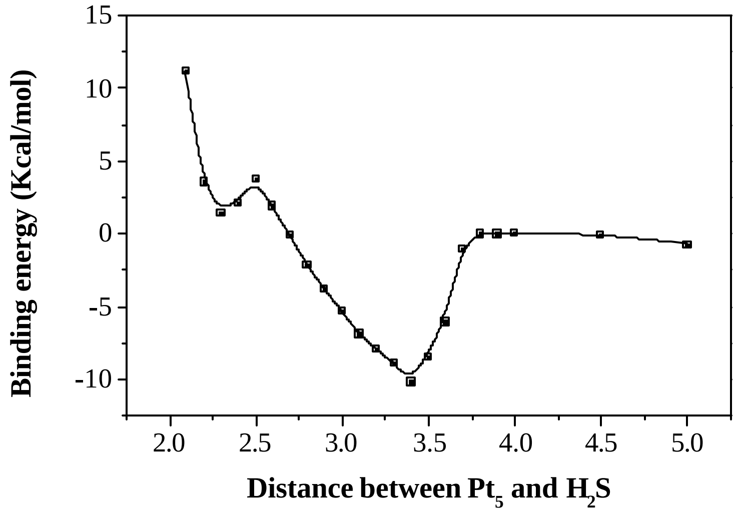

Fig. 2.26. Influence of the distance between Pt_5 and H_2S on binding energy.

2.9. SUMMARY

This chapter summarizes the synthesis and modification procedures used in making zeolite catalysts. The characterization techniques used in this study are also explained. The relationships between composition and basicity are clearly brought out by many methods such as FTIR spectroscopy of CO_2, TPD of CO_2 and calculations of intermediate electronegativity (S_{int}).

The second part of this chapter describes the methodology and models used in the computational study. The quantum chemical method is explained in detail. The model generation procedure and the models are also explained for all the zeolite systems considered. The procedure followed to study the incorporation of Pt as well as the interaction of benzene and H_2S molecules with Pt is also explained. The methodology used to fit the Pt cluster and molecules in suitable locations of the zeolites is also revealed.

2.10. REFERENCES

1. J.P. Verdujin and E.P. Gillings, *Eur. Pat. Appl*., 280 513 (1988).
2. M.A. Camblor and J. Perez-Pariente, *Zeolites*, 11 (1991) 202.
3. M.A. Camblor, A. Mifsud and J. Perez-Pariente, *Zeolites*, 11 (1991) 792.
4. D.M. Ginter, in "*Synthesis of Microporous Materials*", D.M. Ginter, A.T. Bell and C.J. Radke in M.L. Occelli, H.E. Robson, eds., Molecular Sieves, V.N. Reinhold, New York, 1 (1992) 6.
5. T.K. Das A.J. Chandwadkar and S. Sivasanker, *J. Chem. Soc. Chem. Commun.*, (1996) 1105.
6. J. Engelhardt, J. Szanyi and J. Valyon, *J. Catal* 107 (1987) 296.
7. A.I. Vogel, "*Text Book of Quantitative Inorganic AnalysisIincluding Elementary Instrumental Analysis*" London (1961).
8. T.K. Das A.J. Chandwadkar, A.J. Budhkar and S. Sivasanker, *Micropor. Mater*. 5 (1995) 195.
9. J. Rocha, A. Ferreira, Z. Lin and M.W. Anderson *Micropor. Mesopor. Mater*., 23 (1998) 253.
10. P.A. Jacobs, *DGMK Tagenbericht*, 171 (1992) 9204.
11. E. Astorino, J.B. Peri, R. Willey and G. Busca, *J. Catal.*, 157 (1995) 482.
12. T. Armaroli, G. Busca, F. Milella, F. Bregani, G.P. Toledo, A. Nastro, P. De Luca, G. Bagnasco and M. Turco, *J. Mater. Chem.*, 10 (2000) 1699.
13. E.I. Kamitsos, A.P. Patsis and E.G. Kordas, *Phys. Rev. B*, 48 (1993) 12499.
14. E.M. Flanigen, in "Ze*olites Chemistry and Catalysis*" ed. J.A. Rabo, ACS, Washington DC, (1979) 80.
15. R. Robert, P.R. Rajmohanan, S.G. Hegde, A.J. Chandwadkar and P. Ratnasamy, *J. Catal.*, 155 (1995) 345.
16. B. Mihailova, V. Valtchev, S. Mintova and L. Konstantinov, L., *Zeolites*, 16(1996) 22.
17. G. Hertzberg, in "*Infrared and Raman Spectra of Polyatomic Molecules*" Van Nostrand, New York, (1945) 178.
18. K. Nakamoto, in "*Infrared and Raman Spectra of Inorganic and Co-ordination Compounds*", 3rd ed. Wiely, New York, (1978) 243.
19. G. Bussca and V. Lorenzeli, *Mater. Chem.*, 7 (1982) 89.
20. F. Solymosi and H. Knözinger, *J. Catal*., 122 (1990) 166.

21. R.M. Barrer and H. Villiger, H. *Zeit. Krystall*. S, 128 (1969) 352.
22. W.J. Mortier, H.J. Bosmans and J.B. Uytterhoeven, *J. Phys. Chem.*, 76 (1972) 650.
23. A.N. Fitch, H. Jobic, and A. Renouprez, *J. Phys. Chem.*, 90 (1986) 1311.
24. J.M. Newsam, M.M.J. Treacy, W.T. Koetsier and C.B. De Gruyter, *Proc. R. Soc. London, Ser. A,* 420 (1988) 375.
25. A. Vimont, F.T. Starzyk and J.C. Lavalley, *J. Phys. Chem.,* 104 (2000) 286.
26. N.D. Parkyns, *J. Phys. Chem.,* 75 (1971) 526.
27. B. Morterra, A. Zecchina, S. Coluccia, *Faraday Trans.*, (1977) 1544.
28. J.M. Newsam, *J. Phys. Chem.,* 93 (1989) 7689.
29. P.C. Heydron, C.J.D. Herein, N. Pfander, H.C. Karge and F.C. Jentoft, *J. Mol. Catal. A,* 162 (2000) 227.
30. B. Bonelli, B. Civalleri, B. Fubini, P. Ugliengo, C.O. Arean and E. Garrone, *J. Phys. Chem. B* 104 (2000) 10978.
31. R.T. Sanderson in "*Chemical Bonds and Bond Energy*", Academic Press, New York, 1976.
32. T. Ito, T. Murakami and T. Tokuda, *J. Chem. Soc. Trans. Faraday I*, 79 (1983) 913.
33. R. Bal, B.B. Tope, S.G. Hegde and S. Sivasanker, 204 (2001) 358.
34. W.J. Mortier, *J. Catal.*, 55 (1978) 138.
35. P.G. Smirniotis and E. Ruckenstein, *Appl. Catal.* A, 123 (1995) 59.
36. R. Mc Weeny, "*Methods of Molecular Quantum Mechanism*" 2nd ed. Academic Press, London (1992).
37. A. Szabo and N.S. Ostlund, "*Modern Quantum Chemistry*" 1st ed. McGraw-Hill, New York (1989).
38. W.J. Hehre, L. Radom, P.V.R. Schleyer and J.A. Pople, "*Ab Initio Molecular Orbital Theory*", Wiley, New York, 1986.
39. W.J. Stevens, H. Basch and M. Krauss, *J. Chem. Phys.*, 81 (1984) 6026.
40. W.J. Stevens, H. Basch, M. Krauss and P. Jasien, *Can. J. Chem.*, 70 (1992) 612.
41. T.R. Cundari and W.J. Stevens, *J. Chem. Phys.*, 98 (1193) 5555.
42. M.W. Scmhidt, K.K. Baldridge, J.A. Boatz, S.T. Elbert, M.S. Gordon, J.H. Jensen, S. Koseki N. Matsunga, K.A. Nguyen, S.J. Su, T.L. Windus, M. Dupuis, J.A. Montgomery, *J. Comput. Chem.*, 14 (1993) 1347.
43. R.L. Wadlinger, G.T. Kerr and E.J. Rosinski., *US Pat.*, 3, 308 069 (1967).

44. J.B. Higgins, R.B. LaPierre, J.L. Schlenker, A.C. Rohrman, J.D. Wood, G.T. Kerr and W.J. Rohrbaugh, *Zeolites*, 8 (1988) 446.
45. M.M.J. Treacy and J.M. Newsam, *Nature*, 332 (1988) 249.
46. G. Young, *US Pat*., 3,329, 481 (1967).
47. S.M. Kuznicki, *US Pat*. 4, 853, 202 (1989).
48. S.M. Kuznicki and K.A. Thrush, *Eur. Pat*, 0, 405, 978 A1 (1990).
49. D.M. Chapman and A.L. Roe, *Zeolite*s, 10 (1990) 730.
50. M.W. Anderson O. Terasaki, T. Ohsuna, A. Philippou, S.P. Mackay, A. Ferreira, J. Rocha and S. Lidin, *Nature*, 367 (1994) 347.
51. M.W. Anderson O. Terasaki, T. Ohsuna, P.J.O. Malley, A. Philippou, S.P. Mackay, A. Ferreira, J. Rocha and S. Lidin, *Philos. Mag*., B, 71 (1995) 813.
52. T. Ohuna, O Tarasaki, D. Watanabe, M.W. Anderson and S. Lidin, *Stud. Surf. Sci. Catal*, 84 (1994) 413.
53. M. Pan, J.M. Cowley and I.Y Chan, *Catal. Lett.*, 5 (1990) 1.
54. A.M. Ferrari, K.M. Neyman, T. Belling, M. Mayer and N. Rösch, *J. Phys. Chem. B*., 103 (1999) 216
55. R. Hoffmann, *J. Chem. Phys.*, 39 (1963) 1397.
56. C. Mealli and D.M. Proserpio, *J. Chem. Ed*., 67 (1990) 399.
57. M. Varkamp, F.S. Modica, J.T. Miller and D.C. Koningsberger, *J. Catal.*, 144 (1993) 611.
58. A. Khodakov, A. N. Barboudt, J. Oudar, F. Villaim, D. Bazin, H. Dexpert and P. Schultz, *J. Phys. Chem. B.*, 101 (1997) 766.
59. W.A. Weber and B.C. Gates, *J. Phys. Chem. B.*, 101 (1997) 10423.
60. P. Gallezot, P. *Catal. Rev.- Sci. Eng.*, 20 (1979) 121.
61. Z. Pall, *Advan. Catal.*, 29 (1980) 273.

CHAPTER 3

n-HEXANE AROMATIZATION OVER LTL, BEA AND FAU ZEOLITES: CATALYTIC STUDIES

3.1. INTRODUCTION

The dehydrocyclization of alkanes to aromatics (catalytic naphtha reforming) has been a subject of great interest because of its important industrial applications.[1-4] Platinum, alone or along with metal promoters such as Re, Ir or Sn, supported on acidic halided alumina[5,6] is currently used to convert alkanes with six or more carbon atoms into aromatic hydrocarbons. The mechanism of dehydrocyclization over these catalysts is believed to be bifunctional involving both the metal (Pt) and the acid function (alumina).[7] The major drawback of these catalysts is their inability to transform significant amounts of the C_6 hydrocarbons such as *n*-hexane and methyl cyclopentane into aromatics besides the occurrence of simultaneous parallel reactions such as isomerization and hydrogenolysis leading to reduced selectivity to aromatics.

It has been reported that the dehydrocyclization of C_6-C_8 alkanes occurs with high selectivities for aromatics over Pt-supported on basic zeolites such as Pt-K-LTL.[8] Based on the above catalysts, a new process (AROMAX) has been commercialized by Chevron.[9-13] Basic zeolites such as Pt-M-BEA and Pt-M-FAU (where M = Li, Na, K, Rb, Cs or Mg, Ca, Sr and Ba) have also been reported to possess larger dehydrocyclization activities than Pt-Al_2O_3.[6,14,15] Since the early reports[8,16,17] almost two decades ago, our understanding of how the Pt/K-LTL system works has deepened and many possible reasons have been suggested for the spectacular activity of Pt-M-LTL. These are: i) there is an electronic interaction between the zeolite and the Pt metal,[17,18] ii) structural parameters of the zeolite are responsible,[19,20] iii) collimation and head on interaction of *n*-hexane molecules and Pt occurs[21] iv) carbon deposition over Pt is inhibited,[19] and v) Pt is highly dispersed with high stability[22-27] and vi) Pt clusters are present in specific locations.[28,29] Jentoft *et al.*[30] have observed that the morphology of the zeolite LTL also influences the performance of the catalyst.

The studies carried out on *n*-hexane aromatization over different alkali and alkaline earth metal exchanged zeolites (LTL, BEA and FAU) are presented in this chapter. The influence of different exchanged cations (M) and zeolite type on the *n*-hexane aromatization activity of Pt supported on the above zeolites is presented. The influences of reaction parameters such as Weight Hourly Space Velocity (WHSV), Time On Stream (TOS), Pt loading and H_2: hydrocarbon (mol) ratios in n-hexane aromatization over the above catalysts are also reported. A relationship between catalytic activity and selectivity for benzene, and Sanderson intermediate electronegativity is established.[31]

3.2. EXPERIMENTAL

3.2.1 Materials and Catalysts: *n*-Hexane (> 99.0 % purity) was obtained from S.D. Fine-Chem. Ltd., India. High purity hydrogen gas (> 99.9 %) was obtained from INOX air products Ltd., India. Pt was loaded on ion exchanged forms of zeolites LTL, BEA and FAU, [Pt-M-LTL, Pt-M-BEA and Pt-M-FAU where M= H, Li, Na, K, Rb, Cs, Mg, Ca, Sr and Ba] and used in *n*-hexane aromatization. The details of the catalyst preparation are presented in chapter 2 (section 2.1 and 2.2). Their physico-chemical characterization is also presented in chapter 2 (section 2.3).

3.2.2. Reaction Procedure: The catalytic reactions were carried out in a fixed bed down flow tubular silica reactor (15 mm i.d.) of 35 cm length provided with a thermowell. The catalyst (2g) was used in the form of granules (10 – 20 mesh) prepared by pelleting of the powders and crushing into the desired size. The catalyst was loaded in such a way that the tip of the thermocouple (kept inside the thermowell) was at the center of the catalyst bed. The catalyst was sandwiched by inert porcelain beads, which provided a more uniform flow distribution. The top portion of the porcelain beads additionally served as a pre heater zone to vaporize the feed. A condenser was attached to the outlet of the reactor, which was cooled by water circulation from a cryostat maintained at approximately 277 K.

The reactor was placed inside a temperature-controlled furnace (Geomecanique, France). The catalyst was activated in N_2 (30 ml min^{-1}) for 5h (773 K), cooled to room temperature and reduced in H_2 (30 ml min^{-1}) for 5 h at 773 K prior to carrying out the reaction at the desired temperature. The feed to the reactor consisted of a mixture of hydrogen and *n*-hexane (molar ratio of 6:1). The feed was passed using a syringe pump (Braun, Germany) along with hydrogen gas. The space velocity (WHSV based on *n*-hexane) was 2 h^{-1}. The reaction products were analyzed in a Hewlett-Packard (model 5880) chromatograph, equipped with a 50m capillary column (HP-5) and a flame ionization detector. Product identification was done by comparing with standards.

3.3. RESULTS AND DISCUSSION

3.3.1. Studies over Pt-M-LTL:

3.3.1.1. Effect of nature of the exchanged metal ion on the aromatization of *n*-hexane*:* The chemical compositions and surface areas measured by the BET method from N_2-adsorption are presented in Table 2.1. The CO_2 TPD profiles of the M-LTL samples are presented in chapter 2 (Fig. 2.13). The peak areas (on constant weight basis) increase in the order: Li < Na < K < Rb < Cs and Mg < Ca < Sr < Ba – LTL. The above trend is exactly as expected; substitution by a more electropositive metal increases the basicity of the catalyst. The Pt dispersion values of the different Pt-M-LTL samples determined by H_2 chemisorption are presented in chapter 2 (Table 2.15). The dispersion values are in the range of 0.5 to 0.9, the values being larger for the more basic samples. The transformation of *n*-hexane was carried out in the temperature range of 673 to 823 K at atmospheric pressure over all the metal exchanged catalysts and a commercial Pt-Al_2O_3 catalyst at identical conditions to compare their performances. The results for the different catalysts at 733 K are presented in Table 3.1. Both conversion of *n*-hexane and benzene yield increase in the case of alkali exchanged metal ions in the order: H < Li < Na < K < Rb < Cs. A similar trend was also observed (conversion increases down the row) in the case of the alkaline earth metals: Mg < Ca < Sr < Ba. The C_6 isomer fraction is less over Pt-LTL than over Pt-Al_2O_3 (Table 3.1). In the case of Pt-Al_2O_3, the isomerization of *n*-hexane is expected to take place by a bifunctional mechanism, while it occurs probably by a monofunctional route through C_5 ring closure and opening reactions over Pt-LTL.[19] The presence of methylcyclopentane in the products suggests such a possibility. The bifunctional and monofunctional routes are shown in Scheme 3.1.

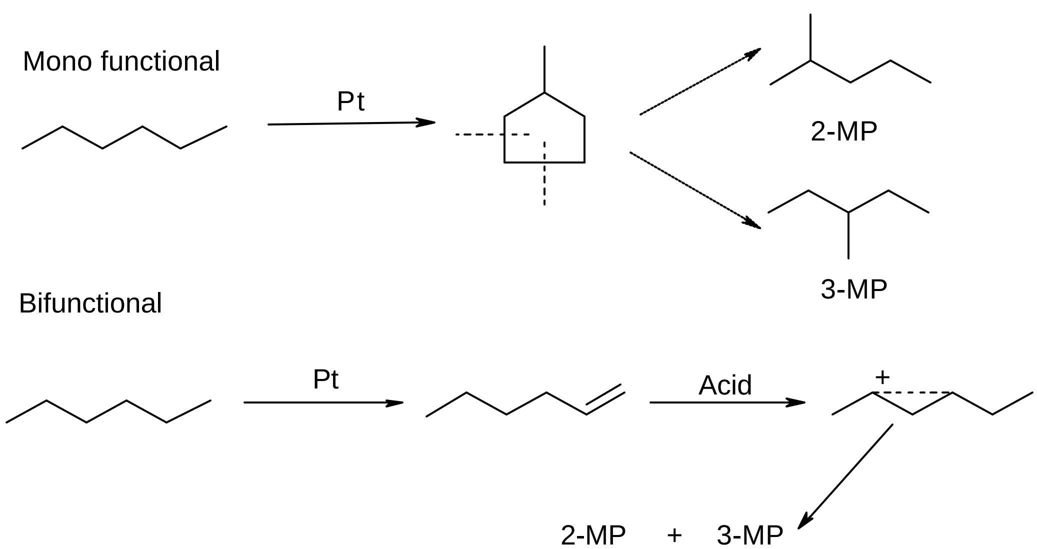

Scheme 3.1: C_6-isomerization by mono- and bifunctional routes

Table 3.1. Comparison of *n*-hexane aromatization activity of different alkali (alkaline earth)-LTL catalysts

	Pt-M-LTL (0.6 %) where M =										$Pt-Al_2O_3$
	H	Li	Na	K	Rb	Cs	Mg	Ca	Sr	Ba	
Conversion (%)	4.1	17.2	21.5	43.1	58.4	72.4	20.3	22.7	46.8	81.1	37.3
<u>Product yield (wt%)</u>											
C_1 to $C_5^{\#}$	1.2	0.7	1.2	2.5	1.3	1.5	0.9	1.3	2.5	0.6	3.5
$i\text{-}C_6^{\$}$	2.3	1.1	1.4	2.6	1.8	1.9	1.4	1.5	1.8	0.4	6.8
MCP^{*}	0.0	2.9	3.2	2.7	2.4	2.7	3.2	2.9	2.5	2.3	1.2
Benzene	0.3	6.3	9.1	30.1	46.1	59.1	9.3	11.2	35.9	73.2	3.2
C_6+ Aromatics**	0.2	2.3	2.5	0.1	0.8	1.1	2.7	2.6	1.1	0.1	7.5
Others	0.1	3.9	4.1	5.1	6.0	6.1	2.8	3.2	3.0	4.5	15.1
Benzene selectivity^{+}	7.3	36.6	42.3	69.8	78.9	81.6	45.8	49.3	76.7	90.2	8.6

Reaction conditions: Temp. 733 K, WHSV = $2h^{-1}$; Pressure = 1 atm.; TOS = 2h; H_2:*n*-hexane (mol) = 6:1; # C_1-C_5 = hydrocarbons from methane to pentane; $ = iso-hexanes, mainly 2 methyl pentane and 3 methyl pentane; * = methyl cyclopentane; ** = toluene + xylenes and + = benzene selectivity = wt of benzene/ wt of all products X 100.

3.3.1.2. Influence of duration run: The activity of the catalyst decreased rather rapidly initially upto about 6 h and then slowly with duration of run (studied upto 16 h; Fig. 3.1). The initial rapid loss of activity is probably due to the deactivation of the active sites at the external surface or the more active ones. All the data reported in the following sections have been obtained at a TOS of 2 h. The general trends in the reported data and the conclusions remain the same irrespective of the deactivation phenomenon. The changes in yields of different products follow the same trend. The deactivation may be due to coke deposition on active sites and in the channels of the zeolites.[22] The observation that the deactivation rate was lower when the experiment was conducted at a higher H_2:*n*-hexane mole ratio (10) supports the above suggestion.

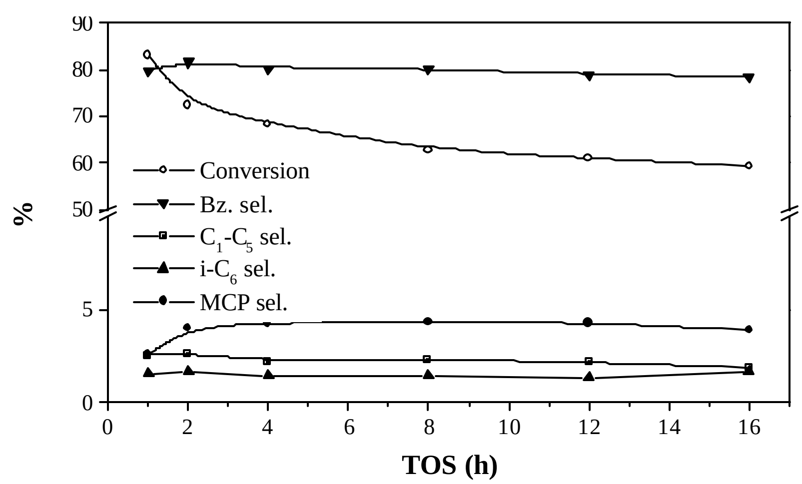

Fig. 3.1. Influence of the time on stream on *n*-hexane aromatization over Pt-Cs-LTL. (Reaction conditions: Temp. = 733 K; WHSV = 2h^{-1}; Pressure = 1 atm.; H_2: *n*-hexane (mol) = 6:1; see footnote of Table 3.1 for definitions).

3.3.1.3. Relationship between S_{int} and conversion (and benzene selectivity) in the aromatization of *n*-hexane: The high basicity of the LTL samples appears to be most important factor responsible for the larger aromatization activity. Besoukhanova *et al.*[17] reported that the activity of supported Pt in *n*-hexane aromatization is a function of the basicity of the support. On a basic support, Pt is electron rich, the richness arising from electron transfer from the basic O^{2-} ions in the framework.[17] The extent of the electron transfer from the lattice to the metal will depend on the net charge on O^{2-} ion and the intermediate electronegativity (S_{int}) of the zeolite; S_{int} is inversely proportional to the oxygen charge.[32] The calculated S_{int} values for the different catalysts are presented in chapter 2 (section 2.3.10). The relationship between conversion benzene selectivity, oxygen charge and S_{int} in the case of Pt-M-LTL samples is presented in Fig. 3.2 A and B. As expected, both conversion and benzene selectivity increase with increasing oxygen charge (decreasing S_{int}). Two different (but similar) trends are noticed for the alkali and alkaline earth exchanged catalysts. Even small changes in oxygen charge (and S_{int}) affect the performance of the alkaline earth catalysts very much.

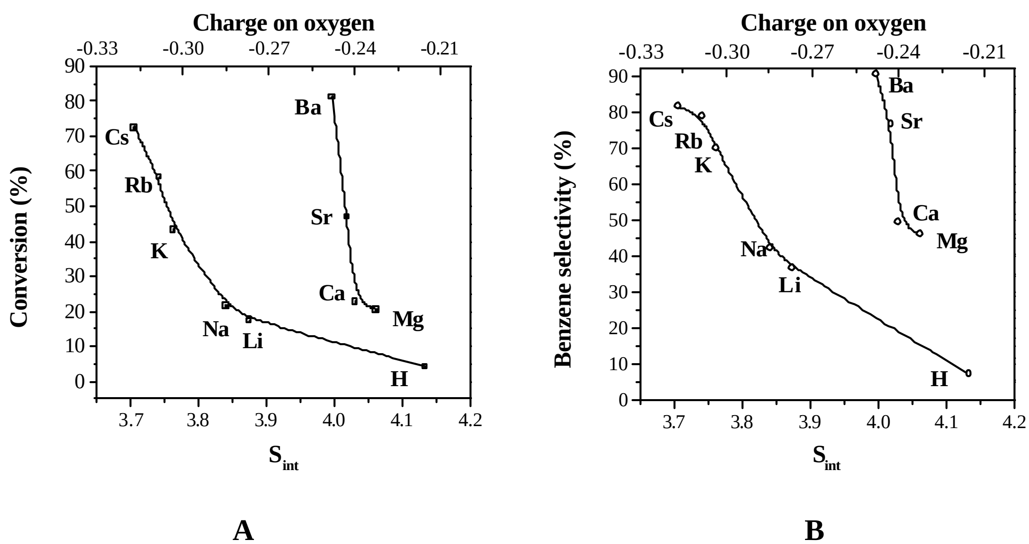

Fig. 3.2. **A) Relationship between *n*-hexane conversion and S_{int}/ charge on oxygen and B) Relationship between benzene selectivity and S_{int}/ charge on oxygen.**

3.3.1.4. Studies on Pt-Cs-LTL: Among the alkali metal exchanged catalysts, Pt-Cs-LTL and Pt-Ba-LTL exhibit higher conversion and aromatics selectivity (Table 3.1). The Pt-Cs-LTL catalyst was investigated in greater detail and compared with other Pt-Cs-zeolites (BEA, FAU) and Pt-Al_2O_3.

3.3.1.4.1. Influence of Pt content: The influence of Pt loading (Pt-Cs-LTL) on conversion and benzene yields at 733 K is presented in the Fig. 3.3. *n*-Hexane conversion increases with Pt loading and becomes steady at about 0.6 wt %. Conversion increases more rapidly with Pt loading at lower Pt levels (0.2 to 0.4 wt %). Benzene yield and selectivity also increase with Pt loading in a similar manner. Such a flattening of activity with increasing Pt content has already been reported by earlier workers in the case of bifunctional catalysts such as Pt-Al_2O_3 and has been attributed to the reaction being faster over the Pt sites and the overall reaction being limited by the constant number of acid centers.

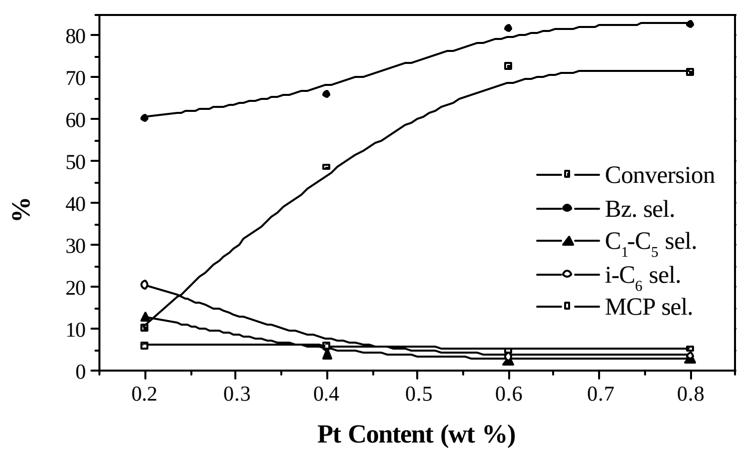

Fig. 3.3. Influence of Pt loading on activity of Pt-Cs-LTL in *n*-hexane aromatization. (Reaction conditions: Temp. = 733 K; WHSV = 2h^{-1}; Pressure = 1 atm.; TOS = 2h; H_2: *n*-hexane (mol) = 6:1 see footnote of Table 3.1 for definitions).

The attainment of a maximum limit in the case of the monofunctional reaction in this study is probably due to the high conversions (> 60 %) attained even at low Pt loading (~ 0.4 wt %) and the presence of diffusion effects inside the zeolite pores.

<u>3.3.1.4.2. Influence of temperature:</u> The influence of temperature on the conversion of *n*-hexane, benzene yield and benzene selectivity is presented in Fig. 3.4. Conversion and benzene selectivity increase with temperature. The benzene selectivity increases upto about 733 K and remain more or less constant at higher temperatures. Due to increased hydrogenolysis of *n*-hexane over Pt, the yield of C_1-C_5 increases with temperature eventhough the selectivity itself decreases due to competition from the aromatization reaction.

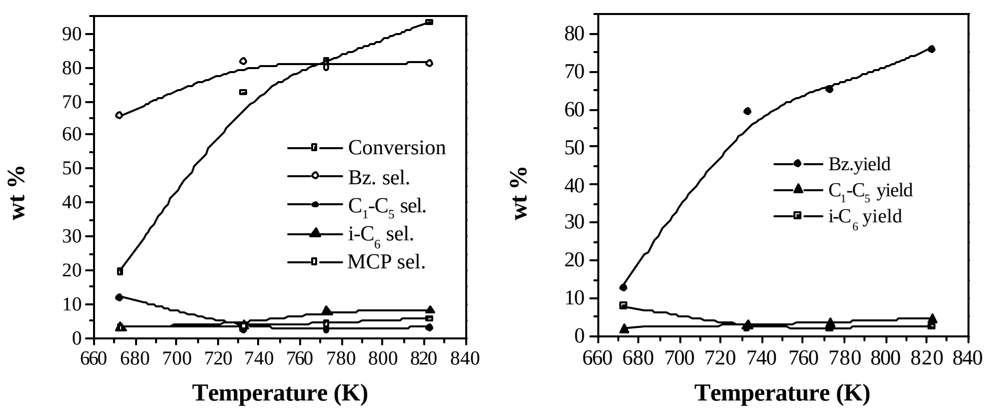

A B

Fig. 3.4. A) Influence of temperature on *n*-hexane aromatization over Pt-Cs-LTL (0.6 wt % Pt) and B) influence of temperature on product yields, (Reaction conditions: WHSV = 2h^{-1}; Pressure = 1 atm.; TOS = 2h^{-1}; H_2: *n*-hexane (mol) = 6:1; see footnote of Table 3.1 for definitions).

<u>3.3.1.4.3. Influence of space velocity:</u> The influence of space velocity on conversion of *n*-hexane and benzene selectivity at 733 K is presented in Fig. 3.5. Conversion decreases slowly with increasing feed rate (WHSV). Conversion decreases from 79.7 % at a contact time (1/WHSV) of 2 h to 63.2 % at a contact time of 0.25 h. Considering the eight-fold change in contact time, the change in conversion is rather small. Benzene selectivity is nearly constant in the contact time range studied. Though hydrogenolysis selectivity is larger at higher contact times, selectivities for i-C_6 and MCP decrease marginally (Fig. 3.5).

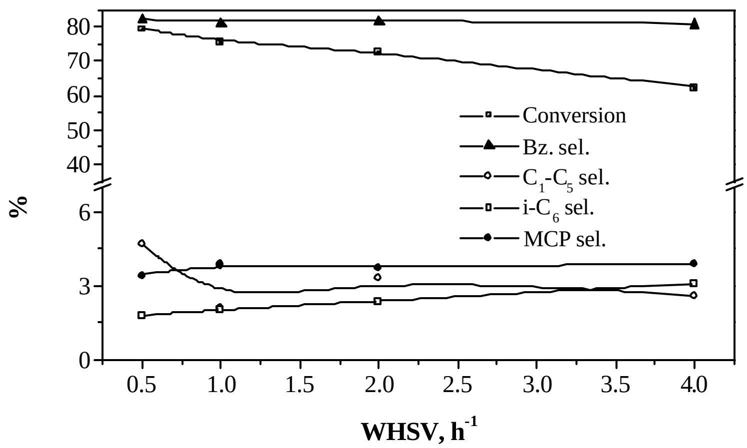

Fig. 3.5. Effect of WHSV on *n*-hexane aromatization over Pt-Cs-LTL (0.6 wt % Pt). (Reaction conditions: Temp. = 733 K; WHSV = 2h^{-1}; Pressure = 1 atm.; TOS = 2h; H_2: *n*-hexane (mol) = 6:1; see footnote of Table 3.1 for definitions).

3.3.1.4.4. Influence of H_2/*n*-hexane (mol) ratio: In this study, the flow rate of H_2 (mol ratios) was varied keeping the feed rate of *n*-hexane constant. The conversion of *n*-hexane decreases with hydrogen to hydrocarbon (HC) molar ratio (H_2/HC) as shown in Fig. 3.6. The decrease, could be due to space velocity effect as the total number of moles flowing through the catalyst is more at higher H_2:HC ratios. It could also be due to a H_2 partial pressure effect. The hydrogenolysis products (C_1-C_5) and benzene selectivity increase marginally with molar ratio. Selectivity for MCP decreases concomitantly with increase in i-C_6 selectivity. This suggests a rapid hydrogenolysis of MCP at higher H_2 partial pressures.

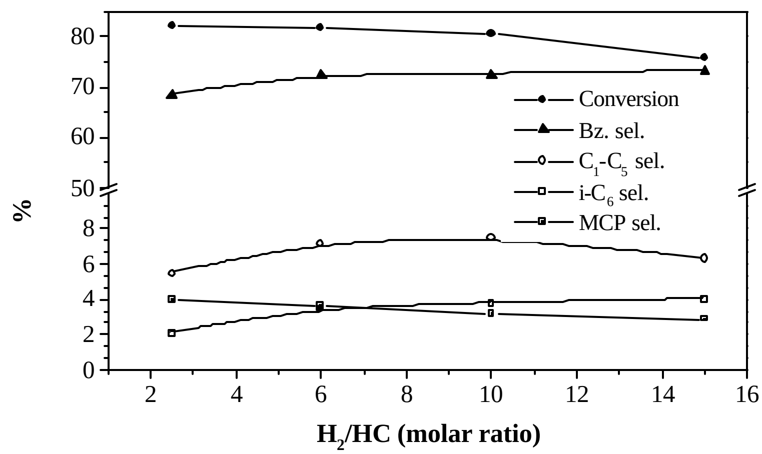

Fig. 3.6. The influence of H_2:HC molar ratio on *n*-hexane aromatization over Pt-Cs-LTL (0.6 wt % Pt). (Reaction conditions: Temp. = 733 K; WHSV = 2h^{-1}; Pressure = 1 atm.; TOS 2h; see footnote of Table 3.1 for definitions).

3.3.1.4.5. Comparison with Pt-Al_2O_3: The results of *n*-hexane aromatization over a commercial Pt-Al_2O_3 catalyst are presented in Table 3.1. Pt-Cs-LTL produces many times more benzene and benzene selectivity is also more than that over Pt-Al_2O_3. The monometallic Pt-Cs-LTL catalyst is therefore more efficient as has been reported earlier.[8,33] Examining Table 3.1, it is noticed that conversion is very low when Pt is loaded over acidic L-zeolite (Pt-H-L). Interestingly, benzene selectivity is similar to that observed over Pt-Al_2O_3. The activity, and more significantly, benzene selectivity rapidly increase on loading the zeolite with alkali ions. Two sets of trends are noticed, one for the alkali and another for the alkaline earth elements. Pt-Cs-LTL is the most active and selective alkali metal loaded catalyst and Ba-Pt-LTL is the most active (and selective) alkaline earth loaded catalyst, Pt-Ba-LTL is more active and selective than Cs-Pt-LTL. The benzene yields over Pt-Cs-LTL and Pt-Ba-LTL are 18 and 22 times more than that obtained over Pt-Al_2O_3. The typical bifunctional (Pt/Al_2O_3) and monofunctional (Pt-K-LTL) routes for the aromatization of *n*-hexane are shown in Scheme 3.2.

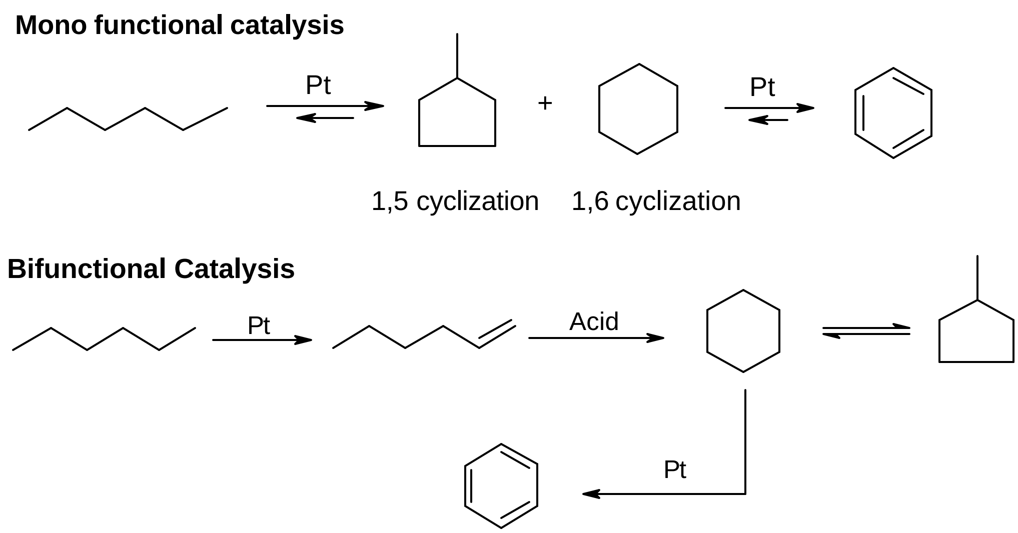

Scheme 3.2 The mechanism of *n*-hexane aromatization by mono- and bifunctional routes

Over bifunctional catalysts, the first and the last steps, namely the dehydrogenation of *n*-hexane and cyclohexane take place over the metallic sites and the isomerization (cyclization) of hexane takes place on acid sites. Over acidic catalysts, side reactions such as the isomerization and cracking of hexane also occur through carbenium ion mechanisms leading to lower benzene selectivity. These acid catalyzed side reactions are not significant over basic catalysts and hence one would expect benzene selectivity to be larger. Besides, coke formation is more over acidic catalysts on both the acid and metal sites due to strong adsorption of electron rich coke-precursors such as poly-olefins and aromatics; it is found that the adsorption of benzene (aromatic compound) on Pt becomes weaker with increase in basicity of the support (chapter 4). These reasons contribute additionally to the better performance of Pt supported on basic materials than Pt-Al_2O_3.

3.3.2. Studies over Pt-M-BEA:

3.3.2.1. Effect of nature of the exchanged metal ion on the aromatization of *n*-hexane: The chemical compositions and BET surface areas measured from N_2-adsorption are presented in Table 2.2 (chapter 2). There is a decrease in surface area with cation exchange on going down the row of alkali and alkaline earth metals. The CO_2 TPD spectra of the M-BEA (M = Li, Cs and Ba) samples are presented in chapter 2 (Fig. 2.15 A). The areas of the peaks (on constant weight basis) increase in the order: Li < Ba < Cs – BEA. The Pt dispersion values of different Pt-M-BEA samples were determined by H_2 chemisorption and are also presented in chapter 2 (Table 2.15). The dispersion values are in the range of 55 to 93 %, the values being larger for the more basic samples.

The catalytic performance of Pt-M-BEA samples in the transformation of *n*-hexane was evaluated at atmospheric pressure at different process parameters. These results are compared with those obtained over commercial Pt-Al_2O_3 and Pt-Cs-LTL catalysts. The results for the different catalysts (Pt-M-BEA; M = H, Li, Na, K, Rb, Cs, Mg, Ca, Sr and Ba) obtained at 733 K at a time on stream of 2 h are presented in Table 3.2. A comparison of the activities indicates that it is in the order: Li < Na < K < Rb < H < Cs and Mg < Ca < Sr < Ba, the activity of Pt-Cs-BEA and Pt-Ba-BEA being more than the other cation exchanged BEA samples. The benzene yield and selectivity also increase in the same order as above expected for the H-form, which is the least selective one.

3.3.2.2. Influence of duration run: The activity of the catalyst decreased rather rapidly upto 2 h and then slowly with passage of time (studied upto 12 h; Fig. 3.7). The initial fast deactivation is probably due to the deactivation of Pt sites at the external surface. Earlier, Iglesia and Baumgartner had attributed the initial rapid deactivation of Pt-Cs-BEA catalysts during *n*-hexane transformation to the presence of larger Pt particles on the external surface of the zeolite crystallites or at the entrance of the pores.[34] Benzene selectivity goes through a maximum with time on stream while i-C_6 decreases. The decrease in i-C_6 may be due to coke deposition on the residual acid sites suppressing the acid catalyzed *n*-C_6 isomerization.[22] It was found that Pt-Cs-BEA and Pt-Ba-BEA are more resistance to catalytic deactivation compared to other cation exchanged zeolites (M-BEA).

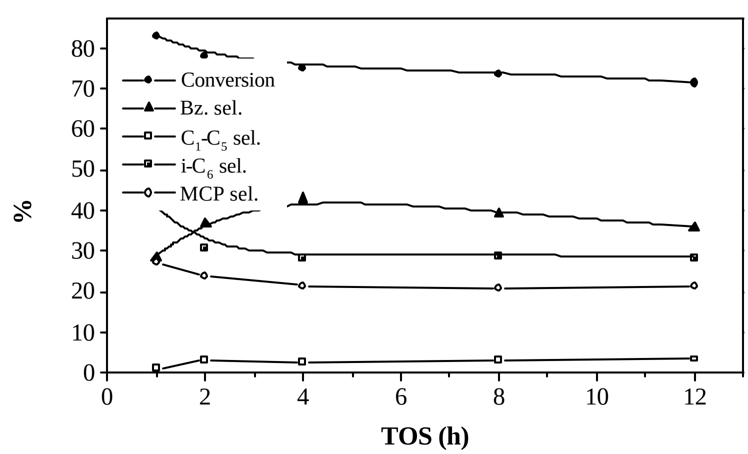

Fig. 3.7. Influence of time on stream on *n*-hexane aromatization over Pt-Cs-BEA. (Reaction conditions: Temp. = 733 K; WHSV = 2h^{-1}; Pressure = 1 atm.; H_2: *n*-hexane (mol) = 6:1; see footnote of Table 3.2 for definitions).

Table 3.2. Comparison of *n*-hexane aromatization activity of different Pt alkali (alkaline earth)-BEA catalysts

	Pt-M-BEA (0.6 %) where M =									
	H	Li	Na	K	Rb	Cs	Mg	Ca	Sr	Ba
Conversion (%)	72.8	57.2	60	68.4	70.7	75.1	60.4	67.3	70.4	77.3
Product yield (wt%)										
C_1 to C_5 #	37.8	11.8	20.1	16.4	13.8	16.1	18.7	17.4	15.7	11.8
i-C_6 $	22.3	25.9	21.4	22.4	23.2	21.2	19.0	20.9	21.4	20.6
MCP*	2.1	2.2	2.1	2.7	2.1	2.0	3.4	3.7	2.0	3.1
Benzene	5.5	14.4	15.1	24.9	29.3	32.2	16.2	21.8	27.9	35.8
C_6+ Aromatics**	3.9	1.8	0.3	1.4	1.8	1.3	0.9	0.8	1.9	2.6
Others	1.2	1.1	1.0	0.6	0.5	2.3	2.4	2.7	1.5	1.4
Benzene Selectivity+	7.6	25.1	25.2	36.4	41.4	42.9	26.8	32.4	39.6	46.3

Reaction conditions: Temp. 733 K, WHSV = $2h^{-1}$; Pressure = 1 atm.; TOS = 2h; H_2:*n*-hexane (mol) = 6:1; # C_1-C_5 = hydrocarbons from methane to pentane; $ = iso-hexanes, mainly 2 methyl pentane and 3 methyl pentane; * = methyl cyclopentane; ** = toluene + xylenes and + = benzene selectivity = wt of benzene/ wt of all products X 100.

The deactivation of the catalysts attributed to the deposition of coke depends on the type of cation and on the localization of the Pt particles on the support, as discussed by earlier workers.[35,36]

3.3.2.3. Relationship between S_{int} and conversion (and benzene selectivity) in the aromatization of *n*-hexane: In the case of Pt-M-BEA also, the activity (except for Pt-H-BEA) and benzene selectivity are inversely proportional to the intermediate electronegativity.[1,17] The values of S_{int} and charge on oxygen are presented in chapter 2, Table 2.14. The relationships between conversion, benzene selectivity, oxygen charge and S_{int} in the case of Pt-M-BEA samples are presented in Fig. 3.8. The detailed product distributions obtained over Pt-M-BEA are presented in Table 3.2. It is seen that both *n*-hexane conversion activity and benzene selectivity increase in the same order as basicity of the support (M-BEA): Li < Na < < K < Rb < Cs and Mg < Ca < Sr < Ba. In the case of Pt-H-BEA, the conversion is very high (72.8 %), but benzene selectivity is low (7.6 %). Most of the converted *n*-hexane is cracked over the acid sites into C_1-C_5 (37.8 %) or isomerized (22.3 %). In comparison, it is found that conversion is 77.3 % over Pt-Ba-BEA and benzene selectivity is 46.3 %. It is also observed that the increase in benzene selectivity with basicity is associated with a concomitant decrease in hydrogenolysis/ hydrocracking (C_1-C_5 formation), isomerization (i-C_6 formation) and other products. It is also observed that benzene selectivities are lower over Pt-M-BEA catalysts than over Pt-M-LTL catalysts eventhough conversions are more over the BEA catalysts. The reason is mainly the greater acidity of the BEA system compared to the LTL system. Due to the lower Si/Al ratio, alkali (alkaline earth) metal content is more in LTL making it more basic. The larger acidity of BEA is also responsible for the larger yield of C_1-C_5 through cracking reactions (Table 3.2).

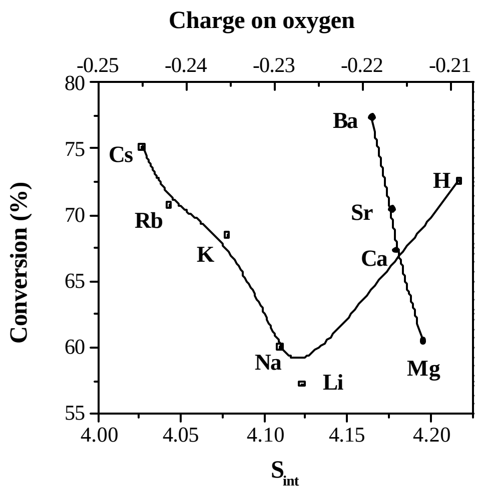

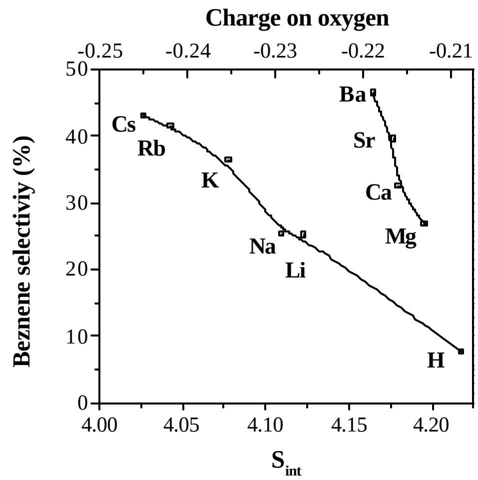

Fig. 3.8. **A) Relationship between *n*-hexane conversion and S_{int}/ charge on oxygen and B) Relationship between benzene selectivity and S_{int}/ charge on oxygen.**

3.3.2.4. Studies on Pt-Cs-BEA: As the Pt-Cs-BEA catalyst was the most active and selective alkali exchanged catalyst, it was further investigated in detail.

3.3.2.4.1. Influence of Pt content: The influence of Pt loading on conversion and benzene selectivity at 733 K is shown in Fig. 3.9. Conversion increases with increase in platinum content from 0.2 to 0.4 wt % and reaches a nearly constant value at higher Pt loadings (Fig. 3.9). Benzene selectivity increases marginally with Pt loading in the 0.2 to 0.4 % range and remains constant at higher loadings. The isomerization (i-C_6 and MCP formation) is also only marginally affected. C_1-C_5 selectivity decreases with increasing Pt loading upto about 0.4 wt %, a slight minimum being noticed at this loading. Wile the decrease in the early stages is attributed to competition from the aromatization reaction, the sight increase at loadings beyond 0.4 % might be due to greater hydrogenolysis over the Pt metal.

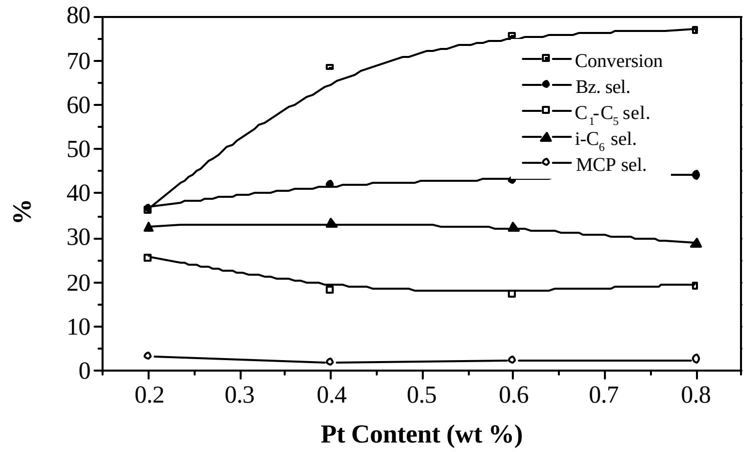

Fig. 3.9. Influence of Pt loading on activity of Pt-Cs-BEA in *n*-hexane aromatization. (Reaction conditions: Temp. = 733 K; WHSV = 2h^{-1}; Pressure = 1 atm.; TOS = 2h; H_2: *n*-hexane (mol) = 6:1; see footnote of Table 3.2 for definitions).

<u>3.3.2.4.2. Influence of process parameters:</u> The influence of temperature, space velocity (WHSV) and H_2: *n*-hexane mole ratios are presented in Fig. 3.10 to 3.12. An increase in the temperature (673 to 823 K) increases the conversion of *n*-hexane rapidly. The selectivities for all the products also increase, the C_1-C_5 and i-C_6 selectivities increasing more rapidly than benzene selectivity. The selectivity for MCP is small (< 2 %) and nearly unaffected by temperature (Fig. 3.10). Conversion increases slightly with contact time. It is about 59.7 and 72.9 % at WSHV (h^{-1}) of 4 and 0.5, respectively. Benzene selectivity decreases while i-C_6 selectivity increases with increasing WHSV. The selectivities for MCP and C_1-C_5 remain nearly constant (Fig. 3.11). *n*-Hexane conversion and benzene selectivity go through maxima with increase in hydrogen to hydrocarbon mole ratio (H_2:HC) as shown in Fig. 3.12. The reason for this behavior is not clear, though a combined effect of lower deactivation at higher H_2 partial pressure and lower activity due to larger effective WHSV (see discussion in the case of Pt-Cs-LTL) could be responsible.

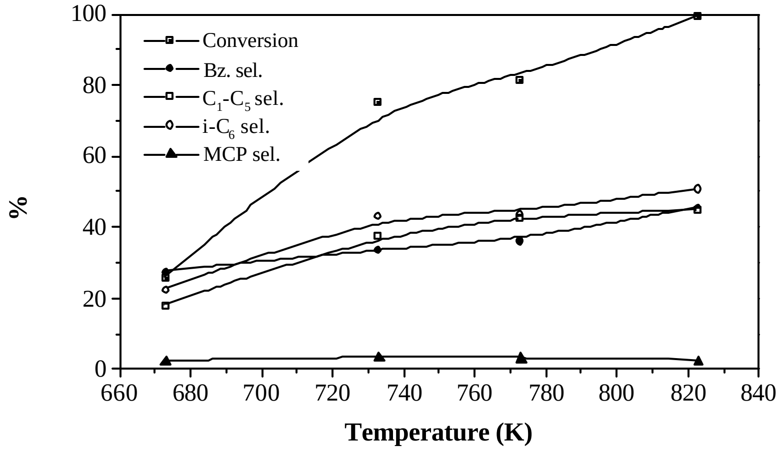

Fig. 3.10. **Influence of temperature on *n*-hexane conversion over Pt-Cs-BEA (0.6 wt % Pt). (Reaction conditions: WHSV = 2h^{-1}; Pressure = 1 atm.; TOS = 2h; H_2: *n*-hexane (mol) = 6:1; see footnote of Table 3.2 for definitions).**

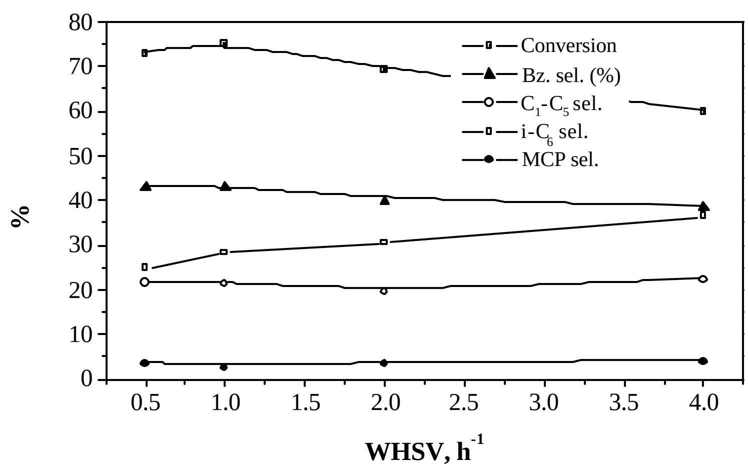

Fig. 3.11. **Effect of feed rate (WHSV) on *n*-hexane aromatization over Pt-Cs-BEA (0.6 wt % Pt). (Reaction conditions: Temp. = 733 K; Pressure = 1 atm.; TOS = 2h; H_2: *n*-hexane (mol) = 6:1; see footnote of Table 3.2 for definitions).**

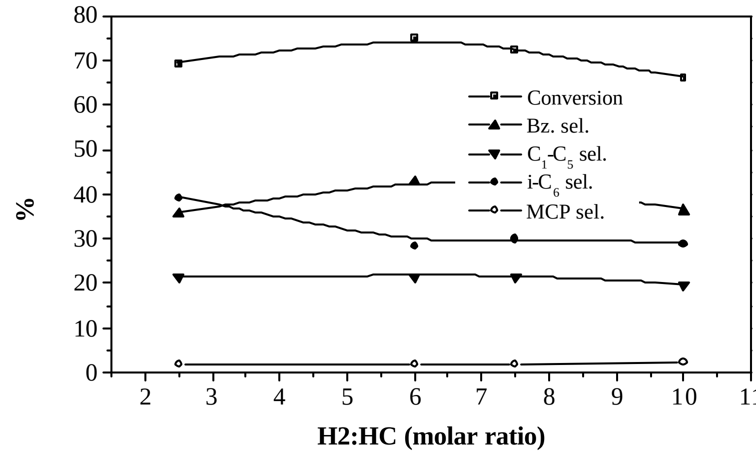

Fig. 3.12. The influence of H_2:HC molar ratio on *n*-hexane aromatization over Pt-Cs-BEA (0.6 wt % Pt). (Reaction conditions: Temp. = 733 K; WHSV = 2h^{-1}; Pressure = 1 atm.; TOS = 2h; see footnote of Table 3.2 for definitions).

3.3.2.4.3. Comparison with Pt-Al_2O_3: The results of *n*-hexane aromatization over a commercial Pt-Al_2O_3 sample containing 0.6 wt % Pt are presented in Table 3.1. Pt-Cs-BEA produces many times more benzene than Pt-Al_2O_3 through not as effectively as Pt-Cs-LTL.

Comparing Pt-Al_2O_3 and Pt-Cs-BEA, the conversion is 37.3 % on the former catalyst and 75.1 % over the latter catalyst; the benzene yields are 3.2 and 32.2 %, respectively for the two catalysts. Interestingly, i-C_6 and C_1-C_5 yields are more over Pt-Cs-BEA. This may be due to the presence of residual acid sites of larger strength than Pt-Al_2O_3 or due the activity of the metalic function in Pt-Cs-BEA. The important point to note is that Pt-Al_2O_3 produces more C_6+ aromatics and other compounds (mostly C_8+ aromatics) compared to the basic catalyst.

3.3.3. Studies over Pt-M-FAU:

3.3.3.1. Effect of nature of the exchanged metal ion on the aromatization of *n*-hexane: The chemical compositions and BET surface areas measured from N_2-adsorption are presented in Table 2.3. The CO_2-TPD profiles of the M-FAU samples are presented in chapter 2 (Fig. 2.15 B). The areas of the peaks (on constant weight basis) increase in order: Li < Ba < Cs - FAU. The Pt dispersion values of Pt-M-FAU samples were determined by H_2 chemisorption and presented in chapter 2 (Table 2.15). The dispersion values are in the range of 45 to 70 %, the values being larger for the more basic samples.

The catalytic performance of the Pt-M-FAU catalysts in the transformation of *n*-hexane was evaluated at 673 to 823 K at 1 atmospheric pressure, at different Pt loadings, different H_2/ hydrocabon molar ratios and various space velocities. These results are compared with those obtained over Pt-Al_2O_3, Pt-Cs-BEA and Pt-Cs-LTL. The results for the different Pt-M-FAU (M = H, Li, Na, K, Rb, Cs, Mg, Ca, Sr and Ba) catalysts obtained at 733 K at a time on stream of 2 h are presented in Table 3.3. A comparison of the activities indicates that the activity is in the order: H < Li < Na < K < Rb < Cs and Mg < Ca < Sr < Ba. The activity of Pt-Cs-FAU and Pt-Ba-FAU is more than that of the other cation exchanged samples (M-FAU). The benzene yield and selectivity also increase in the same order, expect for Sr-FAU, which posses a slightly larger selectivity that Ba-FAU. The over all activity of Pt-M-FAU is less than Pt-Al_2O_3 but benzene selectivity is more than the latter catalyst. Comparing the three types of zeolite catalysts, the order of aromatization selectivity is found to be Pt-M-LTL > Pt-M-BEA > Pt-M-FAU.[37]

3.3.3.2. Relationship between S_{int} and benzene conversion (and benzene selectivity) in the aromatization of *n*-hexane: The relationship between S_{int}/ oxygen charge and *n*-hexane conversion/ benzene selectivity for Pt-M-FAU samples are presented in Fig. 3.13. The results are similar to those observed earlier for the Pt-M-LTL and Pt-M-BEA samples. Again, the influence of S_{int} (and oxygen charge) on conversion is more significant for the alkaline earth samples.

3.3.3.3. Studies on Pt-Cs-FAU: Among the alkali metal exchanged catalysts Pt-Cs-FAU was more active and more selective. This catalyst was therefore investigated in greater detail.[37]

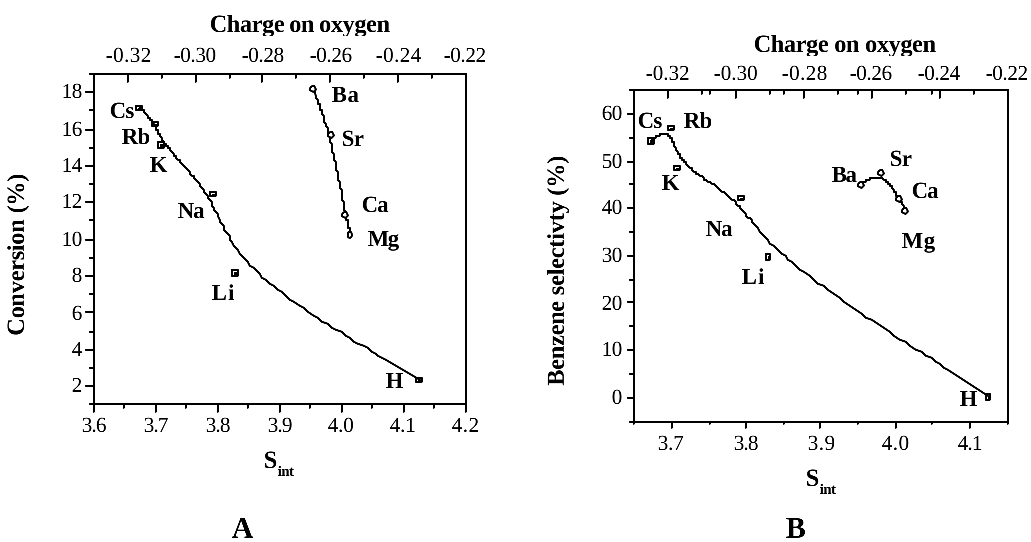

Fig. 3.13. A) Relationship between *n*-hexane conversion and S_{int}/ charge on oxygen and
B) Relationship between benzene selectivity and S_{int}/ charge on oxygen.

3.3.3.3.1. Influence of Pt content: The influence of Pt loading on conversion of *n*-hexane and benzene selectivity at 733 K is presented in the Fig. 3.14. Conversion increases with Pt loading and reaches a steady state at about 0.6 wt % Pt (Fig. 3.14). Similarly, benzene selectivity also increases with Pt loading and reaches a near steady state about 0.4 % Pt. The results are similar to those observed in the case of Pt-M-LTL and Pt-M-BEA.

Table 3.3. Comparison of *n*-hexane aromatization activity of different Pt alkali (alkaline earth)-FAU catalysts

	Pt-M-FAU (0.6 %) where M =									
	H	Li	Na	K	Rb	Cs	Mg	Ca	Sr	Ba
Conversion (%)	3.4	8.1	12.4	15.1	16.2	17.1	10.2	11.3	15.6	18.1
Product yield (wt %)										
C_1 to C_5 #	2.3	2.2	2.5	2.1	1.9	1.4	2.3	2.4	2.1	1.9
iC_6 $	0.7	0.9	1.3	2.4	1.8	1.0	1.3	1.5	1.9	0.3
MCP *	0.2	1.2	2.1	2.7	2.4	2.4	1.4	1.7	1.0	3.3
Benzene	0.0	2.4	5.2	7.3	9.2	8.9	4.0	4.7	7.4	8.1
C_6+ Aromatics **	0.1	0.4	0.6	0.3	0.5	1.1	0.3	0.7	0.8	0.1
Others	0.1	1.0	0.7	0.3	0.4	2.3	0.9	1.3	2.5	4.4
Benzene selectivity +	-	29.6	41.9	48.3	56.8	52.1	39.2	41.6	47.4	44.8

Reaction conditions: Temp. 733 K; WHSV = $2h^{-1}$; pressure = 1 atm.; TOS = 2h; H_2:*n*-hexane (mol) = 6:1; # C_1-C_5 = hydrocarbons from methane to pentane; $ = iso-hexanes, mainly 2 methyl pentane and 3 methyl pentane; * = methyl cyclopentane; ** = toluene + xylenes and + = benzene selectivity = wt of benzene/ wt of all products X 100.

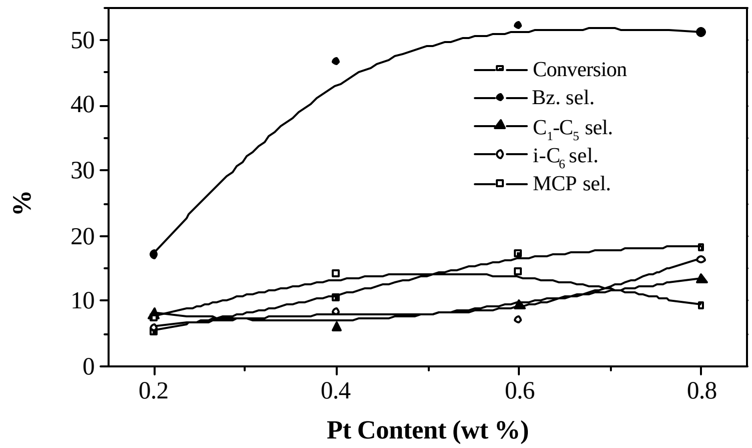

Fig. 3.14. Influence of Pt loading on *n*-hexane aromatization over Pt-Cs-FAU. (Reaction conditions: Temp. = 733 K; WHSV = 2h^{-1}; Pressure = 1 atm.; TOS = 2h; H_2: *n*-hexane (mol) = 6:1; see footnote of Table 3.3 for definitions).

<u>3.3.3.3.2. Influence of process parameters:</u> The influence of temperature on the conversion of *n*-hexane and product selectivities is presented in Fig. 3.15. Conversion increases with temperature, but benzene selectivity goes through a maximum. Selectivities for C_1-C_5 and i-C_6 increase with temperature while that for MCP decreases. The influence of space velocity on the conversion of *n*-hexane and product selectivities is presented in Fig. 3.16. Conversion of *n*-hexane decrease with increasing feed rate. Benzene selectivity goes through a maximum at WHSV (h^{-1}) = 2. This trend is probably due to increased hydrogenolysis selectivity at lower WHSV (h^{-1}) = 0.5 and increased i-C_6 formation at higher WHSV. The influence of H_2:HC molar ratio is shown in Fig. 3.17. Both conversion and benzene selectivity go through maxima at an intermediate value of H_2:HC ratio. The trends are similar to those observed for Pt-M-BEA.

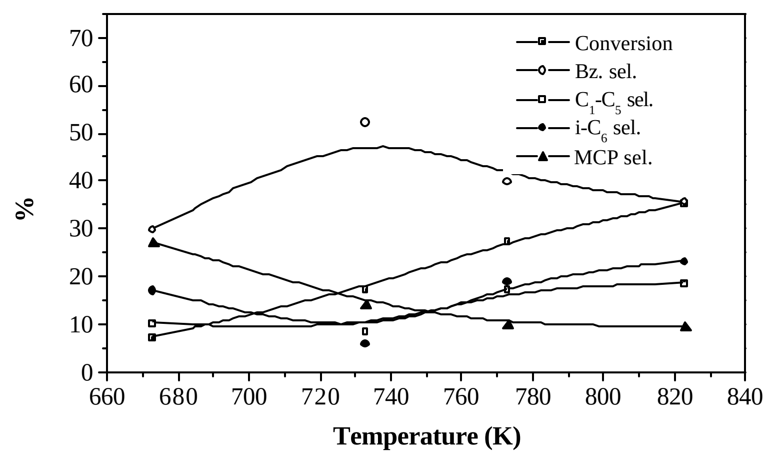

Fig. 3.15. **Influence of temperature on *n*-hexane conversion over Pt-Cs-FAU (0.6 wt % Pt). (Reaction conditions: WHSV = 2h^{-1}; Pressure = 1 atm.; TOS = 2h; H_2: *n*-hexane (mol) = 6:1; see footnote of Table 3.3 for definitions).**

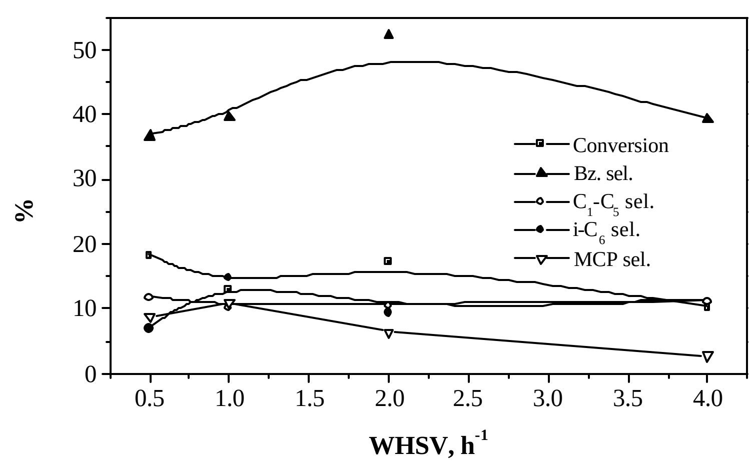

Fig. 3.16. **Influence of feed rate (WHSV) on *n*-hexane conversion over Pt-Cs-FAU (0.6 wt % Pt). (Reaction conditions: Temp. = 733 K; Pressure = 1 atm.; TOS = 2h; H_2: *n*-hexane (mol) = 6:1; see footnote of Table 3.3 for definitions).**

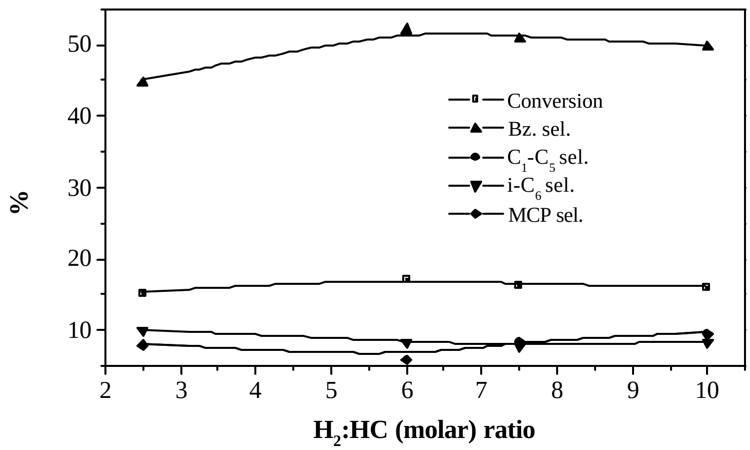

Fig. 3.17. Influence of H_2:HC molar ratio in *n*-hexane aromatization over Pt-Cs-FAU (0.6 wt % Pt). (Reaction conditions: Temp. = 733 K; WHSV = 2h^{-1}; Pressure = 1 atm.; TOS 2h; see footnote of Table 3.3 for definitions).

3.3.3.3.3. Comparison with Pt-Al_2O_3: The results of *n*-hexane aromatization over a commercial Pt-Al_2O_3 sample containing 0.6 wt % Pt is presented in Table 3.1. Conversion of *n*-hexane is less (17.1 %) over Pt-Cs-FAU than over Pt-Al_2O_3 (37.3 %). However, the yield of benzene is more (8.9 %) over the former catalyst than over the latter catalyst (3.2 %). However, comparing Pt-Cs-FAU with the corresponding LTL and BEA catalysts, it is the less active and selective.

3.4. CONCLUSIONS

Among the zeolites investigated, LTL is more active for *n*-hexane aromatization. The activities are in the order: Pt-M-FAU < Pt-M-BEA < Pt-M-LTL. Conversion of *n*-hexane increases with the basicity of the samples in the order: Li < Na < K < Rb < Cs and Mg < Ca < Sr < Ba. Benzene selectivity also increases with basicity in the above order. Cracking and isomerization reactions occur over on less basic catalysts. The activities and selectivities of the different catalysts correlate well with S_{int} and charge on oxygen, which quantify their basicity. The studies reveal that basicity (electronic properties) and structural factors are important in determining the aromatization activity and selectivity of Pt supported on zeolites.

3.5. REFERENCES

1. D. Barthomeuf, *Catal. Rev.-Sci. Eng*., 38 (1996) 521.
2. G.J. Antos, A.M. Aitani and J.M. Parera, "*Catalytic Naphtha Reforming, Science and Technology*", eds.; Marcel Dekker, Inc.; New York, 1995.
3. B.C. Gates, *Chem. Rev.*, 95 (1995) 511.
4. P. Meriaudeau and C. Naccache, *Catal. Rev.-Sci. Eng*., 39 (1997) 5.
5. H.E. Kluksdahl, *US Patent*, 3 417 737 (1968).
6. J.H. Sinfelt, in *"Catalysis Science and Technology"*, J.R. Anderson and M. Boudart, eds., Springer-Verlag, Berlin, 1 (1981) 257.
7. G.A. Mills, H. Heineman, T.H. Mulliken and A.G. Oblad, *Ind. Eng. Chem.*, 45 (1953) 134.
8. J.R. Bernard, in "*Proceedings of the 5th International Zeolite Congress*," Napoli, 1980; Rees, L.V.C., eds., Heyden, London, 1980; p. 686.
9. T.R. Hughes, R.L. Jacobson and P.W. Tamm, *Stud. Surf. Sci. Catal*., 38 (1987) 317.
10. *Oil Gas J.*, 190 (1992) 29.
11. D. Rotman, *Chem. Weekly*, 150 (1992) 8.
12. P.W. Tamm, D.H. Mohr and C.R. Wilson, *Stud. Surf. Sci. Catal*., 38 (1987) 335.
13. D.V. Law, P.W. Tamm and C.M. Detz, *Energy Process* 7 (1987) 215.
14. J. Zheng, J.L. Dong, Q.H. Xu, Y. Lui and A.Z. Yan, *Appl. Catal.* A, 126 (1995) 141.
15. J.A. Martens, M. Tielen and P.A. Jacobs, Stud. Surf. Sci. Catal., 46 (1985) 49.
16. T.R. Hughes, W.C. Buss. P.W. Tamm and R.L. Jacobson, *Stud. Surf. Sci. Catal*., 28 (1986) 725.
17. C. Besoukhanova, J. Guidot, D. Barthomeuf, M. Breysse and J.R. Bernard, *J. Chem. Soc. Faraday Trans*. I, 77 (1989) 1595.

18. G. Larson, G.L. Haller, *Catal. Lett.*, 3 (1989) 103.
19. E.G. Derouane and D. Vanderveken, *Appl. Catal,*. 45 (1988) L15.
20. J.M. Newsam, B.G. Silbernagel, A.R. Garcia, M.T. Melchow and S.G. Fung, *Stud. Surf. Sci. Catal*, 67 (1991) 211.
21. S.J. Tauster and J.J. Steger, *J. Catal.*, 125 (1990) 387.
22. M.M.J. Treacy, *Micropor. Mesopor. Mater.*, 28 (1999) 271.
23. E. Mielczarski, S.B. Hong, R.J. Davis and M.E. Davis, *J. Catal.*, 134 (1992) 359.
24. G. Jacobs, W.E. Alvarez and D.E. Resasco, *Appl. Catal. A*, 206 (2001) 267.
25. S.C. Fung, S.J. Tauster and J.Y. Kao, *US Patent*, 4 925 819 (1990)
26. G.B. McVicker, J.L. Kao, J.J. Ziemiak, W.E. Gates, J.L. Robbins, M.M.J. Treacy, S.B. Rice, T.H. Vanderspurt, V.R. Cross and A.K. Ghosh, *J. Catal.*, 139 (1993) 48.
27. S.J. Tauster, A.A. Montagna, J.J. Steger, S.C. Fung, V.R. Cross and J.L. Kao, *US Pat*,. 4 595 670 (1986).
28. E. Iglesia and J.E. Baumgartner, in "*Proceedings of 10th International Congress on Catalysis*", Budapest, (1992) 157.
29. G. Jacobs, F. Ghadiali, A.P. Pisanu, A. Borgna, W.E. Alvarez and D.E. Resasco, *Appl. Catal*,. A, 188 (1999) 79.
30. R.E. Jentoft, M. Trapatsis, M.E. Davis, B.C. Gates, *J. Catal.*, 179 (1998) 565.
31. R.T. Sanderson, "*Chemical Bonds and Bond Energy*", Academic Press, New York, 1976.
32. D. Barthomeuf, *Stud. Surf. Sci. Catal.*, 65 (1991) 157.
33. J.A Rado, V. Schomaker and P.E. Picket, in "*Proceedings of 3rd Congress on Catalysis*", W.M.H. Sachtler ed., North Holland Amsterdam 2 (1965) 1264.
34. E. Iglesia and J.E. Baumgartner, in "*Proceedings of 9th International Zeolite Conference*", R.Von Ballmoos, J.B. Higgins and M.M.J. Treacy, eds., Butterworth-Heinemann, Boston, 2 (1993) 421.
35. F.J. Maldonado, T. Becue, J.M. Silva, M.F. Riberio, P. Massiani and M. Kermarec, *J. Catal.*, 195 (2000) 342.
36. F.J. Maldonado, J.M. Silva, T. Becue, F.R. Riberio and M.F. Riberio, *Catal. Lett.*, 48 (1997) 69.
37. P.G. Smirniotis and E. Ruckenstein, *Appl. Catal.* A, 123 (1995) 59.

CHAPTER 4

n-HEXANE AROMATIZATION *OVER LTL, BEA AND FAU ZEOLITES: MOLECULAR MODELING STUDIES*

4.1. INTRODUCTION

Information on both the strength and number of basic sites in basic zeolites is important in designing catalysts.[1-4] The charge on framework oxygen ions in zeolites characterizes their basicity and may be calculated as for any other compound.[5,6] Charge on the oxygen ions is related to the chemical composition (Al content, cation identity and number of cations) as well as bond angles and bond lengths in the structure. Many researchers have carried out theoretical calculations on the acidity/ basicity of zeolites[7-19] using *ab initio* or semi empirical approaches. It has been shown that the charge on oxygen is larger as the Si-O-Al angle becomes narrower and the T-O distance is longer.[1] The introduction of elements other than Si will change not only the electronegativity but also the bond angles and lengths and the charge on the oxygen. The lowest oxygen charge is obtained for H forms of zeolites. *Ab initio* calculations performed on small clusters shows that the absolute value of the charge on oxygen (basicity) increases for the cationic forms of the zeolites in the order H < Li < Na < K < Rb < Cs.[13]

Mortier[19] was the first to introduce the concept of intermediate electronegativity (S_{int}) for zeolites. It reflects the mean electronegativity reached by all the atoms in the material. S_{int} and oxygen charge are inversely related. Even when assuming that the right atom electronegativity values are used in the calculations, it has to be realized that the approach takes into account only the chemical composition of the zeolite and structural effects are not considered.[20]

Besoukhanova *et al*.[21] have shown that the activity of Pt supported on LTL zeolite in benzene hydrogenation and *n*-hexane aromatization increases with the basicity of the ion (Cs > Rb > K > Na > Li) exchanged in the zeolite. They have also showed a relationship between activity and benzene selectivity (in *n*-hexane aromatization) with S_{int} of the support (M-LTL). Based on the vibrational frequency shifts of CO adsorbed on Pt as observed in the IR spectrum, the authors have concluded that the Pt particles interact electronically with the O^{2-} ions in the lattice.[21] Larsen and Haller[22] have also made similar conclusions based on their studies on benzene and toluene hydrogenation. The framework structural effect of the LTL zeolite has also been reported to be responsible for the exceptional dehydrocyclization activity of the Pt-LTL. Larsen and Haller[22] have also suggested that the electron rich nature of Pt in Pt-K-LTL is responsible for its greater S sensitivity in contrast to the greater S-tolerance of Pt-H-FAU in which the Pt is electron deficient.[23]

In this chapter, the aim is to apply molecular modeling tools for understanding and improving catalysts for aromatization. They are:

1) to study the influence of zeolite framework structure
2) to study the influence of extra-framework cations
3) to study the influence of location and size of Pt cluster
4) to identify the active sites
5) to examine the role of S and
6) to correlate the properties of the catalyst to their performance

4.2. CLUSTER MODELS AND METHODOLOGY

The detailed description of the methodology used in the calculations over different cluster models is presented in chapter 2 (section 2.4). *Ab initio* HF methods have been used to study the electronic properties of the cluster models of zeolite LTL, BEA and FAU. The effective core potential (ECP) basis sets are used in the calculation. The rationale for the choice of the cluster models of zeolite LTL, BEA and FAU is described in chapter 2 (section 2.6.1 to 2.6.3, respectively).

4.3. RESULTS AND DISCUSSION

4.3.1. Studies on LTL Zeolite: The LTL zeolite cluster models were generated from the reported literature crystal data by Barrer and Villger.[24] The framework structure of LTL zeolite is shown in Fig. 2.20. The cluster model is described in detail in chapter 2 (section 2.6.1). The framework structure of LTL contains 6, 8 and 12-M rings. The diameter of 12-MR in LTL is 7.4 Å. There are four types of non-framework cationic sites A, B, C and D[25] (Fig. 2.20). Site D has been used for locating the cation as cations in site D are most easily exchanged and they are exposed to reactants diffusing through the main 12-MR channel of LTL. The molecular fitting of Pt_5 clusters near cation site D in the 12-MR channel is described in chapter 2 (section 2.8.1).

4.3.1.1. Location of Al substitution in LTL framework: The cluster model used in this study and the location of the T sites are shown in Fig 4.1. The unsaturated valences of the terminal oxygen atoms are saturated with hydrogen atoms. The O-H distance has been kept as 1.03 Å and the vector of the O-H bond has been kept the same as the O-Si bond of the lattice. The isomorphous substitution of Al^{3+} with Si^{4+} creates a negative charge. The excess negative charge of the cluster model was compensated by cations (M_I and/or M_{II}) located at site D. The influence of aluminum substitution at different T sites in the cluster model on the total energy of the cluster and the charge on the Al ion was calculated and the results are presented in Table 4.1. Four T_1 and four T_2 sites are present in an 8-MR.[24] It is observed that the substitution of Al atom at T_1 position is energetically the most favored (Table 4.1) substitution. The presence of two Al atoms in suitable T_1 and T_2 sites was also considered, as allowed by the Löwenstein rule. It is observed that the location of two Al atoms at the farthest T_1 positions is energetically the most favorable (Table 4.1) one. According to the crystal structure reports,[24-25] these T_1 sites are common to the 12-MR channel also.

Table 4.1. Aluminum substitution at different T sites in LTL[a]

Sites	Total energy (a.u.)	Charge on[b] Al
T_1a or T_1d	-414.5411	1.58
T_1b or T_1c	-414.5401	1.53
T_2a or T_2d	-414.5411	1.54
T_2b or T_2c	-414.5401	1.53
T_1a and T_2b	-412.7176	1.54, 1.55
T_1a and T_1c	-412.7480	1.58, 1.56
T_1a and T_1d	-412.7531	1.57, 1.54
T_1a and T_2c	-412.7234	1.55, 1.57
T_1a and T_2d	-412.7073	1.54, 1.57

[a] Cluster = [$Si_7AlO_{24}H_{16}$] (Fig. 4.1) or [$Si_6Al2O_{24}H_{16}$] and [b] Mulliken population (atomic charge).

4.3.1.2. Influence of exchanged cations in M_I location: A cluster model representing an 8-MR encompassing site D for the location of extra-framework cations is considered. The situation, wherein one of the Si in site T_1 is replaced by Al (as in above section 4.3.1.1) and the resulting negative charge is compensated by different extra-framework cations is examined. The locations of cations were fixed at a distance from the bridging oxygens present in site D (M_I) and the model is shown in Fig. 4.2. The sum of the ionic radii of M^+ and O^{2-} was chosen as the distance for locating the cation. The stoichiometry of the cluster model used is [$M_ISi_7AlO_{24}H_{16}$]. The electronic properties of this cluster model for different cations [where M_I = H, Li, Na, K, Rb, Cs, Mg(OH), Ca(OH), Sr(OH) or Ba(OH)] were calculated and listed in Table 4.2. For the alkaline earth cations, the univalent $M(OH)^+$ species were used in the calculations. The ease of cation exchange for different cations is approximately related (inversely) to the binding energy of the cation (M_I or M_{II}), which is calculated according to equation (4.1). The binding energy of the cations (M_I) to the zeolite

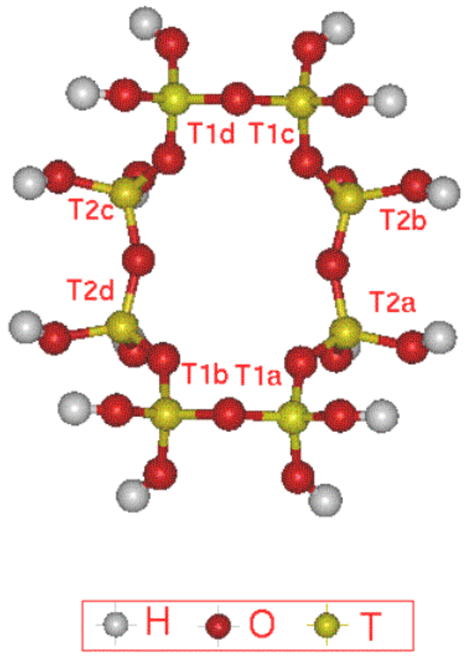

Fig. 4.1. Molecular graphics picture of 8-MR cluster of zeolite -LTL considered for *ab initio* calculations.

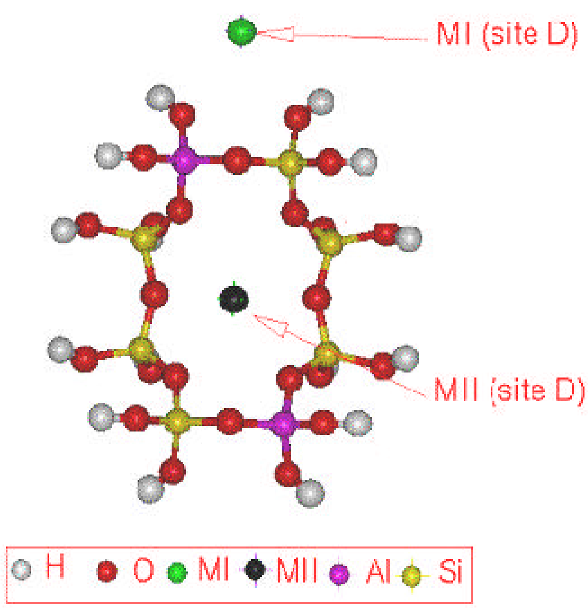

Fig. 4.2. Molecular graphics picture of 8-MR cluster of zeolite-LTL showing the distribution of Si and Al sites as well as extra-framework cations M_I and M_{II}.

Table 4.2. The electronic properties of the cluster model, M-LTL[a]

Alkali metals		Total energy	B.E.[b]	Net charge[c] on
M_I	M_{II}	(a.u.)	(kcal/mol)	M_I / M_{II}
H	-	-414.9823	-179.2367	0.36
Li	-	-414.8107	-169.1741	0.67
Na	-	-414.7877	-154.7412	0.81
K	-	-414.7528	-132.8421	0.87
Rb	-	-414.7815	-150.8610	0.91
Cs	-	-414.7503	-131.2731	0.87
Mg(OH)	-	-431.4606	-127.9067	1.33
Ca(OH)	-	-431.3683	-120.2586	1.66
Sr(OH)	-	-431.2814	-111.5433	1.76
Ba(OH)	-	-431.2150	-65.0826	1.81
-	H	-414.8578	198.5711	0.49
-	Li	-414.7896	-155.9341	0.74
-	Na	-414.7575	-135.7912	0.84
-	K	-414.7815	-150.8510	0.91
-	Rb	-414.7179	-110.9417	0.97
-	Cs	-414.7086	-105.1060	0.97
-	Mg(OH)	-431.5238	-147.5331	1.43
-	Ca(OH)	-431.4183	-151.6092	1.71
-	Sr(OH)	-431.2930	-118.8170	1.78
-	Ba(OH)	-431.2718	-100.6964	1.82

[a] Cluster: $[M_I/M_{II}Si_7AlO_{24}H_{16}]$, where M_I and M_{II} are the cations present in locations I and II of site-D. [b] calculated according to equation (4.1) given in text; [c] Mulliken population (atomic charge).

cluster decreases from H to Cs (except Rb) and Mg(OH) to Ba(OH) (Table 4.2). The results confirm the general observation in zeolite chemistry that the exchange of smaller ions by larger ones (of the same charge) becomes more difficult with increase in the size of the latter ion. The net charge on M_I increases linearly with the size of the cation.

$$B.E.= T.E. \{[M_I/M_{II}Si_7AlO_{24}H_{16}] - \{T.E. [Si_7AlO_{24}H_{16}]^- + T.E. [M_I/M_{II}]^+\} \qquad (4.1)$$

4.3.1.3. Influence of exchanged cations in M_{II} location: Cationic site D is parallel to the 12-MR channel.[24,25] The 8-MR wherein one of the silicon T_1 site is replaced by aluminum and the resulting negative charge is compensated by an extra-framework cation present in site D (M_{II}) [stoichiometry is $M_{II}Si_7AlO_{24}H_{16}$] is shown in Fig. 4.2. The electronic properties of this cluster model, [where M_{II} = Li, Na, K, Rb, Cs, Mg(OH), Ca(OH), Sr(OH) and Ba(OH)] are presented in Table 4.2. In general, from Li to Rb and Mg(OH) to Ba(OH), the net charge increases with the size of the metal ion (except Rb $\cong$ Cs). The binding energy of the cations to the zeolite cluster decreases from Li to Cs and Mg(OH) to Ba(OH). The binding energy of M_{II} with the LTL zeolite cluster is slightly more than for M_I in the case of the alkaline earth ions suggesting a stronger binding (more stable) with the cluster. In general, alkali ions and H^+ appear to be more stable in site D (M_I) than D (M_{II}).

4.3.1.4. Influence of exchanged cations in M_I and M_{II} locations: A cluster model containing six silicon and two Al atoms, so as to simulate the typical composition of LTL with Si/Al = 3 has been chosen for the calculations. In this model, both M_I and M_{II} are present in sites D (Fig. 4.2). Various combinations of alkali and alkaline earth metals have been located in the two cation sites: i) both (M_I and M_{II}) ions are the same (Li to Cs) and ii) keeping M_I as K and changing M_{II} from Li to Cs and Mg(OH) to Ba(OH) (as LTL is generally synthesized in the K-form) (Fig. 4.2). The electronic properties for all the clusters were calculated and are presented in Table 4.3. The binding energies were calculated according to equation (4.2).

$$B.E.= T.E. \{[M_IM_{II}Si_6Al_2O_{24}H_{16}] – \{T.E. [Si_6Al_2O_{24}H_{16}]^{2-} + T.E. [M_I]^+ + [M_{II}]^+\} \quad (4.2)$$

Table 4.3. The electronic properties of the cluster model, M-LTL[a]

Alkali metals		Total energy	B.E.[b]	Net charge[c] on	
M_I	M_{II}	(a.u)	(kcal/mol)	M_I	M_{II}
H	H	-413.4231	-357.2521	0.42	0.38
Li	Li	-413.3554	-317.0058	0.72	0.68
Na	Na	-413.2983	-342.1129	0.75	0.81
K	K	-413.2296	-299.0036	0.86	0.85
Rb	Rb	-413.2477	-310.3614	0.87	0.91
Cs	Cs	-413.2129	-288.5244	0.88	0.88
K	Li	-413.2762	-328.2762	0.72	0.67
K	Na	-413.2500	-311.8047	0.73	0.83
K	K	-413.3396	-299.0036	0.75	0.96
K	Rb	-413.2455	-308.9810	0.86	0.91
K	Cs	-413.2193	-292.5405	0.86	0.88
K	Mg(OH)	-429.9658	-266.9385	0.95	1.40
K	Ca(OH)	-429.8014	-265.4952	0.95	1.69
K	Sr(OH)	-429.7880	-236.5675	0.96	1.76
K	Ba(OH)	-429.7432	-226.2765	0.96	1.82

[a] Cluster: $[M_IM_{II}Si_6Al_2O_{24}H_{16}]$ where M_I and M_{II} are the cations present in site D (details of this cluster are shown in Figs. 2.20 and 4.2); [b] Binding energy calculated according to equation (4.2) given in text; [c] Mulliken population (atomic charge).

When both M_I and M_{II} are the same, the binding energy of the alkali metals increases with increasing size of the ion from Li to K. It decreases in the case of Rb and increases again for Cs (Table 4.3). When M_I is K, the binding energy increases steadily with increasing size of the alkali and alkaline earth ions (Table 4.3). The net charge on M_I and M_{II} also increase down the row (Table 4.3), the increase being less marked for M_I. The charge on the metal ion increases more in the case of M_{II}, especially for the alkaline earth ions.

4.3.1.5. Electronic structure of Pt in the vicinity of M_{II}: A single platinum atom has been located inside the M-LTL cluster [$Pt:M_IM_{II}Si_6Al_2O_{24}H_{16}$] by a suitable cluster model (shown in Fig. 4.3). Given the large size of the platinum atom (2.77 Å), it can be present only inside the 12-MR channels. The platinum atoms present inside the 12-MR channel are easily accessible to the diffusing reactant (*n*-hexane) molecule. The distance between the Pt and M is fixed as the sum of the radii of Pt and the alkali metal cation. The electronic properties were derived, systematically by varying M_{II} from H, Li to Cs and Mg(OH) to Ba(OH) and locating a single Pt atom above the cation. The binding energy of Pt or Pt_5 with the M-LTL cluster was calculated from equation (4.3).

$$B.E.=T.E.\ [Pt/Pt_5:M_IM_{II}Si_6Al_2O_{24}H_{16}]-\{T.E.\ [M_IM_{II}Si_6Al_2O_{24}H_{16}] +T.E.\ [Pt/Pt_5]\} \qquad (4.3)$$

When a single Pt atom is located in the LTL cluster model, the trend in binding energy correlates with the binding energy of the alkali metal to the zeolite cluster, that is it decreases with increasing size of the cation (Table 4.4). The electron density on platinum increases as the cation varies from Li to Cs and Mg(OH) to Ba(OH), indicating a decrease in transfer of electrons from Pt to the support with cation size. In some cases, there is an actual net transfer of electronic charge from the support to the Pt (Table 4.4). The electronic properties of Pt were extremely sensitive to the distance between Pt and the LTL surface. The electron density of platinum in these models increases in the order, Li < Na < K < Rb < Cs and Mg(OH) < Ca(OH) < Sr(OH) < Ba(OH).

Table 4.4. The electronic properties of the cluster model, Pt-M-LTL[a]

Cations M_I	Cations M_{II}	Total energy (a.u)	B. E.[b] (kcal/mol)	Net charge[c] on M_I	Net charge[c] on M_{II}	Net charge[c] on Pt
H	H	-532.1657	-13.4578	0.51	0.32	0.56
Li	Li	-532.1657	-8.9105	0.70	0.44	0.33
Na	Na	-532.0647	-4.6435	0.73	0.79	0.10
K	K	-532.0293	-2.5687	0.80	0.79	0.02
Rb	Rb	-532.0571	-2.5180	0.82	0.86	-0.08
Cs	Cs	-532.0162	-0.6902	0.82	0.92	-0.18
K	Li	-532.1102	-7.1234	0.79	0.56	0.19
K	Na	-532.0831	-2.9312	0.80	0.78	0.08
K	Rb	-532.0545	-2.5321	0.81	0.86	0.02
K	Cs	-532.0317	-2.3954	0.80	0.89	-0.01
K	Mg(OH)	-548.8214	-33.4818	0.95	1.20	0.22
K	Ca(OH)	-548.7344	-25.5816	0.96	1.37	0.18
K	Sr(OH)	-548.6359	-22.3839	0.96	1.60	0.09
K	Ba(OH)	-548.5688	-14.6718	0.96	1.74	0.07

[a] Cluster: $[Pt{:}M_IM_{II}Si_6Al_2O_{24}H_{16}]$, where M_I and M_{II} are the cations present in site D (details of this cluster are shown in Figs. 2.20 and 4.3); [b] Binding energy of the Pt atom to the cluster is calculated according to equation (4.3) given in text; [c] Mulliken population (atomic charge).

4.3.1.6. Electronic structure of Pt_5 in the vicinity of M_{II}: The cluster model with the stoichiometry $[Pt_5{:}M_IM_{II}Si_6Al_2O_{24}H_{16}]$ is shown in Fig. 4.4. The electronic properties of $[Pt_5{:}M_IM_{II}Si_6Al_2O_{24}H_{16}]$ were derived by systematically varying M_I and M_{II} as described in section 4.3.1.2 and 4.3.1.3. The binding energy of Pt_5 in $[Pt_5{:}M_IM_{II}Si_6Al_2O_{24}H_{16}]$ clusters was again calculated according to equation (4.3). The results of the calculations are presented in Table 4.5.

The following observations are made from the results given in Table 4.5. The positive charge on M_I is in the order Li < Na < K < Cs < Rb and on M_{II} also it increases from Li to Rb (~ Cs) when the same element occupies M_I and M_{II} positions. When M_I is kept as K and M_{II} is varied from Li to Cs, the charge on M_{II} increases in the order, Li > Na > K > Rb > Cs. The positive charge on M_{II} in the case of the alkaline earth metals is in the order, Mg(OH) ~ Ca(OH) < Sr(OH) < Ba(OH) (where M_I is K).

Table 4.5. Electronic properties of the cluster model, Pt_5-M-LTL[a]

Alkali metals M_I	Alkali metals M_{II}	Total energy (a.u)	B. E.[b] (kcal/mol)	Net charge[c] on M_I	Net charge[c] on M_{II}	Net charge[c] on Pt[d]
H	H	-1007.7687	-37.6727	0.34	0.64	0.60
Li	Li	-1007.4354	-38.9477	0.24	0.73	0.39
Na	Na	-1007.3933	-36.3322	0.51	0.83	0.31
K	K	-1007.3791	-32.0732	0.58	0.87	0.02
Rb	Rb	-1007.3857	-31.3851	0.70	0.93	0.00
Cs	Cs	-1007.3409	-24.4947	0.59	0.97	-0.01
K	Li	-1007.3926	-36.335	0.51	0.76	0.10
K	Na	-1007.3550	-32.7355	0.52	0.87	0.03
K	Rb	-1007.3873	-31.2403	0.63	0.93	0.00
K	Cs	-1007.3474	-27.7355	0.69	0.97	-0.01
K	Mg(OH)	-1024.1416	-54.6553	0.90	0.97	0.31
K	Ca(OH)	-1024.0527	-57.8555	0.92	1.36	0.20
K	Sr(OH)	-1023.9598	-58.1573	0.93	1.57	0.01
K	Ba(OH)	-1023.8995	-55.4310	0.96	1.48	-0.02

[a] Cluster: [Pt_5:$M_IM_{II}Si_6Al_2O_{24}H_{16}$], where M_I and M_{II} are the cations present in site D (details of this cluster are shown in Fig. 4.5). A Pt_5 cluster-representing [111] plane of platinum is placed above site M_{II}; [b] Binding energy calculated according to equation (4.3) given in text; [c] Mulliken population (atomic charge) and [d] Average charge per Pt atom in Pt_5 cluster.

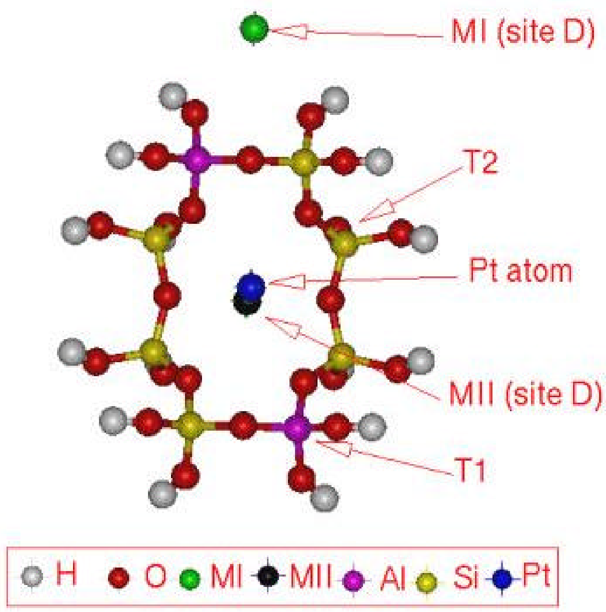

Fig. 4.3. Molecular graphics picture of 8-MR cluster of LTL showing the locations of T sites; a single Pt atom is placed over M_{II} site.

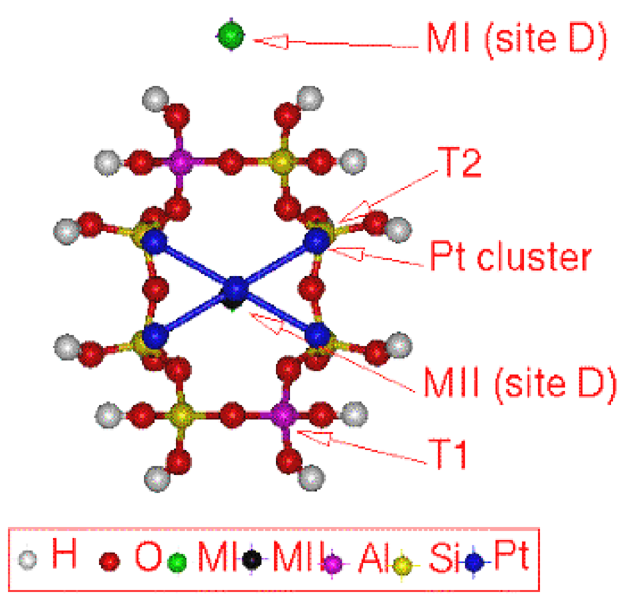

Fig. 4.4. Molecular graphics picture of 8-MR cluster of zeolite-LTL. This picture also shows the Pt_5 cluster above the 8-MR in the energetically favorable parallel orientation.

The charge on M_I (K) is affected when M_{II} are alkali metal ions and not when they are alkaline metal ions. The important observation is that the average electron density per platinum atom increases as the extra-framework cation varies from Li to Cs, indicating less transfer of electrons from Pt_5 to a more basic support. When M_I is K [and M_{II} is Cs or Ba(OH)], the charge on Pt is negative suggesting that there is electron transfer from the support to the Pt_5 cluster. The binding energies of the clusters decrease, as already reported, with increase in the size of the cation. The binding energy of Pt_5 when M_I is K and M_{II} is Ba(OH) is more than when M_I and M_{II} are Cs. Interestingly, it is observed that the dispersion of platinum is more over the Ba exchanged LTL samples containing both Ba and K ions (chapter 2; section 2.3.10).

4.3.1.7. Behavior of adsorbed benzene over Pt-M-LTL: Molecular graphics pictures of benzene adsorbed on Pt_5-LTL are shown in Fig. 4.5 and 4.6 in two views (90° Y-rotation). The distance between platinum and benzene was optimized and the most favorable distance was found to be 3.75 Å. The binding energy of the C_6H_6 or H_2S molecule with the Pt-zeolite clusters was calculated according to the equation (4.4).

$$B.E.=T.E.[C_6H_6/H_2S:Pt_5:M_IM_{II}Si_6Al_2O_{24}H_{16}]-\{T.E.[Pt_5:M_IM_{II}Si_6Al_2O_{24}H_{16}]+T.E.[C_6H_6/H_2S]\} \quad (4.4)$$

Electronic properties of the model clusters were calculated for various combinations of M_I and M_{II} (Table 4.6). The binding energy of benzene with the cluster decreases with increasing size and electropositive nature of the alkali ions in the case of LTL in the order, Li > Na > K > Rb > Cs and Mg(OH) > Ca(OH) > Sr(OH) > Ba(OH). This suggests that desorption of benzene from the Pt_5 cluster is easier when the support is more basic. This is probably one of the reasons for the high benzene selectivity observed when Pt is supported on basic materials. Comparing the charge on Pt in the presence and absence of adsorbed benzene (Table 4.5 and 4.6), it is found to be smaller when benzene is adsorbed revealing the donation of electronic charge by benzene to Pt. In the case of K, Rb and Cs (M_I and M_{II}), the charge on Pt is negative. Again, when M_I is K and M_{II} is Cs, Sr or Ba, the charge on Pt is also negative. Calculations for benzene on unsupported Pt_5 (C_6H_6: Pt_5; last row in Table 4.6) also reveal a slightly negative charge on Pt. The B.E. of benzene with neat Pt_5 is more than with supported Pt_5.

Table 4.6. Electronic properties of the cluster model, C_6H_6-Pt_5-M-LTL[a]

Alkali metals		Total energy	B. E.[b]	Net charge [c] on		
M_I	M_{II}	(a.u)	(kcal/mol)	M_I	M_{II}	Pt[d]
H	H	-1043.7682	-12.3471	0.34	0.65	0.05
Li	Li	-1043.7085	-8.0190	0.51	0.73	0.05
Na	Na	-1043.6927	-5.6031	0.57	0.92	0.02
K	K	-1043.6911	-3.9120	0.58	0.95	0.02
Rb	Rb	-1043.6959	-1.4645	0.70	0.97	-0.01
Cs	Cs	-1043.6438	-0.9551	0.72	0.98	-0.03
K	Li	-1043.7026	-5.3922	0.23	0.95	0.08
K	Na	-1043.6961	-4.1382	0.48	0.96	0.02
K	Rb	-1043.6941	-3.3858	0.48	0.97	0.00
K	Cs	-1043.6541	-3.3231	0.51	0.98	-0.02
K	Mg(OH)	-1060.4496	-4.1382	0.81	1.03	0.02
K	Ca(OH)	-1060.3571	-1.8810	0.81	1.41	0.01
K	Sr(OH)	-1060.2634	-1.3794	0.83	1.57	-0.01
K	Ba(OH)	-1060.2051	-2.6334	0.84	1.49	-0.04
C_6H_6: Pt_5		-630.3878	-5.5918	-	-	-0.01

[a] Cluster: [Pt_5:C_6H_6:$M_IM_{II}Si_6Al_2O_{24}H_{16}$], where M_I and M_{II} are the cations present in site D (details of cluster is shown in Figs. 4.5. and 4.6). Benzene is placed parallel to Pt_5; [b] Calculated according to equation (4.4) given in text; [c] Mulliken population (atomic charge) and [d] Average charge per Pt atom in Pt_5 cluster.

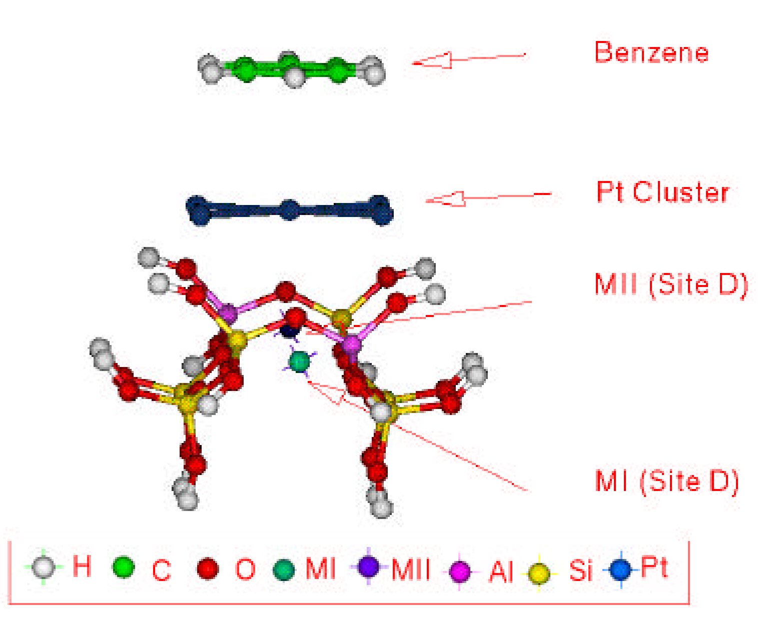

Fig. 4.5. Molecular graphics view of C_6H_6 adsorbed on Pt_5 in Pt_5: LTL.

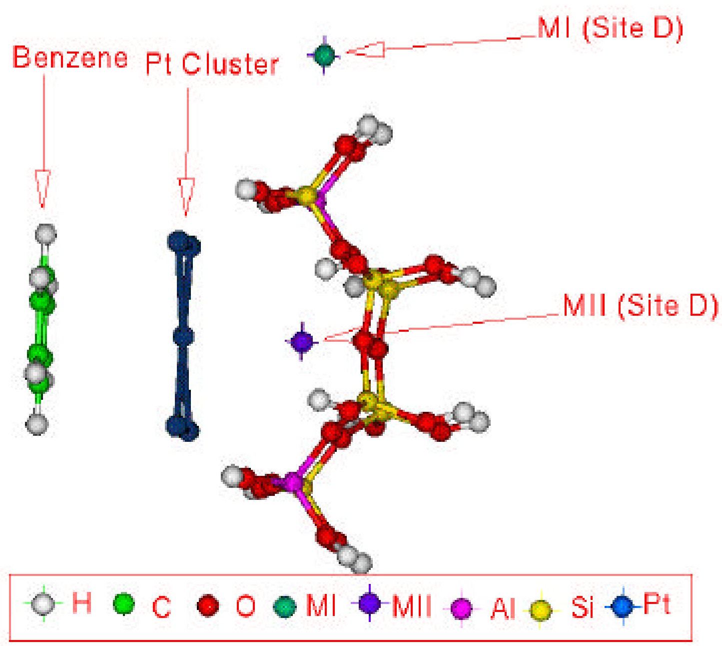

Fig. 4.6. Molecular graphics view of C_6H_6 adsorbed on Pt_5 in Pt_5: LTL, after 90 degrees rotation.

4.3.1.8. Behavior of adsorbed H_2S over Pt-M-LTL zeolite: Molecular graphics picture of H_2S adsorbed on Pt_5-LTL is shown in Fig. 4.7. The distance between the platinum cluster and H_2S was optimized and the most favorable distance was found to be 3.4 Å (chapter 2; section 2.8.3). The binding energy of the H_2S molecule with the Pt-zeolite cluster was calculated according to equation (4.4) (substituting H_2S or C_6H_6) The electronic properties of the model clusters were calculated for various

Table 4.7. Electronic properties of the cluster model of H_2S adsorbed on Pt_5-M-LTL[a]

Cations		Total energy	B.E.[b]	Net charge[c] on			
M_I	M_{II}	(a.u.)	(kcal/mol)	S	Pt[d]	M_I	M_{II}
H	H	-1018.4669	-25.2312	-0.037	0.56	0.64	0.44
Li	Li	-1018.1831	-31.9143	-0.057	0.42	0.42	0.81
Na	Na	-1018.1361	-32.2341	-0.058	0.39	0.52	0.86
K	K	-1018.1276	-30.2312	-0.059	0.23	0.53	0.95
Rb	Rb	-1018.1256	-28.1623	-0.060	0.17	0.57	0.96
Cs	Cs	-1018.0765	-24.7166	-0.062	0.03	0.58	0.98
K	Li	-1018.1523	-38.9654	-0.059	0.27	0.49	0.74
K	Na	-1018.1021	-31.0594	-0.060	0.25	0.43	0.78
K	Rb	-1018.1312	-29.0515	-0.060	0.14	0.44	0.91
K	Cs	-1018.0791	-21.3965	-0.058	0.09	0.50	0.97
K	Mg(OH)	-1034.8942	-34.5104	-0.058	0.34	0.40	1.13
K	Ca(OH)	-1034.8034	-33.3183	-0.059	0.26	0.41	1.27
K	Sr(OH)	-1034.7094	-32.6281	-0.62	0.08	0.45	1.34
K	Ba(OH)	-1034.6439	-29.3339	-0.072	0.05	0.45	1.44
	H_2S	-10.6976	-	0.019	-	-	-

[a] Cluster:[Pt_5:H_2S:$M_IM_{II}Si_6Al_2O_{24}H_{16}$], where M_I and M_{II} is the alkali metal present in site D. H_2S is adsorbed over Pt_5 and zeolite cluster. Pt_5 cluster representing (111) plane of platinum is placed above site I (Fig. 4.7); [b] calculated according to equation (4.4) given in text; [c] Mulliken population (atomic charge) and [d] Average charge per Pt atom in Pt_5 cluster.

combinations of M_I and M_{II} (Table 4.7). The binding energy of H_2S with the cluster is in general more for the basic supports (containing alkali ions) than for the acidic support (H-LTL). The negative charge on the S atom increases with the basicity of the support. Besides, comparing tables 4.6 and 4.7, the charge on Pt is more positive in the presence of S. The much larger binding energy of S with Pt in basic clusters (compared to H-LTL) suggests a greater poisoning effect of S on Pt over these supports, an observation well documented by earlier workers.[26,27] The withdrawal of electrons from a Pt cluster by S may also cause the Pt to be less active in the aromatization of *n*-hexane in the presence of S.

4.3.1.9. Electron density on Pt and S_{int} of Pt-M-LTL: Earlier researchers have quantified the basicity of ion exchanged zeolites using Sanderson's intermediate electronegativity, S_{int}.[21,27] This parameter gives an average electronegativity value for the cluster under consideration and measures its overall basicity, which increases with decreasing value of S_{int}. As the LTL-zeolite cluster used in these calculations possess different compositions, the S_{int} values of the clusters can also be used to quantify their basicity. Plots of the average charge per Pt atom versus S_{int} (calculated according to Mortier[19]) are presented in Fig. 4.8 for the Pt_5-LTL clusters. The plots reveal the general trend of decreasing charge (increasing electron density) on Pt with decreasing S_{int} suggesting decreasing electron transfer from Pt to the support with increase in support basicity. In fact, in the case of K-LTL and Ba-K-LTL, the charge on Pt is negative (electron rich) suggesting a reverse electron transfer. The plots are different for the alkali and alkaline earth ions. The S-shaped plots point out that small changes in S_{int} of the support can cause a substantial change in the electron density of Pt in a limited charge region. It appears that it is difficult to increase the charge on Pt above 0.3 – 0.35 or decrease it below 0.05 – 0.1 by altering support basicity.

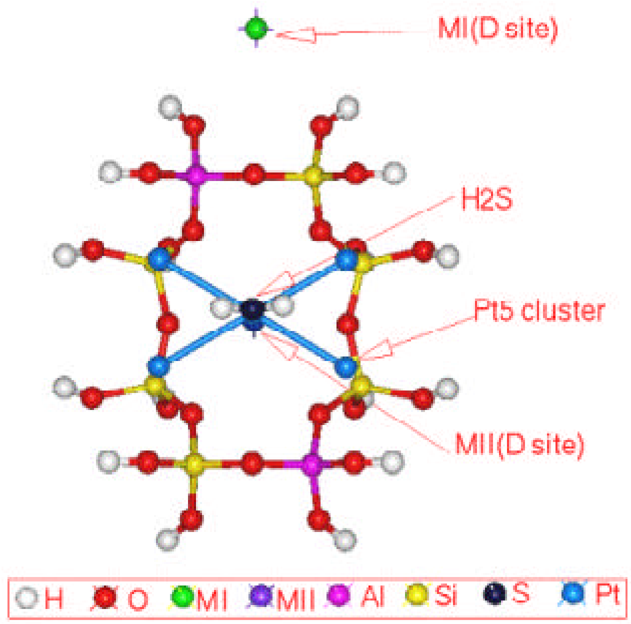

Fig. 4.7. Molecular graphics view of H_2S adsorbed on Pt_5 cluster in Pt_5: LTL.

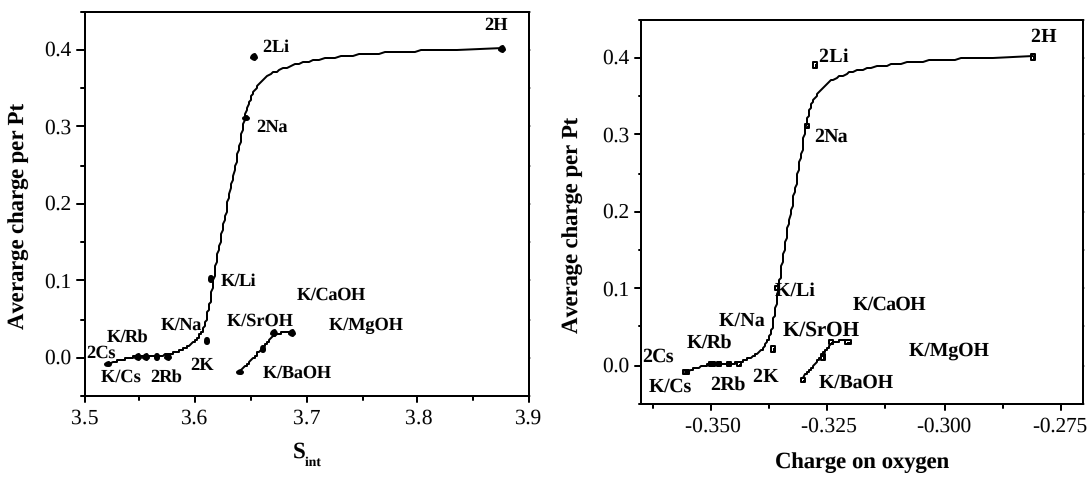

A **B**

Fig. 4.8. In cluster model, M-LTL: relationship between average charge on Pt in Pt_5 cluster and S_{int} (A) and relationship between average charge per Pt and oxygen charge (B).

Similarly, it is also possible to calculate the average charge on oxygen using the Sanderson's intermediate electronegativity principle. A plot of charge on Pt against oxygen charge is presented in Fig. 4.8 B. It is seen that Pt becomes more electron rich with increasing charge on framework oxygen (basicity of support).

4.3.2. Studies on BEA Zeolite:

The BEA zeolite cluster models were generated from the reported crystal structure by Newsam.[28,29] The framework structure of zeolite BEA is shown in Fig. 2.21. The cluster model of BEA and the cation locations are described in chapter 2 (section 2.6.2). A cluster model having the formula [$MSi_9AlO_{30}H_{20}$] (where M = Li, Na, K, Rb, Cs, Mg(OH), Ca(OH), Sr(OH) and Ba(OH)) of polymorph A of zeolite BEA[28] is considered in these studies. A Si/Al ratio of 9 for the cluster, which is close to the typical values found in synthetic zeolites[30] has been chosen. Again, the Al has been located in an energetically favored position in 6-MR. The Pt_5 cluster fitting is described in chapter 2 (section 2.8.1).

4.3.2.1. Location of Al substitution in BEA frame work: The cluster model of BEA used in these studies is shown in Fig. 4.9. The cluster model contains nine Si and one Al atom with 6-MR. The 6-MR consists of one Al and five Si atoms (Fig. 4.9). Different T site locations are present in the 6-MR: $2T_1$, $2T_3$ and $2T_8$ sites. The substitution of Al in above sites has been investigated. The 6-MR, wherein one of the silicon in site T_1 is replaced by aluminum and the resulting negative charge is compensated by an extra-framework cation (M), was chosen for developing the cluster model. The influence of Al substitution in different locations in the cluster model on the total energy of the system has been calculated and the results are presented in Table 4.8. It is found that the T_1 position is slightly more energetically favorable for Al substitution than the other positions (Table 4.8). The T_1 position is accessible through 5, 6 and 12-MR pore openings.[28,32] The extra-framework cation is located in the middle of the 6-MR.

Table 4.8. Aluminum substitution at different T sites in BEA[a]

Al substituted in sites	Total energy (a.u)	Net charge on Al
T_1	-518.4945	1.54
T_3	-518.4844	1.53
T_8	-518.4832	1.52

[a] Cluster: $[Si_9AlO_{30}H_{20}]$ shown in Fig. 4.9.

4.3.2.2. Influence of exchanged cation: A molecular graphics cluster model representing the BEA cluster along with an extra-framework cation is shown in Fig. 4.10. As the Si/Al ratio for zeolite BEA is large (Si/Al > 10), only one Al atom and one cation were located in the cluster so as to be representative of typical BEA. The cation M was varied from Li to Cs and Mg(OH) to Ba(OH). The distance between the cation and oxygen was taken as the sum of the atomic radii of M^+ and O^{2-}. The calculations were carried out for all the above clusters and the results are presented in Table 4.9. As the cation size increases [Li to Cs and Mg(OH) to Ba(OH)], its binding energy decreases linearly except for Rb and Sr(OH). The binding energy of the cluster model is calculated from equation (4.5). The net charge on M increases from H, Li to Rb $\cong$ Cs and Mg(OH) to Ba(OH) (Table 4.9).

$$\text{B.E.} = \text{T.E.}\ [MSi_9AlO_{30}H_{20}] - \{\text{T.E.}\ [Si_9AlO_{30}H_{20}]^- + \text{T.E.}\ [M]^+\} \quad (4.5)$$

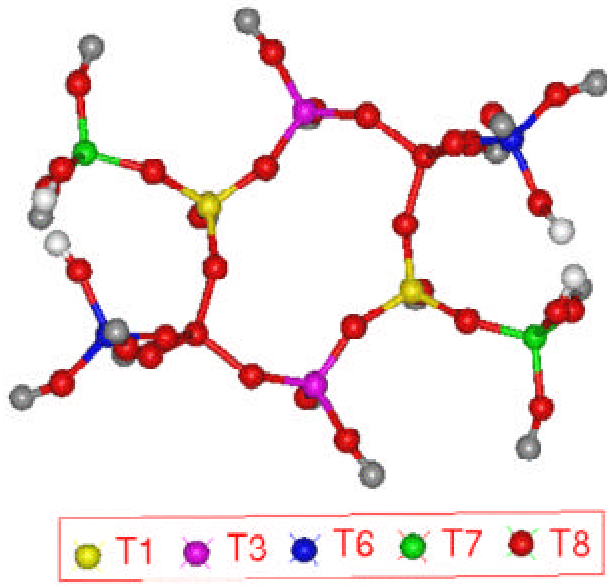

Fig. 4.9. **Six-member ring cluster of zeolite-BEA used in *ab initio* calculations; the location of T sites is shown.**

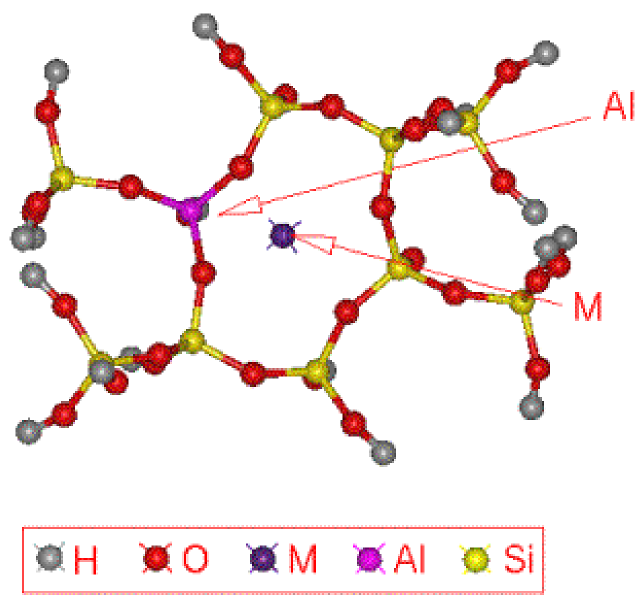

Fig. 4.10. **Molecular graphics picture of 6-MR cluster of zeolite-BEA; the location of the cation is shown.**

Table 4.9. The electronic properties of the cluster model, M-BEA[a]

M	Total energy (a.u.)	B.E.[b] (kcal/mol)	Net charge[c] on M
H	-518.9698	-197.8881	0.50
Li	-518.7650	-169.4780	0.59
Na	-518.7343	-150.2291	0.72
K	-518.7023	-130.1652	0.88
Rb	-518.7155	-138.4421	0.93
Cs	-518.6942	-125.0873	0.93
Mg(OH)	-535.4627	-168.3161	1.39
Ca(OH)	-535.3789	-155.9980	1.62
Sr(OH)	-535.2128	-97.6239	1.79
Ba(OH)	-535.2858	-138.5672	1.85

[a] Cluster: $[MSi_9AlO_{30}H_{20}]$, where M is the alkali metal present in the cationic site; [b] Binding energy is calculated according to equation (4.5) given in text and [c] Mulliken population (atomic charge).

4.2.2.3. Electronic structure of Pt in the vicinity of the cation: The cluster model representing a single platinum atom and the M-BEA cluster that is $[Pt{:}MSi_9AlO_{30}H_{20}]$ is shown in Fig. 4.11. The major pores in zeolite-BEA are 12-MR channels. The alkali metal cations considered in these studies are accessible through 12-MR pore openings. The 6-MR is a little small to accommodate a Pt atom, whereas Pt can be comfortably included in the 12-MR channels. The platinum atoms present inside the 12-MR channels are easily accessible to the diffusing *n*-hexane molecule. Therefore, a single platinum located inside the 12-MR channel has been used in these studies. The electronic properties of the $[Pt{:}MSi_9AlO_{30}H_{20}]$ cluster were derived by systematically varying the cation from H, Li to Cs and Mg(OH) to Ba(OH) and keeping a single Pt over it. The binding energy of Pt or Pt_5 with the M-BEA cluster was calculated from equation (4.6).

$$B.E. = T.E.\ [Pt/Pt_5{:}MSi_9AlO_{30}H_{20}] - \{T.E.\ [MSi_9AlO_{30}H_{20}] + T.E.\ [Pt/Pt_5]\} \quad (4.6)$$

When a single platinum atom is deposited over the BEA cluster, the trend of binding energy is similar to that obtained over the zeolite cluster without Pt; there is a general decrease in binding energy with increasing cation size. The relatively small binding energy of Pt suggests that the platinum atom is rather loosely bound to the zeolite cluster. The interaction of Pt with M-BEA decreases with the electropositive nature of the exchanged ion from Li to K and Cs; the interaction is slightly larger for Rb. Similarly, a decrease in interaction is noticed on going from Mg to Ba. The electron density on platinum increases as the extra-framework cation varies from Li to Cs and Mg(OH) to Ba(OH). The charge on Pt suggests a decreasing transfer of electrons from the Pt to the support with increase in basicity (Table 4.10). The electronic charge on platinum is negative when M = Cs and Ba(OH) indicating electron transfer from the zeolite cluster to Pt.

4.3.2.4. Electronic structure of Pt_5 in the vicinity of the cation: The molecular graphics visualization of the location of the Pt_5 cluster and the segment of the BEA-framework used as the cluster model is shown in Fig. 4.12. The electronic properties of the Pt_5-BEA cluster calculated from this model are presented in Table 4.10. The platinum cluster is assumed to be in the 12-MR channel in BEA zeolite. The average net electron charge on platinum (electropositivity) decreases (electron density on Pt increases) as the alkali metal cation size increases from Li to Cs (Table 4.10) and also from Mg(OH) to Ba(OH). The binding energy of the platinum atoms with the zeolite cluster decreases down the row from Li to Rb and Mg to Ba. The order of the binding energy is Li > Na > K > Cs and Mg(OH) > Ca(OH) > Sr(OH) > Ba(OH). The net electron charge on alkali metal increases from Li to Rb and Mg(OH) to Ba(OH). The

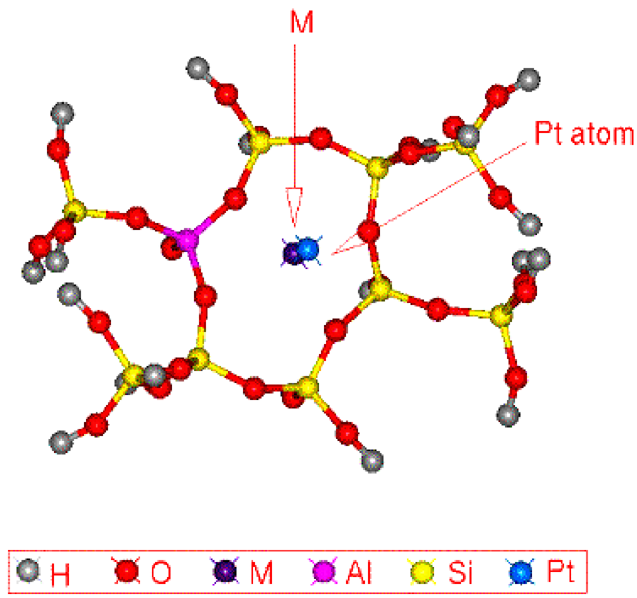

Fig. 4.11. Molecular graphics picture of 6-MR cluster of zeolite-BEA; the location of cation and Pt are shown.

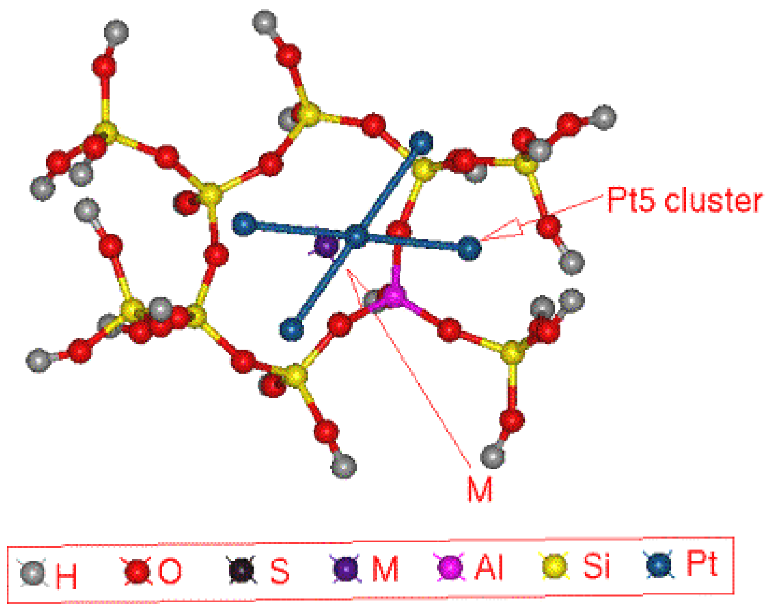

Fig. 4.12. Molecular graphics picture of the Pt_5-BEA cluster model. This picture shows the Pt_5 cluster above the 6-MR in the energetically favorable parallel orientation.

Table 4.10. The electronic properties of the cluster model, Pt/ Pt_5-BEA[a]

Cluster	$[Pt:MSi_9AlO_{30}H_{20}]$				$[Pt_5:MSi_9AlO_{30}H_{20}]$			
M	Total energy (a.u.)	B.E. [b] (kcal/mol)	Net charge[c] on M	Net charge[c] on Pt[a]	Total energy (a.u.)	B.E.[b] (kcal/mo)	Net charge[c] on M	Net charge[c] on Pt[a]
H	-637.6201	-15.3040	0.73	0.04	-1112.8560	-41.4512	0.34	0.42
Li	-637.5761	-5.2041	0.32	0.33	-1112.8441	-33.0120	0.20	0.18
Na	-637.5412	-2.5707	0.66	0.14	-1112.8365	-31.4833	0.34	0.11
K	-637.5005	-2.5081	0.81	0.02	-1112.8228	-22.4017	0.47	0.04
Rb	-637.5231	-3.5739	0.87	0.01	-1112.8421	-26.9198	0.71	0.02
Cs	-637.4943	-1.5675	0.92	-0.002	-1112.8133	-22.0838	0.61	0.00
Mg(OH)	-654.2853	-12.7908	1.13	0.12	-1129.5778	-28.4321	1.19	0.04
Ca(OH)	-654.2000	-11.8503	1.42	0.05	-1129.4734	-24.7831	1.36	0.03
Sr(OH)	-654.0323	-10.8471	1.54	0.02	-1129.3621	-25.1134	1.47	0.02
Ba(OH)	-654.1027	-9.2169	1.65	-0.001	-1129.2311	-24.1892	1.63	-0.01

[a] Cluster: $[Pt/Pt_5:MSi_9AlO_{30}H_{20}]$, where M is the alkali metal present in the cationic site, Pt and Pt_5 cluster representing (111) plane of platinum is placed above cationic site (Fig. 4.11 and 4.12, respectively); [b] Binding energy is calculated according to equation (4.6) given in text; [c] Mulliken population (atomic charge) and [d] Average charge per Pt atom in Pt_5 cluster.

net charge on alkali metal in the cluster is less positive compared to the earlier investigated single platinum cluster. Platinum atoms are more electron rich down the row (Table 4.11). Platinum atoms in the Ba(OH) exchanged cluster posses a negative charge indicating that the zeolite cluster donates electrons to the platinum atoms.

4.3.2.5. Behavior of adsorbed benzene over Pt-M-BEA: Molecular graphics pictures of benzene adsorbed on Pt_5-BEA are shown in Figs. 4.13 and 4.14 in two views (90°, X- rotation). The binding energy of the C_6H_6 molecule with Pt-zeolite clusters was calculated according to equation (4.7). Electronic properties of the model clusters were calculated for various cations (Table 4.11).

$$B.E.=T.E.[C_6H_6{:}Pt_5{:}MSi_9AlO_{30}H_{20}] - \{T.E.[Pt_5{:}MSi_9AlO_{30}H_{20}] + T.E.(C_6H_6)\} \qquad (4.7)$$

Table 4.11. The electronic properties of the cluster model of C_6H_6-Pt_5-BEA[a]

M	Total energy (a.u.)	B.E. [b] (kcal/mol)	Net charge [c] on Pt[a]	Net charge [c] on M
H	-1149.1711	-8.5899	0.45	0.08
Li	-1149.1546	-5.7057	0.23	0.06
Na	-1149.1451	-4.5144	0.45	0.05
K	-1149.1297	-3.4485	0.51	-0.02
Rb	-1149.1456	-1.3167	0.59	-0.04
Cs	-1149.1166	-1.1913	0.61	-0.006
Mg(OH)	-1165.9133	-8.8407	1.15	0.141
Ca(OH)	-1165.7802	-3.3858	1.23	0.008
Sr(OH)	-1165.6671	-2.2572	1.29	-0.001
Ba(OH)	-1165.5387	-3.8874	1.40	-0.005

[a] Cluster: $[C_6H_6{:}Pt_5{:}MSi_9AlO_{30}H_{20}]$, where M is the alkali metal present in the cationic site. Pt_5 cluster representing (111) plane of platinum is placed above site I (Fig 4.13 and 4.14); [b] BE calculated according to equation (4.7) given in text; [c] Mulliken population (atomic charge) and [d] Average charge per Pt atom in Pt_5 cluster.

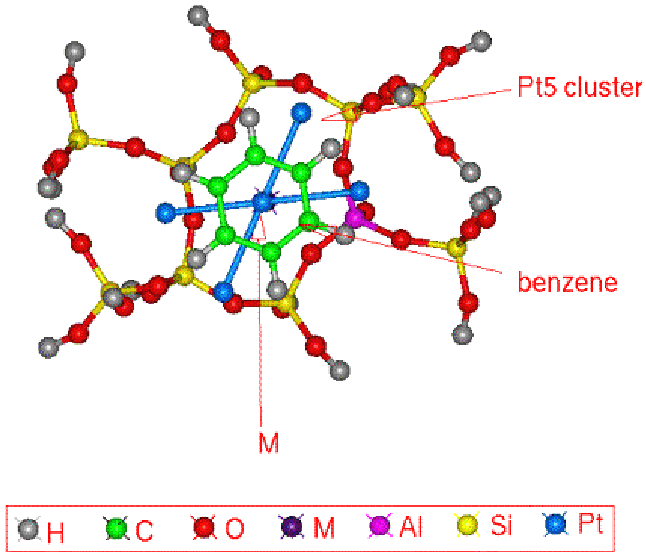

Fig. 4.13. Molecular graphics view of C_6H_6 adsorbed on Pt_5 cluster in Pt_5: BEA.

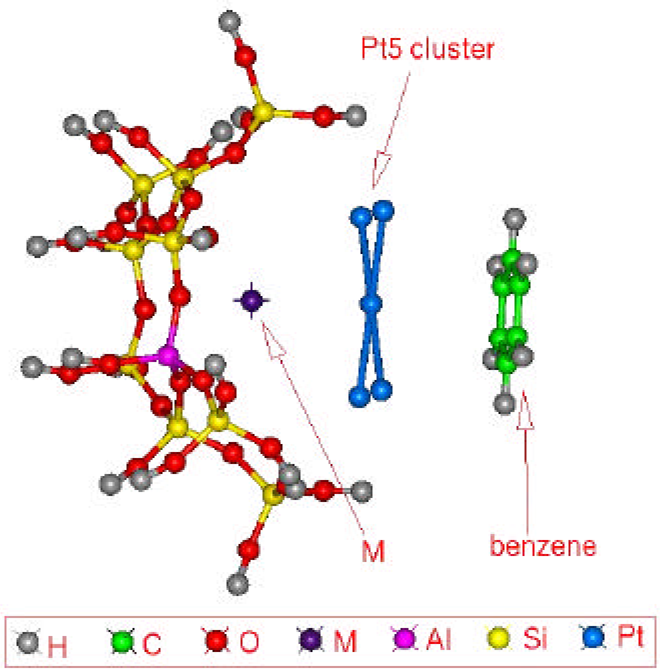

Fig. 4.14. Molecular graphics view of C_6H_6 adsorbed on Pt_5 cluster in Pt_5: BEA after rotation of cluster by 90 degrees.

The binding energy of benzene with the cluster decreases with increasing size and electropositive nature of the alkali and alkaline earth metal cations in BEA zeolite. The binding energy decreases from Li to Cs and Mg(OH) to Ba(OH). The results are similar those obtained over Pt:LTL clusters

4.3.2.6. Electron density on Pt and S_{int} of Pt-M-BEA: Plots of the average charge per Pt atom versus S_{int} (calculated according to Mortier[19]) are presented in Fig. 4.15 for Pt_5-BEA clusters. The S_{int} values for M-BEA are in the range of ~ 3.55 to 3.75 and Pt charge between 0.01 to 0.34. The plot reveals the general trend of decreasing charge (increasing electron density) on Pt with decreasing S_{int} suggesting a decreasing electron transfer from Pt to the support with increasing support basicity. In the case of Ba-BEA, the charge on Pt is negative (electron rich) suggesting a reverse electron transfer. The S-shaped plots point out that small changes in S_{int} of the support can cause substantial change in the electron density of Pt in a limited charge region.

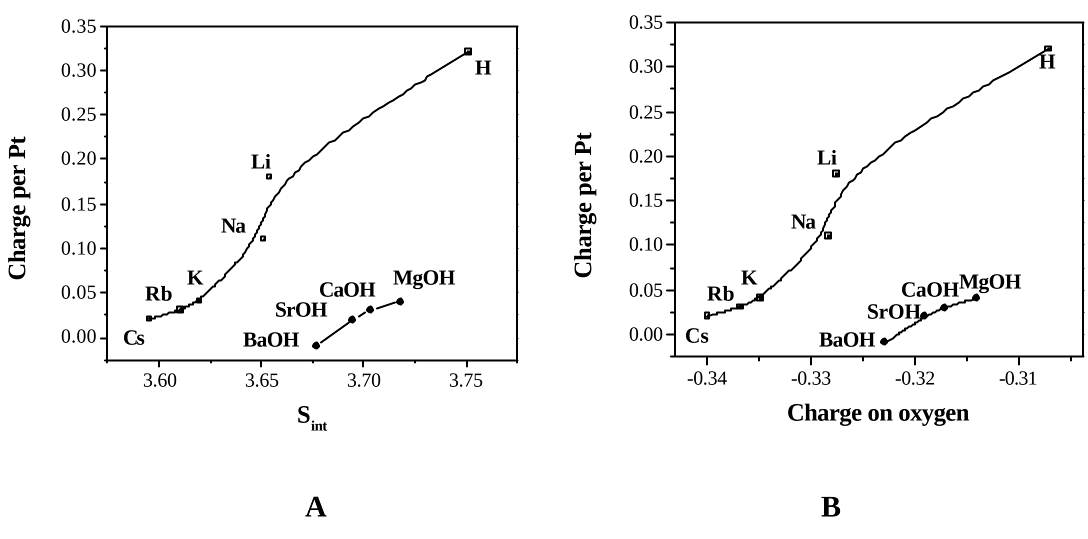

Fig. 4.15. A) In the cluster model, M-BEA: relationship between average charge on Pt in Pt_5 cluster and S_{int} and

(B) relationship between average charge per Pt and oxygen charge.

4.3.3. Studies on FAU Zeolite:

The details of the cluster model generated for FAU zeolite are presented in chapter 2 (section 2.6.3). The studies on this model are presented below.

4.3.3.1. Location of Al substitution in FAU framework: A cluster model representing 6-MR of zeolite FAU structure containing one Al either in T_1 or T_2 location was generated. Initially one T site was substituted with one Al atom. The T_1 site is the most energetically favorable one (Table 4.12). On the other hand when another Al atom is substituted in T_1 or T_2 site, two possible distributions of the two aluminum atoms in 6-MR as allowed by the Löwenstein are possible.[31,32] These have been considered. It was observed that the presence of two Al atoms at the farthest positions is energetically the most favored arrangement. The excess negative charge of the cluster with two Al atoms was compensated by two cations (M_I and M_{II}) located at sites I and II, respectively (Figs. 4.16 and 4.17).

Table 4.12: Substitution of Al in T sites of FAU[a]

Location	Total energy (a.u.)	Charge on[b] Al
T_1	-310.4727	1.55
T_1, 1 and 3	-308.6431	1.55
T_1, 1 and 4	-308.6565	1.55

[a] Cluster: $[Si_5AlO_{18}H_{12}]$ T-sites are shown in Fig. 4.16 and [b] Mulliken population (atomic charge).

4.3.3.2. Influence of exchanged cations in M_I and M_{II} locations: Here the presence of two Al atoms in the 6-MR are considered. This leads to the occupation of two cations at sites I and II as shown in Fig. 4.17. This cluster model represents a Si/Al ratio of 2, a value close to that of typical synthetic FAU (Si/Al ~ 2.4 - 2.6). Isomorphous substitution of Si by Al is assumed in T_1 and T_2 sites. As FAU is generally synthesized in the Na-form, M_I was kept as Na and M_{II} was varied (Li to Cs and Mg to Ba). Again, sets of calculations were also done with the same element in M_I and M_{II} sites (Li, Na and K). However, as ions larger than K cannot occupy M_I sites (inside hexagonal prisms) due to size constraints, calculations were done with H^+ in site M_I for Cs and Rb. As the cation size increases, the binding energy with the cluster

Table 4.13. The electronic properties of the cluster model, M-FAU[a]

Alkali metals		Total energy	B. E.[b]	Net charge on[c]	
M_I	M_{II}	(a.u.)	(kcal/mol)	M_I	M_{II}
H	H	-309.3972	-512.2281	0.64	0.74
Li	Li	-309.2468	-370.4133	0.66	0.66
Na	Na	-309.1949	-337.8461	0.75	0.85
K	K	-309.1270	-295.2392	0.88	0.92
H	Rb	-309.3449	-472.1944	0.62	0.94
H	Cs	-309.3155	-454.6242	0.62	0.93
Na	Li	-309.2107	-347.7612	0.66	0.82
Na	Na	-309.1949	-337.8461	0.85	0.88
Na	K	-309.1622	-317.3272	0.81	0.89
Na	Rb	-309.1854	-331.8853	0.82	0.93
Na	Cs	-309.1537	-311.9933	0.81	0.94
Na	Mg(OH)	-325.9123	-293.9837	0.80	1.39
Na	Ca(OH)	-325.8449	-392.2080	0.81	1.63
Na	Sr(OH)	-325.7790	-291.5365	0.81	1.78
Na	Ba(OH)	-325.6793	-246.7957	0.81	1.73

[a] Cluster:[$M_IM_{II}Si_4Al_2O_{18}H_{12}$] where M_I is the alkali metal present in the cationic site I and M_{II} is alkali metal present in the site II (Fig. 4.17); [b] Binding energy calculated according to equation (4.8) given in text and [c] Mulliken population (atomic charge).

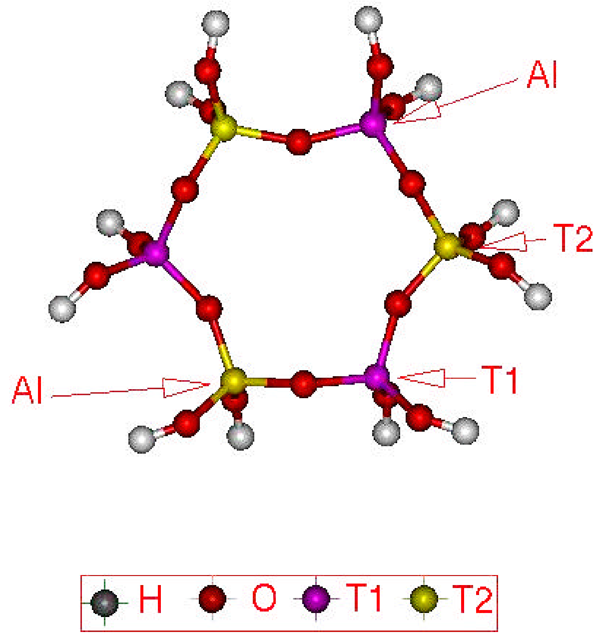

Fig. 4.16. Molecular graphics picture of 6-MR cluster of zeolite-FAU showing location of T sites.

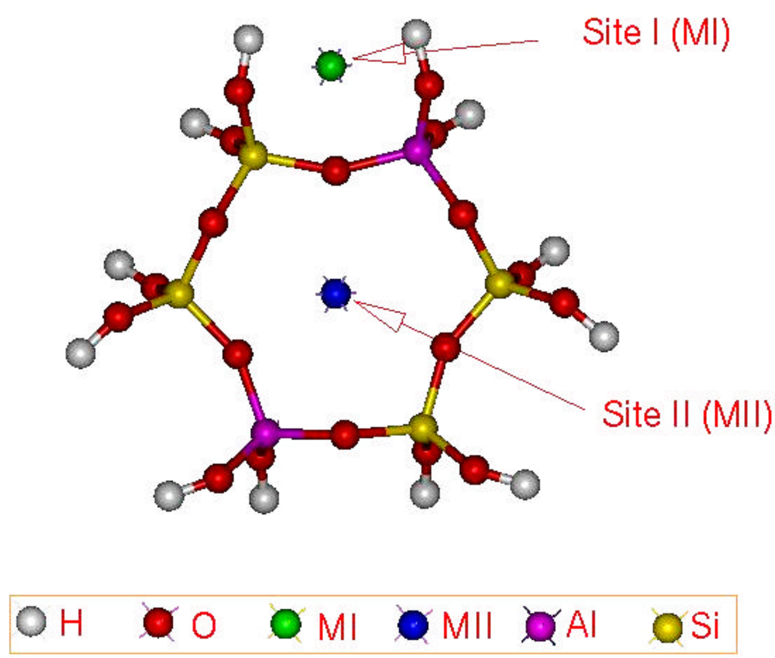

Fig. 4.17. Molecular graphics picture of 6-MR cluster of zeolite -FUA; the location of the two cations is shown.

decreases (becomes more positive; Table 4.13). Again, the net charge on M_I increases with the size of the ion (Table 4.13). The net charge on M_I is the same when it is Na and M_{II} is varied from Li to Cs and Mg to Ba.

$$B.E.= T.E.[M_IM_{II}Si_4Al_2O_{18}H_{12}] – \{T.E. [Si_4Al_2O_{18}H_{12}]^{2-} + T.E. [M_I^+ \text{ and } [M_{II}]^+\} \quad (4.8)$$

4.3.3.3. Electronic structure of Pt in the vicinity of M_{II}: A cluster model representing a 6-MR and a Pt atom in the α-cage encompassing sites I and II for extra-framework cations is shown in Fig. 4.18. The cation at M_I was varied from H to K and

Table 4.14: The electronic properties of the cluster model, Pt-M-FAU[a]

Alkali metals		Total energy	B. E.[b]	Net charge on[c]		
M_I	M_{II}	(a.u.)	(kcal/mol)	M_I	M_{II}	Pt
H	H	-428.4756	-438.0901	0.34	0.48	0.600
Li	Li	-428.0547	-373.9811	0.42	0.67	0.351
Na	Na	-427.9927	-335.0770	0.65	0.83	0.162
K	K	-427.9161	-287.0122	0.73	0.93	0.021
H	Rb	-428.2164	-475.4461	0.48	0.85	0.019
H	Cs	-428.1843	-455.3043	0.48	0.89	0.004
Na	Li	-428.0179	-350.8901	0.79	0.73	0.352
Na	K	-427.9592	-314.0570	0.80	0.82	0.017
Na	Rb	-427.9907	-333.8220	0.82	0.87	0.012
Na	Cs	-427.9559	-311.9861	0.81	0.95	0.001
Na	Mg(OH)	-444.7379	-333.6971	0.70	1.09	0.110
Na	Ca(OH)	-444.6616	-356.0982	0.72	1.40	0.051
Na	Sr(OH)	-444.5960	-360.7424	0.81	1.65	0.014
Na	Ba(OH)	-444.5944	-354.9061	0.82	1.76	0.008

[a] Cluster:$[Pt:M_I/M_{II}Si_4Al_2O_{18}H_{12}]$ where M_I present in the cationic site I and M_{II} is present in the site II (Fig. 4.18). Pt atom is placed over the cationic site II; [b] B.E. calculated according to equation (4.9) given in text and [c] Mulliken population.

M_{II} was varied from H to Cs and Mg(OH) to Ba(OH). Again M_{II} was varied from Li to Cs and Mg(OH) to Ba(OH) keeping M_I as Na. The results of the calculations carried out on the above cluster are shown in Table 4.14. The binding energy for Pt or Pt_5 with cluster models was calculated from the following equation (4.9).

$$B.E.=T.E.\ [Pt/Pt_5{:}M_IM_{II}Si_4Al_2O_{20}H_{12}] - \{T.E.[M_IM_{II}Si_4Al_2O_{20}H_{12}] + T.E.(Pt/Pt_5)\} \quad (4.9)$$

The binding energy and charge on cations M_I and M_{II} are similar to those reported in the case of the cluster without Pt (Table 4.13). The charges on M_I and M_{II} increase with the basicity of the cations. When M_I is Na and M_{II} varies from Li to Cs, the charge on M_I is less affected compared to M_{II}. The average net electron charge on platinum decreases as the alkali metal cation size increases from Li to Cs and from Mg(OH) to Ba(OH) (Table 4.14). This trend in Pt charge is similar to that observed in the case of LTL and BEA clusters.

4.3.3.4. Electronic structure of Pt_5 in the vicinity of M_{II}: The molecular graphics picture of the cluster as viewed through the supercage is shown in Fig. 2.22. A cluster model representing a 6-MR and a Pt_5 cluster in the α-cage encompassing sites I and II for extra-framework cations is shown in Fig. 4.19. The electronic properties of the Pt_5-FAU were calculated from this model. The cation at M_I was varied from H to K and the cation at M_{II} was varied from H to Cs and Mg(OH) to Ba(OH). The results of the calculations carried out for the above clusters (zeolite: Pt_5) are shown in Table 4.15. The binding energy for this cluster model was calculated from equation (4.9). The changes in binding energy and charge on cations M_I and M_{II} are similar to those reported in the case of the cluster without Pt (Table 4. 13). The average net electron charge on platinum decreases as the alkali metal cation size increases from Li to Cs and from Mg(OH) to Ba(OH) (Table 4.15).

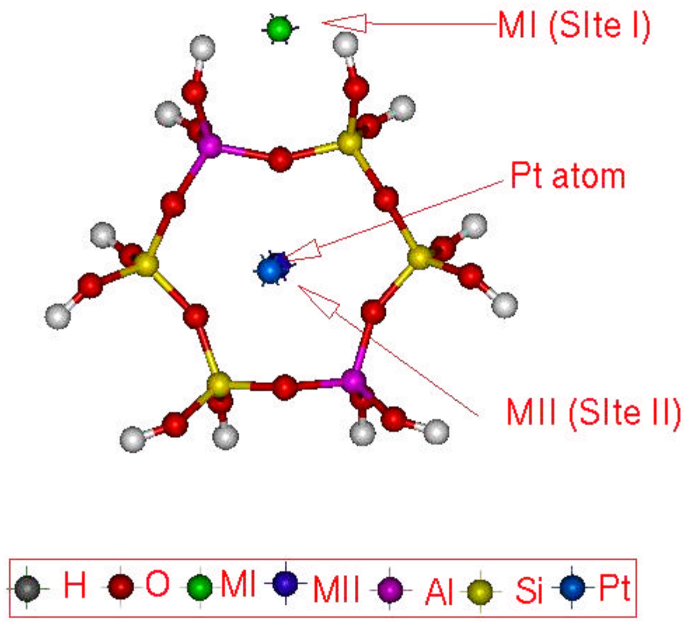

Fig. 4.18. Molecular graphics picture of 6-MR cluster of zeolite-FAU with a Pt above site II.

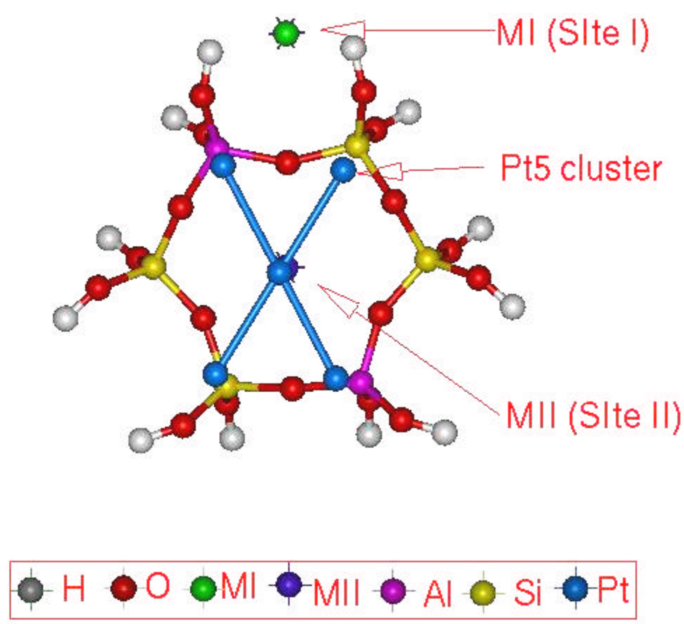

Fig. 4.19. Molecular graphics picture of a 6-MR window in FAU with Pt_5 above site II.

Table 4.15: The electronic properties of the cluster model, Pt_5-M-FAU[a]

Alkali metals		Total energy (a.u.)	B. E.[b] (kcal/mol)	Net charge on[c]		
M_I	M_{II}			M_I	M_{II}	Pt[d]
Li	Li	-903.3347	-22.1281	0.68	0.71	0.12
Na	Na	-903.3087	-18.7622	0.68	0.85	0.10
K	K	-903.2404	-18.5113	0.75	0.93	0.06
H	Rb	-903.5108	-11.2322	0.48	0.70	0.04
H	Cs	-903.4951	-18.9505	0.48	0.67	0.03
Na	Li	-903.3278	-25.9307	0.72	0.73	0.12
Na	K	-903.2762	-17.4473	0.78	0.87	0.06
Na	Rb	-903.3035	-21.4605	0.82	0.96	0.04
Na	Cs	-903.2650	-17.1923	0.81	0.98	0.03
Na	Mg(OH)	-920.0495	-33.4458	0.82	1.03	0.05
Na	Ca(OH)	-919.9876	-32.8970	0.82	1.21	0.05
Na	Sr(OH)	-919.9196	-31.5793	0.82	1.51	0.03
Na	Ba(OH)	-919.9191	-30.3421	0.82	1.58	0.01

[a] Cluster:[Pt_5:M_I/$M_{II}Si_4Al_2O_{18}H_{12}$] where M_I is the alkali metal present in the cationic site I and M_{II} is alkali metal present in the site II). Pt_5 cluster representing (111) planes of platinum is placed above site II (Fig. 4.19); [b] Calculated according to equation (4.9) given in text; [c] Mulliken population and [d] Average charge on Pt in Pt_5 cluster.

4.3.3.5. Behavior of adsorbed benzene over Pt-M-FAU: Molecular graphics pictures of benzene adsorbed on Pt_5-FAU are shown in Fig. 4.20 and 4.21 in two views (90°, Y-rotation). The binding energy of the C_6H_6 molecule with the Pt-zeolite cluster was calculated according to equation (4.10).

$$B.E.=T.E.[C_6H_6{:}Pt_5{:}M_IM_{II}Si_4Al_2O_{18}H_{12}]-\{T.E.[Pt_5{:}M_IM_{II}Si_4Al_2O_{18}H_{12}]+T.E.(C_6H_6)\} \quad (4.10)$$

Electronic properties of the model clusters were calculated for various combinations of M_I and M_{II} (Table 4.16). The binding energy of benzene with the cluster decreases with increasing size and electropositive nature of the alkali ions. For a given M_I ion (Na), the binding energy decreases from Li to Cs and Mg(OH) to Ba(OH). This suggests that desorption of the benzene from the Pt cluster is easier with increasing basicity of the support. Comparing the electronic charge on Pt in the presence and absence of adsorbed benzene, it is found to be smaller when benzene is adsorbed revealing the donation of electronic charge by benzene to Pt. In general, the results are similar to those observed in the case of LTL and BEA.

Table 4.16. The electronic properties of the cluster model, C_6H_6-Pt_5-M-FAU[a]

Alkali metals		Total energy	B. E.[b]	Net charge on[c]		
M_I	M_{II}	(a.u.)	(kcal/ mol)	M_I	M_{II}	Pt[d]
H	H	-939.6732	-2.9469	0.34	0.45	0.09
Li	Li	-939.6415	-3.9511	0.48	0.48	0.07
Na	Na	-939.6129	-2.3218	0.51	0.61	0.05
K	K	-939.5432	-1.3805	0.54	0.63	0.04
H	Rb	-939.8337	-9.9932	0.48	0.71	0.03
H	Cs	-939.7988	-1.2550	0.48	0.73	0.00
Na	Li	-939.5858	-6.6674	0.73	0.70	0.06
Na	Na	-939.5963	-2.3218	0.75	0.71	0.05
Na	K	-939.5792	-1.5688	0.82	0.86	0.02
Na	Rb	-939.6067	-1.6926	0.83	0.95	0.00
Na	Cs	-939.5682	-1.6926	0.81	0.98	0.00
Na	Mg(OH)	-956.3561	-3.2604	0.82	1.13	0.06
Na	Ca(OH)	-956.2943	-3.3231	0.82	1.25	0.04
Na	Sr(OH)	-956.2251	-2.5707	0.83	1.59	0.01
Na	Ba(OH)	-956.2230	-1.5675	0.83	1.68	0.00

[a] Cluster:[C_6H_6:Pt_5:M_I/$M_{II}Si_4Al_2O_{18}H_{12}$] where M_I and M_{II} are the cations present in sites I and II (details of cluster is shown in Fig. 4.21). Pt_5 representing (111) plane of platinum placed above site II; [b] Calculated according to equation (4.10) given in text; [c] Mulliken population and [d] Average charge on platinum.

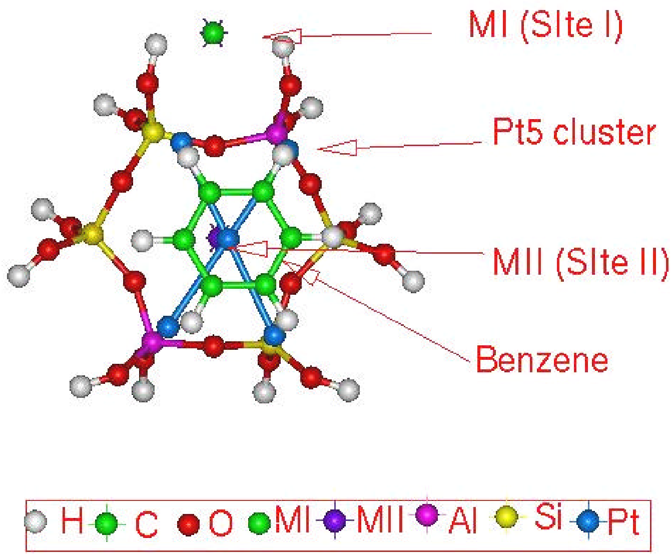

Fig. 4.20. Molecular graphics picture of benzene adsorbed over the Pt_5: FAU cluster model, viewed through the supercage of FAU zeolite.

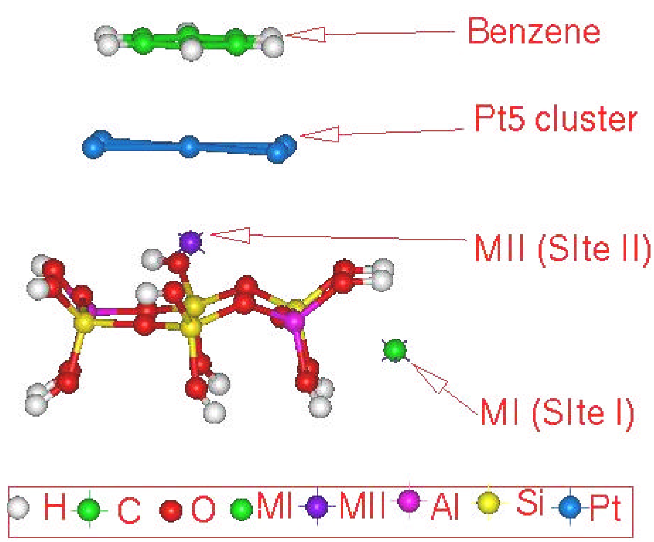

Fig. 4.21. Molecular graphics of benzene adsorbed over Pt_5: FAU cluster model, viewed after by rotation of Y 90 º

4.3.3.6. Electron density on Pt and S_{int} of Pt-M-FAU: Plots of the average charge per Pt atom obtained from modeling versus S_{int} of the clusters are presented in Fig. 4.22 for the different (M) Pt_5-zeolite clusters. The plots reveal the general trend of decreasing charge (increasing electron density) on Pt with decreasing S_{int} suggesting decreasing electron transfer from Pt to the support with increase in support basicity. The plot is different for the alkali and alkaline earth ions. The results are again similar to those observed for LTL and BEA clusters.

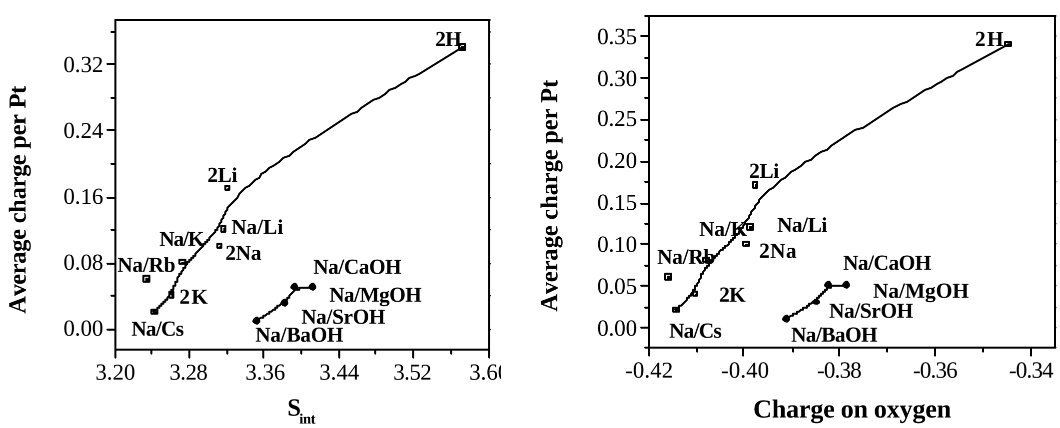

A B

Fig. 4.22. In the cluster model, M-FAU: relationship between average charge on Pt in Pt_5 cluster and S_{int} (A) and relationship between average charge per Pt and average oxygen charge (B).

4.3.4. n-Hexane Aromatization Activity of Pt-zeolite Catalysts: Activities of the different Pt-zeolite (LTL, FAU and BEA) catalysts in the transformation of *n*-hexane were discussed in chapter 3. The relationships between charge on Pt in each Pt_5: zeolite cluster and benzene yield in the aromatization of *n*-hexane are presented in Fig. 4.23 (a – c) for Pt-M-LTL, Pt-M-BEA and Pt-M-FAU, respectively. It is noticed that benzene yield [Fig. 4.23 (a – c)] depends on both the exchanged cation and the zeolite geometry. Conversion and selectivity for benzene increase with the basicity of the cations in the case for all the zeolites. The three zeolites can be arranged in the following order with respect to conversion and selectivity: zeolite BEA > LTL > FAU (conversion) and LTL > BEA > FAU (benzene yield). Conversion is more over BEA than over the other two zeolites; however, benzene yield is rather low making it a less useful catalyst than LTL. The H-BEA form is more active due to its large acidity and greater occurrence of isomerization and cracking reactions (chapter 3; Table 3.3). The benzene yields over Pt-M-BEA catalysts are intermediate between those of zeolite LTL and FAU. A similar observation that Pt-LTL is more selective than Pt-BEA and Pt-USY for aromatics has already been made by Zheng *et al.*[33] and Smirniotis and Ruckenstein.[34] The general conclusion of these studies is that the yield of benzene increases with increase in the electron density on Pt irrespective of the zeolite. In the whole range of charges on Pt considered, zeolite LTL is more selective to benzene than the other two zeolites, suggesting a structure effect also. In Fig. 4.23 (a – c), Pt-charge values calculated for ideal clusters have been related to the activity of actual catalysts even though the reactions were not carried out over catalysts possessing the ideal cluster compositions used in the calculations. The actual catalysts used in the catalytic tests were not pure exchanged forms as assumed in the computational calculations. They contained more than one metal ion and were only partially (mostly) exchanged (Tables 2.1, 2.2, 2.3 and 2.4) with the desired ion, M. In spite of this limitation, the data does point out that the activity of the catalysts for benzene production is related to the charge on Pt and the zeolite structure.

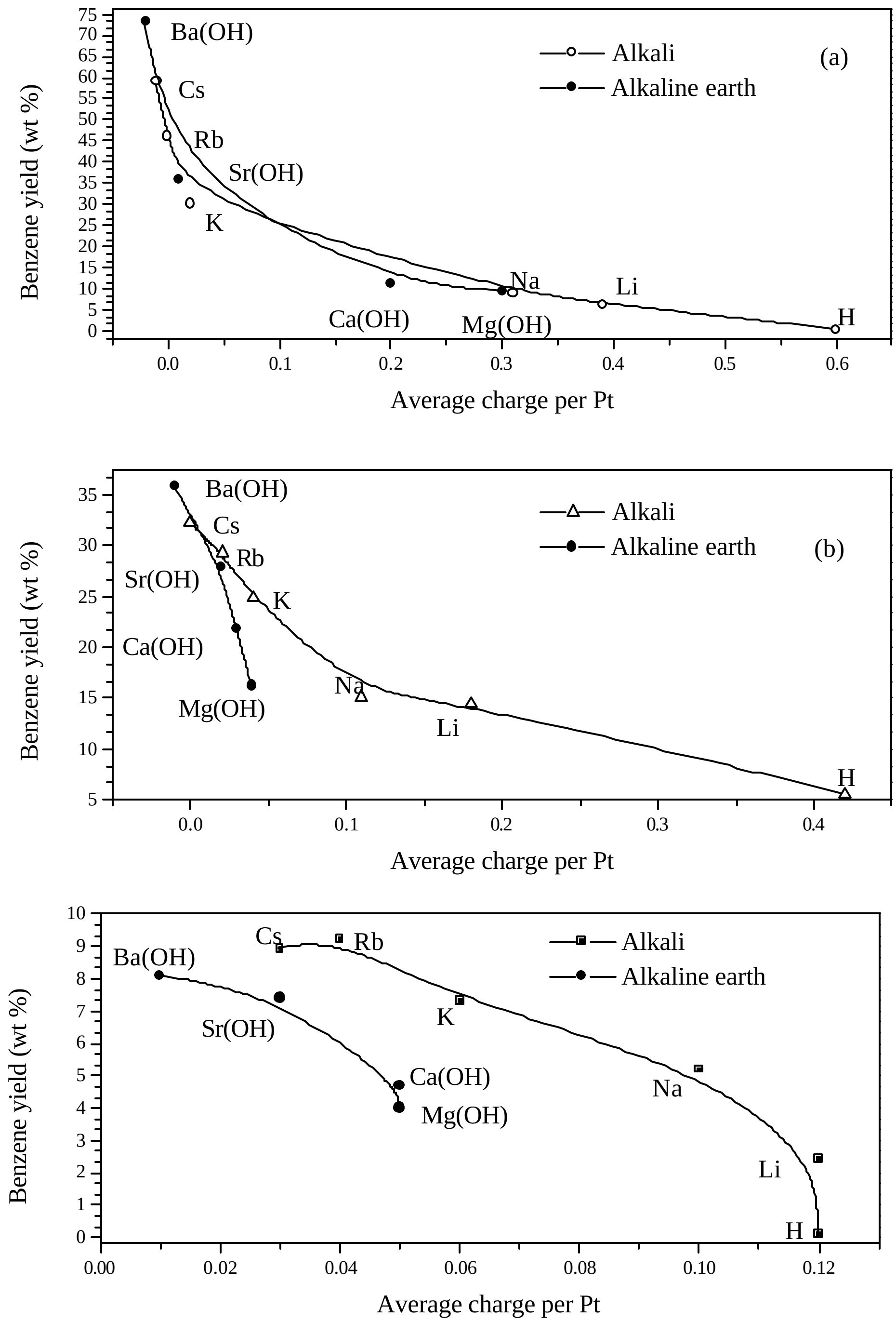

Fig. 4.23. Relationship between average charge per Pt in Pt_5 cluster and benzene yield over Pt-M-LTL; Si/Al = 3 (a), Pt-M-BEA; Si/Al = 9 (b) and Pt-M-FAU; Si/Al = 2 (c).

Interestingly, the conversion and selectivity observed for the Ba-samples are larger (especially for LTL and BEA) than for the others. In this context, it is interesting to note that the Pt-LTL catalyst used commercially in the AROMAX process is believed to be Ba-K-LTL.[35,36] The present calculations show that Pt in Ba-K-LTL is the most electron rich (negative charge; Table 4.6) of all the clusters investigated by us.

The relationship between intermediate electronegativity (S_{int}) of the catalysts calculated based on their actual compositions and charge on Pt is presented in Figs. 4.8, 4.15 and 4.22 for LTL, BEA and FAU, respectively. The relationship between S_{int}, oxygen charge and conversion and selectivity are presented in chapter 3 (Figs. 3.2, 3.8 and 3.13).

4.4. CONCLUSIONS

The salient features investigated by computational studies can be summarized as follows:

1) The isomorphous substitution of Al atom in place of silicon preferably occurs at T_I site of LTL zeolite. When two Al atoms are isomorphically substituted, they prefer the locations farthest from each other. As far as the binding energy of these cations is considered, cations present in M_{II} site are more strongly bound to the zeolite than those present in M_I. The binding energy of the cation with the zeolite cluster decreases from Li to Cs and Mg(OH) to Ba(OH). The charge on the cation increases from Li to Cs and Mg(OH) to Ba(OH). The charge on M_{II} cationic sites is more electropositive than on M_I sites. This indicates that cations in M_{II} sites will exhibit higher catalytic activity (acidity).
2) The higher basicity of the zeolite imparts a larger negative charge to the supported Pt. The basicity of the zeolite itself is dependent on the framework geometry (such

as T-O distance, T-O-T angles, etc.) as well as on the location and nature of the exchanged cations, 'M'.

3) The net electron transfer from Pt_5 cluster to M-zeolite in different zeolites is in the decreasing order, FAU > BEA > LTL and this correlates with the experimentally observed higher activity and benzene selectivity of Pt-LTL and Pt-BEA, compared to Pt-FAU. The net electron transfer from Pt to M-zeolite decreases in the order, H > Li > Na > K > Rb ~ Cs in the case of the alkali metal ions and in the order Mg(OH) > Ca(OH) > Sr(OH) > Ba(OH) for the alkaline earth metal ions. The most active and selective catalysts are the Cs and Ba exchanged catalysts. In these catalysts, the transfer of electron is from the M-zeolite to the Pt_5 cluster, making Pt electron rich.

4) Binding energy values for the adsorption of benzene over Pt supported on highly basic zeolites are lower. These results suggest that the adsorption of benzene is weaker on electron-rich Pt clusters. The weaker adsorption of benzene could translate into larger activity of these catalysts due to faster desorption of the product benzene from the active centers (Pt).

5) Binding energy values for the adsorption of H_2S are larger for Pt supported over basic zeolites than for Pt supported over acidic zeolites. During the interaction of H_2S, electron transfer takes place from Pt to S and is more when Pt is supported on a basic support. This suggests that Pt supported on basic catalysts is more vulnerable to sulfur poisoning.

Thus the important role played by the electronic structure of Pt in *n*-hexane aromatization is clearly brought out. The various factors such as structure of the zeolite, basicity of the zeolite, Pt dispersion that influence the electronic structure of Pt have been identified, suitable metrics devised and quantified (charge on Pt is in the range - 0.02 to 0.01) based on *ab initio* calculations.

4.5. REFERENCES

1. D. Barthomeuf, *Stud. Surf. Sic. Catal*, 65 (1991) 157.
2. D. Barthomeuf and A. de Mallmann, *Stud. Surf. Sci. Catal*, 37 (1988) 365.
3. R.T. Sanderson, "*Chemical Bonds and Bond Energy*", Academic Press, New York 1976.
4. R.T. Sanderson, *J. Am. Chem. Soc.,* 105 (1983) 2259.
5. R. Vetrivel, C.R.A. Catlow, E.A. Colbourn and M. Leslie, *Stud. Surf. Sci. Catal.*, (1989) .
6. D. Barthomeuf, in "*Acidity and Basicity of solids*", J. Fraissard and L. Petrakis eds., *NATO ASI Ser. C*., 19 (1994) 327.
7. G.V. Gibbs, E.P. Meagher, J.V. Smith and J.J. Pluth, *ACS Symp. Ser*., 40 (1977) 19.
8. R.A. van Santen, B.W.H. Van Beest and A.J.M. de Man, in "*Guidelines for Mastering the properties of Molecular Sieves*", D. Barthomeuf, E.G. Derouane and E. Hölderich eds., NATO ASI series, Plenum Press, New York, *Ser. B. Physics*, 221 (1990) 201.
9. I.N. Senchenya, V.B. Kazansky and S. Beran, *J. Phys. Chem*., 90 (1986) 4857.
10. P.J. O'Malley and J. Dwyer, *J. Phys. Chem*., 92 (1988) 3005.
11. S. Beran and J. Dubsky, *J. Phys. Chem*., 83 (1979) 2538.
12. G.M. Zhidomirov and V.B. Kazansky, *Adv. Catal*., 34 (1986) 131.
13. E.G. Derouane and J.G. Fripiat, *J. Phys. Chem*., 91 (1987) 145.
14. E. Kassab, K. Seiti and M. Allavena, *J. Phys. Chem*., 92 (1988) 67.
15. P.J. O'Malley and J. Dwyer, *Chem. Phys. Lett.*, 143 (1988) 97.
16. A. Goursot, F. Fajula, C. Dual and J. Weber, *J. Phys. Chem*., 92 (1988) 4456.
17. K.P. Schroder and J. Sauer, in "*Proceedings of 9th International Zeolite Conference*", R. Von Ballmoos, J.B. Higgins and M.M.J. Treacy, eds., Butterworth-Heinemann, Boston, I (1993) 687.
18. G.N. Vayssilov and N. Rösch, *J. Catal*., 186 (1999) 423.
19. W.J. Mortier, *J. Catal*, 55 (1978) 138.
20. W.J. Mortier, *Stud. Surf. Sci. Catal.*, 37 (1988) 253.
21. C. Besoukhanova, J. Guidot, D. Barthomeuf, M. Breysse and J.R. Bernard, *J. Chem. Soc. Faraday Trans*. I, 77 (1989) 1595.

22. G. Larsen and G.L. Haller, *Catal. Lett.*, 3 (1989) 1003.
23. S.J. Tauster and J.J. Steger, *J. Catal.*, 125 (1990) 387.
24. R.M. Barrer and H. Villiger, *Zeit. Krystall. S*, 128 (1969) 352.
25. J.M. Newsam, *J. Phys. Chem.*, 93 (1989) 7689.
26. T.R. Hughes, W.C. Buss, P.W. Tamm and R.L. Jacobson, *Stud. Surf. Sci. Catal.*, 28 (1986) 725.
27. J.L. Kao, G.B. McVicker, M.M.J. Treacy, S.B. Rice J.L. Robbins, W.E. Gates, J.J. Ziemax, J.R. Cross and T.H. Vanderspur, *Stud. Surf. Sci. Catal.*, 75 (1993) 1019.
28. J.M. Newsam, M.M.J. Treacy, W.T. Koetsier and C.B. De Gruyter, *Proceedings of Royal Society London, Ser. A,* 420 (1988) 375.
29. R.B. Borade and A. Clearfield, *Chem. Commnu.*, (1996) 625.
30. M.M.J. Treacy and J.M. Newsam, *Nature*, 332 (1988) 249.
31. A.N. Fitch, H. Jobic and A. Renouprez, *J. Phys. Chem.*, 90 (1986) 1311.
32. W.J. Mortier, H.J. Bosmans and J.B. Uytterhoeven, *J. Phys. Chem.*, 76 (1972) 650.
33. J. Zheng, J.L. Dong, Q.H. Xu, Y. Lui, A.Z. Yan, *Appl. Catal.* A, 126 (1995) 141.
34. P.G. Smirniotis and E. Ruckenstein, *Appl. Catal. A*, 123 (1995) 59.
35. P.W. Tamm, D.H. Mohr and C.R. Wilson, *Stud. Surf. Sci. Catal.*, 1987, 38, 335.
36. D. Rotman, *Chem. Week*, 150 (1992) 8.

CHAPTER 5

n-HEXANE AROMATIZATION *OVER ETS-10: CATALYTIC AND MOLECULAR MODELING STUDIES*

5.1. INTRODUCTION

Engelhard titanosilicate – 10 (ETS-10) possesses a Si/Ti ratio of 5. The Ti^{4+} ions posses octahedral coordination and the Si^{4+} ions have tetrahedral coordination. The presence of Ti^{4+} in an octahedral arrangement of O^{2-} ions leads to two negative charges that are compensated by two mono-valent alkali ions for each Ti^{4+} ion making the molecular sieve highly basic in the alkali ion exchanged form. The effective basicity (alkali content) of ETS-10 is equivalent to that of a zeolite with a Si/Al of about 2.5 (similar to FAU). In the first part of this chapter (Part-A), ETS-10 is being explored as a basic support for Pt. This chapter also reports the influence of different alkali metal ions on the activity of Pt-ETS-10 for *n*-hexane aromatization. In the second part of this chapter (Part-B), molecular modeling and quantum chemical methods have been used to examine the electronic properties of Pt in different locations in Pt-M-ETS-10. The likely location of the active Pt species is identified. This chapter is divided into two parts; A) experimental: *n*-hexane aromatization and B) molecular modeling studies.

PART A: EXPERIMERNTAL STUDIES

5.2. *n*-HEXANE AROMATIZATION

5.2.1 Materials and Methods*:* Ion exchanged forms of the molecular sieve, namely Pt-M-ETS (where M= H, Li, Na, K, Rb, Cs, Mg, Ca, Sr and Ba) were used to study the *n*-hexane aromatization reaction. The details of the preparation of the catalysts are presented in chapter 2 (section 2.1 and 2.2). Their physicochemical characterization is presented in chapter 2 (section 2.3). The description of the catalytic reactor and the procedure adopted for the reaction are also presented in chapter 3 (section 3.2).

5.3. RESULTS AND DISCUSSION

5.3.1. Studies over Pt-M-ETS-10: *n*-Hexane aromatization was carried out over various Pt-loaded alkali metal exchanged ETS-10 samples in order to evaluate the influence of the alkali metal ion on the catalytic properties of Pt-ETS-10. The Pt-Cs-ETS-10 sample was evaluated in detail at different process conditions and Pt loadings.

5.3.1.1. Effect of nature of the exchanged metal ion on the aromatization of *n*-hexane: The chemical compositions of the samples and BET surface areas measured from N_2-adsorption have been presented in chapter 2 (Table 2.4). The CO_2-TPD spectra of the M-ETS-10 molecular sieves are presented in chapter 2 (Fig. 2.16). The CO_2 desorbed (on constant weight basis) increases for the cation exchanged samples in the order: Li < Na $\cong$ K < Rb < Cs-ETS-10 and Mg < Ca < Sr < Ba - ETS-10. The CO_2 uptake (desorbed) noticed is related to the basicity of the samples. Pt dispersion of the Pt-M-ETS-10 samples was determined by H_2 chemisorption and presented in chapter 2 (Table 2.14). The dispersion values are in the range of 43 to 83 %.

The transformation of *n*-hexane was carried out in the temperature range of 673 to 823 K at atmospheric pressure over Pt-loaded metal exchanged ETS-10 catalysts and a commercial Pt-Al_2O_3 catalyst at identical conditions to compare their performances. The *n*-hexane aromatization activities of a series of Pt-M-ETS-10 catalysts containing different exchanged alkali and alkaline earth metal ions are presented in Table 5.1. It is noticed that the more basic catalysts are more active in *n*-hexane aromatization. The benzene selectivity in the products shows a similar trend.

The activity increases linearly with increase in the electropositive nature of the exchanged metal cation in the order Li < Na < K < Rb < Cs and Mg < Ca < Sr < Ba. In the case of the acidic Pt-H-ETS-10, though *n*-hexane conversion is very high

Table 5.1. *n*-Hexane aromatization over various ion exchanged Pt-M-ETS10 catalysts

	Catalyst: Pt-M-ETS10 (Pt 0.6 %) where M =										
	H	Li	Na	K	Rb	Cs	Mg	Ca	Sr	Ba	Pt- Al_2O_3
Conversion (%)	78.3	9.2	15.3	25.6	48.9	81.4	27.9	32.1	52.7	85.9	37.3
Product yield (wt%)											
C_1 to C_5#	36.4	2.5	3.9	6.9	11.7	16.2	7.1	2.1	4.9	4.8	3.5
i-$C_6$$	31.1	0.7	0.9	1.2	1.3	2.3	1.4	4.4	4.4	3.4	6.8
$McyC_5$*	1.5	0.4	0.5	0.7	1.7	4.3	4.1	2.6	2.1	10.9	1.2
Benzene	1.2	1.3	2.5	5.2	15.1	39.5	6.3	9.2	23.7	52.1	3.2
C_6^+Aromatics**	5.4	0	2.3	3.1	2.2	2.0	1.7	4.7	5.7	4.5	7.8
Others	2.7	4.3	5.2	8.5	16.9	17.1	7.3	9.1	11.9	10.2	14.8
Benzene selectivity (%)+	1.5	14.1	16.3	20.3	30.9	48.5	22.6	28.7	44.9	60.7	8.6

Reaction conditions: WHSV = $2h^{-1}$; Pressure = 1 atm.; TOS 2h; H_2: *n*-hexane (mol) = 4.5; Temp. = 733 K; # C_1-C_5 = products from methane to pentanes; $ = iso hexanes, mainly 2 methyl pentane and 3 methyl pentane; * = methyl cyclopentane; ** = toluene + xylenes and + = benzene selectivity = wt of benzene/wt of all products X 100.

(78.3 %), benzene yield is very low (1.2 %); most of the *n*-hexane is converted into the C_1-C_5 fraction (36.4 %) and iso-hexanes (31.1 %). In the case of the alkaline catalysts, benzene yield increases with the basicity, 1.3 % for Pt-Li-ETS-10, 48.5 % for Pt-Cs-ETS-10 and 60.7 % for Pt-Ba-ETS-10. The C_1-C_5 yield also increases with the basicity of the sample, being 2.5 % in the case of Li and 16.2 % in the case of Cs. While it is expected that the light products (C_1-C_5) are produced due to cracking reactions over Pt-H-ETS-10, they are presumably formed by hydrogenolysis over Pt in the case of the basic samples. Apparently, the hydrogenolysis activity of Pt is more when supported on basic ETS-10; this is especially apparent over the alkali exchanged catalysts. However, Pt-Ba-ETS-10 shows the highest benzene selectivity. It produces less light products (C_1 to C_5) compared to Pt-Cs-ETS-10, the most active alkali exchanged catalyst. The isomerization activity of the basic catalysts ($\leq$ 4.4 %) is much smaller than that observed for the acid Pt-H-ETS-10 (31.1 %). It is interesting to note that the more basic catalysts (eg., Pt-Cs-ETS-10) possess slightly larger isomerization activity than the less basic ones (eg., Pt-Li-ETS-10). The increased isomerization activity with basicity suggests that the isomerization occurs by a monofunctional route via C_1-C_5 cyclization and ring opening reactions over the Pt metal. The increased yield of methylcyclopentane (MCP) over the more basic catalysts confirms this mechanism for isomerization. The results reveal that Pt supported on basic samples is more selective for the aromatization reaction. It is interesting to note that the most selective catalyst (Pt-Ba-ETS-10) produces more MCP than the other catalysts suggesting that it possesses a greater cyclization activity than that the others. However, an increase in isomerization and hydrogenolysis reactions also occurs with increase in the basicity of the support. The basic catalysts deactivated more slowly compared to Pt-H-ETS-10. The deactivation of Pt-Ba-ETS-

10 was marginally less than Pt-Cs-ETS-10. The deactivation of Pt-Cs-ETS-10 was more than Pt-Cs-LTL and Pt-Cs-BEA samples.

5.3.1.2. Relationship between S_{int} and benzene yield in aromatization of *n*-hexane:

The calculation procedure and the values of S_{int} are presented in chapter 2 section 2.3.10. Over basic supports, Pt is believed to be electron rich, the richness arising from electron transfer from the basic O^{2-} ions in the lattice.[1-3] The S_{int} values for different M-ETS-10 samples are presented in chapter 2 (section 2.3.10). The relationship between benzene selectivity, oxygen charge and S_{int} in the case of Pt-M-ETS-10 samples is presented in Fig. 5.1. A distinct relationship between the intermediate electronegativity (S_{int}) of the different metal exchanged ETS-10 samples and benzene yield is noticed (Fig 5.1) suggesting the activation of Pt by the basicity of the exchanged metal. It is noticed that though the conversion is very high over H-

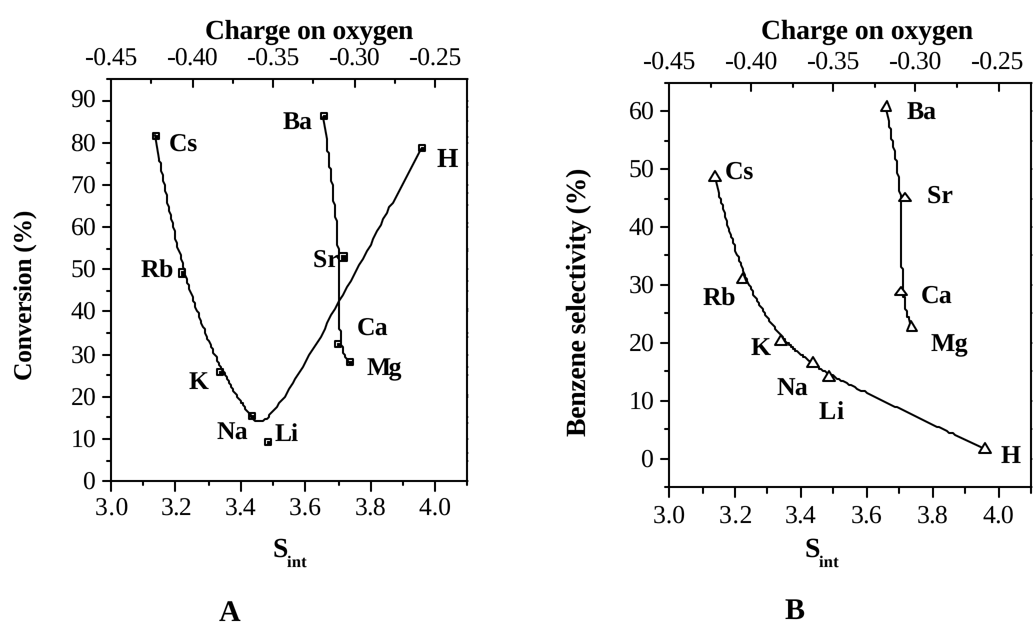

Fig. 5.1. **A) Relationship between *n*-hexane conversion and S_{int}/charge on oxygen and B) relationship between benzene selectivity and S_{int}/charge on oxygen.**

ETS-10 (78.3 %), benzene selectivity is very low (1.5 %); most of the *n*-hexane is transformed into cracked and isomerized products.

5.3.1.3. Studies on Pt-Cs-ETS-10: Among all the cation exchanged samples, Pt-Cs-ETS-10 and Pt-Ba-ETS-10 exhibit higher activity and benzene selectivity (Table 5.1). The activity of Pt-Cs-ETS-10 catalyst is investigated in greater detail in this section.

5.3.1.3.1. Influence of duration run: Deactivation of the catalyst was observed during the run. Initially, up to about 2 h, the deactivation was rapid, becoming slower at longer duration of run (studied up to 12 h; Fig. 5.2). The yields of the products also follow a similar trend as conversion. As the changes in conversion and product selectivity become small beyond a TOS of 2 h, all the data reported in the following sections in this chapter were collected at duration of run of 2h.

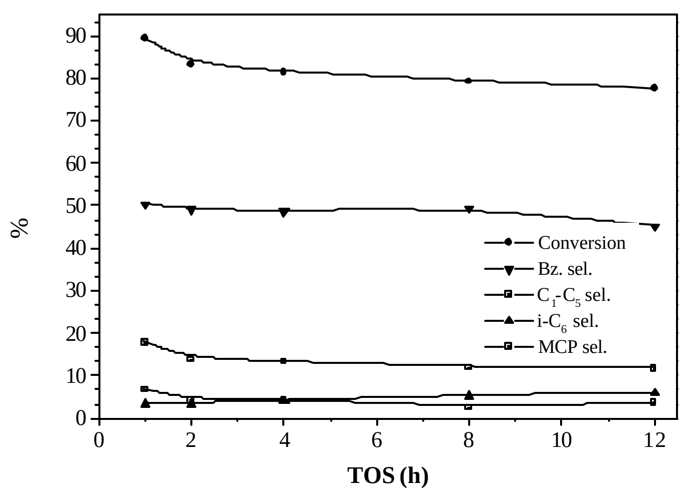

Fig. 5.2. Influence of duration of run on *n*-hexane conversion over Pt-Cs-ETS-10 (Reaction conditions: Temp. = 733 K; Press. = 1 atm.; WHSV = 2 and H_2:*n*-hexane (mol) = 6:1; see foot note of Table 5.1 for definitions).

5.3.1.3.2. Influence of Pt content: The influence of Pt loading (Pt-Cs-ETS-10) on conversion and product selectivity at 733 K is presented in the Fig. 5.3. *n*-Hexane conversion increases as a function of Pt loading up to about 0.5 wt % and remains nearly constant at higher loadings. Benzene selectivity increases marginally with Pt loading. However, selectivities for the products decrease marginally with Pt content. The constant conversion observed at higher Pt loading is probably a result of diffusion effects in the channels of ETS-10 (pore diameter ~ 8Å).

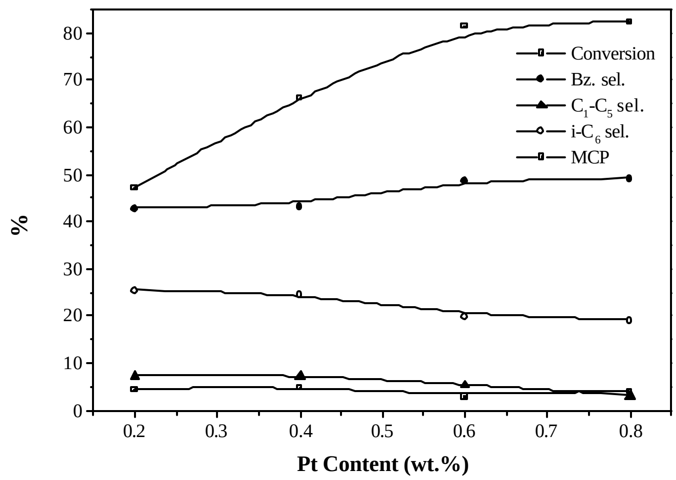

Fig. 5.3. Influence of Pt loading of Pt-Cs-ETS-10 on *n*-hexane aromatization (Reaction conditions: Temp. = 733 K; WHSV = 2 h^{-1}; Press. = 1 atm.; TOS = 2 h and H_2:*n*-hexane (mol) = 6:1; see foot note of Table 5.1 for definitions).

<u>5.3.1.3.3. Influence of temperature:</u> The influence of temperature on the conversion of *n*-hexane and product selectivities is presented in Fig. 5.4. Conversion increases rapidly and reaches a maximum (~ 100 %) at about 780 K. Increasing the temperature also increases benzene selectivity while decreasing the selectivities for the other products.

<u>5.3.1.3.4. Influence of space velocity:</u> The influence of space velocity on conversion of *n*-hexane and benzene selectivity at 733 K is presented in Fig. 5.5. Conversion

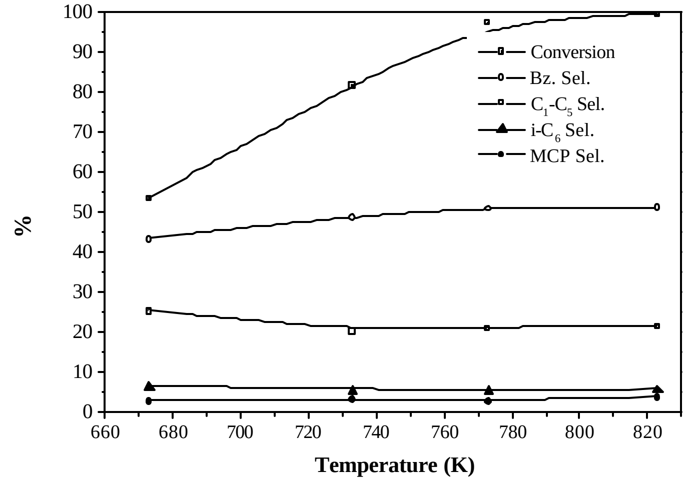

Fig. 5.4. **Influence of temperature on *n*-hexane aromatization over Pt-Cs-ETS-10 (0.6 wt % Pt) (Reaction conditions: WHSV = 2 h^{-1}; Press. = 1 atm.; TOS = 2 h and H_2:*n*-hexane (mol) = 6:1; see foot note of Table 5.1 for definitions).**

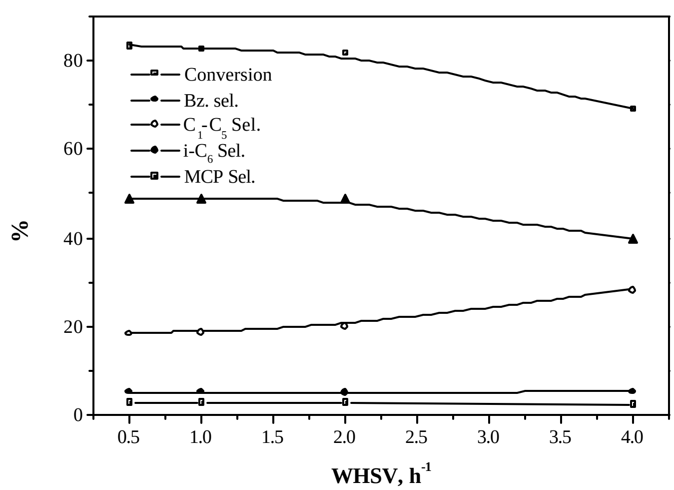

Fig. 5.5. **Effect of WHSV on *n*-hexane aromatization over Pt-Cs-ETS-10 (0.6 wt % Pt) (Reaction conditions: Temp. = 733 K; Press. = 1 atm.; TOS = 2 h and H_2:*n*-hexane (mol) = 6:1; see foot note of Table 5.1 for definitions).**

decreases rapidly with feed rate (WHSV from 0.5 to 4 h^{-1} at 733 K). A maximum conversion of 84.7 % is achieved at the lowest feed rate studied (WHSV = 0.5^{1}). It is interesting to note that the hydrogenolysis selectivity increases slightly with WHSV while benzene selectivity decreases. The WHSV for the other products are unaffected by selectivity in the investigated range.

5.3.1.3.5. Influence of H_2/*n*-hexane (mol) ratio: The effect of hydrogen content on conversion and product yield over Pt-Cs-ETS-10 is presented in Fig. 5.6. The conversion of *n*-hexane decreases with increasing H_2:HC (mol) ratio. Both benzene yield and selectivity follow the same trend. However, the C_1-C_5 selectivity increases with H_2 content, due to increased hydrogenolysis of the reactant/ primary products. An increase in iso-hexane selectivity is also noticed with increasing H_2:HC (mol) ratio. In these experiments, the *n*-hexane feed rate was kept constant and the H_2 flow rate was changed. As a result, the total flow rate was more at higher H_2 partial pressures. The decreased conversion noticed at higher H_2: HC (mol) ratio is probably a result of the contact time effect. The loss of benzene selectivity is a result of greater hydrogenolysis activity at higher H_2 partial pressures, the adsorbed intermediate undergoing hydrogenolysis and isomerization to a larger extent.

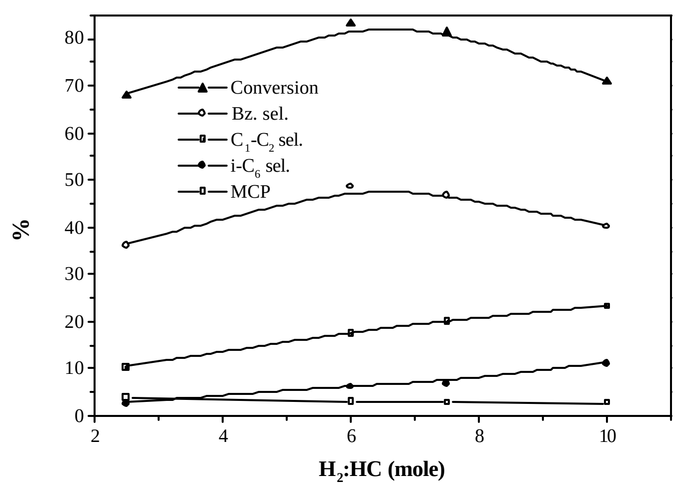

Fig. 5.6. Influence of H_2: HC (mol) ratio in *n*-hexane aromatization over Pt-Cs-ETS-10 (0.6 wt % Pt) (Reaction conditions: Temp. = 733 K; Press. = 1 atm.; TOS = 2 h and WHSV = 2 h^{-1}; see foot note of Table 5.1 for definitions).

5.3.1.3.6. Comparison with Pt-Al_2O_3 and other catalysts: The results of *n*-hexane aromatization over a commercial Pt-Al_2O_3 (0.6 wt % Pt) are presented in Table 5.1. Conversion and benzene yields are more over the more basic Pt-ETS-10 catalysts than over Pt-Al_2O_3. Besides, Pt-Al_2O_3 deactivated faster than the ETS-10 catalysts especially when compared to Cs-ETS-10. Bar charts of benzene yield and *n*-hexane conversion are presented in Fig. 5.7 for Pt-Cs-ETS-10, Pt-Cs-LTL, Pt-Cs-BEA, Pt-Cs-FAU and Pt-Al_2O_3. Comparing the different Pt-zeolite samples (Cs exchanged) investigated in this work, the ranking of the catalysts for benzene yield (at identical conditions) is Pt-Cs-LTL > Pt-Cs-ETS-10 > Pt-Cs-BEA > Pt-Cs-LTY > Pt-Al_2O_3. As the morphology of crystallites of LTL, BEA and FAU were similar (cubic; size ~ 1 μm), the selectivity trend noticed for these three systems should mainly be a refection of the differences in their electronic effects on Pt and their structures.

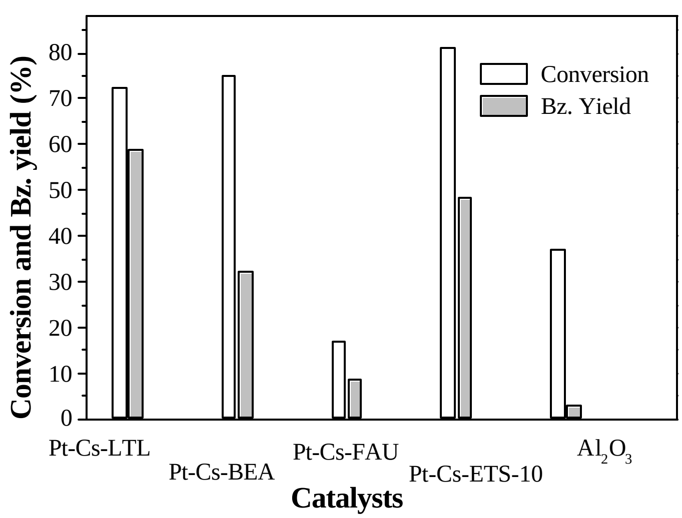

Fig. 5.7. *n*-Hexane conversion and benzene yield over different catalysts (Pt-Cs-LTL, Pt-Cs-BEA, Pt-Cs-FAU, Pt-Cs-ETS-10 and Pt-Al_2O_3) (Reaction conditions: Temp. = 733 K; Pressure = 1 atm; WHSV = 2 h^{-1} and H_2:n-hexane (mol) = 6:1).

PART B: MOLECULAR MODELING

5.4. CLUSTER MODEL AND METHODOLOGY

The molecular graphics picture of ETS-10 lattice is shown and described in chapter 2 (section 2.6.4). The cluster models of ETS-10 have been derived from the crystal structure of ETS-10 - polymorph B [(Unit cell: $\{[M^+]_{32}\ [(TiO_3)^{2-}]_{16}[SiO_2]_{80}\}$, (where $M^+ = Li^+$, Na^+, K^+, Rb^+ or Cs^+)] reported by Anderson *et al.*[4,5] Two likely locations for Pt (or Pt_5) inside the 12-MR are considered; one in proximity to the $[TiO_6]$ Oh (Fig. 2.23; model 1) and another in proximity to the $[SiO_4]$ (Fig. 2.23; model 2). Initially, two simple clusters were used, [Pt/ Pt_5:$M_2TiO_6H_6$] and [Pt/ Pt_5:$M_2TiSi_4O_{16}H_{10}$]. These two clusters are from two typical regions in ETS-10 framework and represent two distinctly different types of locations for Pt. Later on, the calculations were carried out with a slightly larger cluster, [Pt/ Pt_5:$M_2TiSi_4O_{16}H_{10}$] with a Si/Ti ratio of 4 (the actual value of Si/Ti in ETS-10 = 5). This cluster can be used to treat both the types of locations for Pt. More details of the cluster models used in this study have been presented in chapter 2 (section 2.6.4).

5.5. RESULTS AND DISCUSSION

5.5.1. Analysis of Small Clusters:

5.5.1.1. Influence of exchanged cations on $[TiO_6]$: The molecular graphics picture of the simple $[M_2TiO_6H_6]$ cluster, where M can be either M can be M_I or M_{II} or both, is shown in Fig. 5.8. The cluster model used in this study is constructed from the reported crystal structure.[4,5] The alkali metal ions are sited at locations predicted by EXAFS.[6] The unsaturated valences of the cluster are saturated by hydrogen atoms. The O-H distance is kept as 1.03 Å and lies along the original vector of the Ti-O-Si in

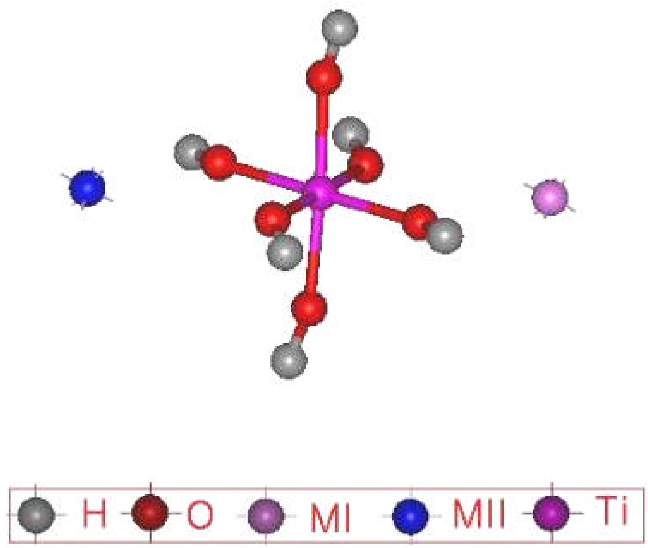

Fig. 5.8. **Molecular graphics picture of [$M_2TiO_6H_6$] (where M = Li, Na, K, Rb or Cs) cluster model.**

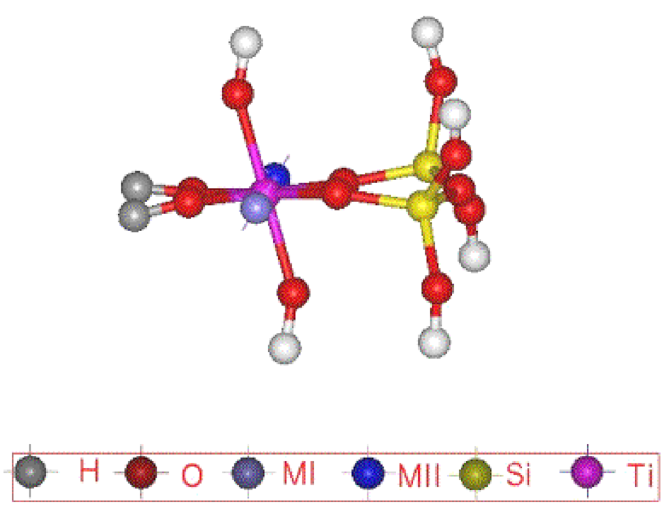

Fig. 5.9. **Molecular graphics picture of [$M_2TiSi_2O_{11}H_8$] (where M = Li, Na, K, Rb or Cs) cluster model.**

Table 5.2. Electronic properties of the cluster models of M-ETS-10

Cluster	$[M_2TiO_6H_6]$			$[M_2TiSi_2O_{11}H_8]$		
M	Total energy (a.u.)	B.E.[a] (kcal/mol)	Net charge[c] on M	Total energy (a.u.)	B.E.[b] (kcal/mol)	Net charge[c] on M
Li	-155.6862	-433.8840	0.66	-242.9197	-418.5610	0.69
Na	-155.6081	-384.9150	0.80	-242.8483	-398.1103	0.83
K	-155.5242	-332.3101	0.92	-242.7697	-358.6114	0.93
Rb	-155.5211	-330.3662	0.96	-242.7629	-318.2316	0.97
Cs	-155.4827	-306.2893	0.96	-242.7308	-308.6619	0.97

[a and b] binding energy calculated from equation (5.1) or (5.2), respectively and [c] average Mulliken population (atomic charge) on alkali earth atoms.

the ETS-10 lattice. The extra negative charges on the TiO_6 cluster are balanced by alkali metal cations. The distance between M-O is the sum of the radii of O^{2-} and M^+. The alkali metal cations are systematically varied from Li to Cs. The charge on alkali metal cations increases from Li to Cs (Table 5.2). The binding energy of the alkali cations with the cluster model is calculated from equation (5.1). The binding energy decreases from Li to Cs.

$$BE = T.E. [M_2TiO_6H_6] - \{T.E [TiO_6H_6]^{2-} + 2T.E [M]^+\} \quad (5.1)$$

5.5.1.2. Influence of exchanged cations on [SiO_4]: Another small cluster model, namely [$M_2TiSi_2O_{11}H_8$], where M can be either M_I or M_{II} or both, used in this study is shown in Fig. 5.9. This cluster consists of two Si and one Ti atoms. The negative charge on the cluster is compensated by alkali metal ions, Li to Cs. The charge on the alkali cations increases from Li to Cs (Table 5.2). The binding energy of the alkali metal cation with the cluster model is calculated from equation (5.2). Binding energy of the alkali metal with the cluster increases from Li to Cs (Table 5.2).

$$BE = T.E. [M_2TiSi_2O_{11}H_8] - \{T.E [TiSi_2O_{11}H_8]^{2-} + 2T.E [M]^+\} \quad (5.2)$$

5.5.1.3. Electronic structure of Pt and Pt_5 located in M-ETS-10: The major pores in ETS-10 are 12-MR channels (Fig. 2.23). These channels are intersected by smaller 7, 5 and 3-MR channels in such a way that the walls of the 12-MR channels are linked with pockets with 7, 5, 4 and 3-MR openings. The Ti - atoms are accessible through pore openings, some of which are blocked by the exchanged alkali metal ions.[6] There are several possible locations for Pt or Pt_5 cluster in Pt-M-ETS-10. Given the large

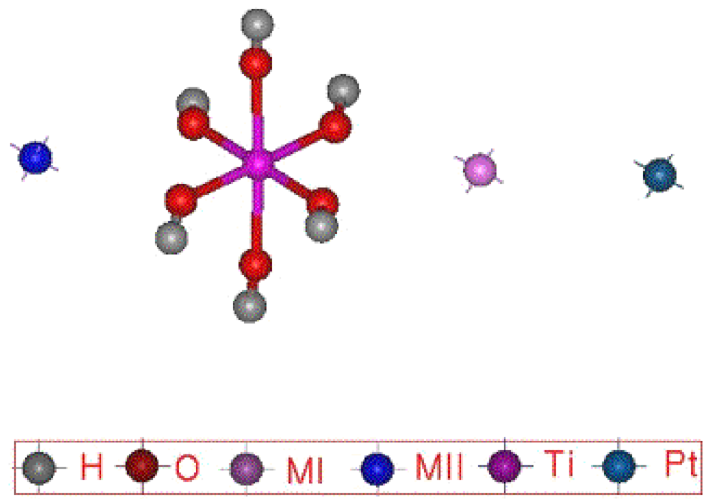

Fig. 5.10. Molecular graphics picture of [Pt:$M_2TiO_6H_6$] (where M = Li, Na, K, Rb or Cs) cluster model. This cluster represents the presence of Pt nearer to [TiO_6].

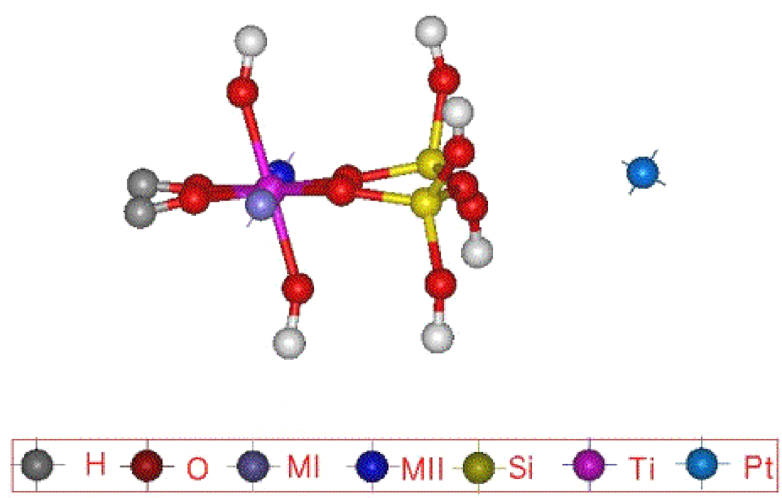

Fig. 5.11. Molecular graphics picture of [Pt:$M_2TiSi_2O_{11}H_8$] (where M = Li, Na, K, Rb or Cs) cluster model. This cluster represents the presence of Pt nearer to [SiO_4].

size of a Pt atom (2.77 Å), atomically dispersed Pt atoms and small Pt clusters can be present only inside the 12-MR (~8 Å) channels. Two distinctly different locations exist for Pt inside the 12-MR, one near [TiO_6] octahedra and another near [SiO_4] tetrahedra.

5.5.1.3.1. Single Pt nearer to [TiO_6]: The cluster model [Pt: $M_2TiO_6H_6$] used in this study is shown in Fig. 5.10. The Pt atom is located above the alkali metal cation. The distance between Pt-M is the sum of the radii of the Pt and alkali metal ion. The alkali ions are systematically varied from Li to Cs. The Pt is located in [110] plane as shown in Fig. 5.10. The binding energy of the Pt or Pt_5 with the cluster model [$M_2TiO_6H_6$] is calculated according to equation (5.3). The binding energy is not significantly affected by the nature of the alkali metal ion (Table 5.3). The charge on Pt is negative for all the cations; the negative charge increases on going from Li to Cs.

$$BE= T.E.\ [Pt/Pt_5\ M_2TiO_6H_6] - \{T.E\ [TiO_6H_6] + T.E\ [Pt/Pt_5]\} \quad (5.3)$$

5.5.1.3.2. Single Pt nearer to [SiO_4]: The cluster model [Pt:$M_2TiSi_2O_{11}O_8$] is shown in Fig. 5.11. The electronic properties of the cluster model are presented in Table 5.3. The charge on the alkali metal cation increases from Li to Cs. The binding energy of Pt or Pt_5 with the cluster is calculated from equation (5.4).

$$BE = T.E.\ [Pt/Pt_5:M_2TiSi_2O_{11}O_8] - \{T.E\ [(M_2TiSi_2O_{11}H_8] + T.E\ [Pt/Pt_5]\} \quad (5.4)$$

The charge on Pt is positive and decreases on going from Li to Cs. Comparing the charge on Pt atom and binding energy for Pt at the two locations (nearer to the TiO_6 octahedra and SiO_4 tetrahedra), the Pt atom nearer to TiO_6 is electron rich even though the binding energies are similar. Besides, the [TiO_6] cluster donates electronic charge to Pt while the [SiO_4] cluster withdraws electronic charge from Pt.

Table 5.3. The Electronic properties of Pt over the cluster models of M-ETS-10

Cluster	$[Pt:M_2TiO_6H_6]$				$[Pt:M_2TiSi_2O_{11}H_8]$			
M	Total energy (a.u.)	B.E.[a] (kcal/mol)	Net charge[c] on M	Net charge[c] on Pt	Total energy (a.u.)	B.E.[b] (kcal/mol)	Net charge[c] on M	Net charge[c] on Pt
Li	-274.4716	-118.7854	0.67	-0.052	-361.7304	-118.5610	0.69	0.015
Na	-274.3957	-118.7876	0.81	-0.073	-361.7304	-118.8110	0.83	0.018
K	-274.3147	-118.7905	0.93	-0.104	-361.7304	-118.8114	0.93	0.020
Rb	-274.3123	-118.7912	0.97	-0.116	-361.7304	-118.8116	0.97	0.018
Cs	-274.2751	-118.7924	0.97	-0.121	-361.7304	-118.8119	0.97	0.019

[a and b] binding energy calculated from equation (5.3) and (5.4), respectively and [c] average Mulliken population (atomic charge) on alkali and platinum atoms.

5.5.1.3.3. Electronic structure of Pt_5 nearer to $[TiO_6]$: The cluster model with stoichiometry $[Pt_5:M_2TiO_6H_6]$ is shown in Fig. 5.12. Several orientations of Pt_5 were considered and the Pt_5 plane oriented perpendicular to the [110] plane as shown in Fig. 5.12 was found to be energetically the most favorable. The electronic properties of $[Pt_5:M_2TiO_6H_6]$ have been derived by systematically varying 'M' from Li to Cs and presented in Table 5.4. The highest occupied molecular orbitals (HOMO) are contributed by oxygen 2p atomic orbitals while the lowest unoccupied (LUMO) are contributed by the p orbitals of M and 1s atomic orbitals of H. The following observations are made from the results of *ab initio* calculations presented in Table 5.4: a) the interaction of Pt_5 with M-ETS-10 increases with the electropositive nature of the exchanged ion (Li < Na < K < Rb < Cs), b) the electronic charge on the cation increases with the presence of Pt_5 over $[TiO_6M_2]$ cluster, c) the electron density on Pt in these cluster models also increases in the order Li < Na < K < Rb < Cs and d) electron transfer occurs from the support to the Pt cluster.

5.5.1.3.4. Electronic structure of Pt_5 nearer to $[SiO_4]$: The cluster model representing this situation is shown in Fig. 5.13 and the stoichiometry is $[M_2TiSi_2O_{11}H_8]$. The *ab initio* calculations were performed as in the earlier case. Pt_5 plane oriented parallel to the 'a' in ab axis is energetically the most favorable orientation.

The results of these calculations are presented in Table 5.4. It is observed that the positive charge on 'M' is comparable to those given in Table 5.2, in spite of the fact that a Pt_5 cluster is included in the model. These results indicate that the electron distribution is a localized phenomenon. The binding energy values calculated for these clusters according to equation (5.4) are also presented in Table 5.4. Though the

Table. 5.4. Electronic properties of the cluster models of Pt_5-M- ETS-10

Cluster	[Pt_5:$M_2TiO_6H_6$]				[Pt_5: $M_2TiSi_2O_{11}H_8$]			
M_I and M_{II}	Total energy (a.u.)	B.E.[a] (kcal/mol)	Net charge[c] on Pt[b]	Net charge[c] on M	Total energy (a.u.)	B.E.[b] (kcal/mol)	Net charge[c] on Pt	Net charge[c] on M
Li	-749.7709	-13.4912	-0.0207	0.71	-836.9932	-7.2790	0.0032	0.69
Na	-749.7065	-22.0880	-0.0224	0.81	-836.9225	-7.8437	0.0034	0.83
K	-749.6431	-36.8970	-0.0276	0.95	-836.8461	-8.7222	0.0037	0.93
Rb	-749.6539	-43.6740	-0.0329	0.98	-836.8397	-9.1615	0.0021	0.97
Cs	-749.6172	-44.7407	-0.0314	0.98	-836.8087	-9.5380	0.0033	0.97

[a] and [b] binding energy calculated from equation (5.4) or (4.5), respectively and [c] average Mulliken population (atomic charge) on alkali and platinum atoms.

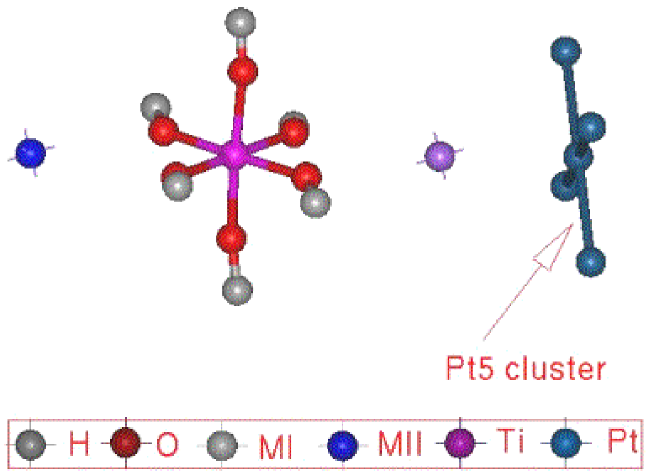

Fig. 5.12. Molecular graphics picture of [Pt_5:$M_2TiO_6H_6$] (where M = Li, Na, K, Rb or Cs) cluster model. This cluster represents the presence of Pt_5 nearer to [TiO_6]. The energetically favorable parallel orientation of Pt_5 is shown.

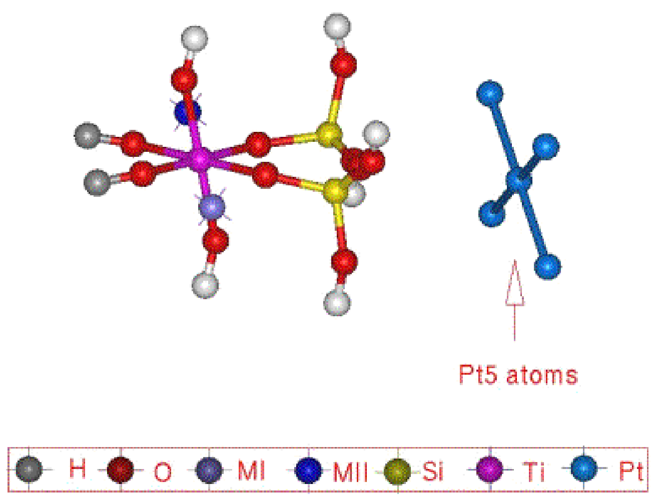

Fig. 5.13. Molecular graphics picture of [Pt_5:$M_2TiSi_2O_{11}H_8$] (where M= Li, Na, K, Rb or Cs) cluster model. This cluster represents the presence of Pt_5 nearer to [SiO_4]. The energetically favorable parallel orientation of Pt_5 is shown.

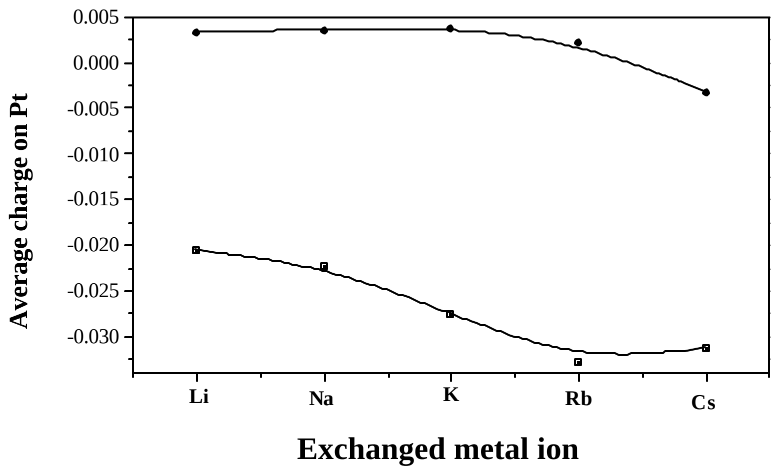

Fig. 5.14. The Variation of average charge on Pt in Pt_5 cluster [when located nearer to [TiO_6] (■) and [SiO_4] (·)] with the nature of exchanged metal cations.

binding energy values increase with increase in the electropositive nature of the exchanged metal, the values are smaller than observed for the [TiO_6] cluster (Table 5.4). This indicates that the preferred location of Pt is nearer to TiO_6 rather than SiO_4.

A comparison of the average charge on Pt in Pt_5 located near the [TiO_6] and [SiO_4] is presented in Fig. 5.14. The charge on Pt is slightly positive when present closer to [SiO_4] and it is slightly negative when closer to [TiO_6] (Fig. 5.14). Also, the charge becomes more negative with increase in the size of the cation (Li to Cs) when Pt_5 is closer to [TiO_6]. The value is nearly the same for Li, Na and K and decreases only for Rb and Cs when the Pt_5 cluster is close to [SiO_4] (Fig. 5.14).

5.5.2. Analysis of a Large Cluster: In the small cluster model used, the influence of Si/Ti ratio could not be investigated. Hence, a larger cluster [$M_2TiSi_4O_{16}H_{10}$] with Si/Ti ratio of 4.0 close to the typical value of 5 reported for ETS-10 was used in the modeling studies and *ab initio* calculations. This larger cluster with a more realistic

Si/Ti ratio is expected to simulate the experimental activity of Pt-M-ETS-10 better than the smaller clusters and to produce more accurate data on the influence of the exchanged cations. The cluster model is already discussed in chapter 2 (section 2.6.4).

5.5.2.1. Influence of exchanged cations on [TiO_6] and [SiO_4]: Molecular graphics picture of the cluster model is shown in Fig. 5.15. The stoichiometry of the cluster model is [$M_2TiSi_4O_{16}H_{10}$] [where M = Li, Na, K, Rb, Cs, Mg(OH), Ca(OH), Sr(OH) and Ba(OH)] and the electronic properties were calculated as for smaller cluster models. The alkali metal cations have been systematically varied. One alkali cation has been kept constant as Na or K in M_{II} site (Fig. 5.15) and the other one varied from Li to Cs and from Mg(OH) to Ba(OH). The results of the calculations are presented in Table 5.5. The electronic charge on alkali metal increases from Li to Cs and Mg(OH) to Ba(OH) (Table 5.5). The binding energy of the alkali metal ion with the cluster

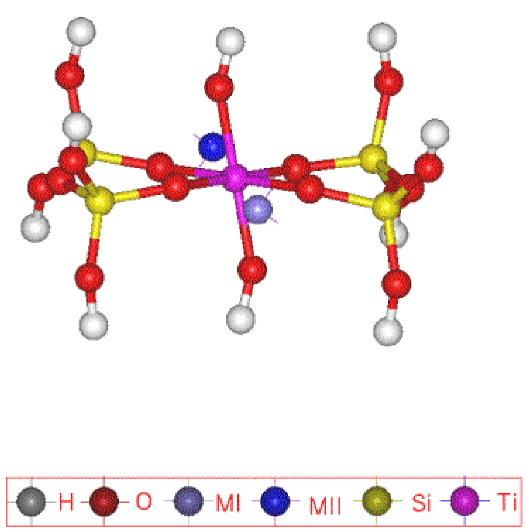

Fig. 5.15. Molecular graphics picture of [$TiSi_4O_{16}H_{10}M_2$] cluster [where M= Li to Cs and Mg(OH) to Ba(OH)].

Table 5.5. Electronic properties of the cluster model, [$M_2TiSi_4O_{16}H_{10}$]

M_I	M_{II}	Total energy (a.u.)	B.E. (kcal/mol)[a]	M_I /M_{II} [b]
H	H	-330.3189	-467.2091	0.43
Li	Li	-330.2071	-397.0582	0.67
Na	Na	-330.1071	-334.3121	0.81
K	K	-330.0596	-304.5083	0.93
Rb	Rb	-330.0591	-304.1944	0.97
Cs	Cs	-330.0261	-283.4881	0.97
Li	Na	-330.1691	-373.2153	0.69
K	Na	-330.0643	-307.4574	0.83
Rb	Na	-330.0801	-317.3712	0.84
Cs	Na	-330.0823	-318.7510	0.83
Li	K	-330.1353	-352.0074	0.83
Na	K	-330.0973	-328.1631	0.90
Rb	K	-330.0592	-304.2572	0.91
Cs	K	-330.0302	-286.0601	0.93
Mg(OH)	Mg(OH)	-363.8039	-460.7201	1.37
Ca(OH)	Ca(OH)	-363.5421	-437.0191	1.64
Sr(OH)	Sr(OH)	-363.3370	-399.9631	1.80
Ba(OH)	Ba(OH)	-363.3225	-381.2160	1.82

[a] binding energy calculated from equation (5.5) and [b] average Mulliken population (atomic charge) on alkali atoms.

model is calculated according to equation (5.5). The binding energy decreases generally with increasing size of the cations (Table 5.5).

$$BE = T.E.\ [M_2TiSi_4O_{16}H_{10}] - \{T.E\ [TiSi_4O_{16}H_{10}]^{2-} + T.E.\ [M_I]^{+} + T.E.\ [M_{II}]^{+}\} \quad (5.5)$$

5.5.2.2. Electronic structure of Pt: The electronic properties are calculated when a single Pt atom is located nearer to the [TiO_6] group (Fig. 5.16) or nearer to a [SiO_4] group (Fig. 5.17). The influence of different exchanged metal ions is studied. The results are presented in Tables 5.6 and 5.7, respectively. Similarly, the electronic properties are calculated when a Pt_5 cluster is located nearer to the $[TiO_6]$ group (Fig. 5.18) or to a $[SiO_4]$ group (Fig. 5.19). Here too, the influence of different exchanged metal ions is studied. The results are presented in Tables 5.8 and 5.9, respectively. Overall, the trends in the binding energy values and charge on exchanged metal as

Table 5.6. Electronic properties of cluster model, $[Pt:M_2TiSi_4O_{16}H_{10}]$ Pt nearer a $[TiO_6]$

M_I	M_{II}	Total Energy (a.u.)	B.E.[a] (kcal/mol)	Net charge[b] on Pt	M_I	M_{II}
H	H	-449.5059	-241.2702	0.29	0.52	0.34
Li	Li	-450.0178	-632.3291	0.19	0.68	0.46
Na	Na	-449.9349	-643.0510	0.16	0.84	0.75
K	K	-449.8566	-623.7401	0.02	0.93	0.86
Rb	Rb	-449.8669	-630.5111	0.02	0.97	0.89
Cs	Cs	-449.8289	-627.3760	0.00	0.97	0.94
Li	Na	-449.5259	-435.1942	0.15	0.68	0.60
K	Na	-449.5115	-400.9041	0.13	0.86	0.75
Rb	Na	-449.4999	-390.9970	0.04	0.94	0.82
Cs	Na	-449.4705	-389.6181	0.02	0.97	0.91
Li	K	-449.4659	-396.3872	0.11	0.67	0.74
Na	K	-449.4609	-380.2130	0.10	0.68	0.83
Rb	K	-449.4592	-374.1014	0.03	0.96	0.95
Cs	K	-449.4498	-373.2841	0.00	0.98	0.96
Mg(OH)	Mg(OH)	-483.3123	-442.7872	0.03	0.97	0.89
Ca(OH)	Ca(OH)	-483.0351	-433.1070	0.03	0.97	0.94
Sr(OH)	Sr(OH)	-482.9010	-378.4821	0.02	1.79	1.79
Ba(OH)	Ba(OH)	-482.6137	-306.6030	0.02	1.81	1.81

[a] binding energy calculated from equation (5.6) and [b] Mulliken population (atomic charge) on alkali and platinum atoms.

well as platinum are similar to the observations made on the smaller clusters, although the absolute values are different. Hence, it may be concluded that the electronic property of Pt is a localized phenomena. However, such large cluster models are more realistic and provide more reliable data.

BE= T.E. [$M_2TiSi_4O_{16}H_{10}$: Pt/Pt_5] - {T.E [$M_2TiSi_4O_{16}H_{10}$] + T.E [Pt/Pt_5]} (5.6)

Table 5.7. Electronic properties of cluster model, [Pt:$M_2TiSi_4O_{16}H_{10}$] Pt nearer to [SiO_4]

M_I	M_{II}	Total energy (a.u.)	B.E.[a] (kcal/mol)	Net charge[b] on		
				Pt[c]	M_I	M_{II}
H	H	-449.5060	-211.7202	0.01	0.44	0.41
Li	Li	-450.1178	-532.3219	0.21	0.54	0.54
Na	Na	-449.0934	-513.0510	0.19	0.79	0.79
K	K	-449.0661	-503.7401	0.16	0.86	0.86
Rb	Rb	-449.0536	-501.5111	0.12	0.93	0.93
Cs	Cs	-449.0289	-497.3760	0.02	0.96	0.96
Li	Na	-449.0105	-415.1942	0.16	0.65	0.66
K	Na	-449.0906	-379.9041	0.12	0.86	0.67
Rb	Na	-449.0700	-370.0197	0.06	0.94	0.72
Cs	Na	-449.0515	-369.1108	0.04	0.97	0.77
Li	K	-449.1091	-396.3273	0.13	0.67	0.74
K	K	-449.0906	-380.2011	0.11	0.88	0.75
Rb	K	-449.0505	-374.1031	0.03	0.96	0.77
Cs	K	-449.0219	-322.2841	0.00	0.98	0.80
Mg(OH)	Mg(OH)	-482.6123	-303.8874	0.02	1.36	1.38
Ca(OH)	Ca(OH)	-482.3506	-297.9501	0.02	1.63	1.63
Sr(OH)	Sr(OH)	-482.3104	-278.1510	0.02	1.79	1.79
Ba(OH)	Ba(OH)	-482.1370	-271.7121	0.01	1.81	1.81

[a] binding energy calculated from equation (5.6); [b] Mulliken population (atomic charge) on alkali and platinum atoms and [c] average charge on Pt in Pt_5.

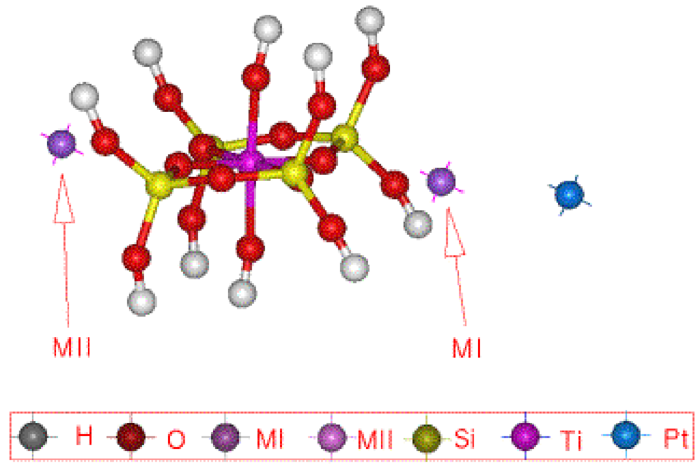

Fig. 5.16. **Molecular graphics picture of [Pt:$M_2TiSi_4O_{16}H_{10}$] (where M = Li to Cs and Mg(OH) to Ba(OH)) cluster model. This cluster represents the presence of Pt near [TiO_6].**

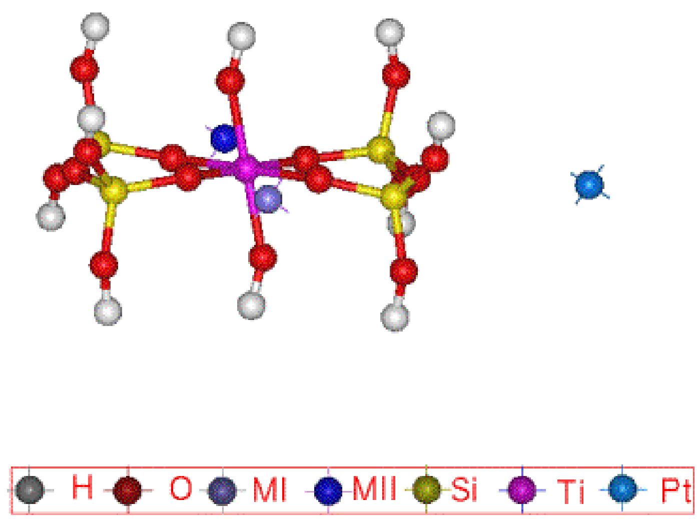

Fig. 5.17. **Molecular graphics picture of [Pt:$M_2TiSi_4O_{16}H_{10}$] (where M = Li to Cs and Mg(OH) to Ba(OH)) cluster model. This cluster represents the presence of Pt near [SiO_4].**

Table 5.8. Electronic properties of cluster model, [Pt_5:$M_2TiSi_4O_{16}H_{10}$]

Cluster	[Pt_5:$M_2TiSi_4O_{16}H_{10}$] (Pt_5 near to [TiO_6])					[Pt_5:$M_2TiSi_4O_{16}H_{10}$] (Pt_5 near to [SiO_4])				
M_I and M_{II}	Total energy	B.E.[a]	Net charge on			Total energy	B.E.[a]	Net charge on		
	(a.u.)	(kcal/mol)	Pt[a]	M_I	M_{II}	(a.u.)	(kcal/mo)	Pt[b]	M_I	M_{II}
H	-924.7463	-21.3751	0.025	0.62	0.52	-924.7895	-24.4610	0.006	0.53	0.53
Li	-924.3369	-38.7793	-0.012	0.69	0.24	-924.2921	-3.6897	0.001	0.68	0.68
Na	-924.2390	-30.0961	-0.024	0.75	0.34	-924.2085	-2.2425	0.001	0.82	0.82
K	-924.1706	-16.9917	-0.034	0.93	0.44	-924.1409	-1.6302	0.000	0.93	0.93
Rb	-924.1580	-9.4051	-0.046	0.97	0.53	-924.1429	-0.0627	-0.001	0.97	0.97
Cs	-924.1381	-12.6187	-0.056	0.97	0.65	-924.1117	-1.0659	-0.003	0.96	0.96
Mg(OH)	-957.9556	-39.3756	-0.011	1.33	1.21	-957.9331	-18.2150	0.001	1.39	1.40
Ca(OH)	-957.7537	-36.8702	-0.019	1.66	1.59	-957.6420	-10.0947	0.001	1.66	1.66
Sr(OH)	-957.5871	-21.3826	-0.022	1.80	1.75	-957.5890	-6.3327	-0.002	1.80	1.80
Ba(OH)	-957.4652	-29.9079	-0.031	1.85	1.83	-957.4151	-5.2041	-0.003	1.85	1.85

[a] binding energy calculated from equation (5.6); [b] Mulliken population (atomic charge) on alkali and platinum atoms and [c] average charge on Pt in Pt_5.

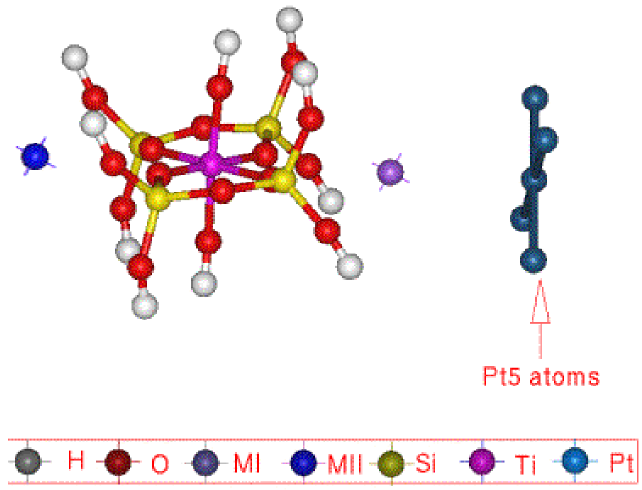

Fig. 5.18. **Molecular graphics picture of [Pt_5:$M_2TiSi_4O_{16}H_{10}$] (where M = Li to Cs and Mg(OH) to Ba(OH)). This cluster represents the presence of Pt_5 nearer to [TiO_6]. The energetically favorable parallel orientation of Pt_5 cluster is shown.**

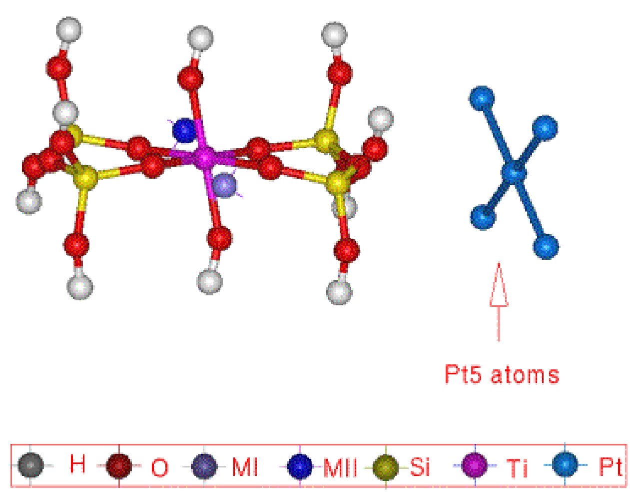

Fig. 5.19. **Molecular graphics picture of [Pt_5:$M_2TiSi_4O_{16}H_{10}$] (where M = Li to Cs and Mg(OH) to Ba(OH)) cluster model. This cluster represents the presence of Pt_5 nearer to [SiO_4]. The energetically favorable parallel orientation of Pt_5 cluster is shown.**

5.5.2.3. Behavior of adsorbed benzene over Pt-M-ETS-10:

5.5.2.3.1. Adsorption of benzene over Pt_5 located near [TiO_6]: Molecular graphics picture of benzene adsorbed over a Pt_5-ETS-10 cluster is shown in Fig. 5.20. The distance between platinum and benzene was optimized and the most favorable distance was found to be 3.75 Å. Electronic properties of the model clusters were calculated for various cations (Table 5.9). The binding energy of the C_6H_6 molecule with the Pt-zeolite clusters was calculated according to equation (5.7). The binding energy of benzene with the cluster decreases from Li to Cs and Mg(OH) to Ba(OH). This observation reveals that benzene adsorption is weaker over Pt supported on more basic supports. Comparing the electronic charge on Pt in the presence and absence of adsorbed benzene, it is found to be slightly more negative when benzene is adsorbed revealing the donation of electronic charge by benzene to Pt. This trend is similar to those observed in case of other basic zeolites (chapter 4).

B.E.=T.E. [$M_2TiSi_4O_{16}H_{10}$:Pt_5:C_6H_6/H_2S]–{T.E. [$M_2TiSi_4O_{16}H_{10}$]:Pt_5+ T.E. (C_6H_6/H_2S)} (5.7)

5.5.2.3.2. Adsorption of benzene over Pt_5 located near [SiO_4]: Molecular graphics picture of this situation is shown in Fig. 5.21. The electronic properties of cluster models were calculated for different M_I and M_{II} ions [(Li to Cs and Mg(OH) to Ba(OH)] (Table 5.9). The binding energy of benzene with the cluster decreases with increasing size and electropositive nature of the cations. Comparing the benzene binding energies with the cluster for the two cases (Pt near [TiO_6] and near [SiO_4]), it is found that the values are slightly larger when Pt is near [SiO_4] tetrahedra (Fig. 5.21). This suggests that the desorption of benzene is relatively easier when the Pt_5 cluster is placed near [TiO_6]. This should make the Pt atom near [TiO_6] relatively more active for *n*-hexane dehydrocyclization (provided benzene desorption is the rate determining step) than those near [SiO_4]. The average charge on Pt in Pt_5 (near [TiO_6]

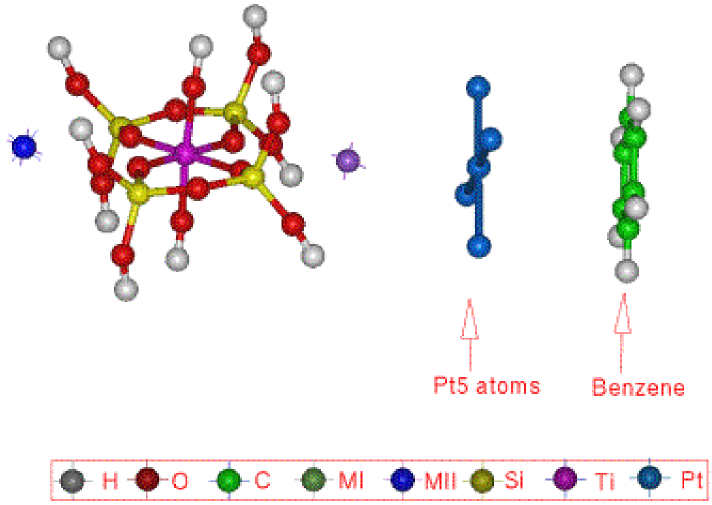

Fig. 5.20. **Molecular graphics picture of [C_6H_6:Pt_5:$M_2TiSi_4O_{16}H_{10}$] [where M= Li to Cs and Mg(OH) to Ba(OH)] cluster model. This cluster represents the presence of Pt_5 nearer to [TiO_6] and benzene is adsorbed over the Pt_5 atoms.**

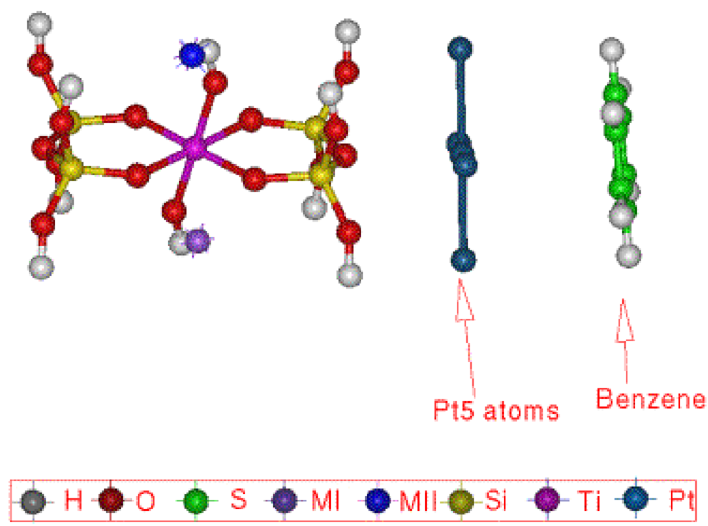

Fig. 5.21. **Molecular graphics picture of [C_6H_6:Pt_5:$M_2TiSi_4O_{16}H_{10}$] [where M= Li to Cs and Mg(OH) to Ba(OH)] cluster model. This cluster represents the presence of Pt_5 nearer to [SiO_4] and benzene is adsorbed over the Pt_5 atoms.**

Table 5.9. Electronic properties of cluster models, [C_6H_6: Pt_5: $M_2TiSi_4O_{14}H_{10}$]

Cluster	[C_6H_6:Pt_5:$M_2TiSi_4O_{14}H_{10}$] (Pt_5 near to [TiO_6])					[C_6H_6: Pt_5:$M_2TiSi_4O_{14}H_{10}$] (Pt_5 near to [SiO_4])				
M_I and	T.E.	B.E.[a]	Net charge[b] on			T.E.	B.E.[a]	Net charge[b] on		
M_{II}	(a.u.)	(kcal/mol)	Pt[c]	M_I	M_{II}	(a.u.)	(kcal/mo)	Pt[c]	M_I	M_{II}
H	-961.1094	-4.6859	-0.055	0.58	0.50	-961.0727	-11.4114	0.021	0.38	0.50
Li	-960.6422	-2.4453	-0.017	0.70	0.20	-960.5798	-8.5899	-0.031	0.64	0.68
Na	-960.5432	-1.7908	-0.026	0.83	0.32	-960.5193	-5.8938	-0.036	0.81	0.83
K	-960.4735	-0.9066	-0.036	0.93	0.31	-960.4453	-1.8810	-0.036	0.93	0.93
Rb	-960.4599	-0.3583	-0.057	0.97	0.52	-960.4452	-0.5643	-0.036	0.97	0.97
Cs	-960.4428	-0.0691	-0.061	0.98	0.64	-960.4121	-0.6271	-0.036	0.98	0.98
Mg(OH)	-994.2791	-13.8755	-0.014	1.31	1.29	-994.2633	-18.1203	-0.033	1.36	1.38
Ca(OH)	-994.0751	-12.5401	-0.020	1.59	1.59	-993.9595	-14.0947	-0.030	1.63	1.63
Sr(OH)	-993.9045	-10.0320	-0.023	1.77	1.78	-993.9093	-11.8503	-0.030	1.76	1.77
Ba(OH)	-993.7805	-8.7153	-0.030	1.80	1.79	-993.7321	-9.8439	-0.031	1.82	1.83

[a] binding energy calculated from equation (5.7); [b] Mulliken population (atomic charge) on alkali and platinum atoms and [c] average charge on Pt in Pt_5.

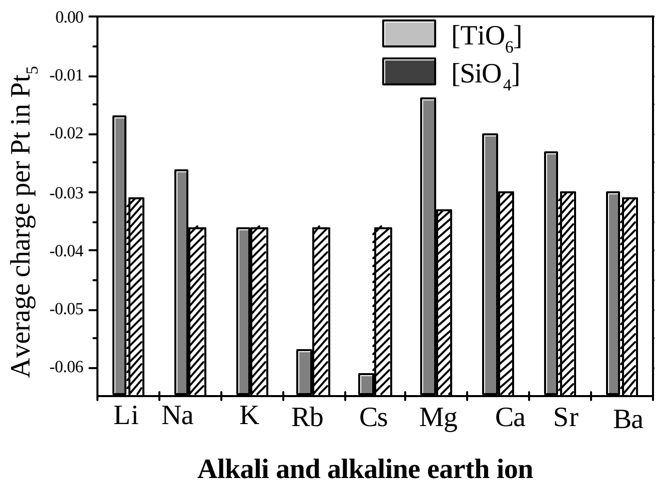

Fig. 5.22. Comparison of average charge on Pt in Pt_5 (When benzene is adsorbed on Pt_5 clusters near $[TiO_6]$ and $[SiO_4]$).

and near $[SiO_4]$) for different cations in the cluster is presented as a bar graph in Fig. 5.22. The electron density on Pt significantly increases from Li to Cs and from Mg(OH) to Ba(OH) when Pt_5 placed near $[TiO_6]$ than $[SiO_4]$.

5.5.2.4. Behavior of adsorbed H_2S over Pt-M-ETS-10: Molecular graphics pictures of H_2S adsorbed on Pt_5 located near $[TiO_6]$ and $[SiO_4]$ groups are shown in Figs. 5.23 and 5.24, respectively. The binding energy of the H_2S molecule with Pt-zeolite clusters was calculated according to the equation (5.7). The electronic properties of the model clusters were calculated for various cations M_I and M_{II} [(Li to Cs and Mg(OH) to Ba(OH)] (Table 5.10). Comparing the binding energies of H_2S adsorbed on Pt_5 located near the two sites, namely $[TiO_6]$ and $[SiO_4]$, it is found that a larger poisoning effect is generally observed for H_2S on Pt near $[TiO_6]$. The negative charge on the S atom increases with increase in the electropositive character of the cation [(Li to Cs and Mg(OH) to Ba(OH)]. Besides, comparing tables 5.8 and 5.10, the charge on Pt becomes more positive in the presence of S, the effect being more noticed when Pt_5 is located

Table 5.10. Electronic properties of $[H_2S:Pt_5:M_2TiSi_4O_{14}H_{10}]$ clusters.

Cluster	$[H_2S: Pt_5:M_2TiSi_4O_{14}H_{10}]$ (Pt$_5$ near $[TiO_6]$)						$[H_2S: Pt_5:M_2TiSi_4O_{14}H_{10}]$ (Pt$_5$ near $[SiO_4]$)					
M_I and	Total energy	B.E.[a]	Charge[b] on				Total energy	B.E.[a]	Net charge[b] on			
M_{II}	(a.u.)	(kcal/mol)	Pt[c]	S	M_I	M_{II}	(a.u.)	(kcal/mo)	Pt[c]	S	M_I	M_{II}
H	-935.8304	-242.3360	0.02	-0.18	0.64	0.51	-935.8323	-216.44	0.009	0.14	0.45	0.45
Li	-935.3712	-211.1112	0.16	-0.17	0.65	0.31	-935.3395	-219.325	0.006	-0.14	0.68	0.68
Na	-935.3077	-232.6801	0.12	-0.18	0.84	0.34	-935.2656	-219.137	0.007	-0.14	0.81	0.81
K	-935.2223	-222.0210	0.10	-0.19	0.93	0.40	-935.1917	-221.456	0.008	-0.14	0.93	0.93
Rb	-935.2093	-221.7701	0.08	-0.21	0.94	0.52	-935.1915	-220.077	0.007	-0.13	0.97	0.97
Cs	-935.1897	-221.9581	0.06	-0.22	0.97	0.63	-935.1585	-218.948	0.007	-0.17	0.96	0.96
Mg(OH)	-969.0225	-231.5512	0.10	-0.19	1.34	1.21	-968.9885	-224.529	0.008	-0.14	1.40	1.41
Ca(OH)	-968.7537	-189.6051	0.05	-0.19	1.66	1.59	-968.6728	-221.77	0.013	-0.14	1.63	1.63
Sr(OH)	-968.6314	-217.3810	0.01	-0.20	1.80	1.74	-968.6258	-218.823	0.013	-0.15	1.80	1.80
Ba(OH)	-968.5094	-217.3182	0.00	-0.21	1.89	1.83	-968.5011	-218.698	0.013	-0.16	1.85	1.85

[a] binding energy calculated from equation (5.7); [b] Mulliken population (atomic charge) on alkali and platinum atoms and [c] average charge on Pt in

Pt_5.

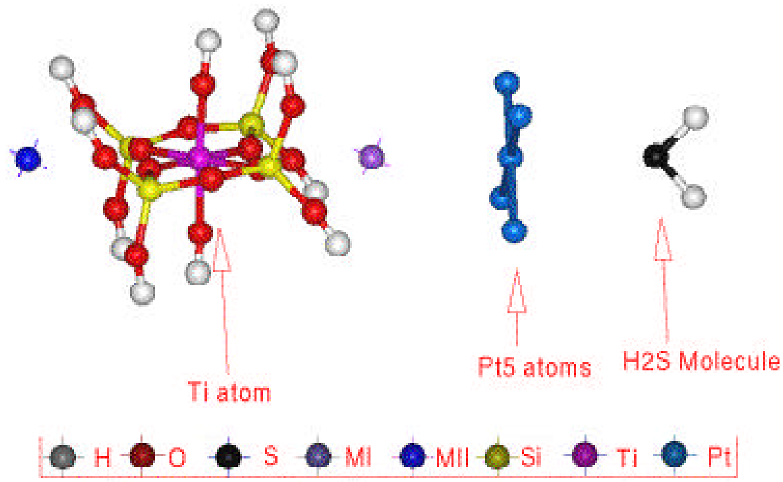

Fig. 5.23. Molecular graphics picture of [H_2S:Pt_5:$TiSi_4O_{16}H_{10}M_2$] (where M = Li to Cs and Mg(OH) to Ba(OH)). This cluster represents the presence of Pt_5 nearer to [TiO_6] and H_2S adsorbed the Pt_5 atom.

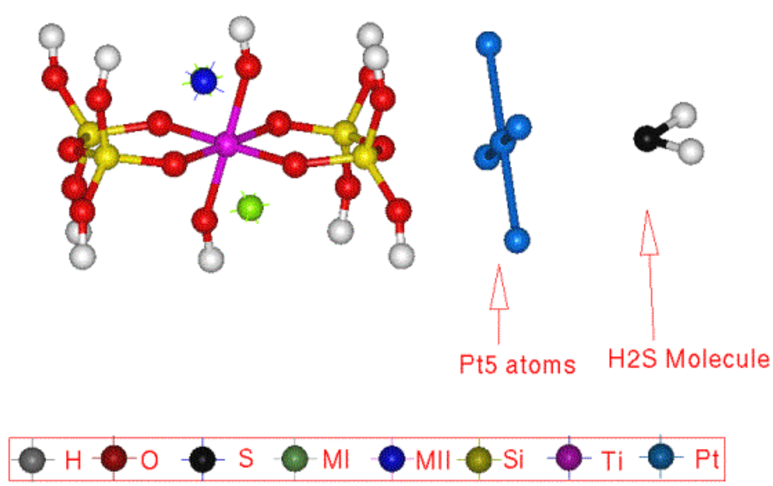

Fig. 5.24. Molecular graphics picture of [H_2S:Pt_5:$TiSi_4O_{16}H_{10}M_2$] (where M = Li to Cs and Mg(OH) to Ba(OH)). This cluster represents the presence of Pt_5 nearer to [SiO_4] and H_2S adsorbed over the Pt_5 atoms.

closer to [TiO_6]. It is well known that Pt highly dispersed in acidic zeolites is sulfur resistant.[7,8] This is explained by the presence of a very weak bond between electronegative S atoms and the electron deficient Pt particles.[7] One may expect that, by contrast, a strong bond would exist between S and electron-rich Pt clusters. In fact, it is known that highly dispersed Pt supported on basic zeolites is highly sensitive to sulfur.[9-12] This is related to the large Pt $\rightarrow$ S electron transfer.[13] The well-known Pt agglomeration upon sulfur poisoning[9,10] may then be suggested to be due to a weakening of the Pt support bond. It is also proposed that sulfur competes with Pt as an electron acceptor for the electron transfer from the zeolite surface.[14]

5.5.2.5. Electron density on Pt and S_{int} in Pt-M-ETS-10: Plots of the average charge per Pt atom versus S_{int} (calculated according to Mortier[15]) are presented in Fig. 5.25 for Pt_5 in the two locations in the [Pt_5:$TiSi_4O_{16}H_{10}M_2$] cluster. The plots reveal the general trend of decreasing positive charge (increasing electron density) on Pt with decreasing S_{int} suggesting less electron transfer from Pt to the support with increasing support basicity. In fact, in some cases, (Rb, Cs, Sr and Ba-ETS-10) the charge on Pt is negative (electron rich) suggesting that electron transfer occurs from the support to Pt. The plots are different for the alkali and alkaline earth metal ions. In general, it is seen that the charge on Pt is more negative when Pt_5 is located near [TiO_6].

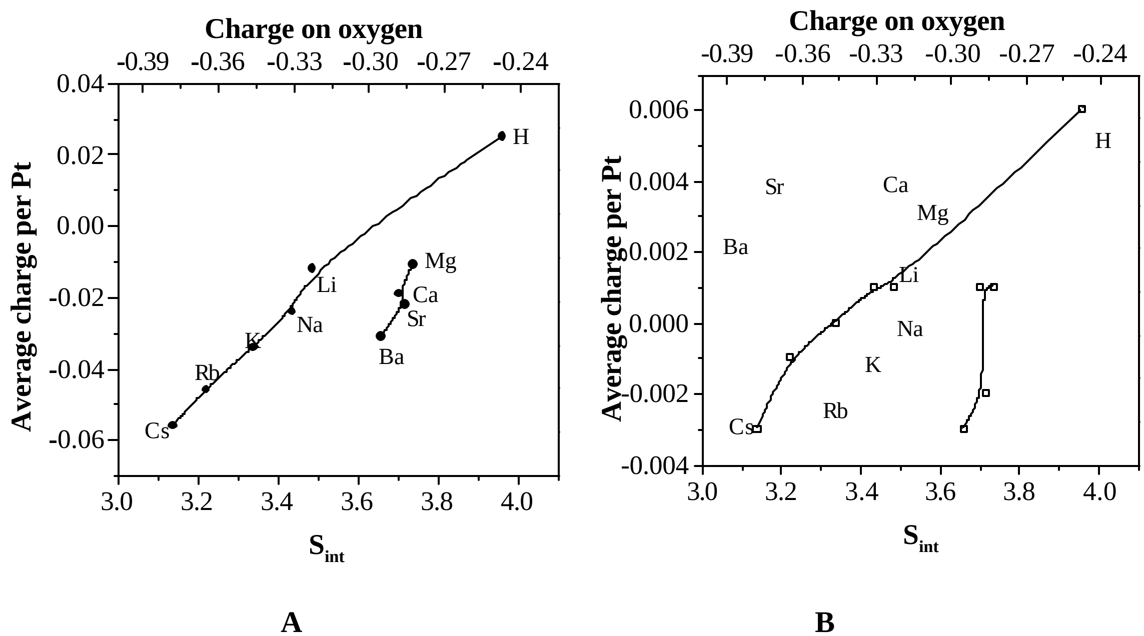

Fig. 5.25. Relationship between average charge per Pt in Pt_5 atom cluster and S_{int}/ charge on oxygen. (A) when Pt_5 is located near $[TiO_6]$ and (B) when Pt_5 is located near $[SiO_4]$.

5.6. CONCLUSIONS

Pt-Ba-ETS-10 and Pt-Cs-ETS-10 show the highest benzene selectivity among the alkali and alkaline earth metal exchanged ETS-10 samples. *n*-Hexane conversion and benzene selectivity increase with basicity of the Pt-M-ETS-10 samples (Li to Cs and Mg to Ba). The highest conversion of *n*-hexane (99.3 %) was observed at 833 K over Pt-Cs-ETS-10. Benzene yield is found to be a function of the intermediate electronegativity (S_{int}) of M-ETS-10, suggesting an increasing transfer of electronic charge from the basic support to the metal with increasing electropositive character of the alkali metal. Pt-Ba-ETS-10 and Pt-Cs-ETS-10 are many times more active than a Pt-Al_2O_3 in the aromatization on *n*-hexane.

The salient features of the computational studies can be summarized as follows:

1) The binding energy of the alkali metal ions with ETS-10 lattice is the largest for Li and the smallest for Cs.

2) The net charge on the alkali metals is positive. The charge increases from Li to Cs is in the order: Li< Na < K < Rb = Cs.

3) The electron transfer from the basic support to the Pt is probably the main reason for its excellent *n*-hexane aromatization activity. Pt atom or Pt_5 cluster have two locations inside the 12-MR channel of ETS-10. There is transfer of electron from ETS-10 to Pt in one of the sites (nearer to $[TiO_6]$) and there is transfer of electron from Pt to ETS-10 in the other site (nearer to $[SiO_4]$). Thus there is a clear preference for the location of platinum inside M-ETS-10 lattice.

4) The binding energy of platinum with ETS-10 lattice is the smallest for Li-ETS-10 and the largest for Cs-ETS-10.

A larger cluster model was used to simulate a realistic Si/Ti ratio. The qualitative correlations remained the same although absolute values of calculated properties are different. The larger clusters certainly served as better models for studying the adsorption of organic molecules. The adsorption of benzene and H_2S over the platinum was studied using these large cluster models. The following conclusions can be derived:

1) Binding energy values for the adsorption of benzene over Pt supported on highly basic zeolites are low. These results suggest that a weaker adsorption of benzene happens on electron-rich Pt clusters. The weaker adsorption of benzene could

translate into larger activity of these catalysts due to faster desorption of the product benzene from the active centers (Pt).

2) Binding energy values for the adsorption of H_2S are larger for Pt supported over basic than for Pt supported over acidic zeolite. Electron transfer takes place from Pt to S and is more when Pt is supported on a basic support. This suggests that Pt supported on basic catalysts is more vulnerable to sulfur poisoning.

5.7. REFERENCES

1. C. Besoukhanova, J. Guidot, D. Barthomeuf, M. Breysse and J.R. Bernard, *J Chem. Soc. Faraday Trans. I*, 77 (1981) 1595.
2. W.J. Han, A.B. Kooh and R.F. Hicks, *Catal. Lett.*, 18 (1993) 193.
3. D. Barthomeuf and A. de Mallmann, *Stud. Surf. Sci. Catal.*, 37 (1988) 365.
4. M.W. Anderson O. Terasaki, T. Ohsuna, A. Philippou, S.P. Mackay, A. Ferreira, J. Rocha and S. Lidin, *Nature*, 367 (1994) 347.
5. M.W. Anderson O. Terasaki, T. Ohsuna, P.J.O. Malley, A. Philippou, S.P. Mackay, A. Ferreira, J. Rocha and S. Lidin, *Philos. Mag., B*, 71 (1995) 813.
6. C. Mealli and D.M. Proserpio, *J. Chem. Ed*., 67 (1990) 399.
7. P. Gallezot, J. Datka, J. Massardier, M. Primet and B. Imelik, in "*Proceedings of 6th International Congress on Catalysis*", G.C. Bond, P.B. Wells and E.C. Tompkins eds., London, *Chem.. Soc., 2* (1977), Vol. 2 p. 696.
8. J.A. Rado, V. Schomaker and P.E. Pickert, in "*Proceedings 3rd International Congress on Catalysis*", 2 (1965) 1264.
9. M. Vaarkamp, J.T. Miller, F.S. Modica, G.S. Lane and D.C. Koningsberger, *J. Catal.*, 138 (1992) 675.
10. G.B. Mc Vicker, J.L. Kao, J.J. Ziemak, W.E. Gates, J.L. Robbins, M.M. J. Treacy, S.B. Rice, T.H. Vanderspurt, V.R. Cross and A.K. Ghosh, *J. Catal.*, 139 (1993) 48.
11. J.L. Kao, G.B. McVicker, M.M.J. Treacy, S.B. Rice J.L. Robbins, W.E. Gates,

J.J. Ziemax, J.R. Cross and T.H. Vanderspurt, *Stud. Surf. Sci. Catal.*, 75 (1993) 1019.

12. T.R. Hughes, W.C. Buss, P.W. Tamm and R.L. Jacobson, *Stud. Surf. Sci. Catal.*, 28 (1986) 725.
13. D. Barthomeuf, *Stud. Surf. Sci. Catal.*, 65 (1991) 157.
14. G. Larsen and G.L. Haller, Catal. Lett., 3 (1989) 103.
15. W.J. Mortier, *J. Catal.*, 55 (1978) 38.
16. L. Uytterhoeven, D. Dompas and W.J. Mortier, *J. Chem. Soc. Faraday Trans.*, 88 (1992) 2753.

CHAPTER 6

SUMMARY AND

CONCLUSIONS

6.0 SUMMARY AND CONCLUSIONS

The aromatization of *n*-hexane over a number of Pt loaded microporous solid base catalysts have been examined in this thesis. Both experimental and computational tools have been utilized to design, make, characterize and evaluate these catalysts. The four types of zeolite catalysts investigated in this thesis are LTL, BEA, FAU and ETS-10. These catalysts had H, Li, Na, K, Rb, Cs, Mg(OH), Ca(OH), Sr(OH) and Ba(OH) as the non-framework cations to impart different levels basicity in them.

The salient aspects of the preparation and characterization of the samples can be summarized as:

1) Four types of zeolites with different structures (LTL, BEA, FAU and ETS-10) were prepared by hydrothermal synthesis followed by calcination.
2) They were exchanged with hydrogen, five alkali metal ions (Li, Na, K, Rb and Cs) and four alkaline earth metal ions (Mg, Ca, Sr and Ba).
3) All these catalysts were loaded with platinum using tetraamine platinum (II) chloride as the impregnating agent.
4) The above catalysts were characterized by XRD, N_2 adsorption, SEM, UV-Vis., FTIR, TPD, platinum metal dispersion and MAS-NMR techniques and the following inferences were made:
   a) All samples were highly crystalline, though a decrease in XRD intensity with the size of the cation was noticed.
   b) The surface areas of the catalysts also decreased with increasing size of the exchanging cations.
   c) The synthesized zeolites had uniform particle sizes: ETS-10 catalyst particles were larger (8-10 μm) than the other zeolite particles (1-2 μm).

d) Prominent IR absorption bands (framework) in the region of 950-1150 cm^{-1} and 300-400 cm^{-1} were observed indicating the typical microporous nature of the silicates. The band in the 950-1150 cm^{-1} region shifted to higher frequencies with increasing size of the exchanged cation.

e) The FTIR spectra of CO_2 adsorbed on different ion exchanged zeolites revealed the presence of different types of adsorption sites on the samples.

f) The basicity of the catalyst can be directly related to the size of the exchanged cation. The larger the size of the exchanged cation, the higher the basicity of the catalyst.

g) The basicity of the catalysts was also correlated to Sanderson's intermediate electronegativity (S_{int}) and calculated charge on oxygen.

h) There are more than one type of basic sites in these zeolite catalysts as revealed by the TPD of CO_2. The exchanged cation remaining the same, the basic strength among different zeolites increased in the order FAU < BEA < ETS-10 < LTL.

i) H_2 Chemisorption revealed the dispersion of Pt in the samples to be in the range of 0.5 to 0.9, the dispersion increasing with the basicity of the catalyst.

Thus the usefulness of the characterization tools for ranking the basicity and the efficiency of the catalysts is clearly brought out.

Evaluations of the catalytic activity of these zeolites were undertaken. The conclusions of these studies are:

1) Among the zeolites investigated, LTL is the most active one for *n*-hexane aromatization. The order of ranking of the different zeolites with respect to aromatization activity is: Pt-M-FAU < Pt-M-BEA < Pt-M-ETS-10 < Pt-M-LTL.

2) Conversion of *n*-hexane increases with the basicity of the samples in the order: Li < Na < K < Rb < Cs and Mg < Ca < Sr < Ba. Benzene selectivity also increases with basicity in the above order. Side reactions such as cracking and isomerization are less over the Pt-alkaline zeolites that Pt-Al_2O_3.
3) These results suggest that basicity (electronic properties) and structural factors are important in aromatization of alkanes over basic zeolites.
4) Pt-Ba-zeolite and Pt-Cs-zeolite showed the highest benzene selectivity among the alkali and alkaline earth metals exchanged. The highest conversion of *n*-hexane (99.3 %) was observed at 833 K over Pt-Cs-ETS-10.
5) The Pt-Ba-Zeolites and Pt-Cs-Zeolites were many times more active than a commercial Pt-Al_2O_3 in aromatization on *n*-hexane.
6) Values of Sanderson electronegativity and oxygen charge of different ion exchanged zeolites (LTL, BEA, FAU and ETS-10) reveal a relationship between benzene yield and basicity of the catalyst. Benzene yield is found to be a function of the intermediate electronegativity (S_{int}) and charge on oxygen of the Pt-M-zeolite, suggesting an increasing transfer of electronic charge from the basic support to the metal with increasing electropositive character of the alkali metal.

The salient features and conclusions of the computational studies are summarized as follows:

1) The isomorphous substitution of Al atom in the place of silicon prefers the T_1 site of LTL. When two Al atoms are isomorphically substituted, they prefer the locations farthest from each other. As far as the binding energy of these cations are considered, cations present in M_{II} site is more strongly bound to the zeolite than those at M_I. The binding energy of the cation with the zeolite cluster decreases from Li to Cs and Mg(OH) to Ba(OH). The charge on the cation increases from Li

to Cs and Mg(OH) to Ba(OH). The charge on M_{II} cationic site is more electropositive than M_I site. This indicates that cations in M_{II} site may exhibit higher catalytic activity (acidity).

2) The net electron transfer between the Pt_5 cluster and the M-zeolite depends on the zeolite and the nature of the exchanged metal ion. The net electron transfer from Pt to M-zeolite increases in the order, H > Li > Na > K > Rb ~ Cs in the case of the alkali metal ions and in the order Mg(OH) > Ca(OH) > Sr(OH) > Ba(OH) for the alkali metal ions. The most active and selective catalysts are the Cs and Ba exchanged catalysts. In these catalysts, the transfer of electron is from the M-zeolite to the Pt_5 cluster, making Pt electron rich.

3) Binding energy values for the adsorption of benzene over Pt supported on highly basic zeolites are low. This suggests that a weaker adsorption of benzene occurs on electron-rich Pt clusters. The weaker adsorption of benzene could translate into larger activity of these catalysts due to faster desorption of the product benzene from the active centers (Pt).

4) Binding energy values for the adsorption H_2S are larger for Pt supported over more basic zeolites than over less basic ones. Electron transfer takes place from Pt to S and is more when Pt is supported on a basic support. This suggests that Pt supported on basic catalysts is more vulnerable to sulfur poisoning.

5) In the case of ETS-10, the electron transfer from the support to the Pt is influenced by the location of Pt. When the Pt is located near a [TiO_6] Oh rather than a [SiO_4] Td, the electron transfer from ETS-10 to Pt is more efficient. Thus the interaction between [TiO_6] and Pt is more favorable than that between [SiO_4] and Pt. There is also a clear preference for the location of small Pt clusters nearer to [TiO_6] inside

M-ETS-10 lattice. It is likely that in Pt-M-ETS-10, the Pt cluster located near [TiO_6] Oh will be more catalytically active than the one located near [SiO_4] Td.

6) Thus, the important role played by the electronic structure of Pt on *n*-hexane aromatization is clearly brought out. The various factors such as the structure of the zeolite, basicity of the zeolite, Pt dispersion etc. that influence the electronic structure of Pt have been identified, suitable metrics devised and quantified based on the *ab initio* calculations. These results provide the design space of Pt-M-zeolite for reforming catalysts and the calculations may be used as a screening tool.

LIST OF PUBLICATIONS

1 Influence of the nature of the exchanged ion on *n*-hexane aromatization activity of Pt-ETS-10

S.B. Waghmode , T.K. Das, R. Vetrivel and S. Sivasanker,
Journal of Catalysis 185 (1999) 265.

2 Molecular modeling studies on zeolite catalysis for shape-selective electrophilic substitution: I acylation of 2-methoxynaphthalene

P. Bharathi, **S.B. Waghmode**, S. Sivasanker and R. Vetrivel,
Bulletin of Chemical Society of Japan, 72 (1999) 2161.

3 Molecular modeling of adsorption and diffusion processes in zeolites relevant to environment protection
R. Vetrivel, R.C. Deka, **S.B. Waghmode** , S. Sivasanker, K. Mizukami, H. Takaba, M. Kubo and A. Miyamoto,
Studies in Surface Science Catalysis, 120 B (1999) 445.

4 Alkylation of long chain olefins over Al-pillared montmorillonite clay
S.P. Katadare, **S.B. Waghmode**, V. Ramaswamy, R. Vetrivel and S. Sivasanker,
"Recent Trends in Catalysis" by V. Murugesan (Ed) Narosa Publication, (1999) p. 112.

5 Molecular modeling studies on zeolite catalysis for shape-selective electrophilic substitution: xylene isomerization

S.B. Waghmode, P. Bharathi, Sivasanker and R. Vetrivel,
Microporous and Mesoporous Materials, 38 (2000) 433.

6 Influence of preparation parameters on characteristics of zirconia-pillared clay using ultrasonic technique and its catalytic performance in phenol hydroxylation reaction

S.V. Awate, **S.B. Waghmode** , K.R. Patil, M.S. Agashe and P.N. Joshi,
Korean Journal of Chemical Engineering, 18 (2001) 257.

7 *n*-Hexane aromatization over Pt-alkaline zeolites: *ab initio* calculations on the influence of the exchanged cations and zeolite type (L, β and Y) on electronic properties of Pt
S.B. Waghmode, P. Bharathi, R. Vetrivel and S. Sivasanker,
Studies Surface Science and Catalysis Vol. 135. 2001.

8 **Characterization of acidic sites in zeolites by heteronuclear double resonance solid state NMR**

S.B. Waghmode , A. Abraham, S. Sivasanker, J.P. Amoureux and S. Ganapathy, *Studies Surface Science and Catalysis, Vol. 135. 2001.*

9 Conformational isomerism and weak molecular and magnetic iteractions in ternary copper (II) complexes of [Cu(AA)L']ClO4.nH2O, where AA = L-phenylalanine and L-histidine, L' = 1,10-phenanthrolline and 2,2-bipyridine, and n=1 or 1.5: synthesis, single-crystal X-ray structures, and magnetic resonance investigations
P.S. Subramanian, E. Suresh, P. Dastidar, S.B. Waghmode **and D. Srinivas,**

Inorganic Chemistry, 40 (2001) 4291.

10 **Liquid phase oxidation of amines to azoxy compounds over ETS -10 molecular sieves**

S.B. Waghmode , S.M. Sabne and S. Sivasanker,

Green Chemistry, 3 (2001) 289.

11 **Efficient liquid phase acylation of alcohols over basic ETS -10 molecular sieves**

S.B. Waghmode , V.V. Thakur, A. Sudalai and S. Sivasanker,

Tetrahedron Letters, 42 (2001) 3145.

12 Linear alkylation of benzene with mesoporous aluminosilicate molecular sieves
K. Chaudari, T.K. Das, **S.B. Waghmode** , S. Sivasanker,
American Chemical Society Div. Pet. Chemistry 46 (2001) 299.

13 Vapor phase nitration of toluene using dilute nitric acid over beta zeolite and molecular modeling studies
S. Dagde, **S.B. Waghmode** , V. Kadam and M.K. Dongre,

Applied Catalysis A: General, 226 (2001) 49

14 *n*-Hexane aromatization by Pt-M-Zeolite catalysts: role of electronic structure of Pt as Brought out by *ab initio* calculations- Part I
S.B. Waghmode , R. Vetrivel and S. Sivasanker,
(Journal of Physical Chemistry B, in press).

15 *n*-Hexane aromatization by Pt-M-Zeolite catalysts: role of electronic structure of Pt as Brought out by *ab initio* calculations- Part II
S.B. Waghmode , R. Vetrivel and S. Sivasanker,
(Communicated to Journal of Physical Chemistry B).

16 Heck reaction over Pd loaded basic ETS-10 molecular sieves
S.B. Waghmode , S. Sabne and S. Sivasanker,
(Communicated to Green Chemistry).

17 **Influence of the exchanged cations in Pt-M-ETS-10 catalyst on *n*-hexane aromatization activity and poisoning: molecular modeling studies**

S.B. Waghmode, **T.K. Das, R. Vetrivel and S. Sivasanker,**

(To be communicated to Microporous and Mesoporous Materials.)

18 FT-IR study of different alkali exchanged ETS-10 molecular sieves and their molecular modeling studies

S.B. Waghmode , B.B. Tope, S.G. Hegde, S. Sivasanker,
(To be communicated to Journal of Physical Chemistry B).

19 Synthesis, characterization and catalytic activity of zirconia pillared montmorillonite prepared by ultrasonics for alkylation of benzene and hydro-isomerization of n-hexane

S.B.Waghmode , K.R. Kamble, Patil, M.S. Agashe, S.V. Awate,
(To be Communicated to Journal of Molecular Catalysis A).

20 **Characterization of acidic sites in MOR by REPDOR and molecular modeling studies**

S.B. Waghmode , S. Sivasanker and S. Ganapathy,
*(**Manuscript under preparation).***

PAPERS AND POSTERS PRESENTED

1 Industrial application of montmorillonite pillared clay
S.B. Waghmode and S.P. Katadare,
Oral Presented in Golden Jubilee Celebration of Pune University Dec. 98.

2 Preparation, characterization and catalytic activity of zirconia pillared montmorillonite for alkylation of benzene and hydroisomerization of *n*-hexane
S.V. Awate**, S.B. Waghmode,** K.R. Kamble, S.I. Kuriyavar & M.S. Agashe,
Poster Presented in IPCAT-2, 2001 (NCL-Pune).

3 Modeling the diffusion of key-intermediates for anti-inflammatory drugs

inside zeolites

S.B. Waghmode, P. Bharathi, R.C. Deka and R. Vetrivel,
Poster Presented in the International symposium at Pune NCL, Jan 99.

4 **Acid site characterization in zeolites using REAPDOR and MQ-REDOR**
A. Abraham, S. B. Waghmode**, S.Ganapathy, J.P. Amoureux and C. Fernandez,**
***Poster Presented in 42nd ENC Conference* (2001).**